

SUPPLEMENTAL INFORMATION:

The dissertation submitted in August 2013, and used as the basis of the papers developed in Chapters 2 to 5 is included here.

**INFRARED THERMOGRAPHY ENHANCEMENTS FOR  
CONCRETE BRIDGE EVALUATION**

By

Khatereh Vaghefi

A DISSERTATION

Submitted in partial fulfillment of the requirements for the degree of

DOCTOR OF PHILOSOPHY

In Civil Engineering

MICHIGAN TECHNOLOGICAL UNIVERSITY

2013

©2013 Khatereh Vaghefi



This dissertation has been approved in partial fulfillment of the requirements for the Degree of DOCTOR OF PHILOSOPHY in Civil Engineering.

Department of Civil and Environmental Engineering

Dissertation Advisor: *Dr. Theresa (Tess) M. Ahlborn, P.E.*

Committee Member: *Dr. Lawrence (Larry) L. Sutter*

Committee Member: *Dr. Devin K. Harris*

Committee Member: *Dr. Timothy (Tim) C. Havens*

Department Chair: *Dr. David (Dave) W. Hand, P.E.*



# Table of Contents

Table of Contents.....	v
List of Figures.....	xi
List of Tables.....	xxi
Acknowledgments.....	xxiii
Abstract.....	xxv
Chapter 1 Introduction.....	1
1.1 Motivation.....	1
1.2 Project Goals and Overview.....	2
1.3 Dissertation Organization.....	4
Chapter 2 Delaminations and Inspection Procedure.....	7
2.1 Preface.....	7
2.2 Current Bridge Inspection Methods and Reporting Systems.....	8
2.2.1 General Types of Bridge Inspection.....	13
2.2.1.1 Initial Inspection.....	13
2.2.1.2 Routine Inspection.....	13
2.2.1.3 Damage Inspection.....	13
2.2.1.4 In-depth Inspection.....	13
2.2.1.5 Special Inspection.....	14
2.2.2 Visual Inspection for Concrete Bridge Decks.....	14
2.2.2.1 Percent Deficiency and the Decision Making Process.....	17
2.2.3 Visual Inspection for Prestressed Concrete Box Beam Bridges.....	22
2.2.3.1 Percent Deficiency and the Decision Making Process.....	24
2.3 Non-Destructive Bridge Evaluation Methods.....	27

2.3.1 Impact-Echo.....	28
2.3.2 Ultrasonic Testing.....	29
2.3.3 Ground Penetrating Radar.....	30
2.4 Summary.....	31
Chapter 3 Infrared Thermography.....	33
3.1 Concepts for Concrete Bridge Evaluation.....	33
3.2 Passive Infrared Thermography.....	36
3.2.1 Advantages of Bridge Inspection with Passive Infrared Thermography.....	40
3.2.2 Limitations of Passive Infrared Thermography and Environmental Effects.....	41
3.3 Active Infrared Thermography.....	43
3.3.1 Advantages of Active Infrared Thermography.....	44
3.3.2 Limitations of Active Infrared Thermography.....	44
3.3.3 Active Infrared Thermography Methods.....	45
3.3.3.1 Pulsed Thermography (Flash Thermography).....	45
3.3.3.1.1 Applications in Civil Engineering.....	48
3.3.3.1.2 Contrast Computation.....	49
3.3.3.2 Pulsed Phase Thermography.....	50
3.3.3.2.1 Applications in Civil Engineering.....	50
3.3.3.3 Lock-in Thermography (Modulated thermography).....	51
3.3.3.4 Vibrothermography.....	52
3.3.3.5 Inductive Thermography.....	52
3.3.4 Quantitative Defect Information.....	53
3.3.5 Heating Sources in Active Infrared Thermography.....	54
3.4 Summary of Infrared Thermography Techniques.....	57
Chapter 4 Study on Passive Infrared Thermography.....	59

4.1 Experimental Passive Infrared Thermography Testing .....	59
4.1.1 Phase 1 – Temperature Monitoring.....	59
4.1.1.1 Method for Calculating the Area of Delamination .....	61
4.1.2 Phase 2 – Time of Day Effects .....	63
4.2 Field Deployment of Passive Infrared Thermography .....	65
4.2.1 Field Deployment Methodology .....	65
4.2.2 Field Demonstration Results and Discussion .....	66
4.2.2.1 Thermal IR Inspection Results for Top of the Bridge Deck.....	67
4.2.2.1.1 Comparing Thermal IR Results with Chain Drag and Hammer Sound Inspection Techniques for Bridge Decks.....	70
4.2.2.1.2 Freer Rd. bridge .....	72
4.2.2.1.3 Willow Rd. Bridge .....	74
4.2.2.1.4 Mannsiding Rd. Bridge (NB).....	76
4.2.2.2 Ground Truth Results.....	78
4.2.2.3 Thermal IR Inspection Results for Bridge Deck Underside and Superstructure .....	81
4.3 Summary.....	83
Chapter 5 Laboratory Study using Active Infrared Thermography .....	87
5.1 Specimen and Equipment .....	88
5.1.1 Thermal Infrared Camera.....	88
5.1.2 Heat Sources .....	88
5.1.3 Concrete Slabs .....	89
5.1.3.1 Concrete Slab I.....	89
5.1.3.2 Concrete Slab II .....	92
5.1.3.3 Concrete Slab III.....	93

5.1.3.4 Concrete Slab IV.....	95
5.1.3.5 Concrete Slab A.....	97
5.2 Phase I – Investigating the Effective Heating Source.....	97
5.2.1 Methodology of Data Collection and Processing.....	98
5.2.2 Results and Analysis.....	101
5.2.3 Discussion.....	106
5.2.3.1 Justification on Background Area Selection.....	107
5.3 Phase II – Developing a Method to Estimate the Depth of Each Delamination	109
5.3.1 Methodology of Data Collection and Processing.....	110
5.3.2 Results and Analysis.....	110
5.3.2.1 Concrete slab I and Concrete slab A.....	110
5.3.2.2 Concrete Slab IV.....	117
5.3.3 Discussion.....	121
5.4 Phase III – Discussion on Width to Depth Ratio of Delaminations.....	123
5.4.1 Methodology of Data Collection and Processing.....	123
5.4.2 Results and Analysis.....	124
5.4.3 Discussion.....	127
5.5 Infrared Thermography on Concrete Slab II.....	132
5.6 Summary.....	134
Chapter 6 Silverbell Bridge Beam Study using Active Infrared Thermography.....	139
6.1 Specimen and Equipment Set-Up.....	139
6.1.1 Thermal Infrared Camera and Heat Source.....	139
6.1.2 Silverbell Bridge Prestressed Box Beam.....	139
6.2 Methodology of Data Collection and Processing.....	145
6.3 Results and Discussion.....	148



6.3.1 Delaminations Located on the West Side of the Beam.....	148
6.3.1.1 Location W1.....	148
6.3.1.2 Location W2.....	152
6.3.1.3 Location W3.....	156
6.3.2 Delaminations Located on the East Side of the Beam.....	159
6.3.2.1 Location E1.....	160
6.3.2.2 Location E2.....	164
6.3.2.3 Location E3.....	168
6.3.2.4 Location E4.....	172
6.3.3 Calculation of the Total Delaminated Area.....	175
6.3.4 Active Infrared Thermography at an Intact Location.....	178
6.3.5 Coring Test Results.....	180
6.4 Summary.....	183
Chapter 7 Concluding Remarks and Future Works.....	187
7.1 Summary of Conclusions.....	187
7.2 Future Works.....	191
References.....	193
Appendices.....	201
Appendix A – Passive Thermography Field Demonstration Results.....	201
Freer Rd. Bridge.....	201
Willow Rd. Bridge.....	205
Mannsiding Rd. Bridge.....	209
Appendix B – Silverbell Bridge Inspection Reports.....	213
Appendix C –Test Set-up for Active Infrared Thermography on the Silverbell Bridge Beam.....	217

Appendix D – Coring Results for Concrete Slabs in Chapter 5 .....	221
Slabs Plan.....	221
Cores .....	224
Appendix E – Permissions to Reprint Copyrighted Materials .....	233
Permission to Reprint Figure 3.2 .....	233
Permission to Reprint Figure 3.3 .....	234

## List of Figures

Figure 2.1 AASHTO repair guidelines for reinforced concrete bridge decks and top flange of prestressed concrete bridges, adopted from (AASHTO 2011).....	12
Figure 2.2 Chain drag and hammer sound techniques.....	15
Figure 2.3 MDOT Bridge Deck Preservation Matrix, adopted from (MDOT 2011b). ....	18
Figure 2.4 Decision making procedure for bridge deck maintenance. ....	19
Figure 2.5 Prestressed concrete box beam configurations used in bridge construction. ..	22
Figure 2.6 AASHTO repair guideline for prestressed concrete closed web/box girders..	26
Figure 3.1 Emitted thermal infrared energy from a concrete deck during the day and night. ....	37
Figure 3.2 The diurnal radiant temperature graph of selected materials (Jenson 2007), reprinted by permission of Pearson Education, Inc. ....	39
Figure 3.3 The diurnal temperature graph for delaminations at different depths (Washer 2010), used with permission from the American Society for Nondestructive Testing.....	40
Figure 3.4 Infrared thermography testing configuration modes. ....	47
Figure 3.5 Different heating methods for infrared thermography inspection. ....	48
Figure 4.1 Layout plan of 48 in. x 48 in. x 6 in. concrete slab (slab A) with simulated delaminations. ....	60
Figure 4.2 Laboratory set-up for passive infrared thermography testing. ....	60

Figure 4.3 Thermal IR image and graphs showing the temperature change of each defect compared to the average temperature of the slab.....	61
Figure 4.4 Thermal IR image and the associated Excel spreadsheet.....	63
Figure 4.5 Comparison of thermal IR images of the concrete slab with simulated delaminations at 8:18 am and 10:59 am. ....	63
Figure 4.6 Plan layout of the concrete slab with simulated delaminations and the thermal IR image showing the temperature data of delaminations placed at different depths (0.5 in., 1 in., 1.5 in., 2 in.).....	64
Figure 4.7 Thermal IR image of the chemical staining on the concrete specimen.....	65
Figure 4.8 (a) Thermal IR camera acquisition cart and (b) sample grid pattern on the bridge deck.....	66
Figure 4.9 Deck delamination map of Freer Rd. bridge, using Thermal IR and post-processed output data results for a typical spreadsheet analysis.....	68
Figure 4.10 Deck delamination map of Willow Rd. bridge, using Thermal IR and post-processed output data results for a typical spreadsheet analysis.....	69
Figure 4.11 Deck delamination map of Mannsiding Rd. bridge, using Thermal IR and post-processed output data results for a typical spreadsheet analysis.....	69
Figure 4.12 Thermal IR and sounding delamination map and the virtual grid pattern over the Freer Rd. bridge displayed on ArcGIS.....	74
Figure 4.13 Thermal IR delamination map and sounding delamination map of Willow Rd. bridge displayed on ArcGIS.....	75

Figure 4.14 Virtual grid pattern over the Willow Rd. bridge deck.....	76
Figure 4.15 Thermal IR delamination map and sounding delamination map of Mannsiding Rd. bridge displayed on ArcGIS.....	77
Figure 4.16 Virtual grid pattern over the Mannsiding Rd. bridge deck.....	77
Figure 4.17 Coring locations on Mannsiding Rd. bridge deck.....	79
Figure 4.18 Core extraction procedure on Mannsiding Rd. bridge deck.....	79
Figure 4.19 Cores that were extracted from Mannsiding Rd. bridge deck.....	80
Figure 4.20 Digital and thermal IR image of Willow Rd. bridge soffit.....	82
Figure 4.21 Digital and thermal IR image of Mannsiding Rd. bridge soffit.....	82
Figure 4.22 Digital and thermal IR image of bridge pier under Willow Rd. bridge.....	83
Figure 4.23 Digital and thermal IR image of bridge pier under Mannsiding Rd. bridge.....	83
Figure 5.1 Layout of concrete test specimen “Slab I” with simulated delaminations.....	90
Figure 5.2 Construction sequence of the concrete slab with Styrofoam blocks used as simulated delaminations.....	91
Figure 5.3 Layout of concrete test specimen “Slab II” with simulated delaminations.....	92
Figure 5.4 Concrete Slab II after it was cured.....	93
Figure 5.5 Layout of the concrete test specimen “Slab III” with simulated delaminations.....	94

Figure 5.6 (a) Mold that was built for slab III before pouring concrete and (b) concrete slab III after it was built and cured. ....	95
Figure 5.7 Layout of concrete test specimen “Slab IV” with simulated delaminations. ..	96
Figure 5.8 Concrete Slab IV after it was built and cured.....	97
Figure 5.9 Active infrared thermography test set-up using halogen lights as an external heat source, shown with the lights off (left) and off (right).....	99
Figure 5.10 Active infrared thermography test set-up using infrared heater.....	101
Figure 5.11 Plot of the temperature variation in an active infrared thermography test using two 500W halogen lights as a heat source, Slab I.....	102
Figure 5.12 Thermal infrared images obtained from an active infrared thermography test using halogen lights on Slab I, shown 15 minutes after data collection began (left) and 20 minutes after data collection began (5 minutes after the heat source was turned off) (right). ....	102
Figure 5.13 Plot of the temperature variation in an active infrared thermography test using a 1500W infrared heater as a heat source, Slab I. ....	103
Figure 5.14 Thermal infrared images of active infrared thermography test using 1500W infrared heater, shown 15 minutes after data collection began (left) and 23 minutes after data collection began (8 minutes after the heat was turned off) (right), Slab I.....	104
Figure 5.15 Absolute contrast plot for an infrared thermography test using two halogen lights (500W each), Slab I. ....	104
Figure 5.16 Absolute contrast above delaminations at 1 in. and 2 in. depth in infrared thermography test using an infrared heater (1500W). ....	106

Figure 5.17 Relative locations of delaminated areas and a single background area selected for analysis (7 minutes after the heat was turned off), Slab I. ....	108
Figure 5.18 Absolute contrast above delaminations at 1 in. and 2 in. depth using a single background area for analysis. ....	109
Figure 5.19 Temperature variation within the delaminated areas F1 and F2 in concrete slab A during an active infrared thermography test. ....	111
Figure 5.20 Absolute contrast above delaminations F1 and F2 during the 15 minutes heating period and 45 minutes after the heat source was turned off. ....	112
Figure 5.21 Thermal infrared images for the active thermography test on slab A, shown at 15 minutes after data collection began and 19 minutes after data collection began (4 minutes after heat source was turned off). ....	113
Figure 5.22 Observation time versus the depth squared of each delamination. ....	115
Figure 5.23 Absolute contrast versus the inverse of the cubic depth for Slabs I and A. ....	116
Figure 5.24 Running contrast versus the inverse of the cubic depth for Slabs I and A. ....	116
Figure 5.25 Temperature variation above each delamination in an active thermography test on the concrete slab IV. ....	118
Figure 5.26 Absolute contrast variations above simulated delaminations in concrete slab IV during an active infrared thermography test. ....	119
Figure 5.27 Thermal infrared images of concrete slab IV, shown at 0, 15, 18, 20, 22 and 26 minutes after data collection began. ....	121

Figure 5.28 Active infrared thermography test set-up for slab III using an infrared heater. .....	124
Figure 5.29 Temperature variation in an active infrared thermography test on Slab III.	125
Figure 5.30 Absolute contrast variations above simulated delaminations in slab III during an active infrared thermography testing. ....	126
Figure 5.31 Thermal infrared images obtained from an infrared thermography testing on the concrete slab III, shown 15, 32 , 42, and 60 minutes after the beginning of the data collection.....	127
Figure 5.32 Observation time versus the depth squared of each observed delamination in Slab A, I and III. ....	130
Figure 5.33 Absolute contrast versus the inverse of the depth cubed for Slabs A, I and III.....	131
Figure 5.34 Running contrast versus the inverse of the depth cubed for Slabs A, I and III. .....	131
Figure 5.35 Thermal infrared images obtained from an active infrared thermography test, shown 15 minutes after data collection began (when the heat source was turned off) and 32 minutes after data collection began.....	132
Figure 5.36 Thermal infrared image obtained from a passive infrared thermography test on Slab II.....	133
Figure 5.37 Slab II after the timber form was removed.....	134
Figure 6.1 Orientation of the Silverbell Bridge. ....	140



Figure 6.2 Silverbell Bridge box beam cross section. ....	141
Figure 6.3 Cross section of Silverbell Bridge box beams.....	141
Figure 6.4 Silverbell Bridge box beam plan. ....	142
Figure 6.5 Silverbell Bridge deck and superstructure in April 2010. ....	143
Figure 6.6 Silverbell Bridge beam in Road Commission Oakland County facility (west face shown). ....	144
Figure 6.7 Placement of Silverbell Bridge in the Michigan Tech laboratory.....	145
Figure 6.8 West side of the Silverbell bridge beam.....	146
Figure 6.9 East side of the Silverbell Bridge beam. ....	147
Figure 6.10 Visible condition of the concrete surface at the location W1.....	149
Figure 6.11 Thermal infrared images taken from location W1 during an active infrared thermography test (timestamps on each image represents the relative times to the beginning of the data collection).....	150
Figure 6.12 Temperature variation above the delamination at location W1.....	151
Figure 6.13 Absolute contrast variations above the delamination at location W1. ....	152
Figure 6.14 Visible condition of the concrete surface at the location W2.....	153
Figure 6.15 Thermal infrared images taken from location W2 during an active infrared thermography test (timestamps on each image represents the relative times to the beginning of the data collection).....	154

Figure 6.16 Temperature variation above delaminations at location W2.....	155
Figure 6.17 Absolute contrast variations above delaminations at location W2.....	156
Figure 6.18 Visible condition of the concrete surface at the W3 location.....	156
Figure 6.19 Thermal infrared images taken from the location W3 during an active infrared thermography test (timestamps on each image represents the relative times to the beginning of the data collection).....	157
Figure 6.20 Temperature variation above the delaminations at location W3.....	158
Figure 6.21 Absolute contrast variations above the delamination at location W3. ....	159
Figure 6.22 (a) Side of the Silverbell Bridge beam showing the grouted segment and the section that was cut during the demolition (b) grout that is delaminated from the precast section. ....	160
Figure 6.23 Visible condition of the concrete surface at location E1.....	161
Figure 6.24 Thermal infrared images taken from the location E1 during an active infrared thermography test (timestamps on each image represents the relative times to the beginning of the data collection).....	162
Figure 6.25 Temperature variation above the delamination at location E1.....	163
Figure 6.26 Absolute contrast variations above the delamination at location E1.....	164
Figure 6.27 Visible condition of the concrete surface at the location E2.....	165

Figure 6.28 Thermal infrared images taken from the location E2 during an active infrared thermography test (timestamps on each image represents the relative times to the beginning of the data collection).....	166
Figure 6.29 Temperature variation above the delamination at location E2.....	167
Figure 6.30 Absolute contrast variations above delaminated areas at location E2.....	168
Figure 6.31 Visible surface crusting on the concrete surface at location E3.....	169
Figure 6.32 Thermal infrared images taken from the location E3 during an active infrared thermography test (timestamps on each image represents the relative times to the beginning of the data collection).....	170
Figure 6.33 Plot of the temperature variation above the delamination at location E3....	171
Figure 6.34 Absolute contrast variations above delaminated areas at location E3.....	171
Figure 6.35 Visible condition of the concrete surface and mild steel at the location E4. .....	172
Figure 6.36 Thermal infrared images taken from the location E4 during an active infrared thermography test (timestamps on each image represents the relative times to the beginning of the data collection).....	173
Figure 6.37 Plot of the temperature variation above the delamination at location E4....	174
Figure 6.38 Absolute contrast variations above delaminations at location E4.....	175
Figure 6.39 Coordinates of the two corners of the rectangle around each delaminated areas that can be obtained from the software.....	176

Figure 6.40 Delaminated areas on the Silverbell Bridge beam considered in the total area calculation. ....	177
Figure 6.41 Location W4 with no delaminations.....	179
Figure 6.42 Thermal infrared images taken from the intact location of the Silverbell Bridge beam, taken at 0, 0.5, 5, 15, 20, 30 min after data collection began. ....	180
Figure 6.43 Coring procedure on the Silverbell Bridge beam. ....	181
Figure 6.44 Voids observed in the cores obtained from the Silverbell bridge box beam. ....	183
Figure 6.45 Concrete core obtained from location W3-A, showing the 1¼ in. cover over the rebar. ....	183

## List of Tables

Table 2.1 National Bridge Inventory (NBI) rating scale, adopted from (MDOT 2011a)...	9
Table 2.2 MDOT bridge deck NBI rating guideline, adopted from (MDOT 2011a) .....	10
Table 2.3 MDOT repair strategies and typical repair activities.....	21
Table 2.4 NBI rating guideline for prestressed concrete box beam condition evaluation in Pennsylvania state, adopted from (Naito et al. 2010) .....	27
Table 3.1 Heating methods and parameters for different applications in civil engineering .....	56
Table 3.2 Evaluation of infrared thermography techniques for concrete bridge condition assessment.....	58
Table 4.1 Environmental condition and overall rating for each bridge .....	67
Table 4.2 Total area of delamination using thermal IR and MDOT sounding techniques	71
Table 4.3 Percentage of delaminated areas calculated from the results of each delamination survey .....	72
Table 4.4 Summary of the core conditions and the depth of delaminations.....	81
Table 5.1 Concrete Structure Specifications for Grade D(a) Concrete .....	90
Table 5.2 Mix proportions for concrete Slab I.....	91
Table 5.3 Mix proportions for concrete Slab II .....	93

Table 5.4 Mix proportions for concrete Slab III.....	94
Table 5.5 Mix proportions for concrete Slab IV.....	95
Table 5.6 Summary of the results of active infrared thermography on slab I and slab A .....	113
Table 5.7 Width to depth ratios for delaminations in slab III.....	123
Table 5.8 Coring results obtained from concrete slabs.....	136
Table 5.9 Relative order of the depth in Slabs I, III, IV and A.....	137
Table 6.1 Total number of pixels and delaminated area at each location on the Silverbell bridge beam.....	178
Table 6.2 Summary of the cores extracted from the Silverbell Bridge beam.....	181
Table 6.3 Summary of the results obtained from the beam study .....	185

## Acknowledgments

Foremost, I would like to express my sincere gratitude to my advisor, Dr. Tess Ahlborn who has shared her expertise and knowledge and provided detailed review and constructive comments for this dissertation. I am in debt to Tess for her spontaneous supports, immense patience and encouragements. To me, Tess is not only an esteemed professor but also a role model and a friend. I feel privileged to be her PhD student and to have worked for her during the past three years.

I would like to thank the members of my committee, Dr. Devin Harris, Dr. Larry Sutter and Dr. Timothy Havens for their time, guidance and input throughout this research. I would also like to thank Colin Brooks and his research team at Michigan Tech Research Institute (MTRI) for help in transferring thermal infrared output into ArcGIS for quantifying the passive infrared thermography information in Chapter 4.

I would like to acknowledge the University Transportation Center for Materials in Sustainable Transportation Infrastructure (UTC-MiSTI) for providing financial support for transferring the Silverbell Bridge box beam to campus and Michigan Tech Facilities Grounds personnel who helped in placing the beam in Benedict lab. Also, I would like to thank Henrique (Kiko) de Melo e Silva for his help around Benedict lab.

The research conducted in Chapter 4 of this dissertation was sponsored as part of a larger *Bridge Condition Assessment Using Remote Sensors* project sponsored by the Commercial Remote Sensing and Spatial Information program of the Research and Innovative Technology Administration (RITA), U.S. Department of Transportation (USDOT). The views, opinions, findings, and conclusions reflected in this dissertation are the responsibility of the author and do not represent the official policy or position of the USDOT/RITA, or any state or other entity. Additional support for completing this dissertation was provided by Michigan Department of Transportation, Michigan Tech Graduate School and Civil and Environmental Engineering department, which I thoroughly appreciate.

I am grateful to have friends like Rita Lederle, Mary Christiansen, Chris Dedene and Sarah Shann, who made the past three years of my life full of adventures and joys in Houghton.

My special thank is for my parents who do anything to make me happy and always provide me with support, inspiration, and love.



## **Abstract**

Infrared thermography is a well-recognized non-destructive testing technique for evaluating concrete bridge elements such as bridge decks and piers. However, overcoming some obstacles and limitations are necessary to be able to add this invaluable technique to the bridge inspector's tool box. Infrared thermography is based on collecting radiant temperature and presenting the results as a thermal infrared image. Two methods considered in conducting an infrared thermography test include passive and active. The source of heat is the main difference between these two approaches of infrared thermography testing. Solar energy and ambient temperature change are the main heat sources in conducting a passive infrared thermography test, while active infrared thermography involves generating a temperature gradient using an external source of heat other than sun.

Passive infrared thermography testing was conducted on three concrete bridge decks in Michigan. Ground truth information was gathered through coring several locations on each bridge deck to validate the results obtained from the passive infrared thermography test. Challenges associated with data collection and processing using passive infrared thermography are discussed and provide additional evidence to confirm that passive infrared thermography is a promising remote sensing tool for bridge inspections.

To improve the capabilities of the infrared thermography technique for evaluation of the underside of bridge decks and bridge girders, an active infrared thermography technique using the surface heating method was developed in the laboratory on five concrete slabs with simulated delaminations. Results from this study demonstrated that active infrared thermography not only eliminates some limitations associated with passive infrared thermography, but also provides information regarding the depth of the delaminations.

Active infrared thermography was conducted on a segment of an out-of-service prestressed box beam and cores were extracted from several locations on the beam to validate the results. This study confirms the feasibility of the application of active

infrared thermography on concrete bridges and of estimating the size and depth of delaminations.

From the results gathered in this dissertation, it was established that applying both passive and active thermography can provide transportation agencies with qualitative and quantitative measures for efficient maintenance and repair decision-making.

## **Chapter 1 Introduction**

The critical condition of highway bridges highlights the need for enhancing current bridge inspection methods and for developing advanced tools for smarter and more reliable data collection procedures. Proper inspection of concrete bridge elements has become critical for bridge inspectors due to the large number of concrete bridges in the nation and challenges associated with inspecting this type of structure. As of December, 2012, 66% of the total 607,000 bridges in the United States have either a reinforced concrete or prestressed concrete superstructure. Also, 69% of all bridges have concrete decks, which indicates the importance of developing tools for easy and accurate evaluation of concrete bridge elements (FHWA 2012).

Crack patterns, crack widths, and spalled or delaminated areas are the main concrete bridge health indicators that are detected and reported by bridge inspection teams. The primary method of inspection practice for detecting delaminations is sounding concrete bridge elements using a hammer. The success of the hammer sounding technique is very dependent on the bridge inspector's experience and expertise; also, this method is labor intensive and time consuming. Delaminations on the concrete bridge elements can turn to spalls and raise safety concerns, especially for the traffic passing under the bridge. However, closing the road to traffic over or under the bridge to conduct the hammer sounding technique is not always possible during a biennial bridge inspection. Therefore, developing an easily-deployable, non-destructive tool with the ability to accurately assess the total area and location of delaminations can provide invaluable information for prioritizing maintenance funding during the decision-making process.

### **1.1 Motivation**

Recent devastating bridge collapses in North America have renewed interest in developing the application of non-destructive testing methods that increase the speed of data collection and obtain more reliable results. Non-destructive testing techniques that

have the potential for subsurface bridge inspection are Impact Echo (IE), Ultrasonic Testing (UT), Ground Penetrating Radar (GPR) and infrared thermography.

Infrared thermography is a recognized non-destructive testing and remote sensing technique for evaluating the concrete bridge elements, such as bridge decks and piers. However, overcoming some of the obstacles and limitations of this technique is necessary to add this invaluable technique into the bridge inspector's tool box. Infrared thermography can be conducted in either a passive or an active test set-up. A thermal infrared (IR) image can yield both quantitative and qualitative indications of condition. Outputs from infrared thermography can be used to create a delamination map of the bridge deck or other bridge elements, which can help during inspection documentation (Vaghefi et al. 2013). Remote sensing or data collection at a distance from the object and without a physical contact, is one of the main advantages of the infrared thermography test that enable the inspection of inaccessible areas (Vaghefi et al. 2012).

Active infrared thermography testing can be more reliable than passive infrared thermography due to the use of an external heating source, instead of the sun, to generate the thermal pulse and quantitative measurements such as estimating the depth of the delamination based on the relationship between temperature, depth of the flaw and observation time. Unlike active infrared thermography, passive infrared thermography has been used for bridge inspection applications (ASTM 2007), even though active infrared thermography has advantages that can overcome some limitations of the passive approach. So far, there have been very limited publications discussing the use of active infrared thermography for concrete bridge inspection (Maierhofer et al. 2002; Pollock et al. 2008), and no research has been found that discusses the estimation of the depth of delaminations in concrete based on the results of active infrared thermography. To allow the widespread use of infrared thermography for assessing the condition of concrete bridges, a greater understanding of test methods and influencing variables is needed.

## **1.2 Project Goals and Overview**

The aim of this dissertation is to investigate the feasibility of applying active infrared thermography to enhance concrete bridge inspection beyond the capabilities of the current passive infrared thermography inspection technique and to develop infrared thermography technology that can quantify the delamination area and depth of the delamination.

The two goals of this dissertation were achieved by accomplishing several tasks. The investigation starts with a thorough literature review of the main indicators of defects in concrete bridges and current bridge inspection practice methods to identify defective areas on the bridge. Additionally, a literature review of infrared thermography techniques and general applications of this non-destructive testing method for civil engineering projects was conducted.

A laboratory study and field tests were conducted using passive infrared thermography techniques to identify limitations outside the laboratory environment and in real-world applications. Field studies of this phase of the investigation were conducted on three prestressed concrete I-beam bridges with concrete decks located in Michigan. Results were validated by sounding techniques conducted by the Michigan Department of Transportation (MDOT). Cores were extracted from a concrete bridge with a deck in very poor condition, which was scheduled for replacement, to further validate the results of passive infrared thermography on bridge decks.

The second stage of this study included a feasibility study of active infrared thermography in the laboratory. This laboratory study was conducted in three phases. The first phase of the study included an investigation of practical and efficient heating sources for active infrared thermography. The second phase of this study discussed the relationship between the depth of each delamination with the observation time and the surface temperature. The final phase of this study consisted of an investigation on the influence of the size of the delaminations on the results obtained from an active infrared thermography test.

In the final stage of this study, active infrared thermography testing was conducted on a deteriorated box beam. The salvaged specimen was part of a prestressed concrete adjacent box beam bridge that was demolished in 2011. Cores were taken from this test specimen to further validate the results of using active infrared thermography for concrete bridge condition assessment.

### **1.3 Dissertation Organization**

This dissertation includes seven chapters:

Chapter 1 has provided an introduction.

Chapter 2 provides a review of subsurface related inspection challenges on concrete bridges and current inspection practices to assess defective areas on concrete bridge elements. Descriptions of potential non-destructive testing methods for evaluating concrete bridge elements and maintenance decision making processes are also included in this chapter.

Chapter 3 covers the literature existing on the theoretical concepts of active and passive infrared thermography testing and application of this technology for concrete materials, specifically for bridge related matters. Advantages and disadvantages of each technique are also discussed in this chapter.

Chapter 4 summarizes the results of a study on passive infrared thermography and deployment on three prestressed concrete I-beam bridges in Michigan. These results were obtained as part of a larger project (Bridge Condition Assessment using Remote Sensors) sponsored by the U.S. Department of Transportation, Research and Innovative Technology Administration (USDOT/RITA).

Chapter 5 contains details of the laboratory study on deploying the active infrared thermography on concrete slabs with simulated delaminations. Three phases were

considered for this stage of the study, an investigation of possible heat sources for active infrared thermography testing on concrete, an estimation of the depth of delaminations, and an investigation on the effect of the delamination size on active infrared thermography results. Results of these three phases are included in this chapter.

Chapter 6 summarizes the details of active infrared thermography test set-up and results of this test on an out-of service prestressed concrete box beam.

Chapter 7 includes overall concluding remarks of this research and recommendations for field application. Potential future works and applications for the research developed in this dissertation are also outlined in this chapter.





## **Chapter 2 Delaminations and Inspection Procedure**

### **2.1 Preface**

Delaminations are the separation of concrete layers within the cover of the top layer of reinforcing steel and can occur as a set of horizontal cracks through the depth of concrete. Delaminations also refer to splitting of overlays and coatings in a plane roughly parallel to the concrete surface. As these gaps are invisible to the human eye, determining the exact location and area of delamination during a regular visual bridge inspection involves numerous challenges. Corrosion of reinforcing steel, cyclic freezing and thawing, and overstress in concrete bridge elements have been highlighted as the most common causes of delamination (Ryan et al. 2006; Jana 2007). Other causes of delaminations in concrete bridges include: premature finishing due to rapid evaporation of surface water, or retard bleeding and surface crusting due to hot, windy and dry weather (Jana 2007).

Delaminated areas can completely separate from the concrete bridge element and develop into spalls; thus, it is important to accurately identify the location and size of these subsurface anomalies. Because these separated layers can cause an interruption in sound wave transmission through the concrete, sounding methods are the most common techniques for detecting delaminated areas. Tapping concrete bridge elements with a metal rod or a light weight hammer, and dragging a chain across the concrete bridge deck are the most common methods for detecting delaminations during a bridge inspection.

Delamination can occur in any concrete bridge element; however, the most susceptible elements are the ones that are directly exposed to chemicals and chloride ingress such as the deck surface, fascia beams or the top flange of girders. Also, in cases where an overlay is present, delaminations can occur at the interface of the overlay and the main deck, or the top flange of prestressed or reinforced concrete girders when the overlay is directly applied.

## **2.2 Current Bridge Inspection Methods and Reporting Systems**

The National Bridge Inspection Program (NBIP) was first initiated in 1970 following the catastrophic failure of the Silver Bridge in Ohio in 1967. The Silver Bridge was a pin-connected suspension bridge that failed due to a crack in one of the eye-bars which resulted in collapse of the entire adjacent tower. This major failure motivated the recognition of the deteriorating condition of the nation's infrastructure and need for routine inspection (Fu 2005). In accordance with the NBIP, state highway agencies are required to inspect bridges every two years and submit the inspection reports for the national bridge inventory (NBI) database. The two year period for bridge inspection is the maximum allowable time, and in more critical cases, the bridge may be required to be inspected more frequently depending on the inspection results and condition of the bridge.

Two main nationwide evaluating scales for bridge inspection that are currently being used by state agencies are the national bridge inventory (NBI) scale and PONTIS. During a routine bridge inspection, bridge elements are rated on a scale of 0 to 9 based on the national bridge inventory guideline. Table 2.1 summarizes the general NBI condition rating for bridges (FHWA 1995). Bridge safety inspection national bridge inventory rating guidelines were developed according to the general NBI rating descriptions and are being used by transportation agencies (MDOT 2011a). Results of bridge inspections based on the NBI scale are added to each bridge safety inspection report. A copy of the bridge safety inspection report for Silverbell Bridge is included in Appendix B of this dissertation.

**Table 2.1 National Bridge Inventory (NBI) rating scale, adopted from (MDOT 2011a)**

NBI rating	Description
9	EXCELLENT CONDITION
8	VERY GOOD CONDITION - no problems noted
7	GOOD CONDITION - some minor problems.
6	SATISFACTORY CONDITION - structural elements show minor deterioration
5	FAIR CONDITION - all primary structural elements are sound but may have minor corrosion, cracking or chipping. May include minor erosion on bridge piers.
4	POOR CONDITION - advanced corrosion, deterioration, cracking or chipping. Also significant erosion of concrete bridge piers.
3	SERIOUS CONDITION - corrosion, deterioration, cracking and chipping, or erosion of concrete bridge piers have seriously affected deck, superstructure, or substructure. Local failures are possible.
2	CRITICAL CONDITION - advanced deterioration of deck, superstructure, or substructure. May have cracks in steel or concrete, or erosion may have removed substructure support. It may be necessary to close the bridge until corrective action is taken.
1	"IMMINENT" FAILURE CONDITION - major deterioration or corrosion in deck, superstructure, or substructure, or obvious vertical or horizontal movement affecting structure stability. Bridge is closed to traffic but corrective action may put back in light service.
0	FAILED CONDITION - out of service - beyond corrective action
N	Not applicable

The Michigan Department of Transportation (MDOT) National Bridge Inventory Guideline categorizes delaminations and spalls based on the deteriorated area relative to the whole bridge deck area. In this guideline, if the combined deteriorated area of the top and bottom surface is more than 25% of the total deck top and bottom surface area, then the bridge deck is classified in the serious condition category (NBI rating of 3) and further structural evaluation and load analysis on the bridge is necessary. If the total combined deteriorated area is between 10-25%, the deck is in poor condition and will receive a NBI rating of 4. Total combined deteriorated areas of 2-10% and less than 2% indicate the fair condition and get the NBI rating of 5 and 6, respectively (MDOT 2011a). Table 2.2 lists the MDOT NBI rating guideline for bridge decks.

**Table 2.2 MDOT bridge deck NBI rating guideline, adopted from (MDOT 2011a)**

NBI rating	Description
9	NEW CONDITION - No noticeable or noteworthy deficiencies which affect the condition of the deck.
8	GOOD CONDITION - Minor cracking less than 1/32 in. wide (0.8 mm) with no spalling, scaling or delamination on the deck surface or underneath.
7	GOOD CONDITION - Open cracks less than 1/16 in. wide (1.6 mm) at a spacing of 10 ft or more, light shallow scaling allowed on the deck surface or underneath. Deck will function as designed.
6	FAIR CONDITION - Deterioration of the combined area of the top and bottom surface of the deck is 2% or less of the total area. There may be a considerable number of open cracks greater than 1/16 in. wide (1.6 mm) at a spacing of 5 ft or less on the deck surface or underneath. Medium scaling on the surface is ¼ in. to ½ in. (6.4 mm to 13 mm) in depth. Deck will function as designed.
5	FAIR CONDITION - Deterioration of the combined area of the top and bottom surface of the deck is between 2% and 10% of the total area. There can be excessive cracking in the surface. Heavy scaling ½ in. to 1 in. in depth (13 mm to 26 mm) can be present. Deck will function as designed.
4	POOR CONDITION - Deterioration of the combined area of the top and bottom surface of the deck is between 10 - 25% of the total area. Deck will function as designed.
3	SERIOUS CONDITION - The deck is showing advanced deterioration that has seriously affected the primary structural components. Deterioration of the combined area of the top and bottom surface of the deck is more than 25% of the total area. Structural evaluation and/or load analysis may be necessary to determine if the structure can continue to function without restricted loading or structurally engineered temporary supports. There may be a need to increase the frequency of inspections.
2	CRITICAL CONDITION - Deterioration has progressed to the point where the deck will not support design loads and is therefore posted for reduced loads. Emergency deck repairs or shoring with structurally engineered temporary supports may be required by the crews. There may be a need to increase the frequency of inspections.
1	"IMMINENT" FAILURE CONDITION - Bridge is closed to traffic due to the potential for deck failure, but corrective action may put the bridge back in service.
0	FAILED CONDITION - Bridge closed. Coordinate with SI&A <sup>1</sup> item 41.
N	Not applicable

<sup>1</sup>Structure Inventory and Appraisal Report

A PONTIS Bridge Inspection Report is an additional report that has to be completed by inspectors. This report includes the quantity of each bridge element at each condition state as well as the total quantity of the element. A copy of the Bridge Inspection Report for Silverbell Bridge is included in Appendix B of this document. AASHTO provides a guideline to identify core bridge elements and condition states associated with each

bridge element. For example, for reinforced concrete bridge decks, areas of moderate spall and patch that are intact are considered as condition state 2 and areas of severe spalls and delaminations are counted as condition state 3 (AASHTO 2011).

The AASHTO Guide Manual for Bridge Element Inspection classifies delamination and spall conditions as moderate when the depth is less than 1 in. and the diameter is less than 6 inches, whereas the medium to severe condition classification is when the depth is more than 1 inch and the diameter is greater than 6 inches (AASHTO 2011). Figure 2.1 shows an example of criteria and guidelines for condition states of reinforced concrete bridge decks and the top flange of prestressed concrete bridges as well as feasible repair methods. According to this guideline, cracking, spalls, delaminations and efflorescence on the surface are classified into four condition states. Any bridge element with conditions beyond the limits of condition state 3 is assigned as condition state 4, when load reduction, bridge closure or replacement is required.

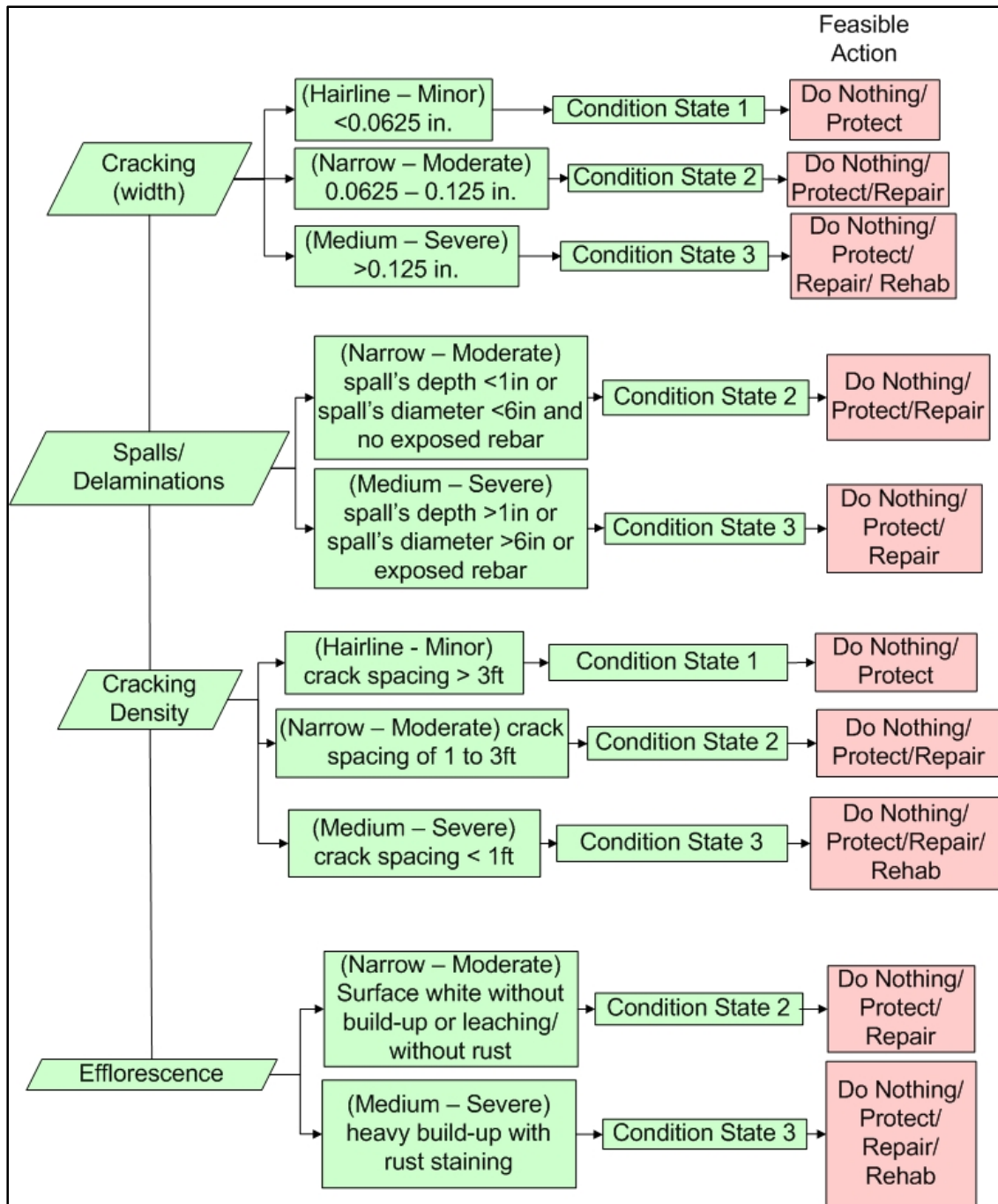


**Figure 2.1 AASHTO repair guidelines for reinforced concrete bridge decks and top flange of prestressed concrete bridges, adopted from (AASHTO 2011).**

### ***2.2.1 General Types of Bridge Inspection***

To ensure the integrity and safety of a bridge structure, several different types of inspections are conducted during the bridge service life. Inspection procedures that are conducted on the bridge include initial inspection, routine inspection, damage inspection, in-depth inspection and special inspection. Selection of the bridge inspection procedure depends on the bridge age and condition evaluation.

#### **2.2.1.1 Initial Inspection**

Initial inspection is the first inspection of a new-build bridge to provide data for the Structure Inventory and Appraisal Report (SI&A) (Appendix B). Results of the initial inspection survey help in establishing a starting point for future bridge inspections, and become part of the bridge's permanent file. This type of inspection is also necessary in case of any changes in the bridge ownership or configuration of the structure (Fu 2005).

#### **2.2.1.2 Routine Inspection**

Routine bridge inspections are generally conducted biennially for all bridges in the nation. Data collection and rating for the routine inspection is based on the general procedures and guidelines provided by National Bridge Inventory (NBI) and Federal Highway Administration (FHWA). During this type of inspection, the entire bridge should be inspected and assessed; however, the main focus of attention should be on deteriorated areas that were detected during the previous inspections. Recommendations for future repair and rehabilitation are often enclosed with this report (Fu 2005).

#### **2.2.1.3 Damage Inspection**

A damage inspection is usually performed to assess a known structural damage resulting from environmental or human factors, such as a high load hit, flood, hurricane or earthquake. The depth of this inspection depends on the severity of the damage. Bridge inspectors are generally expected to provide sufficient measurements and calculations to determine the need for emergency closures or load restrictions for the bridge (Fu 2005).

#### **2.2.1.4 In-depth Inspection**

An in-depth inspection is usually performed to obtain further information regarding the safety and integrity of a specific bridge element. This type of inspection most often requires specific tools and equipment either for accessibility or further non-destructive testing investigations. In some cases in-depth inspection may require lane closures over or under the bridge. Results of this type of assessment are gathered in a scoping report and associated with a detailed photo inventory (Fu 2005).

#### **2.2.1.5 Special Inspection**

A special inspection refers to the inspection of a specific element with previously known or suspected deteriorating conditions. Scour monitoring, foundation settlement, and bearing corrosion are some examples that require a special bridge inspection (Fu 2005).

#### ***2.2.2 Visual Inspection for Concrete Bridge Decks***

Visual inspection is the most common practice method used by bridge inspectors during bridge inspections. Most often, this inspection is conducted without lane closures on or under the bridge. However, safety issues associated with passing traffic is the main concern that would necessitate specific precautions, such as a lane closure. Although the bridge inspector's visual observations are the main assessment tool during visual inspection, other assessment tools, such as a crack width gage, hammer for sounding, chain drag, magnifying glass, flashlight and tape measure, are often included in the inspector's tool box (Fu 2005). These assessment tools help bridge inspectors to assess the elements that are not directly accessible or to detect defects that are not visible. Detecting delaminations in concrete is one example of the need to employ an assessment tool other than vision to carry out a thorough bridge condition assessment.

Hammer sounding a concrete bridge element is the most common practice method to detect delaminations. Delaminated areas sound hollow when tapped with a hammer, compared to a sharp tone of intact concrete, and the sound difference can indicate a defective area. Hammer sounding is mainly used under the bridge and for accessible areas. This technique can also be used to detect delaminations on the entire bridge deck



by tapping the deck with a metal rod. Another more time efficient sounding method for detecting delaminations on a concrete bridge deck is the chain drag testing technique. The chain drag technique is also based on the generated sound from the deck surface. This testing method involves dragging a heavy chain across the bridge deck and marking the hollow sounding areas with a spray paint, similar to the hammer sound technique (Ryan et al. 2006; Jana 2007). Figure 2.2 shows hammer sounding and chain dragging surveys being conducted on a concrete bridge deck. The main disadvantages of these data collection methods are that they are time consuming and labor intensive. Also, results of these surveys are subjective and are based on inspector's interpretation of different sounds.



**Figure 2.2 Chain drag and hammer sound techniques.**

General sounding techniques for detecting delaminations along with a more commercialized version of an electro-mechanical sounding cart are standardized in ASTM D4580. In both methods a gridline system is required over the bridge deck. This grid pattern should be laid down on the bridge prior to the sounding inspection using a stringline and tape measures. The increment of this grid pattern depends on the required

accuracy of the location of delaminations. A delamination map should be created based on the painted marks on the bridge deck. The total delaminated area can be calculated based on the delamination map obtained from the results of the ASTM test (ASTM 1997a; Fu 2005).

An electro mechanical sounding system is an automated version of the hammer sound technique. The main components of an electro mechanical cart include a battery, two tapping wheels, two sonic receivers and a strip recorder (ASTM 1997a). Two rigid steel tapping wheels, located 6 in. apart, tap concrete at a rate of 33 times per second and two receiving transducers record the noise induced by the impact on the concrete surface. These receiving transducers are piezo-electric hydrophones that are connected to the concrete surface through oil-filled plastic tires. These two plastic tires are located parallel to their corresponding tapping wheels and they are approximately three inches apart from the tapping wheels. This device can detect delaminations up to 2.6 in. below the surface (Jana 2007).

As an electro mechanical sounding cart is pushed over the bridge deck and taps the concrete, acoustic signals are generated inside the concrete bridge deck. Return signals are collected by the sonic receiver and transmitted to the strip recorder. Strip recorder only records signals that are within the range of 300-1200 Hz and occurred during the first 3ms after tapping. These signals are then electronically rectified and interpreted to create a visual delamination map of the bridge deck. Total area of delamination can be determined by summing the individual delaminated areas. The percent of delaminations can be computed by finding the percentage of the delaminated area over the entire bridge deck area (ASTM 1997a; Ryan et al. 2006).

In an investigation of the reliability of routine and in-depth visual inspections for highway bridges, Moore et al. (2000) reported significant variability in deck delamination surveys conducted by 22 bridge inspection teams. Basic hammer sounding and chain dragging were the only tools used in this survey and the range of delamination percentage results varied from 2 to 35% (Moore et al. 2000). Studies, such as this, highlight some of

the limitations of current techniques and reveal the need for an easy-to-use inspection tool to help bridge inspectors locate and sketch delaminations more accurately. While allocating a National Bridge Inventory (NBI) rating for the condition of the bridge deck in the scale of 0 to 9 depends on the total percentage of delaminated areas over the entire bridge area, locations of these defective areas are also important factors in the bridge deck maintenance decision making. Furthermore, determining the size of the delaminations are helpful in rating the condition of the concrete bridge elements based on the PONTIS scheme in the scale of 1 to 4 (AASHTO 2011).

#### **2.2.2.1 Percent Deficiency and the Decision Making Process**

During routine biennial bridge inspections, both the top and bottom surface of the bridge deck are inspected and the total percent deck deficiency is included in the bridge safety inspection report. Also, the qualitative assessment of the deteriorating condition, such as location and significance of the spalls, cracks or delaminations, is explained for each bridge element. The Michigan bridge deck preservation matrix provides good guidance for decision making based on the condition of the bridge deck (Figure 2.3). BSIR 58a is the rating for the top surface of the bridge deck and BSIR 58b is the rating for the bottom surface of the bridge deck, which are included in Bridge Safety Inspection Report (BSIR).

The percentage of deficiency in this matrix is defined as the total percent of the deck surface area that is spalled, delaminated or patched with temporary patch materials. This guideline was created based on the element deterioration data and the best knowledge of individuals from MDOT's Construction and Technology Division, MDOT's Maintenance and Design Divisions, and FHWA with years of experience with bridges. This guideline in most cases leads to an economical repair decision which can be Capital Scheduled Maintenance (CSM), Capital Preventive Maintenance (CPM), Rehabilitation or Replacement (MDOT 2011b).

Deck Condition State				Repair Options	Potential Result to Deck BSIR		Anticipated Fix Life
Top Surface		Bottom Surface			Top Surface BSIR #58a	Bottom Surface BSIR #58b	
BSIR #58a	Deficiencies % (a)	BSIR # 58b	Deficiencies % (b)				
≥ 5	N/A	N/A	N/A	Hold ( c ) Seal Cracks/Healer Sealer (d)	No Change	No Change	1 to 4 years
	≤ 5%	> 5	≤ 2%	Epoxy Overlay	8, 9	No Change	10 to 15 years
	≤ 10%	≥ 4	≤ 25%	Deck Patch (e)	Up by 1 pt.	No Change	3 to 10 years
4 or 5	10% to 25%	5 or 6	≤ 10%	Deep Concrete Overlay (h)	8, 9	No Change	25 to 30 years
		4	10% to 25%	Shallow Concrete Overlay (h, i)	8, 9	No Change	20 to 25 years
				HMA Overlay with water-proofing membrane (f, h, i)	8, 9	No Change	8 to 10 years
				HMA Cap (g, h, i)	8, 9	No Change	2 to 4 years
≤ 3	> 25%	> 5	< 2%	Deep Concrete Overlay (h)	8, 9	No Change	20 to 25 years
		4 or 5	2% to 25%	Shallow Concrete Overlay (h, i)	8, 9	No Change	10 years
				HMA Overlay with water-proofing membrane (f, h, i)	8, 9	No Change	5 to 7 years
				HMA Cap (g, h, i)	8, 9	No Change	1 to 3 years
		2 or 3	> 25%	Replacement with Epoxy Coated Rebar (ECR) Deck	9	9	60+ years

(a) Percent of deck surface area that is spalled, delaminated, or patched with temporary patch material.  
(b) Percent of deck underside area that is spalled, delaminated or map cracked.  
(c) The "Hold" option implies that there is on-going maintenance of filling potholes with cold patch and scaling of incipient spalls.  
(d) Seal cracks when cracks are easily visible and minimal map cracking. Apply healer sealer when crack density is too great to seal individually by hand. Sustains the current condition longer.  
(e) Crack sealing can also be used to seal the perimeter of deck patches.  
(f) Hot Mix Asphalt overlay with waterproofing membrane. Deck patching required prior to placement of waterproofing membrane.  
(g) Hot Mix Asphalt cap without waterproofing membrane for ride quality improvement. Deck should be scheduled for replacement in the 5 year plan.  
(h) If bridge crosses over traveled lanes and the deck contains slag aggregate, do deck replacement.  
(i) When deck bottom surface is rated poor (or worse) and may have loose or delaminated concrete over traveled lanes, an in-depth inspection should be scheduled. Any loose or delaminated concrete should be scaled off and false decking should be placed over traveled lanes where there is potential for additional concrete to become loose.

**Figure 2.3 MDOT Bridge Deck Preservation Matrix, adopted from (MDOT 2011b).**

The Bridge Deck Preservation Matrix can be used in two approaches. The first approach is to use the table from left to right when the percent deck deficiency information is available to the bridge inspector or management team. In this first approach, both top and bottom surfaces of the bridge deck are rated using the NBI scale (Table 2.2 for MDOT bridges) and the best repair option can be selected. The three columns located on the right side of this matrix help to estimate the change in the NBI rating and anticipated repair life after the repair is performed on the deck. The second approach is to use this table from right to left. Bridge inspectors can select a repair method based on the desired fix duration. In this case, it is important to consider the condition of the structure at the time of repair. If the structure is in worse condition than the left columns of this matrix, the anticipated fix life of the structure will be less than what is declared in this matrix (MDOT 2011b).

Figure 2.4 is an illustration of the first approach (reading Figure 2.3 from left to right) of using this preservation matrix for bridge deck maintenance decision making. In this approach, the feasible repair action can be selected based on the NBI rating for the deck top and bottom surfaces (#58 in BSIR) (Appendix B).

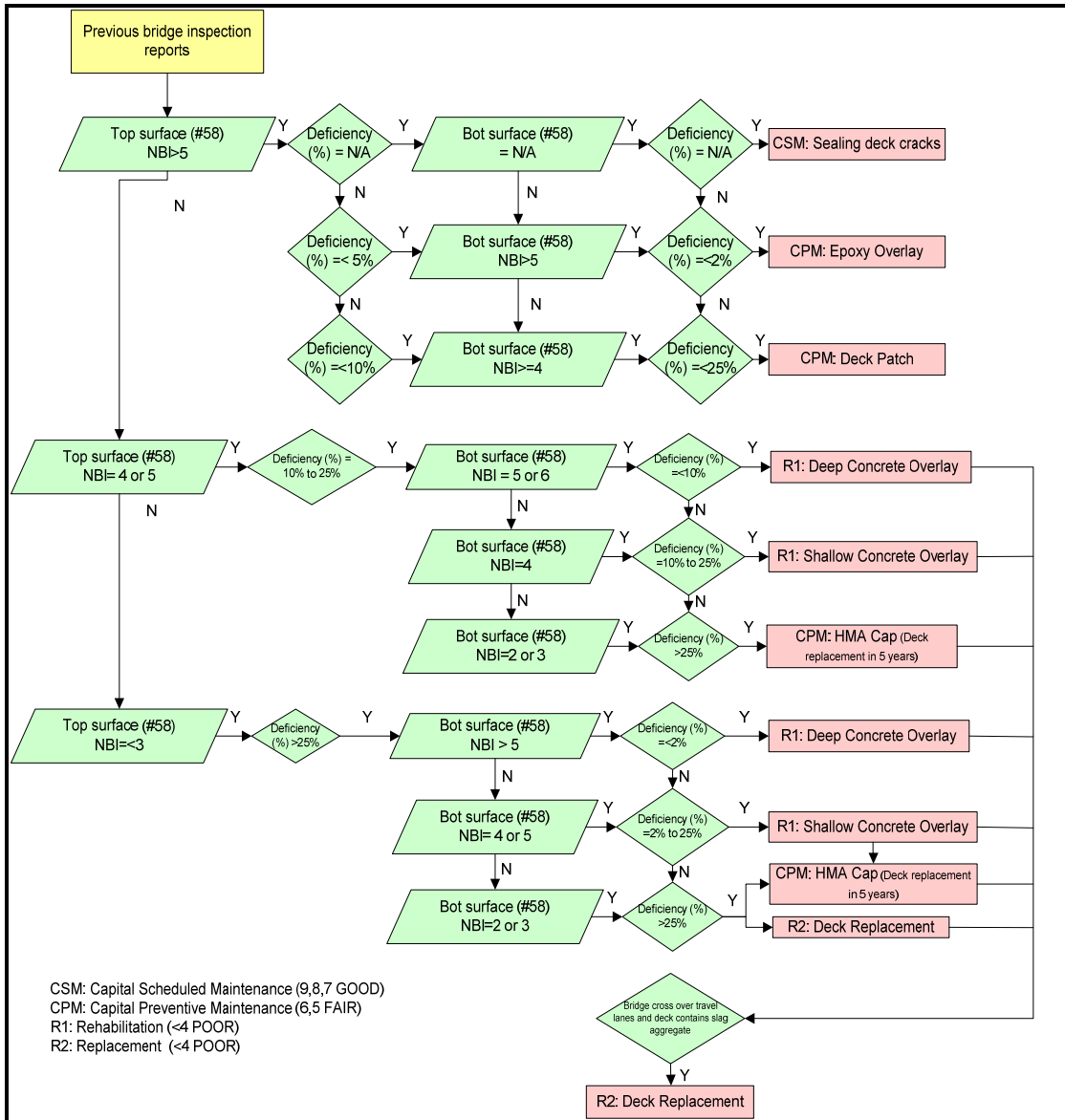


**Figure 2.4 Decision making procedure for bridge deck maintenance.**

Table 2.3 summarizes the typical activities performed for bridge maintenance, preservation and repair activities (MDOT 2008; MDOT 2009). Decisions regarding these

preservation activities are made based on bridge inspection results, the condition of bridge elements and available maintenance funding. In Michigan, Capital Scheduled Maintenance (CSM), Capital Preventive Maintenance (CPM) and Rehabilitation and Replacement (R1 and R2) are general preservation decisions that can either sustain the good condition of the bridge or improve the bridge condition.

Capital Scheduled Maintenance (CSM) activities typically extend the life of the structure and delay structural deterioration. These activities can be completed without traffic disruption and in a short period of time (MDOT 2009). CSM activities can extend the anticipated repair life of the structure by 5 years (TransSystems Corporation 2011).

Capital Preventive Maintenance (CPM) activities for bridges are defined as activities that can improve the condition of a fair bridge element to a good rating. CPM activities are performed with the goal of preventing the condition of a bridge element from becoming critical (MDOT 2009). CPM repair activities are anticipated to increase the service life of the structure by 10-15 years (TransSystems Corporation 2011).

Rehabilitation and Replacement practices for bridges are generally conducted in the case of deck, substructure and superstructure deterioration, or for resolving issues related to functional obsolescence (MDOT 2009). Functional obsolete issues for bridges are generally bridge deficiencies in geometry, clearance or load capacity (Markow and Hyman 2009). Rehabilitation activities are performed to extend the service life of the bridge and upgrade the structural and functional deficiencies. Deep and shallow overlays, substructure and superstructure repairs, and resolving the bridge structure geometry are some typical activities that can be performed in the case of a rehabilitation decision. Replacement strategies include activities that cause significant changes in the structure. Bridge deck replacement is the most common type of this repair activity. Superstructure replacement and complete replacement of the bridge are also included in the replacement decision category (MDOT 2009). Rehabilitation and replacement activities can increase the service life of the structure by 25-40 years or longer (TransSystems Corporation 2011).

**Table 2.3 MDOT repair strategies and typical repair activities**

NBI Rating	MDOT strategies	Work Activities
9,8,7 (GOOD)	Capital Scheduled Maintenance (CSM)	<ul style="list-style-type: none"> <li>-Washing the superstructure for roads and bridges</li> <li>- Removing vegetation</li> <li>- Cleaning and/or repairing the drain system</li> <li>- Spot-painting</li> <li>- Resealing bridge construction joints</li> <li>- Sealing concrete</li> <li>- Sealing deck cracks</li> <li>- Minor concrete patching</li> <li>- Repairing bridge deck spalls</li> <li>- Provide pressure relief joints in the concrete bridge approach</li> <li>- Repairing or replacing spot locations of failed or damaged slope paving</li> </ul>
6,5 (FAIR)	Capital Preventive Maintenance (CPM)	<ul style="list-style-type: none"> <li>- Replacing pins and hangers</li> <li>- Painting zones of the bridge beams</li> <li>- Complete painting of beams</li> <li>- Patching the deck</li> <li>- Patching the bridge substructure (minor)</li> <li>- Applying a hot mix asphalt (HMA) cap (with no waterproofing membrane)</li> <li>- Applying an HMA overlay (with waterproofing membrane)</li> <li>- Installing scour countermeasures</li> <li>- Replacing joints</li> <li>- Applying an epoxy overlay</li> </ul>
Below 4 (POOR)	Rehabilitation and Replacement (R1&R2)	<p><b>Rehabilitation:</b></p> <ul style="list-style-type: none"> <li>- Applying a shallow overlay on the deck (hydro-demolishing the deck surface to a depth of ¾ in., then applying a latex-modified concrete that is typically 1½ in. thick)</li> <li>- Applying a deep overlay on the deck (hydro-demolishing to remove the deck concrete below the top reinforcement, replacing deficient rebar, and placing a Grade 45 D Modified concrete such that a depth of 3 in. covers the top transverse reinforcement)</li> <li>- Repairing the bridge superstructure (the part of the bridge above the piers and abutments, typically steel or concrete beams, girders and stringers that support the deck)</li> <li>- Repairing the bridge substructure (the piers and abutments which carry the superimposed load of the superstructure to the underlying soil or rock)</li> </ul> <p><b>Replacement:</b></p> <ul style="list-style-type: none"> <li>- Replacing the bridge rail</li> <li>- Replacing and widening the superstructure (to maintain same number of lanes)</li> <li>- Replacing the entire bridge/Replacing a culvert (10-20 ft)</li> <li>- Adding lanes to the bridge via one or more of the following: <ul style="list-style-type: none"> <li>Widening the bridge / Replacing and widening the deck</li> <li>Replacing and widening the superstructure / Replacing the bridge</li> </ul> </li> </ul>

### ***2.2.3 Visual Inspection for Prestressed Concrete Box Beam Bridges***

Construction of prestressed box beam concrete bridges in the United States began in the early 1950s and gained popularity due to fast and economic construction (Russell 2009; Naito et al. 2010). The majority of prestressed concrete box beam bridges were constructed using hollow rectangular girders as the main superstructure, and placing a concrete or asphalt surfacing on the top. In box beam bridge construction, box beams can be placed in two different arrangements, adjacent or spread. In constructing adjacent box beam bridges, box beams are typically placed side by side to each other. The box beams are post tensioned transversely and shear keys are grouted to ensure the interactive performance of the bridge box beams. Another application of box beams is in the construction of spread box beam bridges in which box-beams are placed at a certain distance (typically between 2 to 6 feet) with a cast-in-place concrete deck on the top (Ryan et al. 2006). Figure 2.5 shows the application of prestressed concrete box beams in bridge construction.

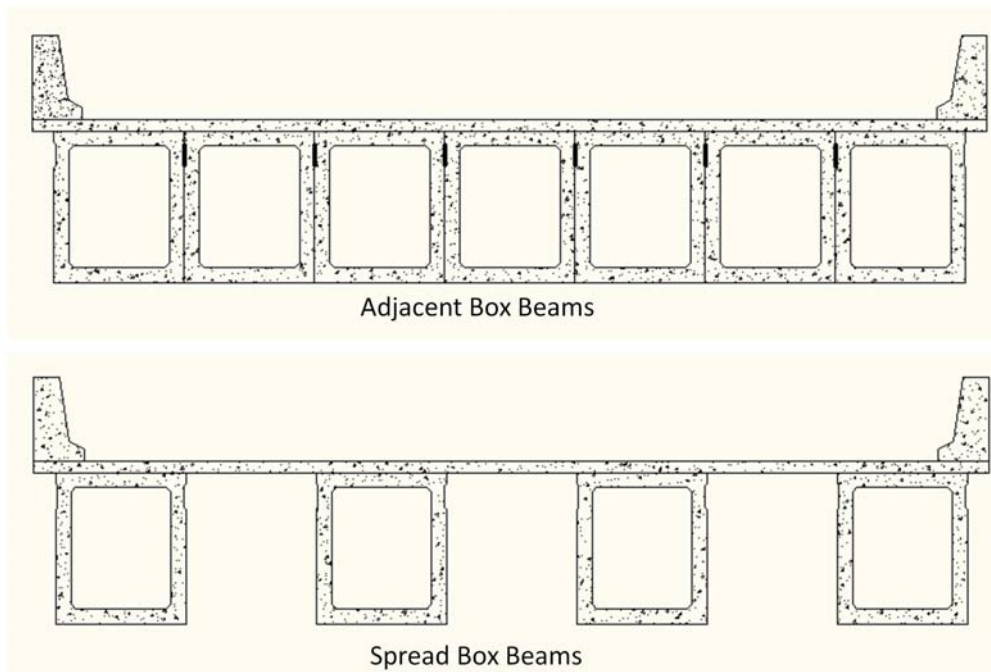


**Figure 2.5 Prestressed concrete box beam configurations used in bridge construction.**



Box beam bridges are typically built for a span length of 20 to 90 ft. The typical width of the AASHTO precast prestressed type girders is either 36 or 48 in., with the height range between 27 to 42 in. (PCI 1997). Box beams in bridges can have a composite action with the cast-in-place deck on the top. In composite construction, stirrups are extended out on the top of the girders and are cast in the concrete deck to assure composite action between the deck and girders. Non-composite construction is another option, in which stirrups are not extended out and bridge girders do not achieve the composite action but rather act as independent elements (Ryan et al. 2006).

In recent years, there have been tremendous efforts to improve bridge inspection practices; however, there exists the challenge of detecting the deteriorating condition of adjacent box beam bridges. Lack of accessibility to the inside surface of these hollow shape structures and around the shear keys is the main factor that prevents having reliable bridge inspection data for this type of structure. The issue of adjacent box beam bridge inspection has grown in importance in response to the Lakeview Drive Bridge collapse in Pennsylvania in 2005. This bridge collapsed due to the failure of one of the fascia box beams and fell to the highway underneath. After further investigation, it was determined that failure was most likely due to the heavily corroded transverse ties and poor consolidation of shear keys which reduced the interaction between adjacent box beams. This condition led to the independent beam action which in this case caused in failure of one of the heavily deteriorated beams. The investigation highlighted the importance of investigating the independent action of each box beam under load and development of a new guideline for assigning NBI ratings for box beam bridge superstructures (Naito et al. 2010).

Cracking, spalling, scaling, delamination and material distress are mentioned in the literature as the most common types of deterioration in prestressed box beam bridges (Ahlborn et al. 2005; Ryan et al. 2006). Cracking in prestressed concrete bridges can be an indicator of different causes depending on the shape and direction of cracks. General crack formation in box beam bridges include long horizontal cracking in the beam web, map cracking, longitudinal reflective cracks on the bridge deck, horizontal cracks at the

beam end, longitudinal cracks at the bottom of the beam and shear or flexural cracking. Different causes of each type of defects, along with the engineering effects, prevention and repair considerations, are discussed in the Prestressed Concrete Box-Beam Superstructure Evaluation Handbook (MDOT 2011c).

Similar to the biennial inspection of other concrete bridge elements, visual inspection is the main inspection method for assessing the condition of prestressed concrete box beam bridges. Identifying and documenting the size and extent of cracks, spalls, delaminations, exposed reinforcement and prestressing strands, section loss and evidence of water staining, corrosion and efflorescence are essential components of each box beam bridge inspection (PCI 2011). Critical locations for inspection includes bearing areas, shear zone, tension zone, joints between adjacent box beams, and areas damaged by collision or previously repaired. More attention has to be paid to reflective cracking on the riding surface of the deck as it can be an indicator of shear key leakage or failure of the transverse post tensioning (Ryan et al. 2006; Russell 2009).

### **2.2.3.1 Percent Deficiency and the Decision Making Process**

The AASHTO Guide Manual for Bridge Element Inspection provides guidelines on the indicators and limits which define a condition state for each bridge element in the PONTIS scheme (AASHTO 2011). The main health indicators that are mentioned in this guideline for prestressed box beam bridge inspection include spalled, delaminated, and patched areas, exposed prestressed strands or rebar, cracks, and efflorescence on the surface. Figure 2.6 shows the decision making procedure of assigning PONTIS condition state ratings to a deteriorated prestressed concrete box beam bridge element. Protection, repair and rehabilitation are general repair actions for the box girder element in condition states 1 to 3. Box girders with conditions beyond the limits in condition state 3 should be assigned as condition state 4. Reviewing the structural capacity, strength and serviceability for both elements and the whole bridge is required in condition state 4.

Rating a box beam bridge superstructure in the NBI rating scheme is more challenging for bridge inspectors as the guidelines for this rating system only provides a general rating system for all types of superstructures and all the structural members below the deck and above the pier cap (MDOT 2011a). Forensic examination of Lake View Drive Bridge in Pennsylvania after its collapse showed that the box beam bridge condition assessment should be defined based on cracking, spalling and strand exposure. Moreover, the superstructure should be rated according to the condition of the worst beam. Based on the findings of this forensic investigation, NBI guidelines for evaluating the box beams in Pennsylvania was updated (Naito et al. 2010) and are presented in Table 2.4. No such similar guide currently exists for Michigan box beam bridges.

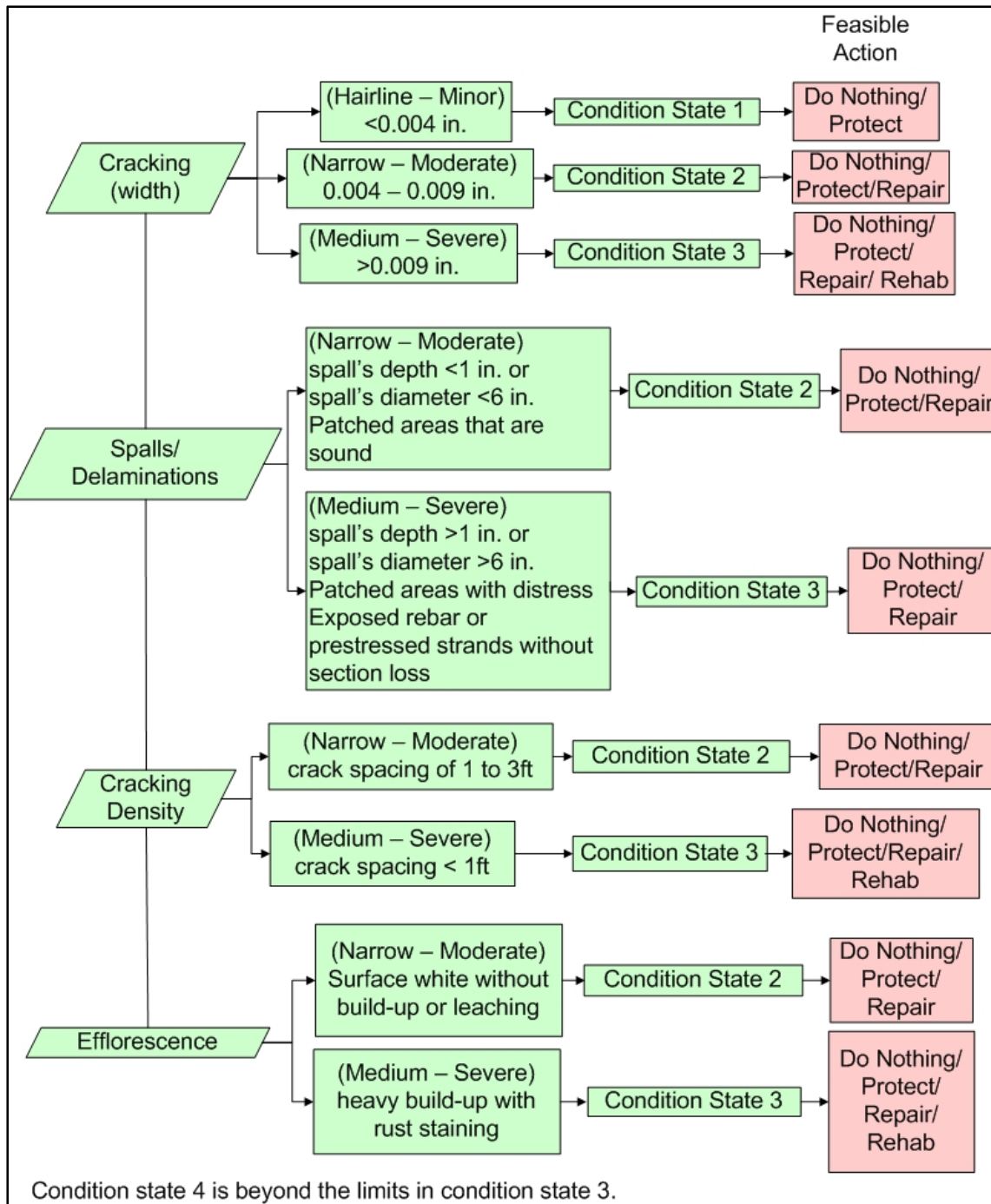


**Figure 2.6 AASHTO repair guideline for prestressed concrete closed web/box girders.**

**Table 2.4 NBI rating guideline for prestressed concrete box beam condition evaluation in Pennsylvania state, adopted from (Naito et al. 2010)**

NBI rating	Percent number of strands exposed in a single beam (%)	Description
9	0	No cracks, stains or spalls
8	0	No cracks, stains or spalls
7	0	Map cracks and miscellaneous hairline cracks
6	0	Spalled and delaminated area < 5 % Map cracking and miscellaneous hairline crack
5	1 to 5	Spalled and delaminated area < 15% Transverse cracks - None Longitudinal cracks - Hairline longitudinal cracks in bottom flange Longitudinal joints - Leakage at joints with light efflorescence
4	6 to 15	Spalled and delaminated area 15-20% Transverse cracks - Hairline flexure cracking across bottom flange Longitudinal cracks - Minor efflorescence or minor rust stains Longitudinal joints - Heavy efflorescence or minor rust stains Transverse tendons - Loose or heavily rusted Web cracks - Initiation of vertical or diagonal cracks in P/S beam near open joint in barrier
3	15 to 20	Spalled and delaminated area > 25 % Transverse cracks - Open flexure cracks in bottom flange Transverse tendons - Loose or heavily rusted Web cracks - Vertical or diagonal cracks in Prestressed concrete beam near open joints in barrier Camber - Sagging/ loss of camber
2	> 20	Any conditions worse than details above.
1		

### 2.3 Non-Destructive Bridge Evaluation Methods

Following the I-35W bridge collapse in Minnesota in 2007, there has been increasing efforts among transportation agencies to enhance bridge inspection and evaluation practices. Developing the use of innovative inspection technologies during bridge

inspections is one example which has led to a renewed interest in the application of non-destructive testing technologies to the field of bridge inspection. The main goal of applying non-destructive testing (NDT) technologies during a bridge inspection is to increase the speed of inspection, reduce the lane closures and have more reliable data than traditional bridge inspections (Ahlborn et al. 2012).

Impact echo, ultrasonic testing (UT), ground penetrating radar (GPR) and infrared thermography are some of the most common non-destructive methods for concrete bridge inspection. The main reason for the growing interest in developing these technologies is the ability to identify delaminations which occurred within the concrete subsurface and are not visible or detectable only through visual inspection. The application of infrared thermography for concrete delamination detection is the main focus of this dissertation; therefore, it is discussed and explained at length in the next chapter. A brief description of other NDT technologies is provided here-in.

### ***2.3.1 Impact-Echo***

Impact-echo (IE) is a nondestructive testing tool which is mainly used in determining the thickness of a concrete plate structure based on change in wave velocity, frequency and travel time as a sound wave is propagated through the concrete. A short-duration mechanical wave is induced into the concrete via an impact and the response is recorded by receiving transducers. Plate thickness can be calculated using the following equation

$$T = \frac{C_p}{2f} \quad \text{Equation 1}$$

where,  $T$  is the plate thickness,  $f$  is the frequency obtained from amplitude spectrum and  $C_p$  is the compression wave propagation velocity, which should be known for the material or determined prior to an impact echo testing (ASTM 1998; Scott et al. 2003; Jana 2007).

Impact-echo has been proven to be a more effective method for structures in which the lateral dimension is five times larger than the thickness, such as bridge decks, slabs and walls (Scott et al. 2003). For structures such as beams, girders, and columns, additional peaks are generated in the amplitude plot due to the reflection from the boundaries (Scott et al. 2003). Due to the capability of the IE method in determining the thickness of the plate structures, the location and depth of delaminations within concrete bridge decks can be identified. The wave's travel time through the concrete thickness above the delaminated layer is less than through the entire concrete plate and it generates a peak in amplitude spectrum at lower frequencies. The IE technique is not applicable for bridge decks with asphalt overlays due to the assumption of the constant P-wave speed throughout the depth of the concrete element (ASTM 1998) and is more effective for detecting delaminations in small areas (Ryan et al. 2006; Jana 2007).

### ***2.3.2 Ultrasonic Testing***

Ultrasonic testing (UT) is a common NDT method to detect discontinuities of solid materials, and lack of penetration and cracks in welds. UT also has the potential to detect areas of flaws and separations in layered composite materials. Data collection with UT involves transmitting a short duration pulse to the material of interest and measuring the arrival time of the reflected pulse from the surface to the receiver. Travel distance can be determined based on the known speed of the transmitted pulse in the material and the measured arrival time (Crowe 2009). UT has been recently introduced as a potential technique to detect delaminations in concrete bridges. A study by Shokouhi et al. showed that this technology can be effective in detecting deeper delaminations (depth of 6 in.) inside concrete (Shokouhi et al. 2011).

In general, advantages of the UT technique for deployment on concrete bridges include the highly portable equipment and sensitivity to detect delaminations in layered and composite structures. This technique can also be deployed on surfaces where only one side of the structure is accessible. Complicated data processing by trained experts to obtain usable results is one of the main limitations of this technique that prevent it from

being adopted by transportation agencies and bridge inspectors (Ryan et al. 2006; Crowe 2009).

### ***2.3.3 Ground Penetrating Radar***

Ground penetrating radar (GPR) is a type of radar (Radio Detection and Ranging) system that can be used to detect voids and buried objects. GPR is a very well known technique in the transportation industry for determining pavement thickness, location of voids in pavement, mapping underground utilities and bridge deck deterioration (Morey 1998; Ryan et al. 2006; Jana 2007). The main components of GPR include a transmitter and receiver antenna, and control unit. Similar to other radar technologies, an electromagnetic signal is transmitted to the object of interest and the distance is measured based on the travel time of the reflected signal (Morey 1998). In general, the GPR antenna can either be a ground-coupled antenna system or air-coupled antenna system. Data collection with the ground-coupled antenna is slower than with the air coupled antenna, however a ground-coupled antenna has a deeper depth of penetration compared to a GPR system with an air-coupled antenna (Morey 1998).

ASTM D6087 provides information on data collection and processing using a GPR system for the evaluation of an asphalt-covered bridge deck; however, it has also been noted that the test method can be applicable for bridge decks with concrete overlays (ASTM 2008). Halabe et al. found that the chloride content of the concrete bridge deck has an influence on the radar waves reflected from the surface (Halabe et al. 1997). Several recent studies also highlighted the effectiveness of GPR in detecting chloride content within the deck thickness, and likely areas of concrete deterioration and the corrosion process (Maser et al. 2012; Gucunski et al. 2013). However, using GPR in the field and interpreting the data requires trained personnel and experts to correlate the results with possible delaminations using destructive sampling (core samples) or other NDT techniques (Gucunski et al. 2013).



## 2.4 Summary

Current bridge inspection practices usually involve visual inspection of the bridge elements, and quantification of crack widths and the dimensions of spalls for accessible areas on the bridge, as much as traffic allows. Visual inspection of a bridge can be conducted in any types of bridge inspection discussed in section 2.2.1 .

Biennial or routine inspection is the most common method of bridge inspection practices. During a routine bridge inspection, a bridge inspector visually observes the bridge and makes notes of deficient areas. These notes along with general measurements of the bridge are included in the Bridge Safety Inspection Report (see Appendix B). Because this type of inspection relies on assessing the bridge visually, there are some limitations for evaluating areas that are not sufficiently visible or raise safety issues for inspectors. Although routine bridge inspection focuses on the overall condition of all bridge components, the main attention is mostly focused on the deficient areas that were found in previous inspections and were indicated in the inspection report (Fu 2005). In-depth inspection, which includes chain dragging, hammer sounding, or the use of other NDT methods, requires lane closures over or under the bridge and is mostly being done for bridges in poor condition, yet it is not a required practice during biennial inspection.

Nondestructive testing (NDT) techniques have proved to have a great potential in identifying the deteriorating condition of concrete bridge elements. However, not many of the NDT techniques can clearly detect delaminations and quantify the area and depth of the defects. Complicated data analysis and the high cost of NDT techniques are some other obstacles impeding deployment of these technologies during routine bridge inspections. None the less, infrared thermography, a NDT technique, is described and explored further in chapters 3 through 7.



## Chapter 3 Infrared Thermography

### 3.1 Concepts for Concrete Bridge Evaluation

Infrared thermography is a technology based on collecting radiant surface temperature and converting that temperature measurement into a visual image. Thermal infrared radiant energy is emitted from all objects that have a temperature greater than absolute zero. The radiant temperature ( $T_{\text{rad}}$ ) of an object is defined by the amount of electromagnetic energy exiting the object in two electromagnetic spectrum windows: 3-5 $\mu\text{m}$  and 8-14 $\mu\text{m}$ . This value is slightly lower than the true kinetic temperature ( $T_{\text{kin}}$ ) of any object due to the fact that objects are not perfect emitters (Jenson 2007).

An object that radiates the absorbed energy at a maximum possible rate is called a blackbody. This theoretical construct helps to define the amount of heat that can be radiated from an object. According to the Stefan-Boltzmann law, the amount of radiant energy exiting a blackbody is proportional to the fourth power of its temperature and expressed as

$$M_b = \sigma T_{\text{rad}}^4 \quad \text{Equation 2}$$

where,  $M_b$  is the total emitted radiation of a blackbody which is equal to the kinetic temperature,  $T_{\text{rad}}$  is the radiant temperature and  $\sigma$  is the Stefan-Boltzmann constant ( $5.6697 \times 10^{-8} \text{ Wm}^{-2}\text{K}^{-4}$ ). However, for real objects the amount of radiated energy is lower than the amount of absorbed energy. Therefore, the radiant temperature of the real object is lower than the true kinetic temperature. Emissivity ( $\epsilon$ ) of the material is the factor that affects the radiant temperature measurement of the material surface and defines the correlation between the true kinetic temperature and the radiant temperature of an object. This correlation is defined as

$$\epsilon = \left( \frac{T_{\text{rad}}}{T_{\text{kin}}} \right)^4 \quad \text{Equation 3}$$

Radiant flux is defined as the amount of electromagnetic energy exiting an object. Emissivity depends on the amount of radiant flux emitted from a material and has a value between 0 and 1. This value is almost equal to 1 for a blackbody; therefore, the radiant temperature for a blackbody is almost equal to the true kinetic temperature.

The value of emissivity of concrete is typically considered to be greater than 0.9. Characteristics such as surface roughness, color, moisture content, viewing angle, and field of view are some of the factors that can influence the emissivity of objects (Jenson 2007). Objects with darker colors absorb and emit more energy than lighter-colored objects due to the higher emissivity of darker-colored objects. Surface roughness can influence the amount of radiant energy absorbed and emitted from an object; therefore, it influences the emissivity and radiant temperature of an object. Objects with higher moisture content have higher emissivity, thus absorb and emit more electromagnetic energy. Also, the emissivity can change based on the viewing angle; this mostly affects the measurements under the bridge and between the bridge girders. A smaller field-of-view results in a higher spatial resolution compared to a larger field-of-view. It is different to look at the 2 ft by 2 ft concrete surface as compared to looking at the whole bridge in one image.

A thermal IR camera is a tool for collecting the radiant surface temperature data of an object and generating a thermal IR image. Each pixel in a thermal infrared image is designated with a temperature data. Commonly, a range of minimum to maximum temperature on each image is shown as a sidebar on the image and assigned with false color values to create a visual image. Radiation, conduction, and convection are three methods of heat transfer that can affect the heat flow through concrete. Although radiated energy is the parameter that can be measured by a thermal IR camera, the heat conductivity within the concrete and heat convection around the concrete can also influence this measurement.

The estimated emissivity value of 0.95 for concrete (ACI 2013) can be considered when collecting thermal IR images with the purpose of detecting subsurface abnormalities and

defects as the actual temperature values are not of interest in this data collection. The emissivity value is inserted as an input on the thermal IR camera software while collecting data to achieve temperature results close to the true kinetic temperature. In measuring the defective areas in concrete, the temperature difference between sound concrete and defective area is of interest to the inspector. Materials with a reflective surface, such as duct tape, have a lower emissivity compared to concrete; therefore, these materials will appear with lower temperature on the thermal infrared image.

Two approaches used in conducting an infrared thermography tests are passive and active. In the literature mostly related to the non-destructive testing (NDT) field, passive infrared thermography is generally defined as a method to detect the flaws in materials without using an external heater. With the passive method, an object radiates heat due to its internal heating system or properties. Inspecting the insulation of building envelopes, heating floors, and gas leaks are some applications of passive infrared thermography. On the other hand, active infrared thermography is described as a method to collect thermal infrared images after heating the object with an external heating system. In this method, the radiated heat from the non-defective is different from the defective areas. Therefore, defective areas are revealed on the thermal infrared image (Maldague 1993; Starnes 2002).

Although these definitions are to some extent applicable for the infrared thermography tests in the laboratory, some aspects of conducting the infrared thermography tests in the field have not been included in these definitions. What is considered an “external heating system” should be explicit in these definitions. For instance, whether the sun should be considered as an external source of heat, or not, or whether conducting the infrared thermography test using solar energy is considered a passive or an active test are some of the ambiguities in these definitions.

Infrared thermography is also categorized as a remote sensing technology as no direct contact to the object is required for collecting data in the laboratory or field. This technology is mostly referred to as thermal infrared imagery in remote sensing

applications. The general definition for passive and active remote sensing is slightly different than the aforementioned definition in the NDT application. Passive remote sensing is generally referred to as recording electromagnetic energy reflected or emitted from the surface of the earth. In this case, the solar energy can be considered as the passive source of heat. However, active remote sensors are ones that are not dependant on the sun's electromagnetic energy or the earth's thermal properties. These sensors create their own electromagnetic energy, transmit it to the object of interest and record the back scatter energy with their receivers (Jenson 2007).

There is clearly a need to clarify exactly what is meant by passive and active infrared thermography for concrete bridge inspection. Passive and active infrared thermography definitions can be modified for bridge applications based on the two abovementioned definitions. The passive infrared thermography method includes collecting radiated energy from the bridge element and does not include generating or transmitting the electromagnetic energy. The source of transmitted electromagnetic energy can be either the sun or thermal properties of the bridge elements. Examples of the latter case can include inspecting a concrete element based on heat of hydration after placing the concrete, or detecting abnormalities in concrete based on the ambient temperature change and not necessarily change caused by solar energy.

On the other hand, the active infrared thermography method involves heating up the surface of interest by an external heater and collecting thermal infrared images during heating or cooling periods. Recording the heating and cooling time is crucial in active infrared thermography to allow for resolving the depth and size of the flaw and obtaining quantitative information. Although an external heater is not part of the thermal infrared sensor, it is a component of the whole active infrared thermography system.

### **3.2 Passive Infrared Thermography**

In this dissertation, the term passive infrared thermography refers to conducting a thermal infrared test using solar energy or ambient temperature change as the source of heat. This

technique is also called thermal infrared imagery in the remote sensing field. The concept behind the application of this technology in concrete bridge evaluation is that anomalies and subsurface delaminations interrupt the heat transfer through the concrete and appear with different temperatures on the thermal IR image compared to the area of surrounding sound concrete (see Figure 3.1). During the day, as the ambient temperature increases, concrete absorbs heat and starts emitting radiant energy. Delaminations and air voids within the concrete will resist the heat transfer and warm up at a faster rate compared to the area of the surrounding sound concrete, thus delaminations will appear as hot areas on the thermal IR image. However, during the night, as the ambient temperature decreases, the area of the sound concrete around delaminations loses heat at a lower rate compared to the delaminations, thus delaminations appear as cold areas on the thermal IR images (Washer et al. 2009a).

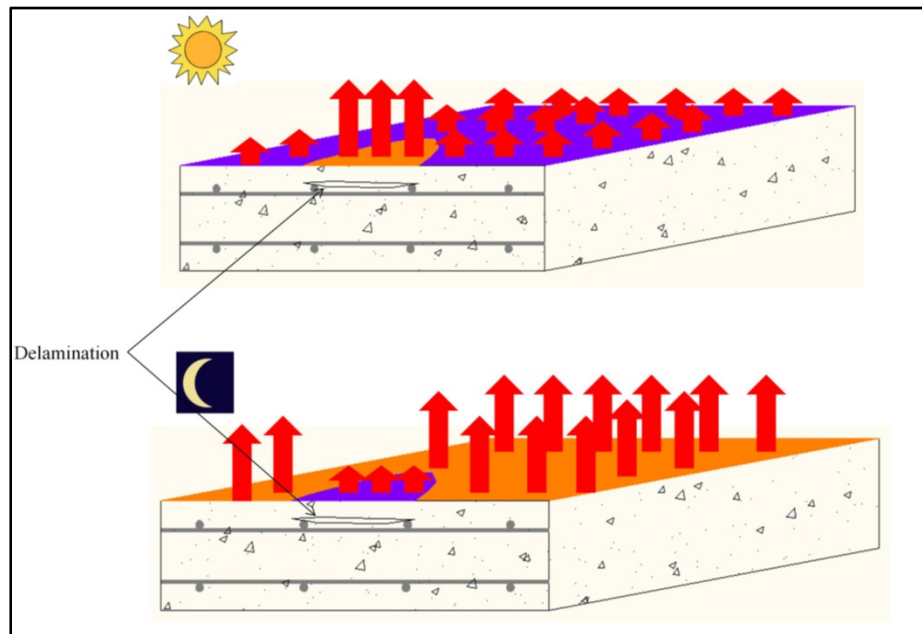


**Figure 3.1** Emitted thermal infrared energy from a concrete deck during the day and night.

Infrared thermography has been cited in the ACI 222 report as a potential tool for detecting delaminations (ACI 2001). ASTM D4788 describes the test method, equipment and environmental conditions for detecting delaminations on the top side of the concrete

bridge decks using this technology (ASTM 2007). This remote sensing technology can yield both qualitative and quantitative indicators of condition. A delamination map, created from the outputs of a thermal IR bridge inspection, can help to document delaminations and can be used to determine the total area and percentage of delaminations over the entire bridge deck.

According to the ASTM D4788, a thermal IR camera (0.2°C thermal resolution), video recorder, video camera, distance measurement device, test vehicle and contact thermometer are the equipment required for the passive infrared thermography test over the bridge deck. A vehicle mounted thermal IR camera and a video recorder are driven over each lane on a bridge deck. The thermal IR camera needs to be mounted on the vehicle in a way that allows the minimum image width of 14ft. The conventional video image camera is used with the infrared image to separate patches and surface defects. Bridge deck dryness is a factor that has to be considered during data collection with this method; as moisture on the surface can affect emissivity and reduce the thermal contrast on the thermal IR image. The maximum speed of the data collection specified by the ASTM standard is 10 mph (ASTM 2007).

Time of data collection is the most critical factor in a passive infrared thermography test. Not all materials in the environment have the same response to the ambient temperature change; this causes the variation of the objects' radiant temperature during a 24-hour period for different materials. The term thermal inertia refers to the thermal response of a material to temperature changes. Thermal conductivity, density and thermal capacity are factors that can influence the thermal inertia of the materials. Thermal capacity refers to a measure of the ability of materials to absorb heat while thermal conductivity is the measure of the heat transfer through materials. Thermal inertia can be calculated with the following equation

$$P = \sqrt{K \rho C} \quad \text{Equation 4}$$



where  $K$  is thermal conductivity,  $C$  is thermal capacity (specific heat) and  $P$  is thermal inertia. Figure 3.2 shows the diurnal radiant temperature of selected materials in the environment. Two thermal crossover times can be identified in the diurnal graphs of radiant temperature of materials. These two times are roughly the local sunrise and local sunset; when the radiant temperatures of the materials are the same and appear with the same temperature on the thermal IR image.

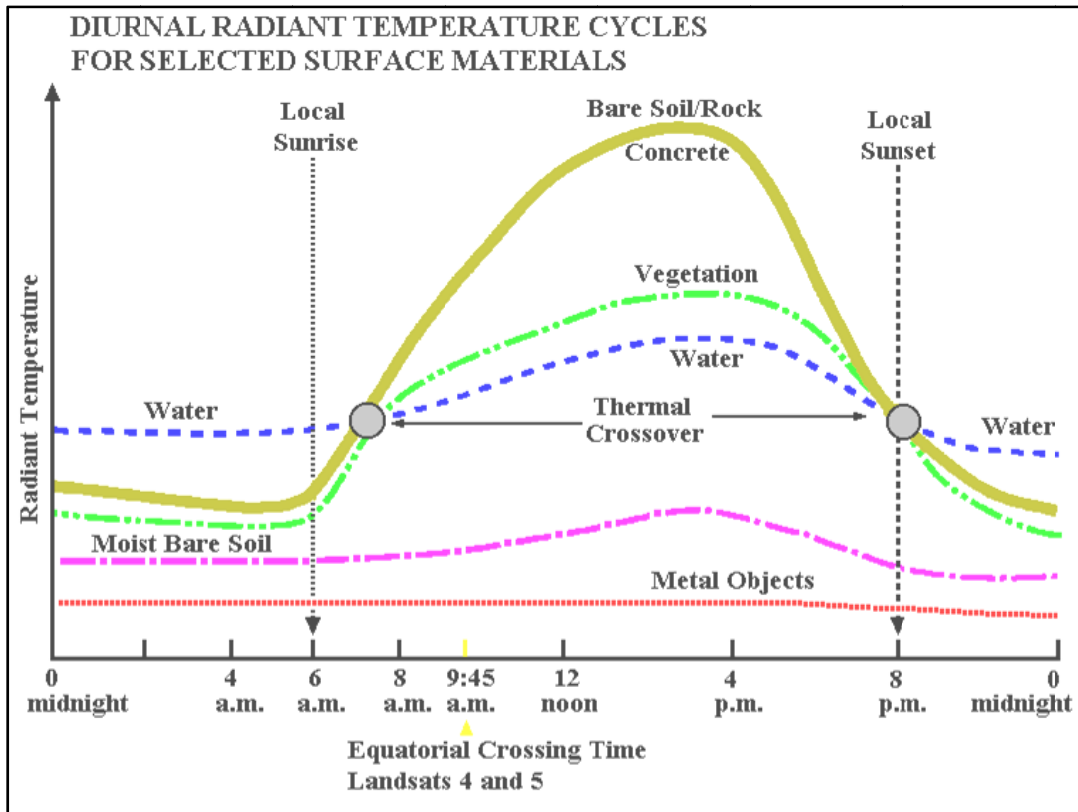


**Figure 3.2** The diurnal radiant temperature graph of selected materials (Jenson 2007), reprinted by permission of Pearson Education, Inc.

Concrete materials and delaminated areas on a bridge have similar behavior with respect to ambient temperature changes. The most contrast between a delaminated area and the surrounding sound concrete area appears a few hours after each cross over time (Figure 3.3). In a study conducted by Washer et al. on developing the infrared thermography inspection technology for bridges, it was found that the effective time to perform a passive infrared thermography survey depends on the depth of the delamination. The

most contrast appears on the thermal IR images approximately 4 hours after sunrise for a 2 in. deep delamination and 7 hours after sunrise for a 3 in. deep delamination. Also, it has been noted in this study that deeper delaminations appear with lower temperatures on the thermal IR image (Washer et al. 2009a).

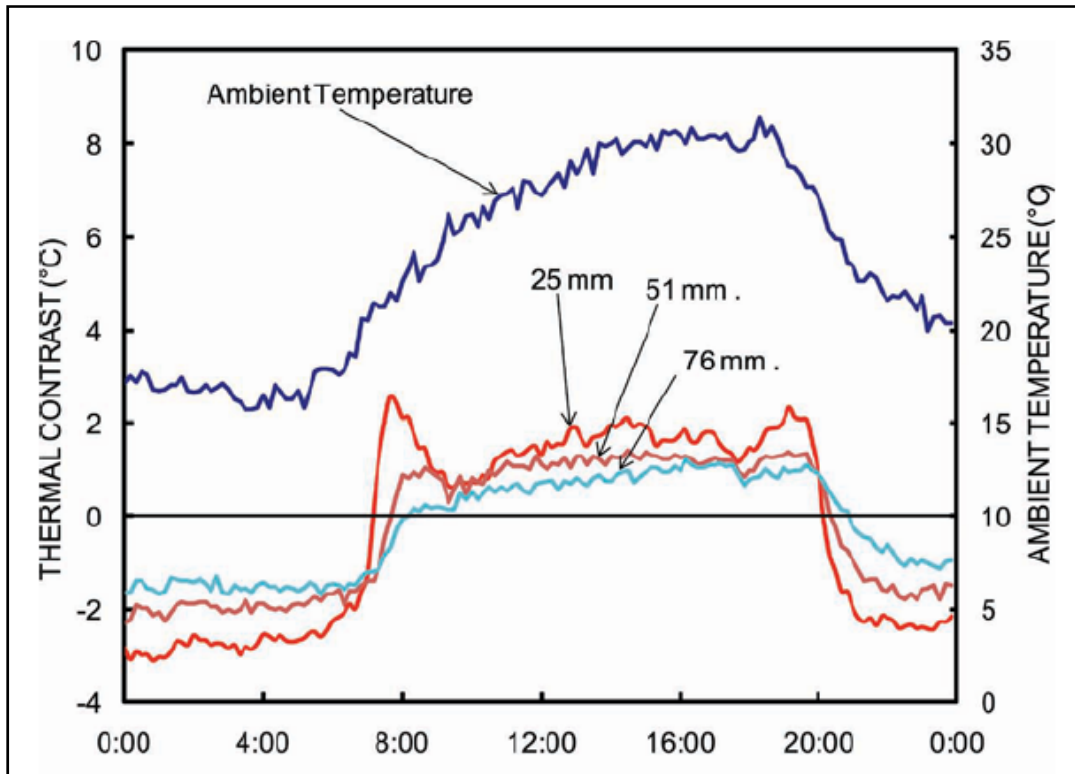


**Figure 3.3** The diurnal temperature graph for delaminations at different depths (Washer 2010), used with permission from the American Society for Nondestructive Testing.

### ***3.2.1 Advantages of Bridge Inspection with Passive Infrared Thermography***

The advantages of the passive infrared thermography technique includes capability of detecting subsurface defects and delaminations, commercial availability, remote sensing, and ease of data collection and image interpretation that highlights the benefits of applying this technique in biennial bridge inspection practices (Ahlborn et al. 2012). Laboratory and field studies of passive infrared thermography for concrete slabs show

that this technique is capable of detecting shallow (up to 3 in. from the top surface) delaminations which can help bridge inspectors identify areas of unsound concrete before they turn into spalls (Ahlborn et al. 2012).

Evaluating the top surface of concrete bridge decks has been mentioned in the literature as the main application of passive infrared thermography for bridge inspection as this element is exposed to direct sunlight. This technology also has the potential to be applied at near highway speed over the bridge deck with more advanced camera models, which can help to conduct bridge inspections more frequently, in a safer manner, and at a faster rate.

Several studies have demonstrated that this technology can also be applied for detecting delamination and damage underneath the deck and within the bridge soffits which can be critical for passing traffic under the bridge (Washer 2010). Remote sensing with thermal IR imagery can reduce traffic disruption and lane closures on and underneath the bridge, as no direct contact is required (Vaghefi et al. 2012). Results from thermal IR imagery can be imported and stored into GIS tools, thus it allows a bridge management team to review the bridge information easier and facilitates the decision making process (Vaghefi et al. 2013).

Another advantage of using passive infrared thermography is that this technique does not require an external heater, thus it is less expensive than active infrared thermography. The only major cost for application of this technique is the thermal infrared camera, which can be inexpensive if collecting images while moving the camera is not necessitated.

### ***3.2.2 Limitations of Passive Infrared Thermography and Environmental Effects***

Previous studies on passive infrared thermography applications for bridge inspection have reported several limitations that should be considered. Clark et al. highlighted the

fact that emissivity of the concrete surface can vary based on the extra materials on the surface, thus the brightness of the materials on the surface does not necessarily correlate with the subsurface concrete defects (Clark et al. 2003). Factors such as soil, moisture, oil spills, and staining on the concrete surface can appear as hot spots and affect the results of passive infrared thermography; therefore, taking optical (visual) images of the concrete surface is necessary to enable the inspector to separate these areas from delaminations.

Wind speed, solar energy, ambient temperature and humidity are environmental factors which influence thermal IR images (Washer et al. 2009b). More advanced thermal IR cameras models have the option to adjust the image based on the relevant humidity and ambient temperature occurring at the time of data collection. The minimum ambient temperature of 32°F and the maximum wind velocity of 30 mph have been highlighted as upper limits on environmental criteria for performing passive infrared thermography of concrete bridge decks in ASTM D4788 (ASTM 2007). Washer et al. investigated the effects of variable environmental conditions on concrete bridge inspections and suggested a maximum wind speed of 8 mph on a sunny day and 10 mph when the surface is not directly exposed to solar energy. Also, it has been noted that consistent solar loading on the concrete can provide a better contrast on a thermal IR image (Washer et al. 2009b).

Infrared thermography inspection is mostly applied for shallow delaminations. The maximum depth of 3 in. has been mentioned in the literature as a limitation of this technology in detecting delaminations. What needs to be considered when interpreting a thermal IR image is the fact that deeper delaminations manifest as areas with less temperature values compared to shallower delaminations.

Determining the quantitative measures with passive infrared thermography is also a challenge that has to be considered while analyzing the results. Although generally more variables are involved in conducting a passive infrared thermography test, some previous studies suggest that processing methods that are applicable for active thermography tests have the potential to be used for passive thermography as well (Abdel-Qader et al. 2008).

### **3.3 Active Infrared Thermography**

Unlike passive infrared thermography, active infrared thermography involves a transient heat transfer phenomena using an external heater other than the sun or thermal properties of the object itself. In this case, electromagnetic energy is transmitted to the specimen by an external heater and emitted radiant energy from the object can be recorded by a thermal IR camera. Therefore, during this test the specimen has to be intentionally warmed up to create the gradient temperature difference on the object's surface. Thermal IR images can be collected during either the heating or cooling period.

Although most of the previous field applications of the infrared thermography in civil engineering have focused on passive thermal IR techniques, Pollock et al. (2008) investigated the possibility of using external heaters to warm up prestressed concrete bridge girders before collecting the thermal IR images. Two methods were considered to perform this test on the bridge. In the first method, a heater was placed inside the prestressed box girder and thermal IR images were taken from the external surface of the box girder underneath the bridge. In this method, irregularities appeared as cold spots in the thermal IR images. Performing this test with this method is not always possible, as it requires access inside the box beams. The second method involved heating the underneath of the bridge box girders by placing a heater on a lift truck platform and heating the girders for one to three hours before taking thermal IR images. Both of these methods showed promise for detecting delaminations in prestressed girders; however cost and accessibility are two factors that need to be considered in applying active thermal IR imaging for bridge inspection (Pollock et al. 2008).

Distinction between active and passive approaches is not as clearly defined in the literature. For examples, in the abovementioned study conducted by Pollock et al. (2008) on detection of voids in prestressed box beam bridges, the external heater was placed inside the box beam. According to the aforementioned definitions, this test method can be categorized as an active approach due to the use of external heating system. However, one can argue that placing the heater inside the test specimen can be similar to the

building insulation inspection and should be categorized as a passive approach. This is the reason that mentioning the “intentional” heating is an important component in the definition of active thermography.

A variety of controllable heating sources, including hot air guns, quartz lamps and heat blankets can be used to produce thermal excitation on the test specimen. Solar energy has been mentioned by some researchers as a potential external heat resource (Spring et al. 2011). However, solar energy is not considered as an external heating source in this study, despite the opinion of some researchers in this field.

### ***3.3.1 Advantages of Active Infrared Thermography***

Ease of data collection and interpretation of thermograms as well as high-speed data collection were mentioned as advantages of active infrared thermography. Moreover, this technique can also be adopted when inspecting elements that are accessible only to one side. One of the major benefits of using this method is the ability to store the data for monitoring the damage growth process during the service life of the structure. This allows for better allocation of maintenance funds for bridges in a region.

Being able to determine the depth of delamination, as well as the location and size, is an important feature in active infrared thermography. Besides, this approach is not dependant on the weather condition and clear sky; therefore, it allows conducting a bridge inspection in a larger time window. Furthermore, this method can be applied on the concrete bridge elements which are not exposed to the direct sunlight, such as girders and underside of the bridge deck.

### ***3.3.2 Limitations of Active Infrared Thermography***

Although, this technique allows for a wider inspection time window and it does not necessarily have to be conducted at a certain time of the day, the sunlight on the bridge deck can interfere the results that are obtained in the field (Hover et al. 2004). Therefore,

applying this technique during the cross over time for the elements that are exposed to the sun is a more viable option. Different emissivity of materials on the surface still are a challenge as it creates a perturbing contrast on the thermal IR image that may not necessarily correspond to subsurface flaws (Maldague 1993).

### ***3.3.3 Active Infrared Thermography Methods***

Active infrared thermography techniques are commonly named based on the source of the external heater. Examples of these methods include: Pulsed (Flash) thermography, Pulsed phase thermography, Lock-in thermography, Vibrothermography, Inductive thermography, Laser spot thermography and Step heating. These techniques are briefly discussed in the following sections.

#### **3.3.3.1 Pulsed Thermography (Flash Thermography)**

The Pulsed thermography technique is one of the most common methods of active infrared thermography. The components of this system include a thermal infrared camera, a high-power flash lamp and computer for data acquisition. A pulse of electromagnetic energy is discharged and absorbed by the surface of the material. The temperature of the material changes rapidly during and after the pulse, due to the heat diffusion which is the cause of thermal propagation along with convection and radiation. Change of temperature due to heating is around 5 to 10°C (9 to 18°F) and no harmful radiation was emitted to the element being inspected (Maldague 1993). The presence of subsurface defects interrupts the heat diffusion through the material and appears with a different temperature than surrounding sound area. Deeper defects or flaws receive the thermal pulse at a later time than shallower defects. Therefore, observing the deeper defects is possible at a later time. The relationship between the depth of the anomalies and observation time is expressed by Equation 5.

$$t \approx \frac{z^2}{\delta}$$

**Equation 5**

where  $z$  is the defect depth,  $t$  is the observation time, and  $\delta$  is thermal diffusivity of the materials and defined by Equation 6.

$$\delta = \frac{K}{\rho C} \quad \text{Equation 6}$$

where  $K$  is thermal conductivity,  $\rho$  is material density and  $C$  is thermal capacity or material specific heat (Maldague 1993; Ghosh and Karbhari 2006) .

According to the abovementioned concepts, a higher material density can result in a lower thermal diffusivity, thus a longer defect observation time. Moreover, the diffusion process weakens the heat as it gets deeper in the material. Therefore, the contrast between the defected area and background decrease by increasing the defect depth. Equation 7 defines the relationship between the loss of contrast “ $c$ ” and the defect depth.

$$c \approx \frac{1}{z^3} \quad \text{Equation 7}$$

This equation highlights one of the limitations of infrared thermography techniques. This technique is mostly effective for shallow delaminations; deeper defects are not detectable with this technique due to the increase in loss of contrast (Maldague 1993). A detectable defect generally should have a radius-to-depth ratio of at least one or greater to create the detectable temperature gradient on the surface (Maldague 1993; Spring et al. 2011).

Active infrared thermography can be applied on a test specimen in two test configuration modes: reflection and transmission (see Figure 3.4). In the reflection mode, the heater and thermal IR camera are placed at one side of the specimen, while in the transmission mode the heater and thermal IR camera are placed on either side of the specimen. These two configuration modes pertain to specific circumstances depending on the required information. Reflection mode can reveal information regarding the defect depth and is generally more applicable for specimen with smaller thicknesses. On the contrary, observation time and defect depth information cannot be resolved by using the transmission mode (Maldague 1993). Heating methods that were used by Pollack et al.



are examples of applying these two configurations for bridge box girders. Placing heaters inside the box and monitoring the temperature gradient on the outside surface simulates the transmission configuration mode while having a heater and camera both on the outside of the box girder simulates the reflection testing mode (Pollock et al. 2008).

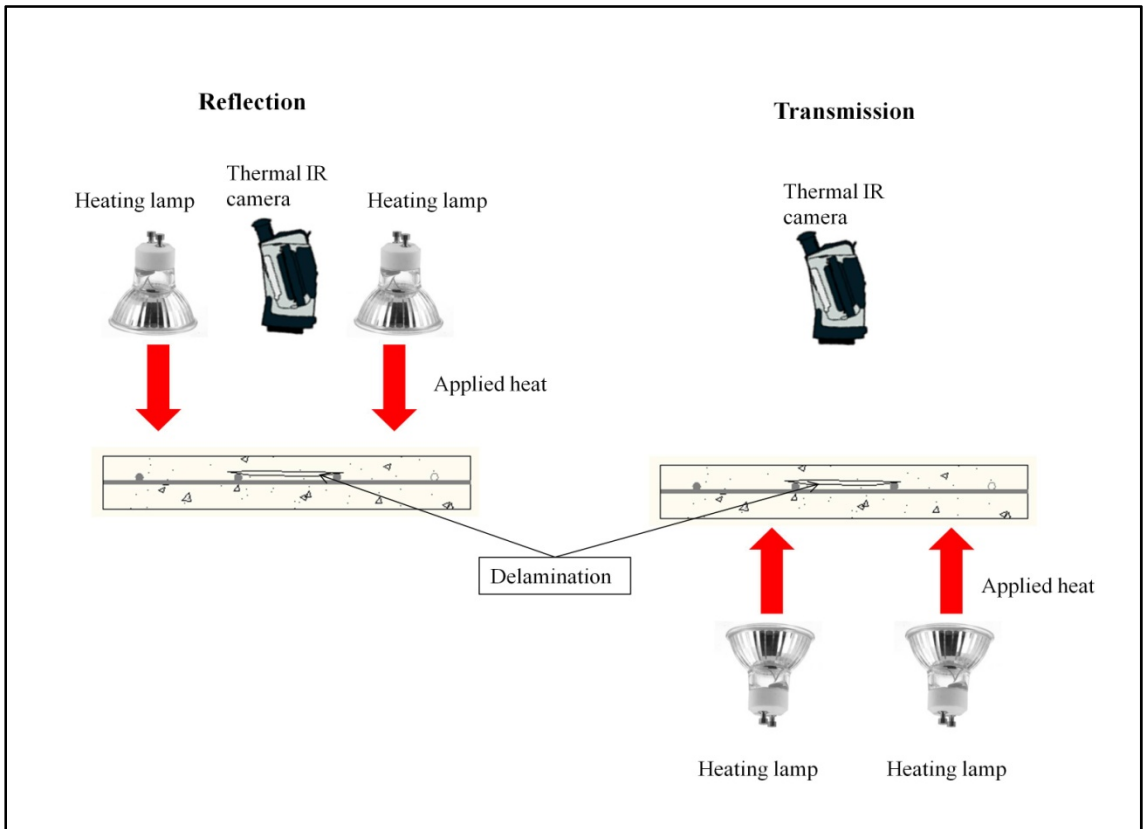


**Figure 3.4 Infrared thermography testing configuration modes.**

Three methods of heating configuration using pulsed infrared thermography include: point, line and surface methods (Maldague and Moore 2001). In the point method, electromagnetic energy is transmitted to the surface with a laser point and reflection from the surface is recorded by a thermal IR camera. Uniform heating and repeatability can be achievable using this technique; however, inspecting a surface with this method is time consuming due to the point by point inspection moving along the specimen. The line method involves heating the specimen surface by moving line lamps, heated wires, a scanning laser or an air jet. Fast inspection and uniform thermal gradient are advantages of using this method. Complete analysis of the phenomena can be obtained using the

surface method. Heating systems in the surface method test includes lamps, flash lamps or a scanning laser. Not all the points on the surface of the specimen are at the same distance to the heating source; therefore, it is hard to achieve uniformity on the specimen surface. Figure 3.5 illustrates these three heating methods.

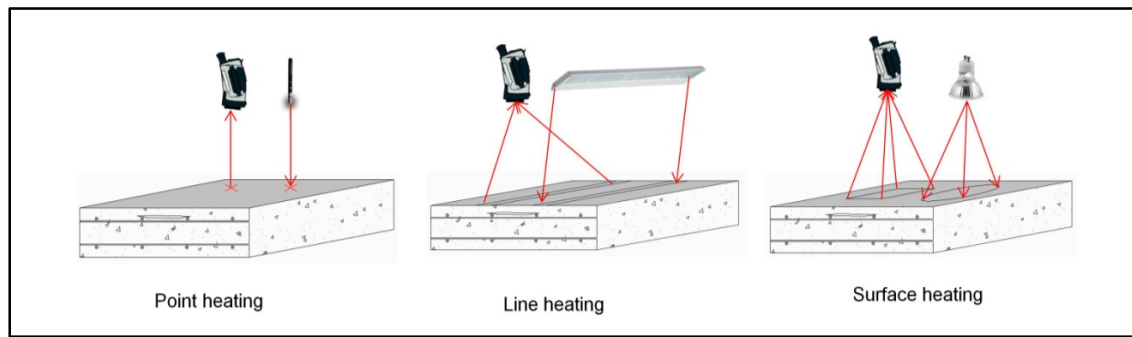


**Figure 3.5 Different heating methods for infrared thermography inspection.**

#### ***3.3.3.1.1 Applications in Civil Engineering***

Pulsed thermography has been successfully used in detecting debonding and delaminations between the Fiber Reinforced Polymer (FRP) layer and concrete, where the FRP layer is commonly used on concrete structures for rehabilitation and retrofitting purposes. Quality of the bond between the FRP layer and existing concrete is one of the major components to ensure the optimum performance of the composite system. Starnes (2002) carried out several laboratory studies to determine the effect of depth, thickness and width of the subsurface flaw under the FRP layers and obtained quantitative measures (Starnes 2002). Moreover, this technique is also proven to be useful for detecting debonding under the CFRP composite layer of flexural members under loading (Levar and Hamilton 2003). Other experimental applications of pulsed thermography includes detection of ungrouted voids inside tendon ducts in prestressed concrete construction and detecting debonding between an asphalt overlay and the concrete bridge deck (Maierhofer et al. 2006).

Research on the application of active infrared thermography for concrete material showed some promising results in both laboratory studies and in the field. One of the difficulties

in deploying this technique on actual concrete bridges is the need for an aerial or bucket truck to locate the heating source at a close distance to the structure. To overcome this limitation, remote heating was studied and deployed by Kurita et al. (2009) on an elevated bridge. A xenon arc lamp used in this study had the ability to heat up an elevated concrete structure from a distance, and thermal IR images were collected from the underside surface of the concrete deck. This method proved to be more effective compared to passive thermography for detecting delaminations between concrete and a FRP layer, previously used as repaired material for the elevated bridge deck (Kurita et al. 2009).

### ***3.3.3.1.2 Contrast Computation***

Contrast values on a thermal IR image can be computed based on the application and image analysis procedures. Absolute contrast ( $C^a$ ) is one of the commonly used definitions which correspond to the relative temperature change at a given time as computed by Equation 8.

$$C^a(t) = \Delta T(t) = T_{\text{def}}(t) - T_s(t) \quad \text{Equation 8}$$

In this equation,  $T_{\text{def}}(t)$  refers to the temperature of the suspected defective area at a particular time ( $t$ ) and  $T_s(t)$  refers to the temperature of the intact area at the same particular time ( $t$ ) (Maldague 2001). This contrast also was referred to as signal in some previous literatures (Starnes 2002).

Running contrast ( $C^r$ ) is also one of the commonly used concepts for defect detection; this definition is less dependent on the actual temperature values or emissivity of the tested materials. The running contrast is defined by Equation 9 (Maldague 2001). This concept also was referred to as loss of contrast (Starnes 2002).

$$C^r(t) = \frac{\Delta T(t)}{T_s(t)} = \frac{T_{\text{def}}(t) - T_s(t)}{T_s(t)} \quad \text{Equation 9}$$

### 3.3.3.2 Pulsed Phase Thermography

Pulsed phase thermography is similar to the pulsed thermography in a sense to collect thermal IR images in a transient state. However, using frequency analysis with the discrete-time Fourier Transform (DTFT) method allows for faster data collection at all frequencies. Monitoring the change in phase ( $\Phi(f)$ ) and amplitude ( $A(f)$ ) for different depth flaws can help to determine the thermal diffusion length of each specific material. The thermal diffusion length ( $\mu$ ) is defined as

$$\mu = \sqrt{\frac{2\delta}{\omega}} \quad \text{Equation 10}$$

where  $\delta$  is material diffusivity and  $\omega$  is angular frequency (Maldague and Moore 2001) . The advantages of applying this method on concrete bridges include detecting deeper delaminations as well as enhancing the resolution for defect extraction and geometry (Maierhofer et al. 2006).

#### 3.3.3.2.1 Applications in Civil Engineering

Pulsed phase thermography has been investigated by Maierhofer et al. for a concrete specimen with inclusions at different depths. Three radiators at a distance of 6 inches were moved along the specimen to ensure uniform heating. In this study, better geometrical resolution was obtained on phase images (Maierhofer et al. 2006). Investigating the influence of concrete properties on the thermal IR data is another remarkable application of this technique. Results of the study conducted on three concrete specimens with different densities show that increasing the porosity of concrete

reduces the thermal conductivity and influences the relative temperature difference between inclusions and sound surrounding concrete (Maierhofer et al. 2007).

A recent study by Van Leeuwen et al. involved applying pulsed phase thermography on a concrete bridge which was exposed to direct sunlight. Plexiglas window and screen protection were used to simulate phase pulsed thermography with solar energy. Although using an external heater in the laboratory study shows better resolution on thermal IR images, solar energy was selected in this experiment to facilitate the testing process. Results from this test showed higher contrast on amplitude images compared to phase images (Van Leeuwen et al. 2011). Note that although solar energy was the source of heat in this test, simulating the pulsed phase heating was still intentionally done with a screen protection to conduct an active infrared thermography test.

### **3.3.3.3 Lock-in Thermography (Modulated thermography)**

The Lock-in thermography technique is based on transferring a modulated excitation (usually a sinusoidal pulse) to the specimen and capturing the thermal IR images at very small time increments. The external heater used in this case can be either a quartz lamp (Photothermic radiometry) or mechanical excitations such as ultrasonic or acoustic excitations (Maldague and Moore 2001). Monitoring the time between the output signal and the reference input signal is one of the critical components of this technique. The depth of the inclusion can be measured based on the phase delay and heating period (Vedula 2010). Capturing both phase and amplitude images based on Fourier transformation of collected data can provide critical information relative to the purpose of study. Phase images are usually independent of the environmental or surface features and can provide information with regards to depth based on computing the thermal diffusion length similar to the pulsed phase thermography (Equation 10).

There has been limited application of lock-in thermography in civil engineering specifically for concrete bridges due to the difficulty of processing the data and capturing information on site. In a study conducted by Sakagami et al., the feasibility of the

application of lock-in thermography for concrete material was investigated (Sakagami and Kubo 2002). This study proved that area and depth of subsurface delaminations can be determined using phase delay images. Also, it has been determined that deeper delaminations appear on the thermal IR image more clearly at longer heating periods while shallower delaminations appear when the period is shorter. This reveals the information with regards to the optimal heating period for a delamination at a specific depth. Furthermore, results from this study provided more evidence to show that defects deeper than 2 in. cannot be detected with this technique (Sakagami and Kubo 2002).

#### **3.3.3.4 Vibrothermography**

In this thermography technique, mechanical excitation is used to monitor the damage progress and stress concentration under loading. Vibrothermography or Thermosonic has been successfully used to locate damage in composite structures (Ghosh and Karbhari 2006). Analyzing the fatigue performance and heat dissipation localization are also mentioned as successful applications of this method. One of the remarkable applications of this technique in civil engineering includes monitoring the performance of the structure and formation of plastic hinges at the column base before cracks become visible. In this application, quasi-seismic loading can be applied to the structure by a mass exciter placed at the top of the structure, and heat dissipation at the bottom of the structure and columns can be monitored (Maldague and Moore 2001). Therefore, this technique is very useful in quality control and refining the design values in large concrete structures.

#### **3.3.3.5 Inductive Thermography**

Inductive thermography is one of the recently developed infrared thermography methods to detect steel rebar or prestressed strand corrosion. This method is based on inducing current in the rebar by generating an electromagnetic field. One of the advantages of this method compared to the previous experimental studies was the use of a non-contact heat induction system which allows for inspecting the inaccessible bridge elements. Previous

experimental studies with this method showed that the higher corrosion level in steel rebar results in the higher heating rate and the higher peak radiated intensity. These results are due to the higher electrical resistivity of corroded rebar (Baek et al. 2012). In addition, this method seems promising for detecting ungrouted tendon ducts. Poor filling of PVC tendon ducts could be detected with an inductive heating system and using phase and amplitude images (Brachelet et al. 2009).

### ***3.3.4 Quantitative Defect Information***

Extracting the quantitative information such as size, depth and location of the defective area from a thermal infrared image is one of the major challenges, especially in the field of bridge inspection. Several studies have covered data and image processing to extract the defective area in the concrete based on image segmentation algorithms, and then used that information to calculate the delaminated area. In this case, a critical threshold greater than the threshold of the false alarm should be defined. In most cases of thermal infrared image interpretation, an operator can segment images as it appears originally due to the powerful combination of human-eye and brain (Maldague 2001).

Image segmentation allows for defect pattern recognition and is an initial step in the process. Image segmentation methods include threshold based, edge detection, region growing and hybrid methods. Preliminary work was conducted by Abdel-Qader et al. to develop a segmentation algorithm based on selecting a threshold and edge detection methods (Abdel-Qader et al. 2008). This algorithm can predict and detect the area of delaminations without human interference. One of the disadvantages of these kinds of algorithms is that selecting a threshold for a single image may increase the risk of removing some small delaminated areas from the data set. Also, in most cases having a subjective interpretation by an operator allows for a more thorough and reliable thermal IR image analysis.

Although calculating the area of delaminations and specifying the locations on the bridge deck is a more critical task during bridge inspection, depth and thickness of the defective

area can give more detailed information that helps in predicting the actual remaining service life of the structure. Monitoring the temperature change in active pulsed thermography can help in estimating the depth of the defective areas. The relationship between the flaw appearance time and depth was investigated by Allport et al. in 1988. Results of this study showed that the running contrast and resolution of thermal patterns are dependent on the flaw depth and size. Flaws appear on the thermal IR image proportional to the square root of the flaw depth (Equation 5). Also, the loss in contrast (running contrast) is estimated to be approximately proportional to the cube of the flaw depth (Equation 7) (Allport and McHugh 1988).

The effect of the defect size in infrared thermography testing was initially introduced by Vavilov and Taylor in 1982 (Vavilov and Taylor 1982). In this paper, it was pointed out that the defect size should be two to three times larger than the material above the defect. This ratio can be calculated by dividing the square root of the defect surface area (A) by the depth (z) at which it is located (Equation 11) (Vavilov and Taylor 1982). Maldague also highlighted this factor as an empirical rule in infrared thermography. He emphasized that the radius of the defect should be at least one or two times larger than the depth, to be detectable by the infrared thermography testing (Maldague 1993).

$$R = \frac{\sqrt{A}}{z} \quad \text{Equation 11}$$

### ***3.3.5 Heating Sources in Active Infrared Thermography***

An IR heating unit, a fan heater, a halogen lamp, and a flash light are the heating methods which have been applied in civil engineering and suggested by previous researchers (Arndt 2010). Table 3.1 summarizes the heating parameters and applications in the previous literature. Selecting a heating source is highly dependent on the thermal output of the heating source and the depth of flaws or delaminations. Generally, sources with lower thermal output can be effective in detecting flaws closer to the surface but if the



defect happens to be deeper inside the material, a source with more heating output is required. Selecting the heat source for an active infrared thermography test also depends on the heating method selected for the study and the area of interest.

**Table 3.1 Heating methods and parameters for different applications in civil engineering**

Heater	Power (W)	Power (Btu/hr)	Distance	Heating Duration (sec)	Application	Area	Source
Six halogen flood lights	3200	11000			Voids in Concrete Slab	4 ft x 4 ft (1.2 m x 1.2 m)	(Abdel-Qader et al. 2008)
Three infrared radiator (moving along the surface)	3x2400	3x8200	6 in. (15 cm)	300, 900, 2700	Voids in Concrete Slab	60 in. x 60 in. (1.5 m x 1.5 m)	(Maierhofer et al. 2002)
Two 250 W infrared heating lamps (200mm)	500	1710	13 in. (33 cm) 2 in. (50 mm)	10	CFRP laminates	24 in. x 9.84 in. x 1.77 in. (610 mm x 250 mm x 45 mm)	(Starnes et al. 2003)
Quartz lamp (laminated FRP)	500	1710	6 in. (152 mm)		FRP laminates	3 ft <sup>2</sup> (0.29 m <sup>2</sup> )	(Levar and Hamilton 2003)
Kerosene heater (larger area - Fabric FRP)	22000	75000	6 in. (152 mm)		FRP laminates	3 ft <sup>2</sup> (0.29 m <sup>2</sup> )	(Levar and Hamilton 2003)
Quartz heater	1500	5200			Existing RC bridge pier		(Halabe et al. 2012)
Fan heater	2000	6800		<300	Voids in Concrete Slab	<10.76 ft <sup>2</sup> (<1 m <sup>2</sup> )	(Arndt 2010)
Halogen lamp	2x650	2x2200		3	FRP delaminations	6.73 ft <sup>2</sup> (0.625 m <sup>2</sup> )	(Arndt 2010)
Flash light	2x1500	2x5200		0.10	FRP delaminations	6.73 ft <sup>2</sup> (0.625 m <sup>2</sup> )	(Arndt 2010)
Xenon arc lamp	6000	21000	18.7 ft (5.7 m)	950	Elevated concrete bridge FRP delamination		(Kurita et al. 2009)
Flash light	2 x 500	2 x 1710	7.9 in. (20 cm)	50ms	FRP composite system	72 in <sup>2</sup> (464.5 cm <sup>2</sup> )	(Brown and Hamilton 2007)
Scan (line heating)	2 x 500	2x 1710	3 in. (7.6 cm)	12	FRP composite system	288 in <sup>2</sup> (1858 cm <sup>2</sup> )	(Brown and Hamilton 2007)
Long pulse (flash lights)	2 x 500	2x 1711	7.25 in. (18 cm)	30	FRP composite system	432 in <sup>2</sup> (2787 cm <sup>2</sup> )	(Brown and Hamilton 2007)
Long pulse (flash lights)	2 x 500	2x 1712	7.25 in. (18 cm)	60	FRP composite system	432 in <sup>2</sup> (2787 cm <sup>2</sup> )	(Brown and Hamilton 2007)

### **3.4 Summary of Infrared Thermography Techniques**

Previous studies on the application of passive infrared thermography on concrete bridge decks proved that this technique has the potential to be deployed on a regular basis. Capabilities and limitations of different infrared thermography methods for concrete bridge condition assessment are summarized in Table 3.2. While passive infrared thermography is an easier option for deployment in the field, it is a time and weather dependant technique. Also, passive infrared thermography is only useful for revealing the information with regards to the area and is not as sensible for estimating the depth information.

Active infrared thermography can resolve not only the defective area and locations, but also the defect depth information. Additionally, it is more difficult to apply active infrared thermography on a regular basis on the bridge deck; however, this technique is not time or weather dependent and does not require solar energy to work. There are several other infrared thermography methods such as step heating and laser-spot thermography that are not applicable for bridge condition assessment and have not been discussed herein.

**Table 3.2 Evaluation of infrared thermography techniques for concrete bridge condition assessment**

<b>Technique</b>	<b>Capabilities in bridge condition</b>	<b>Limitations in bridge condition assessment</b>
Passive Thermography*	<ul style="list-style-type: none"> <li>▪ Easy deployment</li> <li>▪ Most applicable for top side of the deck</li> <li>▪ Ease of thermogram interpretation (Maldague 2001)</li> <li>▪ No physical contact is required (Vaghefi et al. 2013)</li> <li>▪ Ability to be deployed at higher speeds</li> </ul>	<ul style="list-style-type: none"> <li>▪ Environmental impacts (weather condition, ambient temperature and humidity) (Washer et al. 2009b)</li> <li>▪ Variable emissivity of the surface material</li> <li>▪ Difficult to achieve uniform heating</li> <li>▪ Take images at a normal angle to allow for extracting quantitative information</li> <li>▪ Applicable for shallow delaminations (up to 3 inches) (Vaghefi et al. 2013)</li> <li>▪ limited application for bridge underside and superstructure</li> </ul>
Pulsed Thermography (Active)	<ul style="list-style-type: none"> <li>▪ Possibility to obtain depth and size information of the anomaly (Maldague 1993)</li> <li>▪ Fast data collection (just a few seconds)</li> <li>▪ Applicable on the areas that are not exposed to the direct sunlight</li> <li>▪ Uniform heating is achievable with line heating</li> </ul>	<ul style="list-style-type: none"> <li>▪ Deploying an external heater additional to the thermal IR camera is necessary</li> <li>▪ Complicated data process</li> <li>▪ Variable emissivity of the surface material</li> <li>▪ Applicable for shallow delaminations (up to 3 inches)</li> </ul>
Pulsed Phase Thermography (Active)	<ul style="list-style-type: none"> <li>▪ Possibility to obtain depth and size information of the anomaly</li> <li>▪ Applicable on the areas that are not exposed to the direct sunlight</li> </ul>	<ul style="list-style-type: none"> <li>▪ Deploying an external heater additional to the thermal IR camera is necessary</li> <li>▪ Complicated data process</li> <li>▪ Variable emissivity of the surface material</li> <li>▪ Applicable for shallow delaminations (up to 3 inches)</li> </ul>
Lock-in Thermography (Active)	<ul style="list-style-type: none"> <li>▪ Large surface inspection</li> <li>▪ Possibility to obtain depth and size information of the anomaly (Sakagami and Kubo 2002)</li> </ul>	<ul style="list-style-type: none"> <li>▪ Deploying an external heater additional to the thermal IR camera is necessary</li> <li>▪ Complicated deployment and data process</li> <li>▪ Variable emissivity of the surface material</li> <li>▪ Applicable for shallow delaminations (up to 3 inches)</li> </ul>
Vibrothermography (Active)	<ul style="list-style-type: none"> <li>▪ Reveal useful information regarding the stress concentration on critical locations of the bridge under heavy load (Maldague and Moore 2001)</li> </ul>	<ul style="list-style-type: none"> <li>▪ Difficult to generate mechanical loading</li> <li>▪ Physical contact is necessary to induce mechanical loading (Maldague 2001)</li> <li>▪ Thermal patterns only appears at specific frequencies (Maldague 2001)</li> <li>▪ Complicated data process</li> </ul>
Inductive Thermography (Active)	<ul style="list-style-type: none"> <li>▪ Possibility to obtain depth and size information of the anomaly</li> <li>▪ Reveal information regarding the corrosion level of rebar inside the concrete element (Baek et al. 2012)</li> </ul>	<ul style="list-style-type: none"> <li>▪ Difficult to deploy the technique on the actual bridge site and generate a magnetic field close to rebars</li> <li>▪ Complicated data process</li> </ul>

\*Primary method used for data collection in Chapter 4 of this document.

\*\*Primary method used for data collection in Chapter 5 and Chapter 6 of this document.

## **Chapter 4 Study on Passive Infrared Thermography**

### **4.1 Experimental Passive Infrared Thermography Testing**

Experiments for investigating passive infrared (IR) thermography included two phases: (1) monitoring the variation in surface radiant temperature of a concrete slab and determining the percentage of delamination in a controlled laboratory condition, and (2) investigating the effects of environmental conditions and time of data collection, as well as determining the maximum depth of delamination that can be measured.

The FLIR i7 and SC640 were the thermal IR cameras used in this study. The FLIR i7 camera is a handheld and easy-to-use camera which costs about \$2000. This camera has a lower field-of-view and lower resolution than the more expensive models of thermal IR cameras. Not having the options of taking thermal IR images at time increments and taking optical images, as well as thermal IR images, are the main limitations of this camera. The ability of the thermal IR camera to take images at time increments is necessary in bridge inspections to enable the application of this technology at highway speed. Taking optical images of the bridge, as well as thermal IR images, is one of the important components of data collection to help a bridge inspector re-visit the collected data at a later time and separate the surface staining from delaminated areas. The analysis software is not included in the price of this camera and has to be purchased separately.

The FLIR ThermaCAM SC640 camera has the option to collect data at time increments of every one second or less (up to 30Hz). This feature helps in collecting the data at speed and creates a sequence of images for each pass. Also, this camera has the option to collect optical images, as well as thermal IR images, of the surface which helps bridge inspector to collect images and store the data in one device. The proprietary software for this camera has the option to analyze the images and help in detecting and calculating the area of delaminations. The price of this research and development camera is around \$40,000.

#### ***4.1.1 Phase 1 – Temperature Monitoring***

A research and development grade thermal IR camera (FLIR SC640) and proprietary software were used to monitor the change in temperature and determine the subsurface anomalies within a concrete slab. Laboratory testing was conducted on a thin (5.5 in. deep) concrete slab (slab A) which was built with simulated delaminations. The layout and size of the inclusions are given in Figure 4.1.

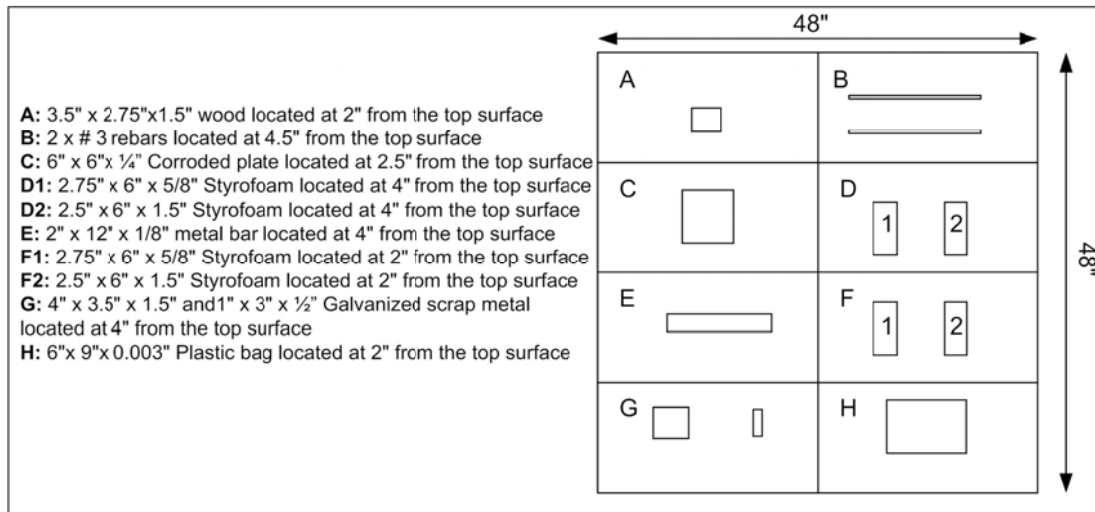


**Figure 4.1** Layout plan of 48 in. x 48 in. x 6 in. concrete slab (slab A) with simulated delaminations.

The slab was placed outside during winter (around 10 to 20°F) for over 24 hours and then brought into the lab, which was at a significantly higher temperature than outside (72.3°F). Thermal IR images were taken inside as the specimen was warming up. Figure 4.2 shows the set-up of this test.

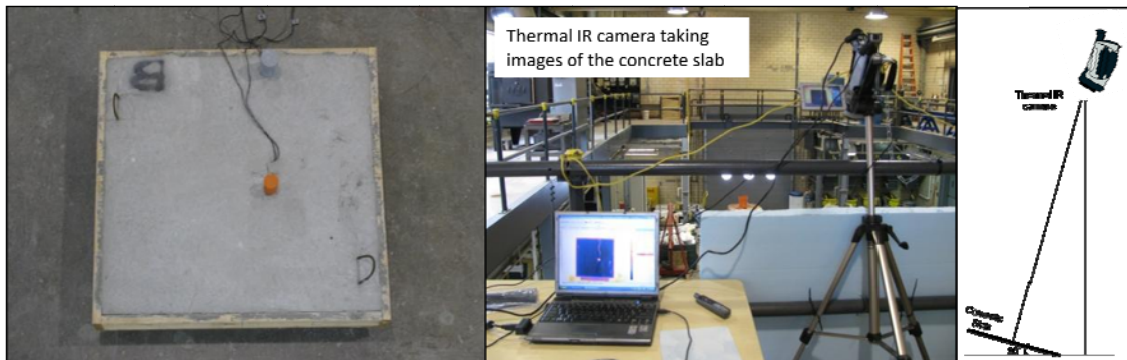


**Figure 4.2** Laboratory set-up for passive infrared thermography testing.

The thermal IR camera was set up at a distance of 16.67 ft above the slab to take images every 10 minutes during a seven hour period (9:28 am to 4:30 pm). The indoor lab temperature was 72.3°F and the relative humidity was 13%. The emissivity value of 0.95 was inputted in the data acquisition and analysis software. Figure 4.3 shows the thermal IR image of the test specimen and the graphs of the temperature change during the seven hour period. Areas 3 and 4 on the thermal IR image correspond to the F1 and F2 delaminations.

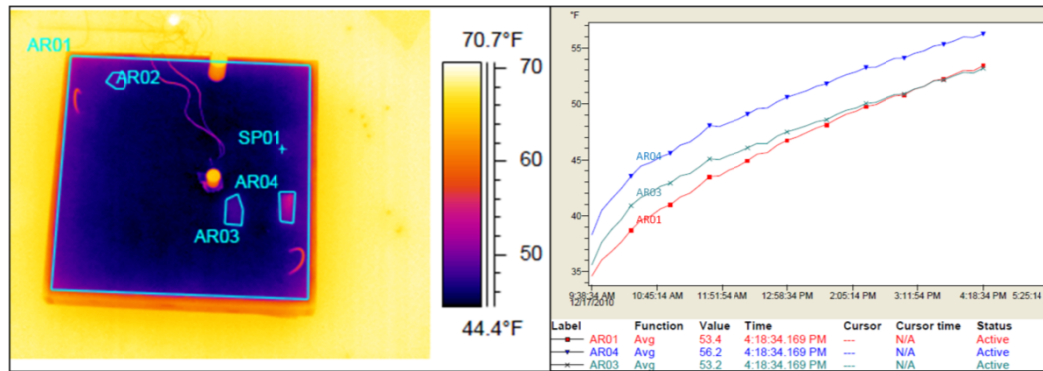


**Figure 4.3 Thermal IR image and graphs showing the temperature change of each defect compared to the average temperature of the slab.**

#### 4.1.1.1 Method for Calculating the Area of Delamination

Determining the percentage of delaminated area was one of the objectives of this phase of the study to provide valuable information for determining the defect areas on concrete bridge decks, soffits and girders. Note that taking thermal IR images at a normal angle to the slab (camera perpendicular to the slab) provides more accurate results than other angles (Washer et al. 2009a).

Two methods were considered to calculate the percentage of delaminated areas in this phase. The first one used the thermal IR camera proprietary software to draw boxes around the warmer areas and count the number of pixels within the box. The percentage of delaminated area in this test was determined by Equation 12.

$$\text{Percentage of delaminated areas} = \frac{\text{Number of pixels within the hot area}}{\text{Number of pixels within the slab}} \times 100$$

The second method involved saving the data in a comma separated format (.csv) and using a spreadsheet to count the number of pixels. In this test, the MS Excel spreadsheet was set up to highlight the number of pixels within a specific temperature range that best fit the shape of the delamination apparent on the thermal infrared image and to count the number of pixels.

One of the errors that appeared in this test was the effect of the thermal gradient from the edge of the slab which made it difficult to assign pixels to delaminated areas close to the edges. The percentage of delaminated areas was calculated by Equation 12. A sample thermal IR image and the associated highlighted MS Excel spreadsheet are presented in Figure 4.4. Because delaminations appear with higher temperature, pixels with higher temperatures than a threshold value can be highlighted in a way to match the bright area on the associated thermal IR image. This threshold value is different for each image due to the various temperature ranges between thermal IR images taken at different time and environmental conditions. Matching the area between the spreadsheet and thermal IR image is subjective and based on the user interpretation of the thermal IR image. For comparison purposes, the actual percentage of delamination was 1.78%. The proprietary software computed 1.61% and the simplified post-processing using a spreadsheet computed 1.84% of the concrete slab area was delaminated.



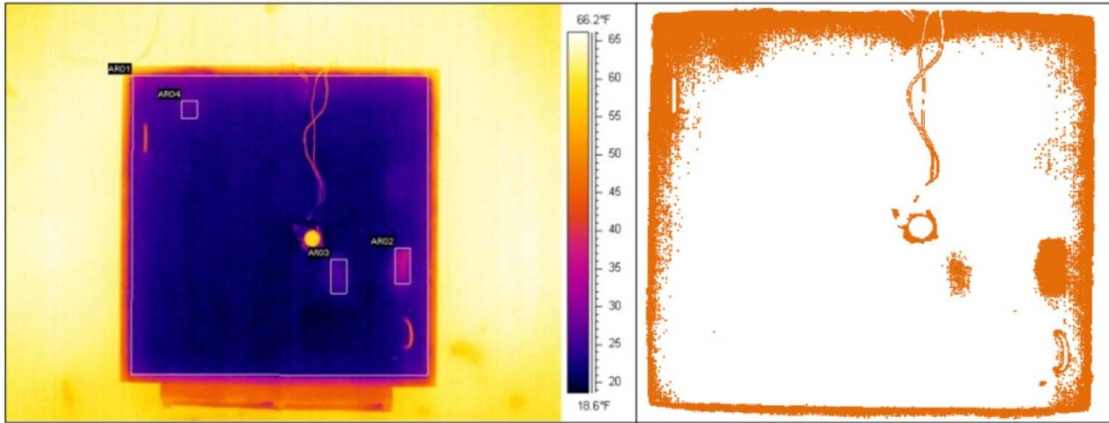


**Figure 4.4 Thermal IR image and the associated Excel spreadsheet.**

#### ***4.1.2 Phase 2 – Time of Day Effects***

To study the effect of time of day in data collection, the same concrete specimen that was used for phase 1 was put outside and thermal IR images were taken at two different times. Figure 4.5 shows these thermal IR images that were taken at 8:18 am and close to 10:59 am to highlight the time of day factor in thermal IR imaging (sunrise time was at 6:40 am). A FLIR i7 handheld thermal IR camera was used for this phase of the experiment.

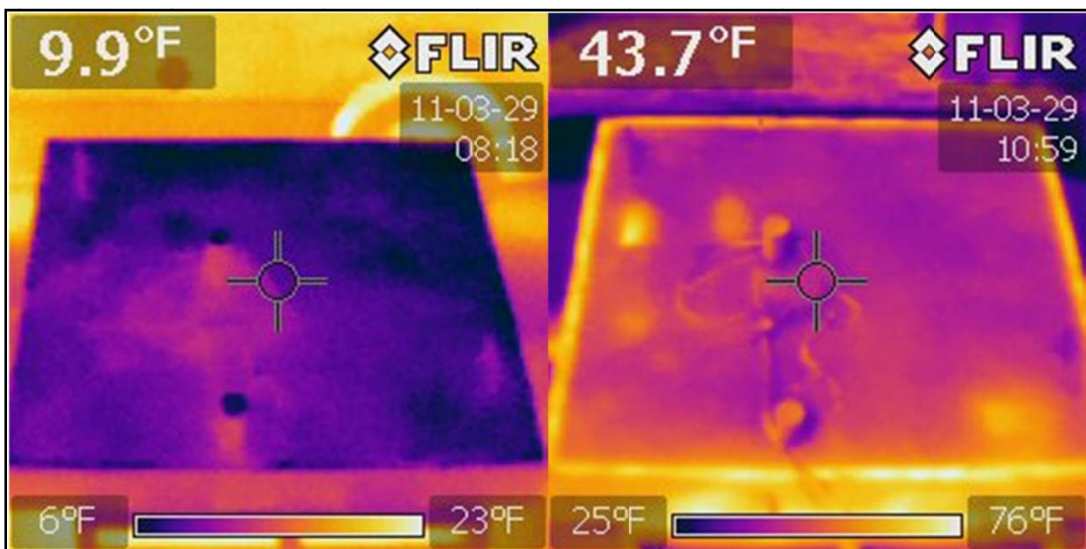


**Figure 4.5 Comparison of thermal IR images of the concrete slab with simulated delaminations at 8:18 am and 10:59 am.**

Determining the depth of delamination was the next step of this phase. To achieve this objective, a concrete slab was built with simulated delaminations (6 in. x 6 in. x 1/8 in. cardboard squares placed at different depths; 0.5 in., 1 in., 1.5 in. and 2 in.) and a thermal IR image was taken around noon to have the maximum contrast on the image. Figure 4.6 demonstrates the plan layout of the concrete slab with the simulated delaminations and spot temperature readings on the thermal IR image. It has been noted that deeper delaminations manifest themselves with lower temperature measures compared to the shallower delaminations.

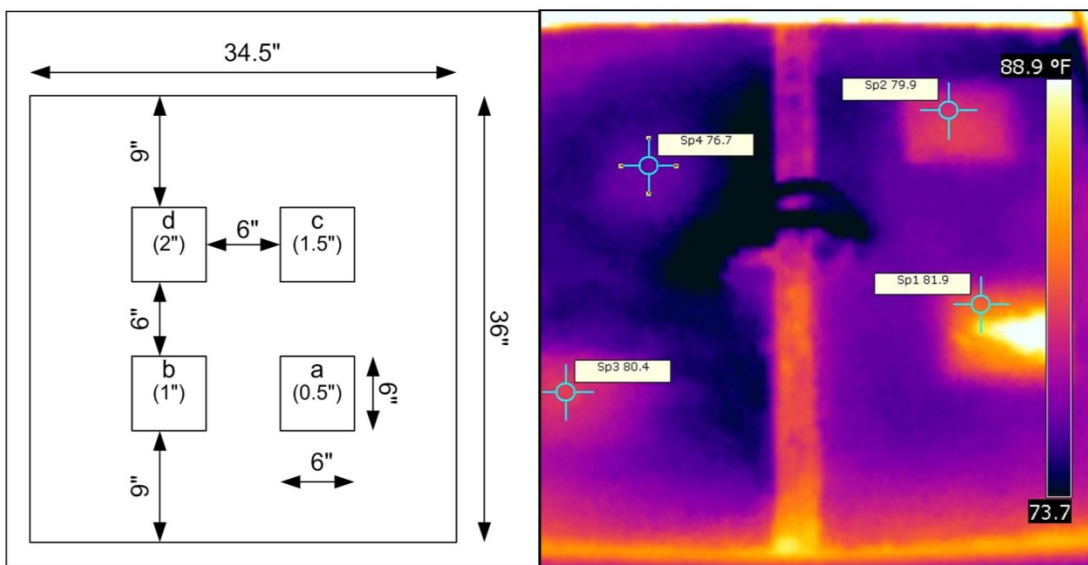


**Figure 4.6 Plan layout of the concrete slab with simulated delaminations and the thermal IR image showing the temperature data of delaminations placed at different depths (0.5 in., 1 in., 1.5 in., 2 in.).**

Figure 4.7 highlights the importance of distinguishing actual delaminations from soil, moisture, oil spills, and staining. This figure shows how a surface concrete stain (a residual chemical released from a cardboard square) on the concrete surface can affect the results by appearing as a higher temperature on the thermal IR image.

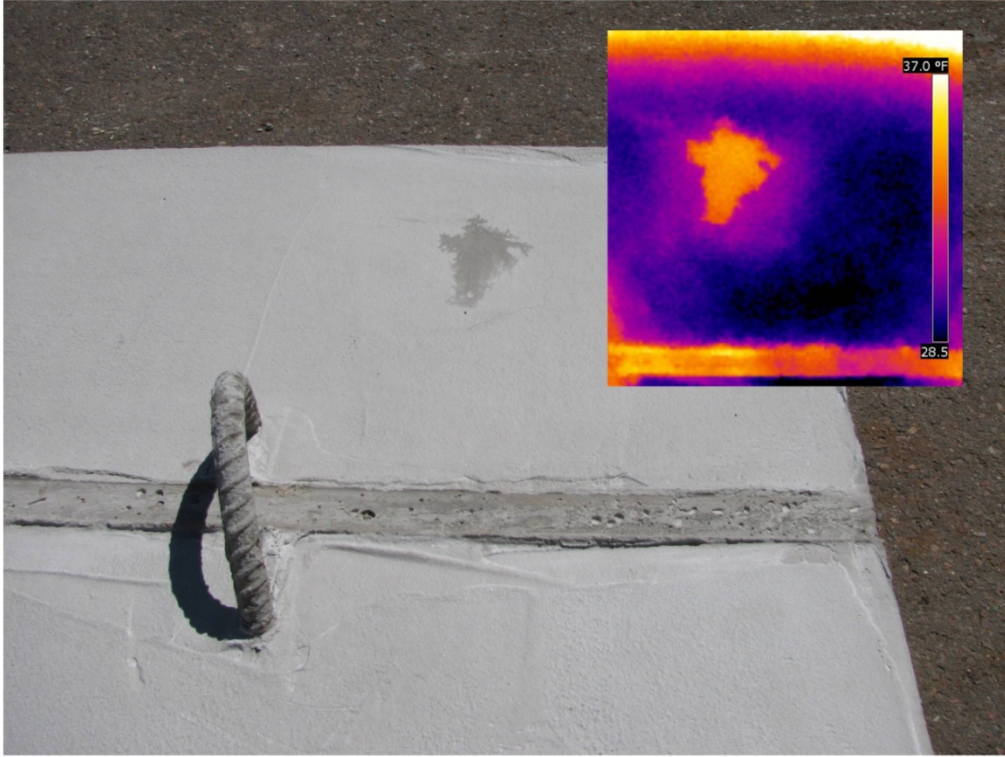


**Figure 4.7 Thermal IR image of the chemical staining on the concrete specimen.**

## **4.2 Field Deployment of Passive Infrared Thermography**

### ***4.2.1 Field Deployment Methodology***

Implementation of passive infrared thermography in the field and on a bridge deck is highly dependent on the type of thermal IR camera and lens used. The best possible option is to cover at least one lane (10 to 12 ft width) in each pass. Increasing the distance between the camera lens and the bridge deck extends the field of view of the camera and helps in collecting the data in fewer passes over the bridge. The thermal IR camera (FLIR SC640) that was used in this project had a 24°x19° lens. This means that this camera should be located 24 ft above the concrete bridge deck to cover the whole lane width in one image, which is not a practical method in the field. Therefore, to collect images on the bridge with this type of camera, the camera height had to be lowered and several passes were required to cover a single lane. In this field demonstration, the thermal IR camera was installed on a cart at 6.2 ft above the deck, covering a 2.6 ft x 2 ft field of

view. Images were collected every second by pulling the cart over the bridge in ten to twelve passes (5 to 6 passes for each lane) at walking speed to cover the entire bridge deck.

A grid pattern was laid on each bridge deck before testing. Duct tape was used on the bridge deck every 10 ft longitudinally and every 4 ft transversely to provide reference points on the bridge deck. Duct tape has a reflective surface and low emissivity compared to concrete; therefore, it appears on the thermal IR image as a lower temperature. The use of duct tape enabled the merging of individual images for creation of a full bridge deck. Figure 4.8 shows a sample grid pattern for field deployment and a working mobile configuration for the camera system on a cart. The proposed data collection method was specific to the camera model and lens that were used in this study. Wider-angle lenses can be used to achieve a more ideal data collection scenario.

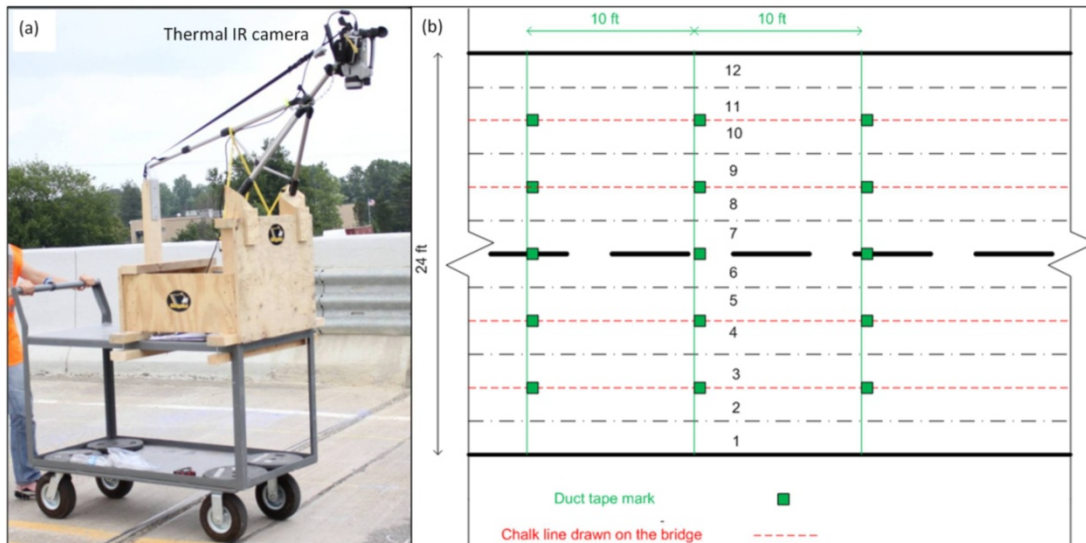


**Figure 4.8 (a) Thermal IR camera acquisition cart and (b) sample grid pattern on the bridge deck.**

#### ***4.2.2 Field Demonstration Results and Discussion***

The thermal IR survey was conducted on three prestressed concrete I-beam bridges with concrete decks in Michigan during August, 2011. The bridges were selected based on

their NBI rating to represent each of a poor, fair, and good condition bridge deck. Results and images of these three selected bridges are discussed in the following sections. Although, the main focus and challenge of this study was trying to collect information while moving the camera over the bridge deck, some images were also taken from the underside surface of the bridge deck and girders to give an overall condition for these elements. The emissivity value of 0.95 was input to the software during data collection and processing of this field demonstration.

#### 4.2.2.1 Thermal IR Inspection Results for Top of the Bridge Deck

The thermal IR survey over the bridge deck was conducted according to the aforementioned described data collection method. Environmental conditions at the time of data collection and the overall rating based on the last inspection are summarized in Table 4.1. Time of data collection specified in this table was the starting time of data collection for each bridge. The total time of data collection for each bridge took approximately one to one and a half hours. Ambient temperature and humidity were added as inputs in the thermal IR data collection software. Sun direction was another factor that was considered while collecting the data to avoid having any shadows projecting on the thermal IR images.

**Table 4.1 Environmental condition and overall rating for each bridge**

Bridge	Last Inspection Date	Overall Condition	Deck NBI rating (0-9)	Time of Data Collection	Weather Condition	Ambient Temperature (°F)	Humidity
Freer Rd.	06/02/2010	Good	6	12:00pm	Partly Cloudy	96.6	45%
Willow Rd.	04/19/2010	Fair	5	10:50am	Mostly Cloudy	86.7	54.5%
Mannsiding Rd. (NB)	10/11/2011	Poor	4	11:50am	Mostly Cloudy	96.4	35.3%

After completion of the data collection on the bridge, thermal IR images for each bridge were merged to create an overall thermal IR map of the bridge deck. A delamination map was created and the percentage of delaminated area was calculated based on the spreadsheet method discussed in Section 4.1.1.1. The thermal IR map and delamination

map for the Freer Rd. bridge, the Willow Rd. bridge, and the Mannsiding Rd. bridge are shown in Figure 4.9, Figure 4.10, and Figure 4.11, respectively. Although having duct tape on some of the thermal IR images was helpful to create a thermal IR map of the bridge deck, delaminations on these images were not as apparent as the rest of the thermal IR images. Also, the rubber expansion joints on the bridge appeared with higher temperature on the thermal IR image due to the higher emissivity factor of rubber and it induced some difficulties in detecting delaminations within these areas.

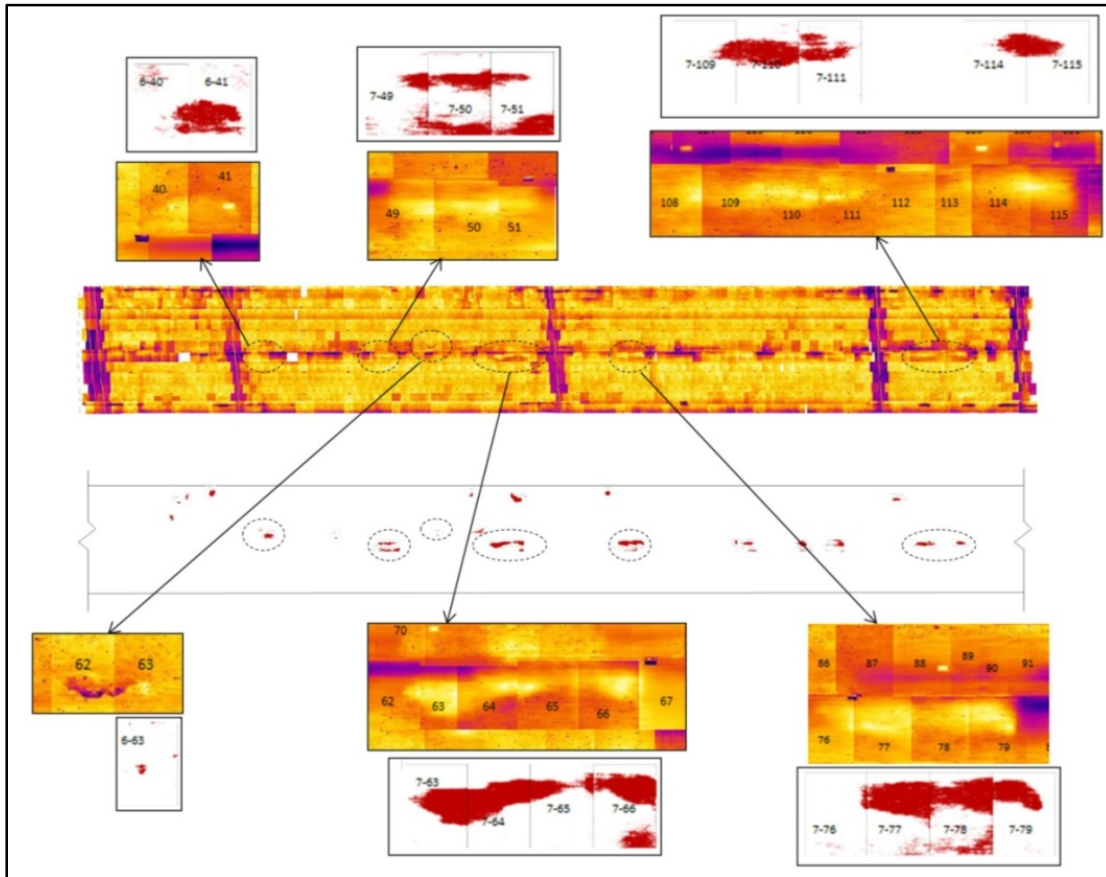


**Figure 4.9 Deck delamination map of Freer Rd. bridge, using Thermal IR and post-processed output data results for a typical spreadsheet analysis.**

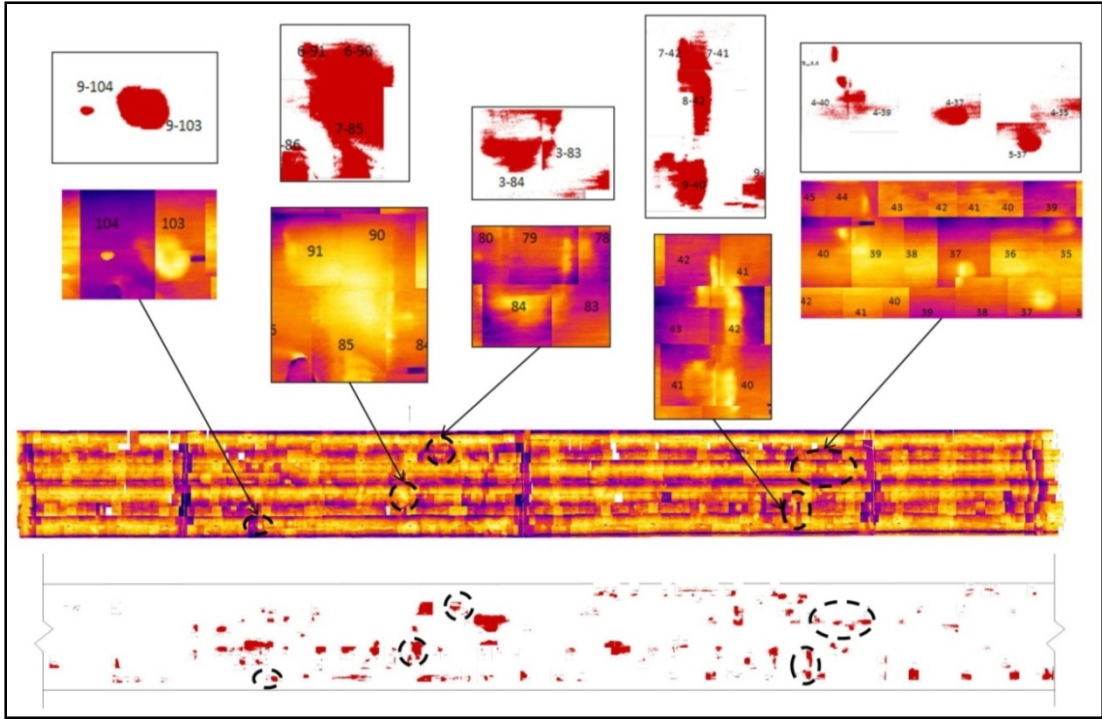


**Figure 4.10 Deck delamination map of Willow Rd. bridge, using Thermal IR and post-processed output data results for a typical spreadsheet analysis.**

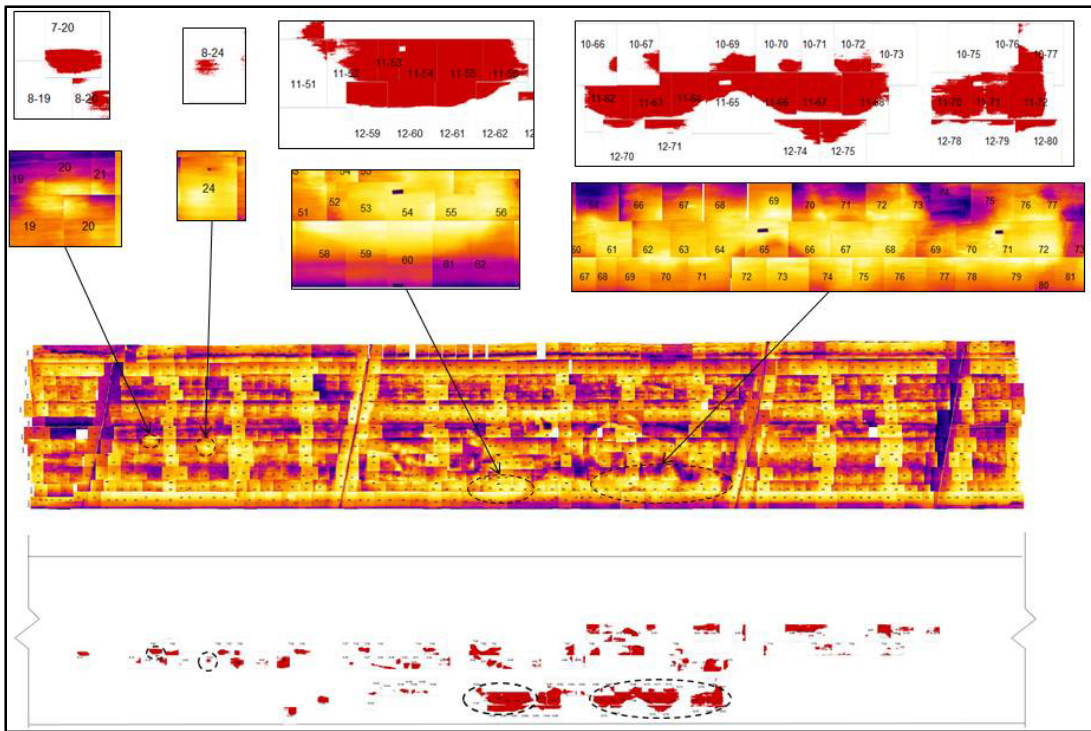


**Figure 4.11 Deck delamination map of Mannsiding Rd. bridge, using Thermal IR and post-processed output data results for a typical spreadsheet analysis.**

#### ***4.2.2.1.1 Comparing Thermal IR Results with Chain Drag and Hammer Sound Inspection Techniques for Bridge Decks***

Concurrent with the field deployment, the Michigan Department of Transportation (MDOT) conducted a delamination survey on all three bridges. The hammer sound technique was used on Freer Rd. and Willow Rd. bridges and the chain drag was used for the Mannsiding Rd. bridge. Both of these methods are sounding techniques and are based on the bridge inspector's expertise on hearing the hollow sound in a delaminated area compared to the surrounding intact concrete area. Delaminated areas for all three bridges were marked on the bridge deck. Optical (digital) images were taken from the marked areas after sounding surveys were completed and merged together to give a better overview of the locations of the delaminated areas.

ArcGIS, a professional version of geographic information systems software, was used to display, analyze and quantify the results. Delamination maps from both MDOT and thermal IR surveys were imported into ArcGIS as two separate layers so as to compare the location and area of each delamination that was detected by each method. The total area of delamination calculated based on the MDOT and thermal IR surveys for the three bridges, as well as the overlapped areas between the two surveys have been summarized in Table 4.2. The total area of delamination is the union of the delaminated area that can be detected by sounding or thermal IR survey. The overlapped area is the intersection between the delaminated areas detected by each method and is common delaminated area between the two methods.



**Table 4.2 Total area of delamination using thermal IR and MDOT sounding techniques**

Bridge	Delaminated Area (ft <sup>2</sup> )						Total
	MDOT Method	MDOT	Thermal IR	Overlapped Areas	Only MDOT	Only Thermal IR	
Freer Rd. (Deck Area = 5652 ft <sup>2</sup> )	Hammer Sound	101.74	29.25	14.13	87.60	15.11	116.84
Willow Rd. (Deck Area = 5231 ft <sup>2</sup> )	Hammer Sound	159.54	157.83	17.49	142.05	140.34	299.88
Mannsiding Rd. (NB) (Deck Area = 3507 ft <sup>2</sup> )	Chain Drag	127.30	136.13	21.43	105.87	114.70	242.00

Table 4.3 demonstrates the percentage of delaminations detected by each method over the entire bridge deck, as well as the percentage of the total delaminations that could be detected by both methods or only by one of the two methods. The overlapped delaminated area between the two methods is also reported as a percentage of the total delaminated area detected by each method. Delaminated areas presented in these two tables were obtained from the ArcGIS delamination layers. The correspondence percentage with each method is the percentage of the common delaminated area (overlapped areas) to the total delaminated area that could be detected by each inspection method.

Percentages of the total overlapped area of the bridge were somewhat surprising; however, further analyses were performed on the displayed data in ArcGIS to compare these areas on the small sections over the bridge deck. These analyses are discussed in the following sections for each bridge.

**Table 4.3 Percentage of delaminated areas calculated from the results of each delamination survey**

Bridge	Delamination (%)		Percentage of total delamination			Correspondence with each method (%)	
	MDOT	Thermal IR	Overlapped Areas	Only MDOT	Only Thermal IR	MDOT	Thermal IR
Freer Rd.	1.80	0.52	12.1	74.97	12.93	13.89	48.31
Willow Rd.	3.05	3.02	5.83	47.37	46.8	10.96	11.08
Mannsiding Rd. (NB)	3.63	3.88	8.85	43.75	47.4	16.83	15.74

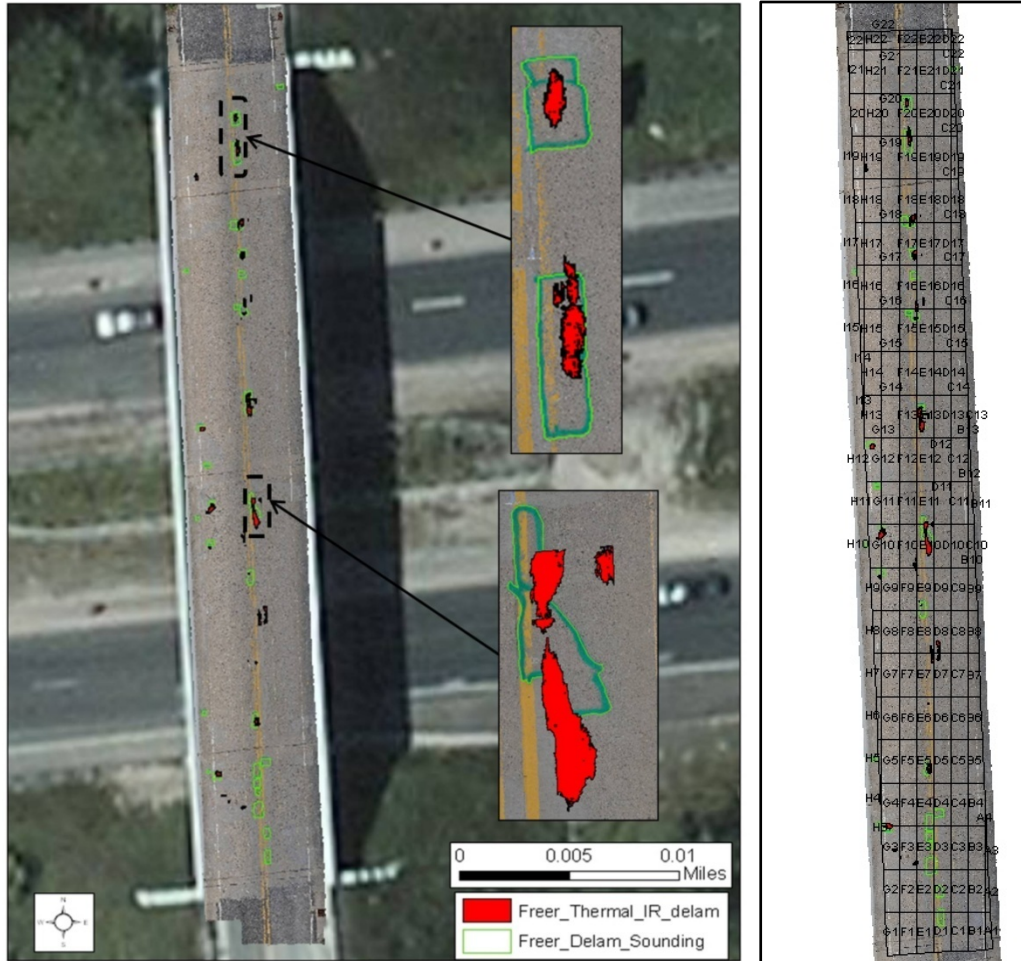
**4.2.2.1.2 Freer Rd. bridge**

Figure 4.12 shows the thermal IR and hammer sound delamination maps for Freer Rd. bridge displayed as two layers in ArcGIS. The main cause of variation between the results of the MDOT and thermal IR surveys on the Freer Rd. bridge is that most of the delaminations on this bridge were around the construction joint and overlapped with the painted centerline on the bridge deck. Reflective paint on the bridge deck has lower emissivity than concrete; therefore, it will appear on the thermal infrared image with lower temperature and cause some difficulties to detect delaminations in those areas. Also, delaminations are most likely to occur around spalled or patched areas, which can help to detect the exact location of delaminations based on the thermal IR and optical images.

To compare the variations between hammer sound and thermal IR inspections, a virtual grid pattern (4 ft x 10 ft) was created over the bridge deck in ArcGIS (Figure 4.12). Delaminated areas within each cell that could be detected by either hammer sound or thermal IR camera or both was calculated in ArcGIS and presented in Appendix A. While the total correspondence between thermal IR and sounding technique is 12.1%, higher correspondence was observed for some sub-section areas such as cell E13 which shows 40.3% correspondence between thermal IR and sounding within the total union

delaminated areas. Correspondence of this overlapped area with the area detected with thermal IR and sounding surveys are 72.7% and 47.5%, respectively. This shows that the sounding survey in this specific location detected more delaminations than what was obtained from the thermal IR survey. On the other hand, for cell H10, total correspondence between thermal IR and delamination survey is 9.81%. The overlapped area has the correspondence of 14.4% and 23.5% with the area detected with thermal IR and sounding techniques, respectively. In cell E13, contrary to cell H10, more area of delamination was detected with thermal IR survey as opposed to sounding.

Larger correspondence was observed for delaminated areas detected by the thermal IR survey within most grid cells on this bridge due to overestimating the delaminated area by the sounding survey. However, these results must be interpreted with caution due to the effect of the painted centerline on influencing the thermal IR images obtained on site. In-depth inspection data (ground truth obtained by coring) is required to make the decision on the potential areas of delamination that were detected by only one of the two surveys.



**Figure 4.12 Thermal IR and sounding delamination map and the virtual grid pattern over the Freer Rd. bridge displayed on ArcGIS.**

#### ***4.2.2.1.3 Willow Rd. Bridge***

Delamination and hammer sound maps for the Willow Rd. bridge are demonstrated in Figure 4.13. To compare the variations between hammer sound and thermal IR inspections, the same virtual grid pattern (4 ft x 10 ft) as Freer Rd. bridge was created over the bridge deck on ArcGIS (Figure 4.14). Delaminated areas were calculated within each cell and results from both methods were compared. Appendix A of this document provides a summary of this analysis. Total delaminated area for cell G4 calculated from thermal IR and hammer sound methods are 4.43 and 5.72 square feet, respectively. The overlapped delaminated area between these two methods in this cell is 3.24 square feet.

Results for this specific cell show 56.7% and 73.12% correspondence with MDOT and thermal IR survey. However, the correspondence of the overlapped area with the total delaminated areas that can be detected by either one of the techniques is 46.93%. Values for percentage of correspondence vary between the specified cells and this fairly high correspondence may not be achievable for other areas. Therefore, the total correspondence between thermal IR and hammer sound survey for this bridge was calculated as 10.96 and 11.08 percent for MDOT and thermal IR surveys, respectively. This variation was anticipated due to the variations in hammer sound results and not having the ideal environmental condition for thermal IR survey on the inspection day.

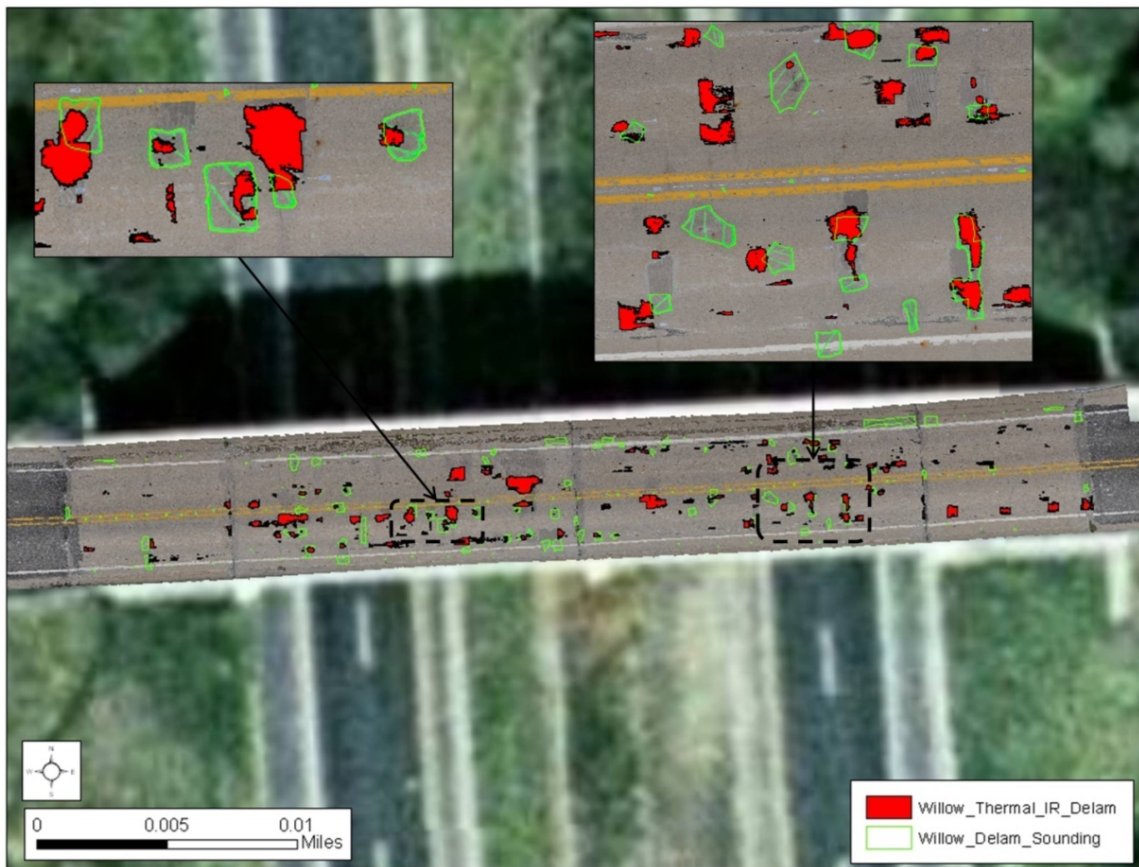


**Figure 4.13 Thermal IR delamination map and sounding delamination map of Willow Rd. bridge displayed on ArcGIS.**

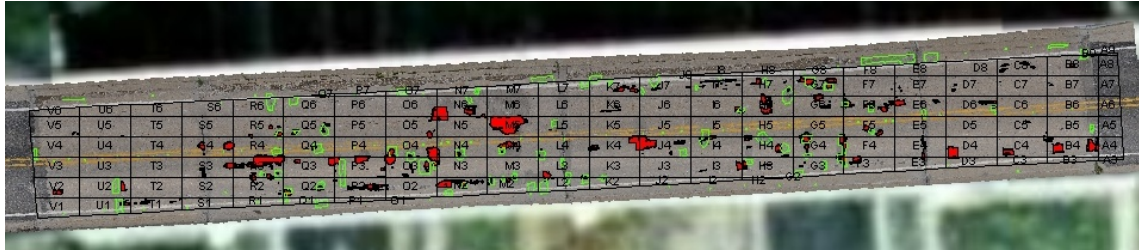


**Figure 4.14 Virtual grid pattern over the Willow Rd. bridge deck.**

#### **4.2.2.1.4 Mannsiding Rd. Bridge (NB)**

Figure 4.15 shows thermal IR and chain drag delamination maps for Mannsiding Rd.-NB on ArcGIS. Similar to the other two bridges, there are some variances between the results of these two techniques that are demonstrated in this figure. A virtual grid pattern, similar to the aforementioned bridges, was created on ArcGIS to compare the results of the two inspection methods considered in this study (Figure 4.16).

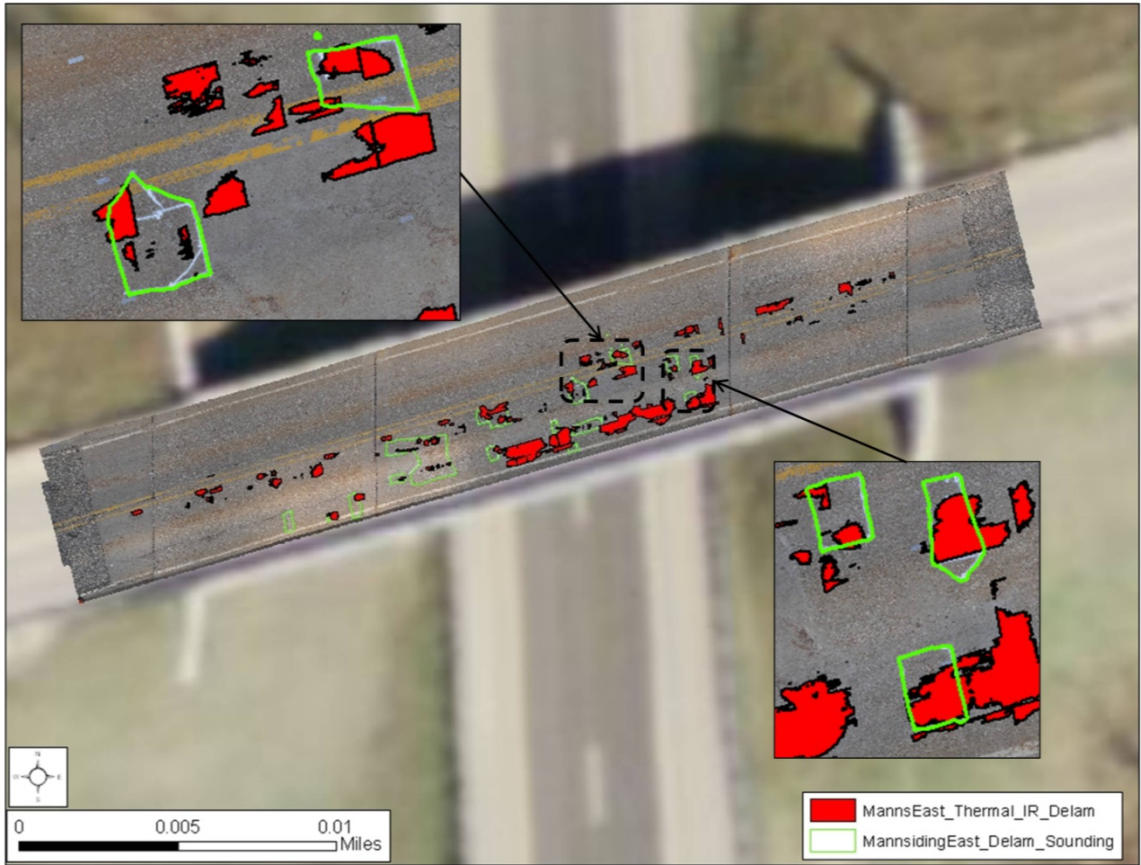


**Figure 4.15 Thermal IR delamination map and sounding delamination map of Mannsiding Rd. bridge displayed on ArcGIS.**

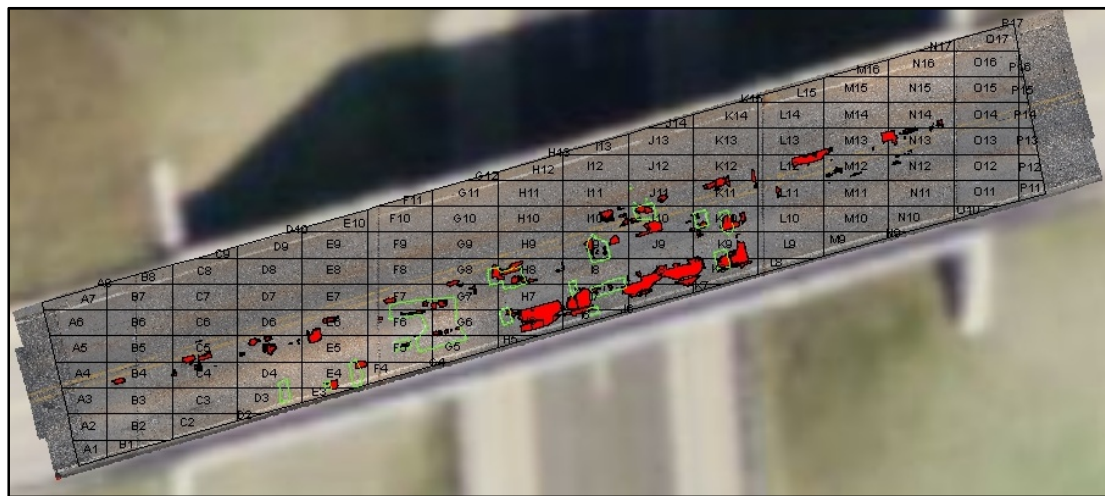


**Figure 4.16 Virtual grid pattern over the Mannsiding Rd. bridge deck.**

Maximum correspondence between the results of the thermal IR and sounding surveys was scrutinized in cell K10, which shows 33.45% correspondence between the results. For this bridge deck, the percentage of correspondence between the overlapped area and the area detected with thermal IR and sounding surveys are 63.76% and 41.29%, respectively. Similar to the other two bridges, the calculated delamination area and percentages within each cell is included in Appendix A.

The deck survey results from sounding conducted by MDOT in 2008 shows that delaminations were mostly occurred on the south side of the bridge in span 2, and somewhat reflects the sounding and thermal IR surveys that were conducted in 2011 and presented herein. However, the total delaminated area that was found in the survey performed in 2008 was 176.5 square feet (4.4%). The chain drag survey conducted in 2011 found 127.3 square feet (3.63%) of delaminated areas and reflects the variation that was anticipated within the results of a sounding study.

Due to the variances in the results obtained by sounding and thermal IR surveys, in-depth scoping surveys with destructive methods such as coring are required to make the decision about the exact location of delaminations on this bridge deck.

#### **4.2.2.2 Ground Truth Results**

Ten cores (12 in. diameter) were extracted from the Mannsiding Rd. bridge deck to validate the results obtained from the chain drag and passive infrared thermography inspection. Locations of these cores relative to the delamination maps are illustrated in Figure 4.17. The attempt was to extract cores from locations of delaminations that were detected by either infrared thermography or chain drag testing, or locations that were on the patched areas and raised concerns over the validity of data on those areas.

Figure 4.18 showed the MDOT coring extraction procedure that was performed on Mannsiding Rd. bridge in July 2012. This procedure include: (a) drill the concrete deck up to 4 in., (b) bringing out the drill and (c) use a metal rod to take out the 12 in. diameter



core. Cores with no delaminations (C4, C9, C10) did not come out easily and were left in place.

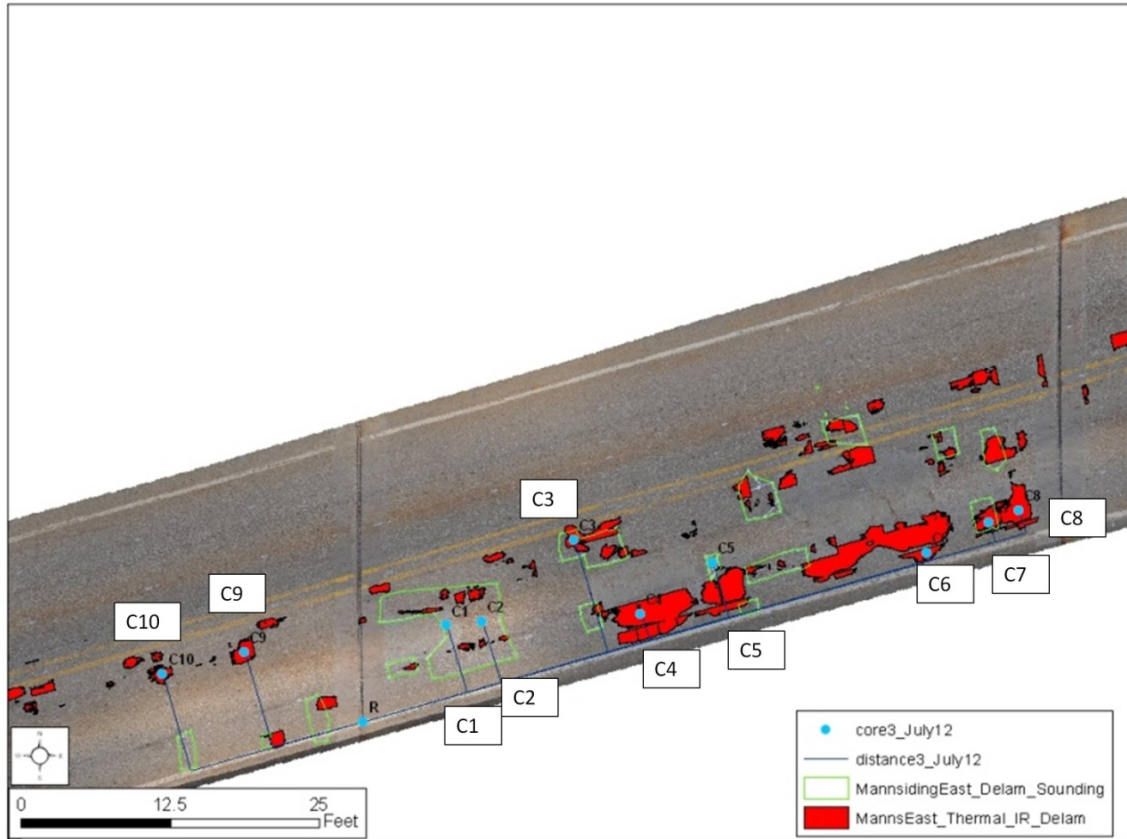


**Figure 4.17 Coring locations on Mannsiding Rd. bridge deck.**



**Figure 4.18 Core extraction procedure on Mannsiding Rd. bridge deck.**

Figure 4.19 shows the cores that were extracted from Mannsiding Rd. Bridge deck. The depth of the delamination for each core is summarized in Table 4.4. Seven out of the ten cores showed visible damage. Four out of seven delaminated cores were evident in

thermal IR imagery results. Core C2 and C5 were 3 inches or deeper (3.125 in.), thus no delaminations were detected with thermal IR imagery. This result may be due to the long period of data collection (approximately one hour), which causes the variation in temperature gradient on the bridge deck, or overcast condition. Delaminations on cores C6 and 8 were only detected by thermal IR imagery. These delaminations were closer to the surface. Cores C4, 9 and 10 were intact (therefore not included in Figure 4.19) and no delaminations were found within 3.5 in. of the top surface for these locations. The reasons for not properly distinguishing between the delaminated and solid areas in these locations (C4, 9 and 10) can be due to delaminated areas smaller than the 12 in. diameter core or patched areas with different concrete properties that influence the emissivity factor, core C4 was placed on the patched area of the deck.

Locations of delaminated areas for five cores out of seven were properly detected using chain drag. However, it was noted that the delamination (C8) that was very close to the surface (<1 in.) could be detected only in thermal infrared images, and delamination (C2) that is deeper than 3 in. could only be detected by chain drag method. Results from this study suggest that passive infrared thermography is more effective for detecting delaminations closer to the concrete surface, and not located within the patched areas. Overall, further investigation is required to determine whether the passive infrared thermography is can detect delaminations within patched areas or deeper than 3 in.

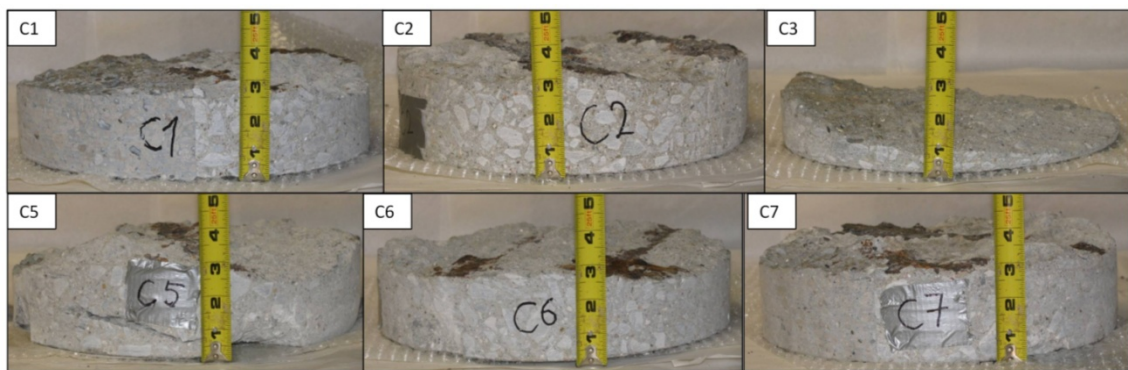


**Figure 4.19 Cores that were extracted from Mannsiding Rd. bridge deck.**

**Table 4.4 Summary of the core conditions and the depth of delaminations**

Core No.	Repair Condition	Ground Truth Results	Detected by Chain Drag	Detected by Thermal IR
C1	Patched	Delamination at 2.75"	Yes	No
C2	Not patched	Delamination at 3.125"	Yes	No
C3	Not Patched	Delamination at 2"	Yes	Yes
C4	Patched	No delamination	No	Yes
C5	Not patched	Delamination at 3"	Yes	No
C6	Not Patched	Delamination at 2.75"	No	Yes
C7	Not patched	Delamination at 3"	Yes	Yes
C8	Patched	Delamination very close to surface	No	Yes
C9	Not Patched	No delamination	No	Yes
C10	Not Patched	No delamination	No	Yes

#### **4.2.2.3 Thermal IR Inspection Results for Bridge Deck Underside and Superstructure**

It has been suggested in the literature that thermal IR imagery can also be used for bridge soffits and girders (Washer 2010). The possibility of using thermal IR imagery has been investigated on the three case studies of the research conducted herein. Because all these three bridges were prestressed I-beam bridges, the main challenge was end-beam cracking. No delaminations were found on the girders using either thermal IR or hammer sound inspection. The bridge soffit was another element that was investigated in the study herein. Figure 4.20 and Figure 4.21 were taken from the Willow Rd. and Mannsiding Rd. bridges. Delaminated areas on these images appeared as cold (darker) areas as opposed to the warm (brighter) areas. This is possibly prominent due to the rainy weather conditions the day before testing and mostly cloudy conditions for both bridges during thermal IR inspection. Times at which images were taken are indicated on each image.

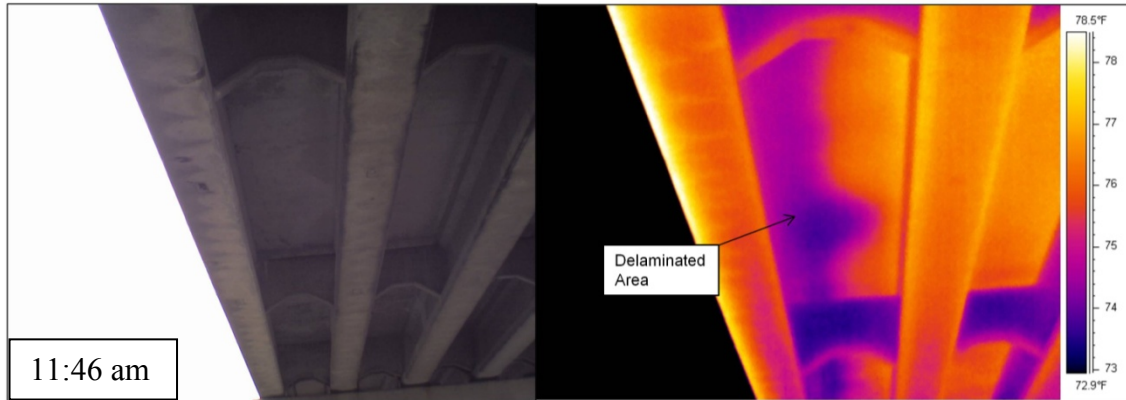


**Figure 4.20 Digital and thermal IR image of Willow Rd. bridge soffit.**

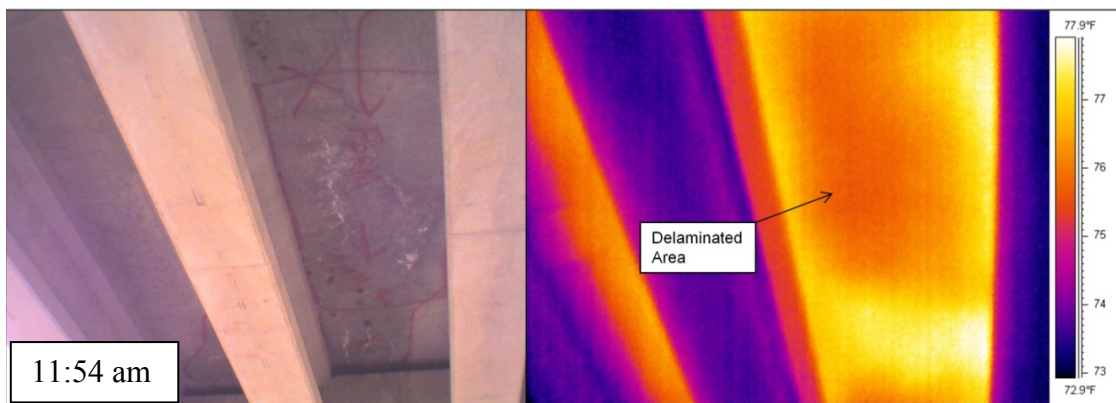


**Figure 4.21 Digital and thermal IR image of Mannsiding Rd. bridge soffit.**

Figure 4.22 and Figure 4.23 show digital and thermal IR images taken from the bridge piers under Willow Rd. and Mannsiding Rd. bridges. Potentially delaminated areas were shown as bright areas (higher temperature) on the thermal IR image.

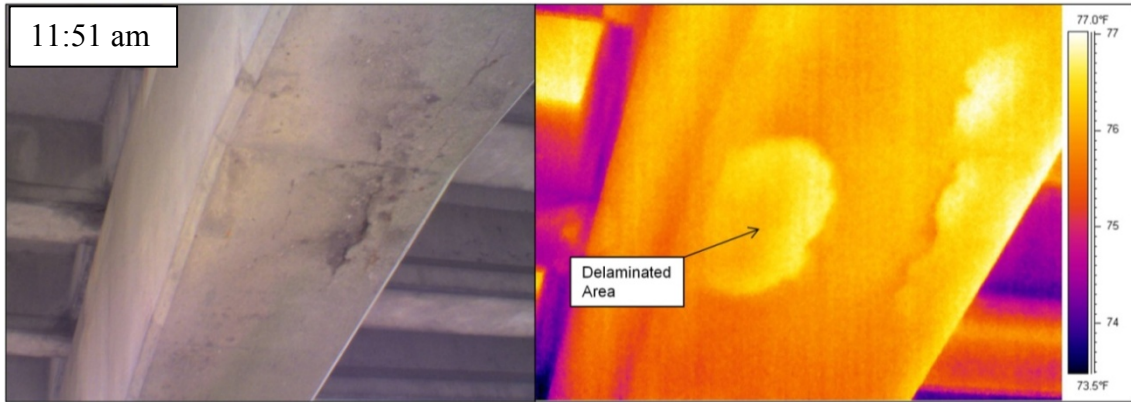


**Figure 4.22 Digital and thermal IR image of bridge pier under Willow Rd. bridge.**

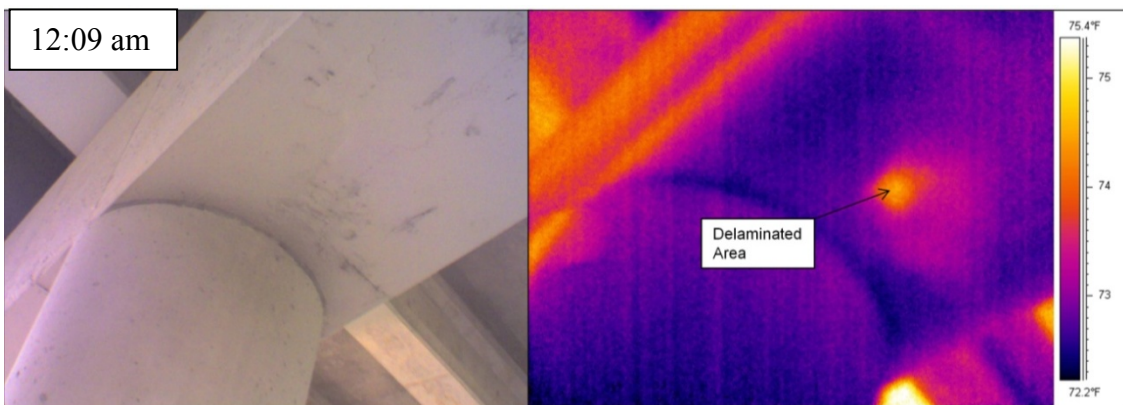


**Figure 4.23 Digital and thermal IR image of bridge pier under Mannsiding Rd. bridge.**

### 4.3 Summary

Identifying the location and area of delaminations on the bridge deck has always been an important challenge for bridge inspectors during routine bridge inspections. Passive infrared thermography can be a useful tool for bridge inspectors to overcome this challenge and get qualitative and quantitative information for delaminated areas on the bridge deck. The thermal IR data collection method is highly dependent on the camera system and field-of-view of the camera being used. However, the main challenge is to create a merged thermal IR map and delamination map from the thermal IR data to make usable information for the bridge management team and help bridge inspectors to rate the bridge deck. Another important challenge is to remove the bright areas that are not

delaminations and appear on the thermal IR image due to different emissivity values such as an oil stain.

Having a grid pattern on the bridge deck is necessary to merge images and assign the specific coordinate system. However, this can affect the results and it will be more practical to use less duct tape on the bridge deck. Having a camera with a larger field-of-view can solve this issue to some extent, and having fewer images on the overall bridge deck can make data processing faster and more practical. However, caution must be applied in using a wide-angle lens for the thermal IR camera as the edges of the thermal IR images may be distorted and not viable for calculating the number of pixels and area of delamination. Presenting the results of infrared thermography bridge inspection on the ArcGIS environment allows for an easy and fast analysis to locate and calculate the delaminated areas within the bridge deck. Also, it will help bridge management teams to compare their results with other delamination survey practices and nondestructive testing techniques, or combine the results with other inspection methods (Vaghefi et al. 2013).

In general, a passive infrared thermography survey provides a good oversight of delaminated and debonded areas within the bridge deck. However, results are highly dependent on the time of the data collection. Several inspections during the day may be required to capture delaminations located at different depths, as the shallower delaminations appear on the thermal IR images earlier than the deeper delaminations. Results from this study were compared to the sounding techniques, hammer sound and chain drag, performed by MDOT inspectors. However, the results of these sounding surveys may vary depending on the inspection teams. Therefore, ground truth information was required to validate the results of the thermal IR survey.

The present study confirms previous findings and contributes additional evidence that suggests passive infrared thermography is a well-established non-destructive tool for concrete bridge deck top surface inspection. However, further study needs to be conducted to develop an easily deployable system and a less subjective data processing

method to help transportation authorities to conduct a thermal IR survey and get reliable information for prioritizing the maintenance needs during the decision making process.





## **Chapter 5 Laboratory Study using Active Infrared Thermography**

A series of experiments were conducted in the laboratory with the objective of developing an active infrared thermography technique (pulsed thermography) applicable to concrete slabs with simulated built-in delaminations. Although the line heating method can provide uniform heating throughout the concrete slabs, the surface heating method was selected for this research because it is a more practical heating method in the field (see Section 3.3.3.1 for more details on different heating methods). To accomplish the objective, four slabs were cast with different numbers of delaminations placed at various depths. Active infrared thermography testing was conducted on these concrete slabs by applying a heat source and collecting thermal infrared images at 30 second intervals. Based on the temperature information obtained from thermal IR images, it is conjectured that the location and depth of the delaminations can be found on concrete bridge elements using active infrared thermography.

This laboratory study was divided into three phases. The first phase involved investigating effective heating methods to conduct pulsed infrared thermography for concrete bridge elements. Selecting the applicable heating source and heating method for conducting the active infrared thermography on a concrete bridge girder were the objectives of the first phase of the study. This phase of the laboratory study was developed based on the previous literature on pulsed thermography testing and available heating sources for research. Results are discussed in Section 5.2.

The goal of the second phase of the study was to develop a method for estimating the depth of the delamination based on the relationship between the delamination depth, the absolute contrast and the observation time discussed in Section 3.3.3.1. Results are listed in Section 5.3.

Phase III of the laboratory study was developed to investigate the minimum size requirements for a defect to be detectable by pulsed infrared thermography in concrete. Previous studies have indicated that the defect length should be at least two times greater than the defect depth to be detectable by infrared thermography. In other words, the ratio of the square root of the defective area to the defect depth should be larger than two (Equation 11 in Section 3.3.4 ) (Vavilov and Taylor 1982). While this finding has been stated as an empirical rule in infrared thermography, no literature has been found to provide information regarding the validity of this rule in application for concrete materials and with the current version of thermal infrared cameras. Therefore, this phase of the laboratory study focused on investigating the effects of the width to depth ratio on active infrared thermography.

## **5.1 Specimen and Equipment**

### ***5.1.1 Thermal Infrared Camera***

The thermal infrared camera used for this research was a FLIR ThermaCAM SC640 model camera. This is the same camera which was also used and discussed in the previous chapter for passive infrared thermography testing. This camera has a 24° x 19° field of view and a display of 480 x 640 pixels. In this study a laptop with the ThermaCAM Researcher Professional software was used to collect data every 30 seconds. Ambient temperature, humidity, and the distance between the front lens of the thermal IR camera and the object should be input in the camera software before testing to compensate for the radiation that is being absorbed in the atmosphere.

### ***5.1.2 Heat Sources***

Possible heat sources for active infrared thermography were previously discussed in Section 3.3.5 and Table 3.1. Two heat sources were selected based on the literature review and availability for research; these two heat sources were two 500W halogen lights and a 1500W infrared heater. In Phase I of this study, the effectiveness of these two

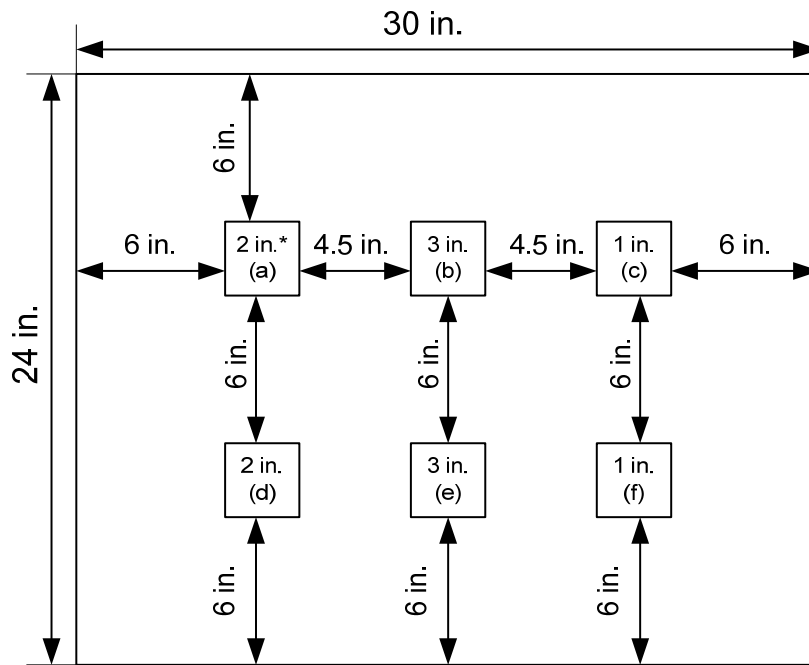
heat sources was investigated and based on the results obtained in this phase, the 1500W infrared heater was selected as the heat source for the rest of the experimental studies in Phases II and III.

### ***5.1.3 Concrete Slabs***

#### **5.1.3.1 Concrete Slab I**

The first specimen constructed for active infrared thermography research was a 2.5 ft x 2 ft x 5.5 in. concrete slab with simulated delaminations at different depths; see Figure 5.1. The size of this slab was selected based on the field-of-view of the camera (SC 640). This camera can capture almost the whole slab (2.5 ft x 2 ft) in one image when it is placed at approximately 5.5 ft from the specimen. A distance of 6 ft to 10 ft between the camera lens and the surface of interest is a more practical distance in the field while taking images from the shoulders or under the bridge deck.

Square-shaped Styrofoam blocks (3 in. x 3 in. x 3/8 in.) were used to simulate delaminations. The thermal conductivity of dry concrete is between 0.4 to 1.8 W/(m<sup>o</sup>K) or 2.8 to 12.5 (Btu·in.)/(hr·ft<sup>2</sup>·°F) (Lamond and Pielert 2006). The thermal conductivity of air (which is part of the delamination) and of Styrofoam is 0.024 W/(m<sup>o</sup>K) (0.166 (Btu·in.)/(hr·ft<sup>2</sup>·°F)) and 0.03 W/(m<sup>o</sup>K) (0.229 (Btu·in.)/(hr·ft<sup>2</sup>·°F)), respectively (Engineering ToolBox ; Maldague 1993). Therefore, because the thermal conductivity of Styrofoam and air are approximately the same, when compared with the thermal conductivity of concrete, the Styrofoam is representative of delaminations and cracks inside the concrete element. These simulated delaminations are square shaped and were selected to be 3 in. x 3 in. so as to be able to fit six delaminations in one slab and still have sufficient distance from the edges.



\* Depth of the delamination from the top surface.

Slab I

**Figure 5.1 Layout of concrete test specimen “Slab I” with simulated delaminations.**

The concrete mix was designed for this experiment was based on the Michigan Department of Transportation (MDOT) standard specifications for structures (MDOT 2003). According to the MDOT specification, the structural concrete mixture for concrete bridge superstructures should be designed based on the concrete grade D(a), which is summarized in Table 5.1.

**Table 5.1 Concrete Structure Specifications for Grade D(a) Concrete**

Cement Content (lb/cyd)	658
Fly Ash (lb/cyd)	0
Slump (in)	0-3½
28 Day Flexural Strength (psi)	725
28 Day Compressive Strength (psi)	4500

In the mix design for concrete Slab I, grade 6A aggregate was used as the coarse aggregate and 2NS grade aggregate was used for the fine aggregate. The gradation for the

coarse aggregate and fine aggregate available in the lab was checked with the standard MDOT specification before use (MDOT 2003). For the coarse aggregate (6A), the oven dry specific gravity was determined to be 2.37 based on ASTM C127 and the absorption was 2.82% (ASTM 2001). The specific gravity for oven dry fine aggregate (2NS) was determined to be 2.51 based on the ASTM C128 (ASTM 1997b). The fine aggregate used in this mix had a moisture content of 1.14% with an absorption of 3.5%. The mix proportions are summarized in Table 5.2. After mixing was completed, slump and air content testing was conducted on fresh mixed concrete according to ASTM C143 (ASTM 2000) and C231 (ASTM 1997c), respectively. The slump of this concrete mix was determined to be 8.5 in. and air content was 8.1%.

**Table 5.2 Mix proportions for concrete Slab I**

Cement (lb)	120.5
Water (lb)	44
Coarse Aggregate (lb)	266
Fine Aggregate (lb)	110
Air Entrainment (mL)	71

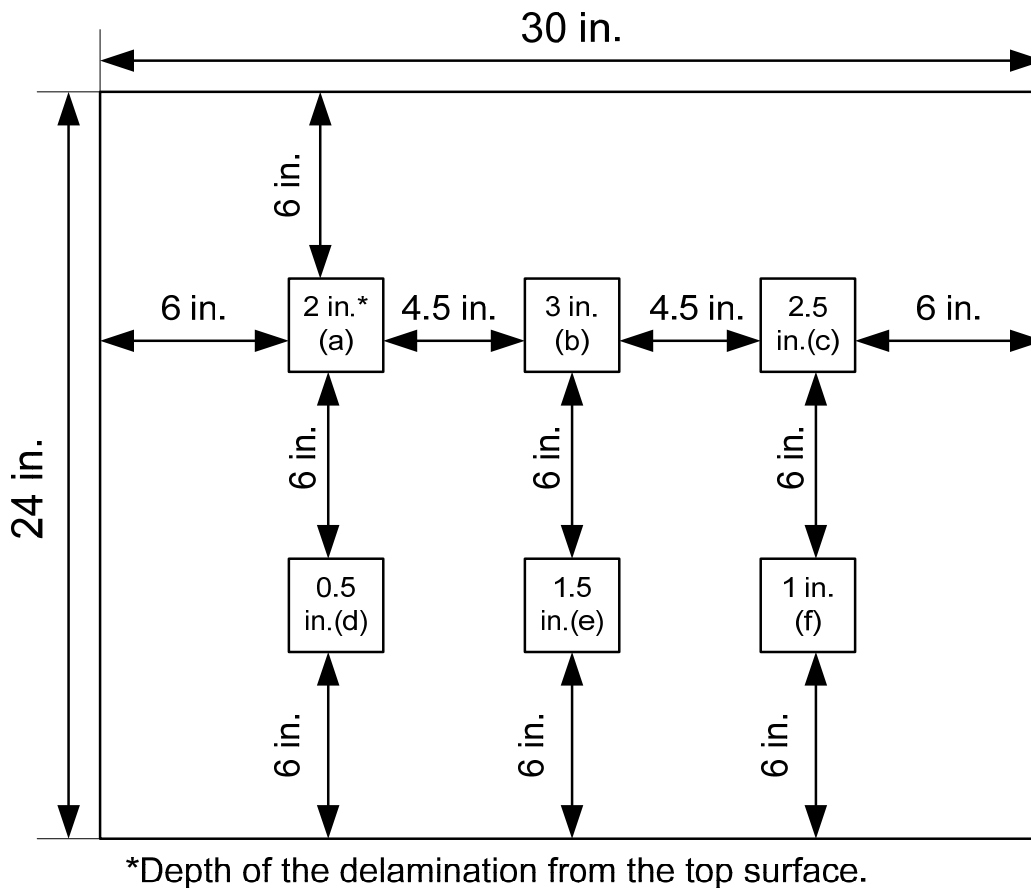
Figure 5.2 shows the construction sequence of this concrete slab with built-in Styrofoam. The Styrofoam pieces were placed at various depths in the slab and held in place with fishing lines. Then concrete was cast around and above the blocks. Care was taken to ensure that the blocks remained level and at the right height as the rest of the concrete was placed. The slab was cured at ambient laboratory conditions.



**Figure 5.2 Construction sequence of the concrete slab with Styrofoam blocks used as simulated delaminations.**

### 5.1.3.2 Concrete Slab II

Concrete Slab II was constructed with simulated delaminations similar to Slab I using square shaped Styrofoam blocks (3 in. x 3 in. x 3/8 in.). A plan layout of Slab II is demonstrated in Figure 5.7. In this slab, depth of the defects varies with ½ in. increments, to enable for more precise estimation of the depth based on the temperature and observation time.



Slab II

**Figure 5.3 Layout of concrete test specimen “Slab II” with simulated delaminations.**

Mix proportions for Slab II were similar to Slab I and are summarized in Table 5.3. This concrete mix had the slump of 0 in. and air content of 2.4%. Similar to the construction

of slab I, Styrofoam blocks were put in place and restrained by fishing line to ensure that the blocks remained level and at the right depths. The slab was cured at ambient laboratory conditions.

**Table 5.3 Mix proportions for concrete Slab II**

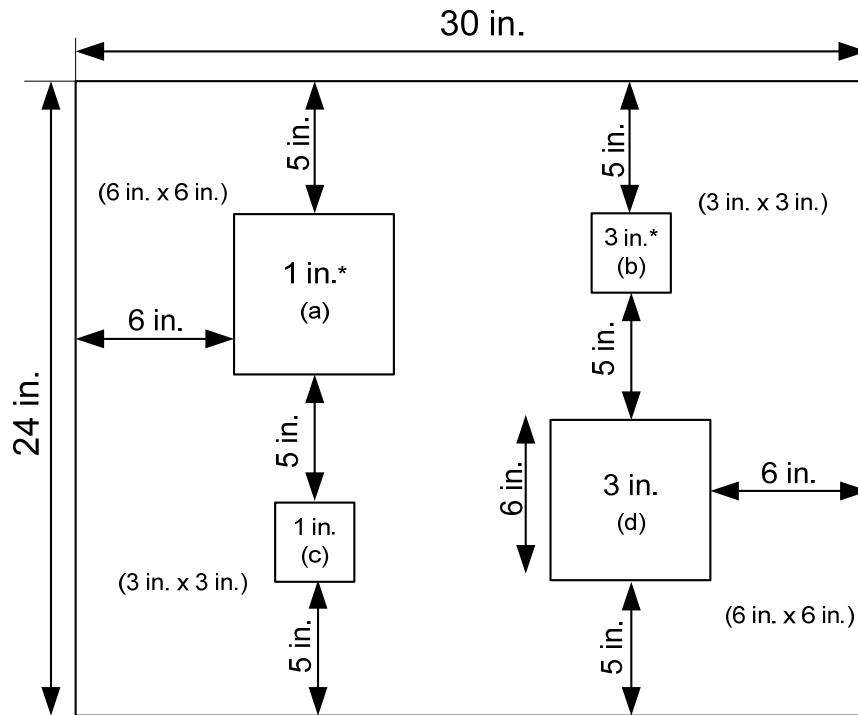
Cement (lb)	120
Water (lb)	44
Coarse Aggregate (lb)	266
Fine Aggregate (lb)	110
Air Entrainment (mL)	35



**Figure 5.4 Concrete Slab II after it was cured.**

### **5.1.3.3 Concrete Slab III**

Concrete Slab III was built with simulated delaminations at 1 in. and 3 in. deep, to investigate the impact of the width to depth ratio of the defects on the results obtained using pulsed infrared thermography test. For Slab III, simulated delaminations (square shaped Styrofoam blocks) were selected to be in two different sizes (3 in. x 3 in. x 3/8 in.) and (6 in. x 6 in. x 3/8 in.). These delaminations were placed in the slab, according to the plan layout in Figure 5.5.



\*Depth of the delamination from the top surface.

### Slab III

**Figure 5.5 Layout of the concrete test specimen “Slab III” with simulated delaminations.**

Similar mix design to Slab I was used to build Slab III. Mix proportions for Slab III are summarized in Table 5.4. This concrete mix had a slump of 2.5 in. and air content of 3.3%. Figure 5.6 shows the mold for concrete Slab III before placing the concrete mix inside and the concrete slab after it was built and cured for about a month. Similar to the construction of Slab I, Styrofoam blocks were put in place and restrained by fishing line to ensure that the blocks remained level and at the right depths.

**Table 5.4 Mix proportions for concrete Slab III**

Cement (lb)	120
Water (lb)	44
Coarse Aggregate (lb)	266
Fine Aggregate (lb)	110
Air Entrainment (mL)	53



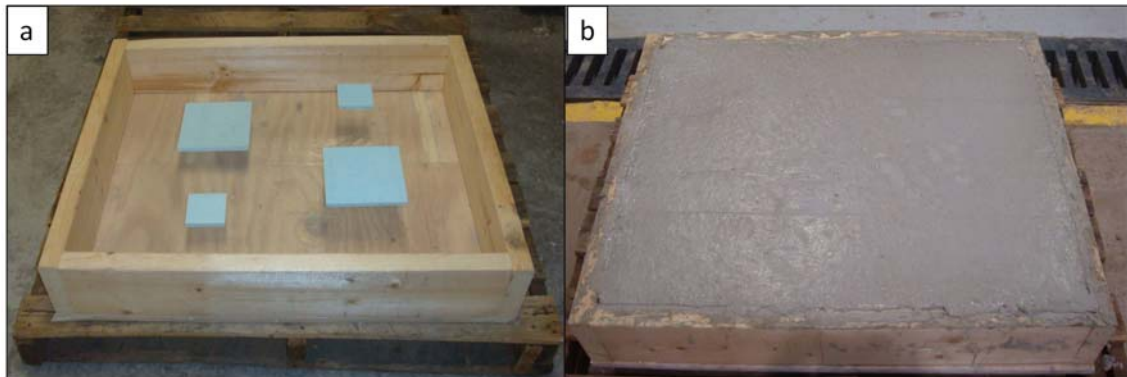


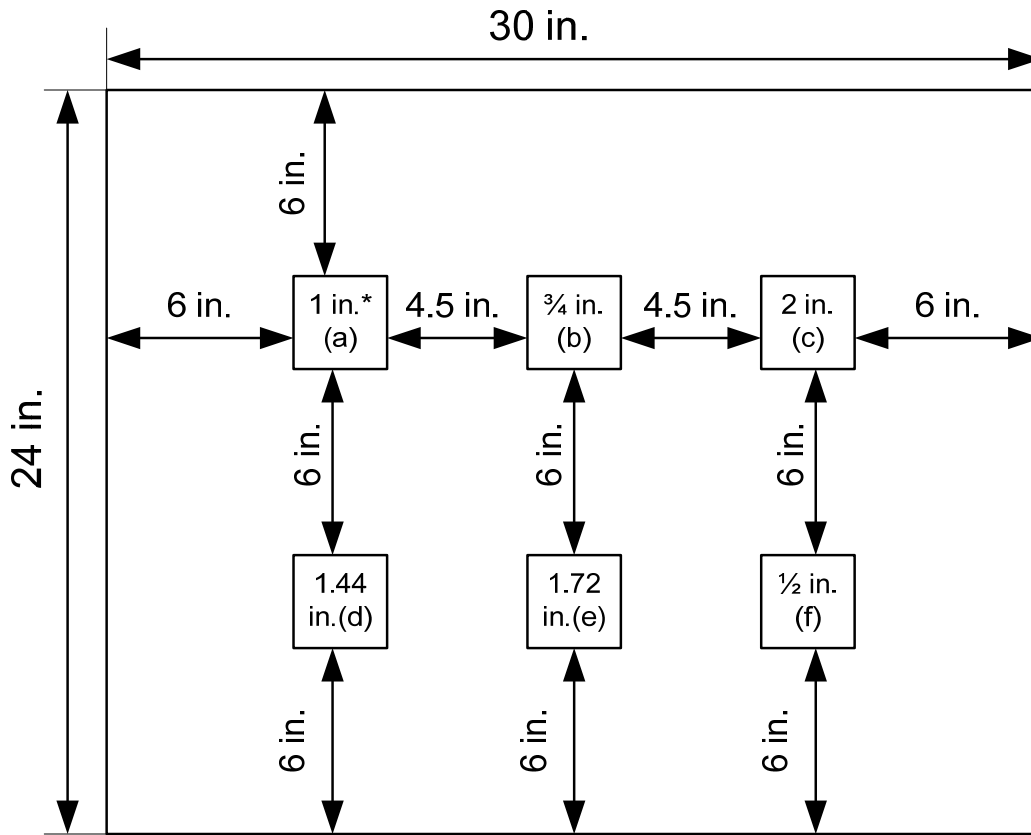
**Figure 5.6 (a) Mold that was built for slab III before pouring concrete and (b) concrete slab III after it was built and cured.**

#### **5.1.3.4 Concrete Slab IV**

To investigate the relationship between the observation time, maximum absolute contrast and defect depth, Slab IV was built with similar simulated defects to Slab I (square shaped Styrofoam). A plan layout of Slab IV is demonstrated in Figure 5.7. In this slab, simulated delaminations were placed at different depths to enable a more precise estimation of the relationship between delamination depth, temperature and observation time. Similar mixing proportions and procedures to phase I were applied for this slab. Mix proportions of the concrete mix used in constructing the Slab IV is shown in Table 5.5. Square shaped Styrofoam blocks (3 in. x 3 in. x 3/8 in.) were used to simulate delaminations inside concrete slab.

**Table 5.5 Mix proportions for concrete Slab IV**

Cement (lb)	84
Water (lb)	40
Coarse Aggregate (lb)	277
Fine Aggregate (lb)	188
Air Entrainment (mL)	0



\*Depth of the delamination from the top surface.

### Slab IV

**Figure 5.7 Layout of concrete test specimen “Slab IV” with simulated delaminations.**

Figure 5.8 shows the concrete Slab IV at the time of data collection after it was built and cured at ambient conditions.



**Figure 5.8 Concrete Slab IV after it was built and cured.**

#### **5.1.3.5 Concrete Slab A**

Slab A was constructed in January 2010 for passive infrared thermography testing. A plan lay-out of slab A is shown in Figure 4.1. Slab A is used Phase II of experimental testing to provide additional information for estimating the depth of the delaminations.

### **5.2 Phase I – Investigating the Effective Heating Source**

Selecting an effective heating source and method of infrared thermography applicable to concrete bridge elements were the objectives of this phase of the laboratory study. The depth of the delamination ( $z$ ), time ( $t$ ), and surface temperature ( $T$ ) were the three variables in this study. Other parameters that can influence the data collected via infrared thermography are: distance from the thermal infrared (IR) camera to the object, distance from the heat source to the object, heating period, heat source power output, ratio of the

delamination depth to the delamination radius (width), and the depth of the delamination to the total thickness of the test specimen.

Two heating sources were selected for investigation. These two heat sources were two 500W halogen lights (heat source A) and a 1500W infrared heater (heat source B). These heat sources were selected based on the previous studies discussed in Section 3.2.5. Both of these heat sources are possible options for deployment on the underside of the bridge, and can be easily powered by a portable generator.

As was discussed in Section 3.2.3.1, point heating, line heating, and surface heating are the three heating methods that can be applied for an active thermography test. The surface heating method was selected for this laboratory study. Although it is unfeasible to achieve uniform heating over the slab surface with surface heating methods, this method is more likely to be applicable for field studies because no additional equipment is required to run the heater over the surface of the concrete bridge element.

### ***5.2.1 Methodology of Data Collection and Processing***

Data collection was conducted on Slab I 10 weeks after construction. In the first stage of the investigation, two halogen lights (500W each) were placed at a distance of 3.5 ft from the test specimen at a normal angle, and the camera was placed at a distance of 5.5 ft from the specimen (see Figure 5.9). The halogen lights and the camera were installed such that lights were not in the field-of-view of the camera and did not affect the thermal image collection. The thermal IR camera was set up to collect images at 30 second intervals throughout the test. Intervals of 30 seconds were selected to assure the constant monitoring and to avoid interruptions due to the auto-focus set-up of the camera. The halogen lights were turned on and heated the slab for 15 minutes. Data collection continued for about 35 minutes after the halogen lights were turned off. The ambient temperature was 69.9°F and ambient humidity was 11.7% in the laboratory at the time of data collection.

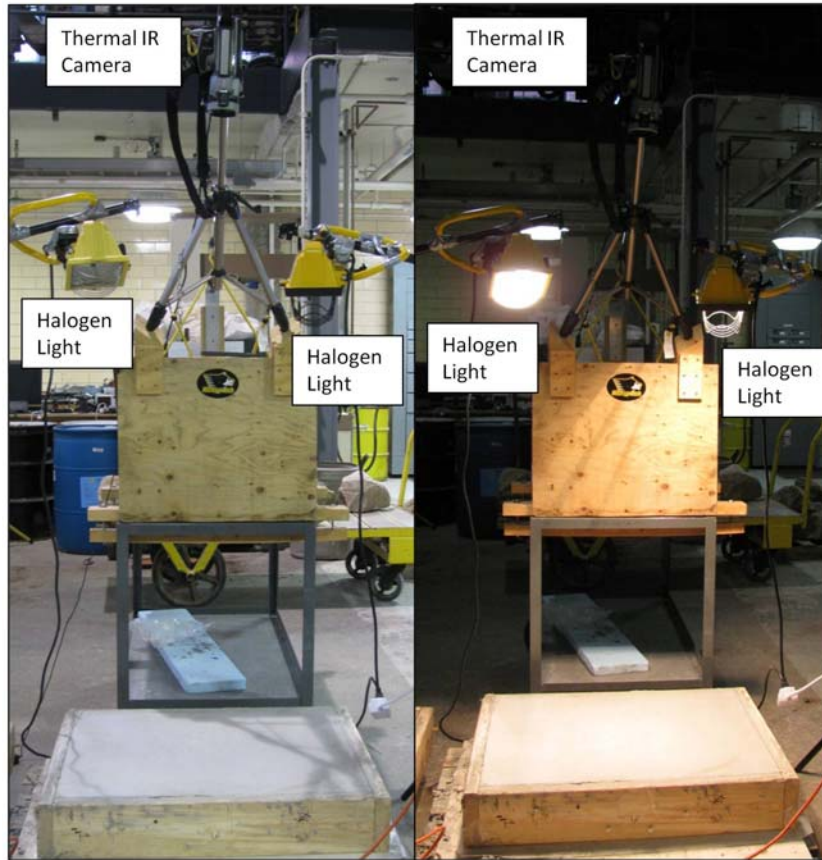


**Figure 5.9 Active infrared thermography test set-up using halogen lights as an external heat source, shown with the lights off (left) and on (right).**

During this test, temperature variations of each simulated delaminated area were monitored over time. Temperature values reported in this study are the average temperature of the concrete surface within the area of each delamination that can be obtained using the ThermaCAM Researcher Professional software. Square shaped areas, which are representative of delaminated areas, can be selected based on the subjective interpretation of the user.

To compare the behavior of the delaminations at different depths, the absolute contrast between delaminations and background was computed according to the discussion in Section 3.3.3.1.2. In pulsed infrared thermography, two methods can be used to compute  $\Delta T$  or absolute contrast for delaminations. The first method involves subtracting the temperature value of one single pixel above the delaminated area from that of one single

pixel above the sound area. In the second method, the temperature difference can be calculated by subtracting the average temperature of the area above delaminations and average temperature of the similar area at the background close to the delaminated area. The second method has proved to be more effective in this case as it diminishes the variability in how to select only one point in the background (Brown and Hamilton 2007). The selected background area has to be close to the area of defect because the  $\Delta T$  calculation is for helping the user to see the contrast between the delamination and its own background on the thermal IR image.

The second stage of this experimental series involved repeating the test using a 1500W infrared heater. In this stage, the heater was placed at a distance of 3.5 ft from the concrete slab and the camera was located at a distance of 5.5 ft from the concrete slab. The camera was slightly tilted ( $<10^\circ$ ) from the normal orientation to prevent having the heater in the field of view of the thermal infrared camera. Similar to the previous stage of Phase I of testing, the thermal IR camera was set up to collect images at 30 second intervals throughout the test. The infrared heater heated the slab for 15 minutes. Data collection continued for about 30 minutes after the heater was turned off. The ambient temperature in the laboratory was 72.3°F and the ambient humidity was 14.1% during the data collection.

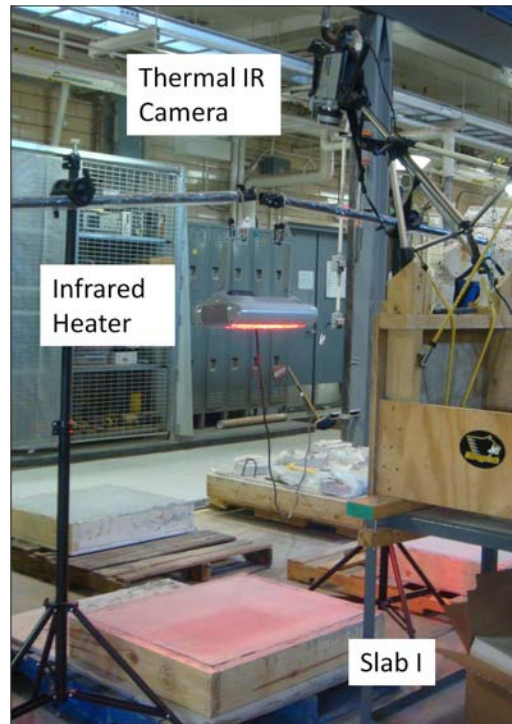


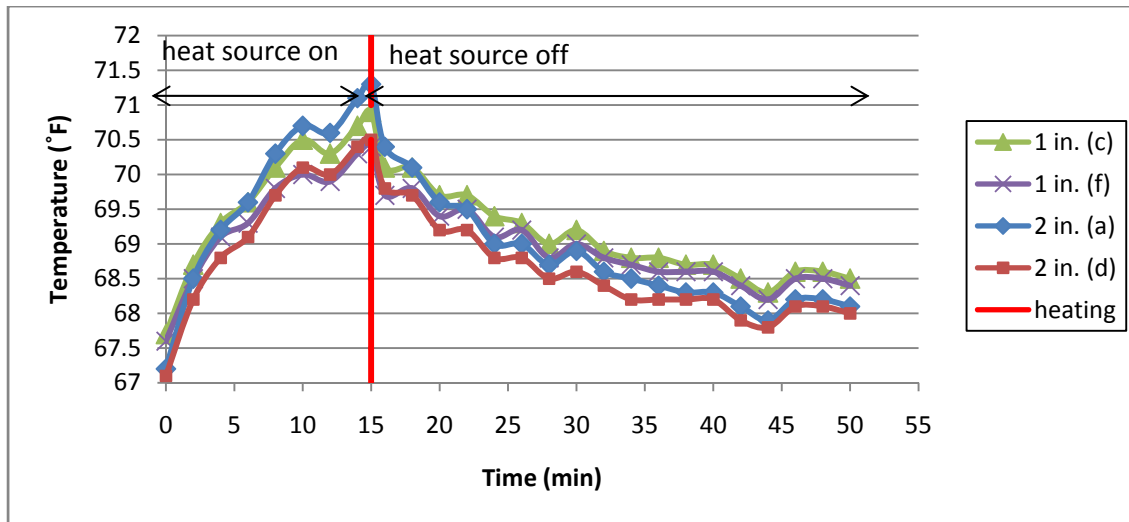
**Figure 5.10 Active infrared thermography test set-up using infrared heater.**

The absolute contrast computation method used for processing data from the infrared heater test was the same as with the halogen lights. In this way, the two sets of data could be compared to investigate the effectiveness of each heating source for active infrared thermography testing on concrete slabs.

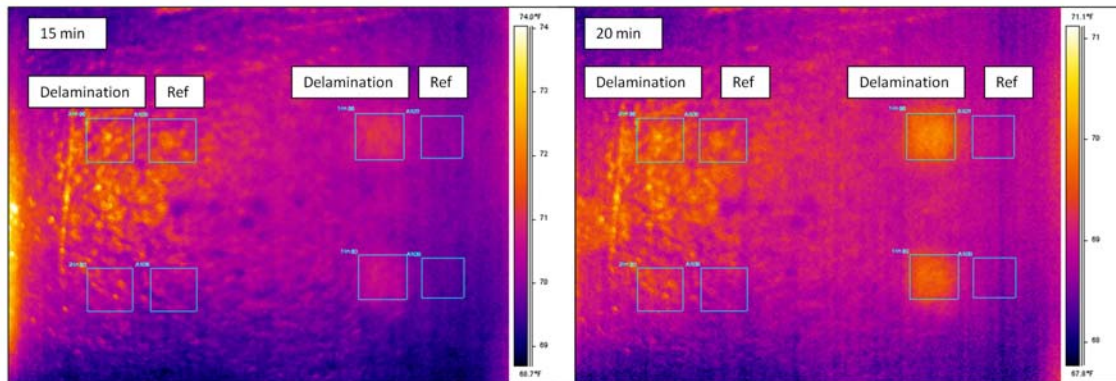
### ***5.2.2 Results and Analysis***

Figure 5.11 shows the variation of temperature for each simulated delaminated area when using two 500W halogen lights. This figure shows the temperature variations during the heating period and for about 35 minutes after heating was terminated. It can be seen from this graph that 10 minutes after the heat source was turned off, delaminations placed at 1 in. deep appeared with a higher temperature compared to delaminations placed at 2 in. deep. Figure 5.12 shows the thermal IR image that was taken when heating stopped (15 minutes after data collection was started) and 5 minutes after the heat source was turned off (20 minutes after data collection was started). Reference background areas (Ref) were selected to be close to each delamination and were used in calculating the absolute

contrast for each delamination. Comparing these images with the plan layout of Slab I in Figure 5.1 indicates that delaminations placed at 3 in. deep did not appear during an active infrared thermography testing on this slab. “Ref” on these images indicates the area at the background and close to the delamination that was considered in determining the temperature of the background and the absolute contrast of each delamination.



**Figure 5.11 Plot of the temperature variation in an active infrared thermography test using two 500W halogen lights as a heat source, Slab I.**

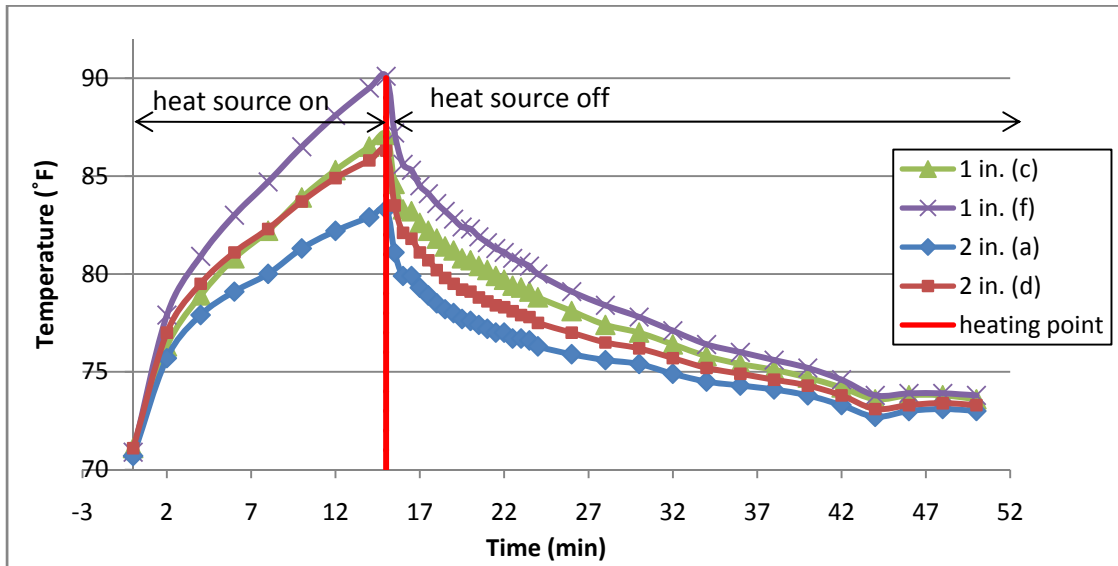


**Figure 5.12 Thermal infrared images obtained from an active infrared thermography test using halogen lights on Slab I, shown 15 minutes after data collection began (left) and 20 minutes after data collection began (5 minutes after the heat source was turned off) (right).**

The variation of average temperature values for each delamination, collected in the second stage of this experiment using heater B, are presented in Figure 5.13. These

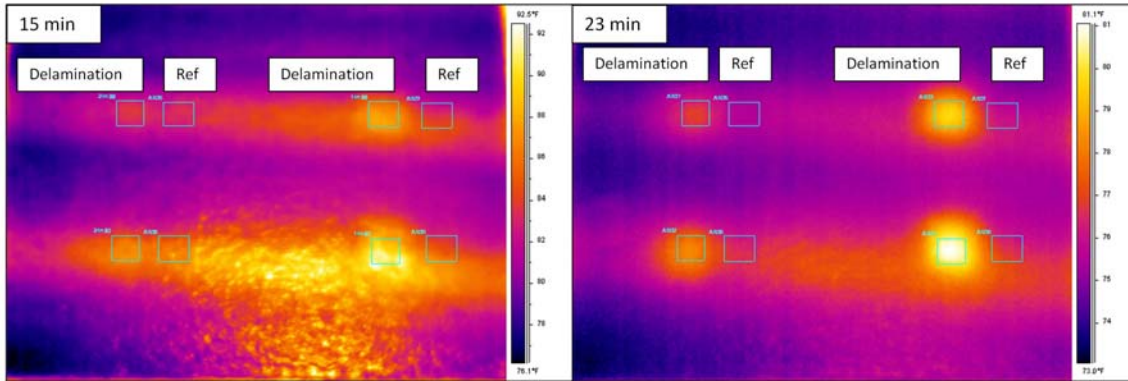


temperature values were obtained based on the same procedure discussed previously in the first stage of the test using two 500W halogen lights.



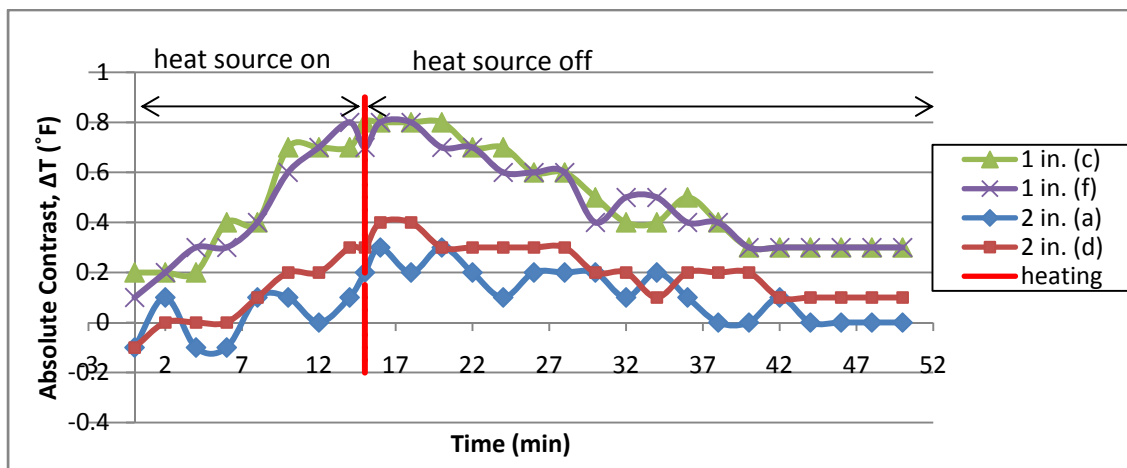
**Figure 5.13 Plot of the temperature variation in an active infrared thermography test using a 1500W infrared heater as a heat source, Slab I.**

Figure 5.14 shows the thermal IR images at 15 minutes and 23 minutes after starting the data collection. 15 minutes is when the heating was stopped, and 23 minutes is when the maximum contrast appeared on the thermal infrared images for delaminations located at 2 in. deep. As it can be seen from these images, both delaminations at 23 minutes are more apparent than 15 minutes. This indicates that a reflection on the surface is prominent due to the surface heating method.



**Figure 5.14 Thermal infrared images of active infrared thermography test using 1500W infrared heater, shown 15 minutes after data collection began (left) and 23 minutes after data collection began (8 minutes after the heat was turned off) (right), Slab I.**

Figure 5.15 provides a plot of the absolute contrast ( $\Delta T$ ) versus time for delaminated areas at depths 1 in. and 2 in., when heated using heat source A.  $\Delta T$  was calculated by subtracting the average temperature above the area of delamination and the average temperature of a similar area adjacent to the delaminated area. Delaminations 3 in. deep were not detectable in this test. Although data were collected at 30 seconds intervals, the data used for this plot is presented at 2 minutes intervals as it shows the same trend. Data were collected at 30 seconds intervals to avoid missing any points in the data set.



**Figure 5.15 Absolute contrast plot for an infrared thermography test using two halogen lights (500W each), Slab I.**

Figure 5.16 shows the plot of the absolute contrast between delaminated areas and background temperature versus time when heated using heat source B. This plot can be compared with the plot in Figure 5.15 which shows that using the 1500W infrared heater increases the absolute contrast significantly and results in better contrast between delaminated areas and sound concrete area on the thermal infrared image. Furthermore, this plot indicates that the delaminated areas located at 2 in. deep from the top surface appeared on the thermal infrared images after the heating was stopped (in this case seven minutes). The time at which the maximum contrast will be observed between the delamination and background area is called observation time (t).

Data points for the absolute contrast variation plot presented in Figure 5.16 were input in the spreadsheet at 2 minute intervals. However, to monitor the temperature changes more precisely after the heating was terminated, data points were plotted at 30 second intervals between the time when the heater was turned off (15 minutes after data collection began) and 9 minutes after the heat was turned off (24 minutes after data collection began). It was noted that after the heat source B was turned on over the concrete slab the absolute contrast for delaminations located at 2 in. depth decreased for about 6 minutes before it increased to the maximum absolute contrast. This reduction in absolute contrast to negative values means that the background temperature was higher than the temperature of the delaminated area. Non-uniform heating of the concrete surface due to the selected heating method is possibly the cause of this drop in absolute contrast to negative values at the beginning of the test.

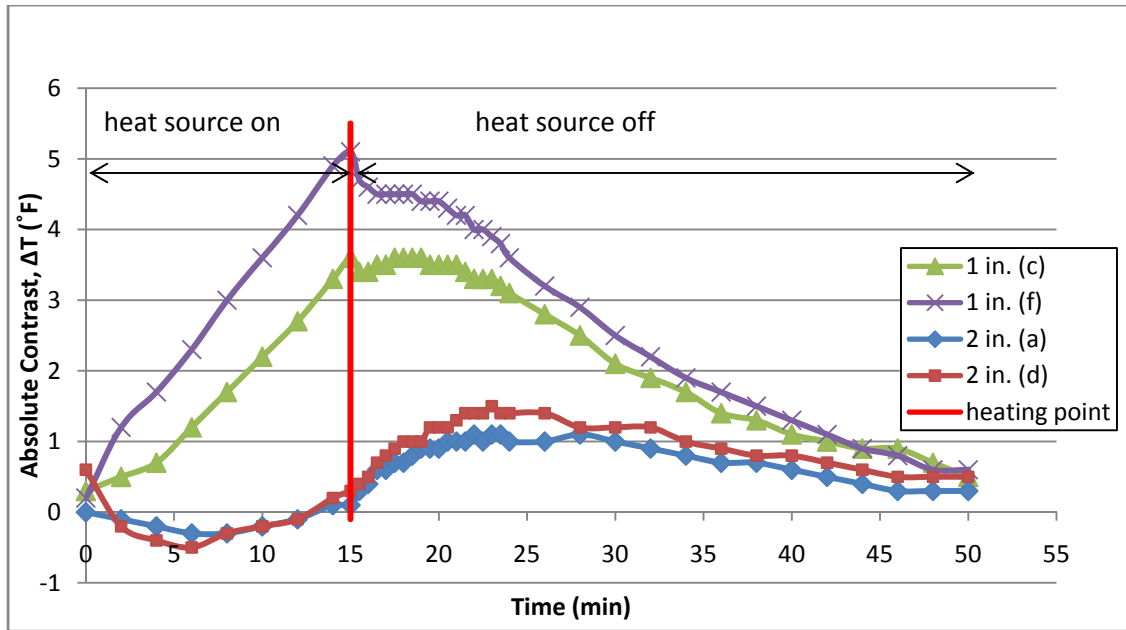


**Figure 5.16 Absolute contrast above delaminations at 1 in. and 2 in. depth in infrared thermography test using an infrared heater (1500W).**

### 5.2.3 Discussion

Phase I investigated the effect of type of heat source on conducting an active infrared thermography test of existing concrete elements. Halogen lights (500W) and an infrared heater (1500W) were compared in this study. Comparing the plots in Figure 5.15 and Figure 5.16 showed that the 1500W infrared heater is a more efficient heat source in active infrared thermography testing of concrete elements; better contrast can be achieved on the thermogram results using a heat source with higher output power. Previous studies showed that halogen lights are a good source of heat for identifying areas of debonding and flaws in fiber reinforced polymer (FRP) overlays on the concrete surface. However, the depth of most flaws in FRP overlays is less than 5 mm (0.16 in.) (Starnes and Carino 2005; Brown and Hamilton 2007), while the delaminations in concrete bridge elements mostly occurred at the depth of the first layer of reinforcement or within the rebar's cover, which is less than 3 in. (AASHTO 2007). Therefore, the larger heat source is needed to heat the concrete deeper in the slab, to the level of the delaminations.

Other variables that can influence the decision in selecting the right heat source are the possible distance from the heater to the surface of the concrete element, and the depth of the delamination. In this experiment, the heater was placed at a distance of 3.5 ft from the test specimen. Heaters with more powerful output may be required when conducting active infrared thermography with a greater distance between the heat source and the concrete. The depth of the delamination is another factor that can influence the heat source selection procedure. In this test, delaminations at a 3 in. depth did not appear on the thermogram of the concrete slab. A higher heat output may have helped in detecting the 3 in. deep delaminations. However, the width to depth ratio of the delamination is another variable that can influence the detection procedure. This variable is investigated and discussed in the Phase III of these experimental series.

#### **5.2.3.1 Justification on Background Area Selection**

As was discussed previously, the absolute contrast in these series of experimental studies was computed based on subtracting the average surface temperature within an area above delamination from the average surface temperature within a background area (Ref) close to the delamination. In this method, a background area should be selected for each delaminated area, especially if the delaminations are far apart. The reason for selecting multiple background areas instead of a single background area is that the computed contrast should help inspectors to detect delaminations; in other words, delaminations should have contrast on their own background to become detectable on a thermal IR image.

To further study this concept, an analysis was performed on the data collected in Phase I using heat source B. In this analysis, a single background area was selected instead of multiple background areas and the contrast for each delamination was calculated relative to that single background area. Figure 5.17 shows the relative location of the delaminated areas to the single background point on the thermal infrared image of Slab I taken at 22 minutes after starting of the test.

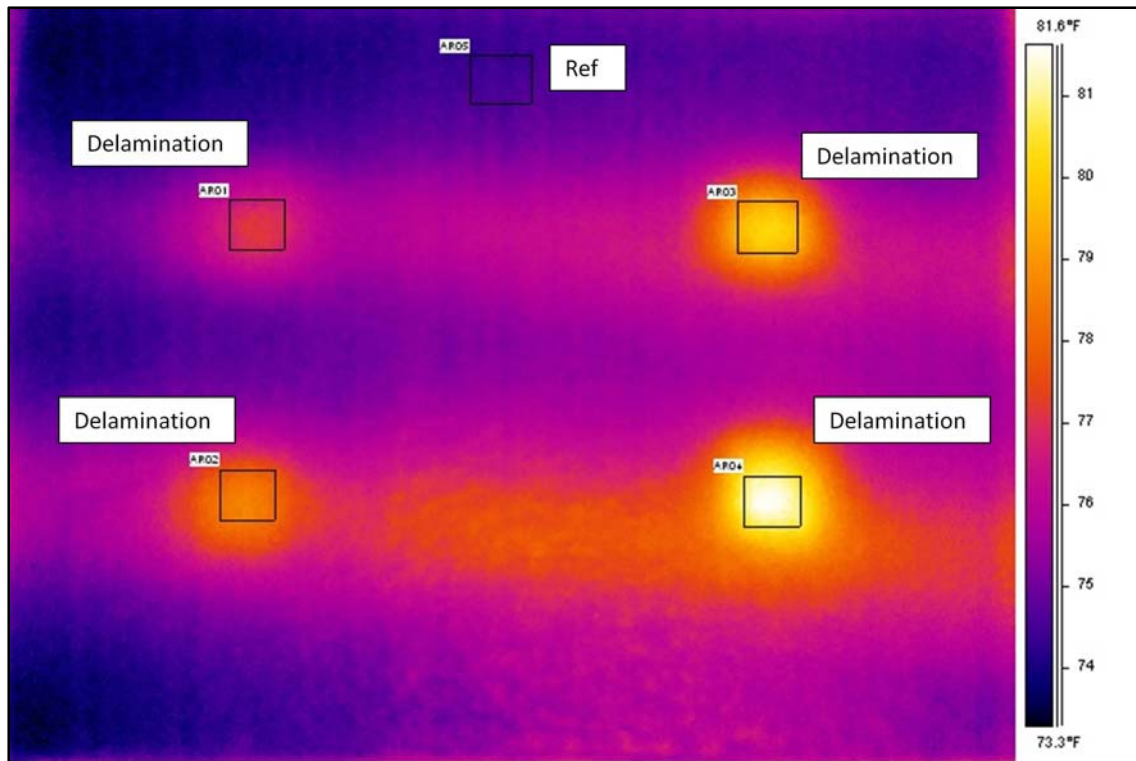


**Figure 5.17 Relative locations of delaminated areas and a single background area selected for analysis (7 minutes after the heat was turned off), Slab I.**

A plot of the variation of the absolute contrast for each delamination versus time is given in Figure 5.18. In this plot, the absolute contrast was computed by subtracting the average temperature within the area above each delamination and the average temperature within a single area selected as background. Comparing this plot (Figure 5.18) with the plot, obtained using multiple background areas for analysis (Figure 5.16), shows that the observation time and associated maximum contrast, which can help in estimating the depth of the delamination, are not obtainable using only one single background area for all four delaminations. The maximum absolute contrast for 1 in. deep delamination is 5.1°F when using a background area close to the delamination and 10.9°F when using a background area further away from the delamination. The maximum absolute contrast for 2 in. deep delamination is 1.4°F and appeared 7 minutes after turning off the heater. The maximum absolute contrast and the observation time values are evident on the absolute contrast plot in Figure 5.16, in which the analysis was based on selecting multiple background areas. The maximum contrast, obtained from the analysis using a single

background area, is 7.1°F and appeared at the same time when the heater was turned off (15 minutes after data collection was started). This contrast does not necessarily correspond to the time and absolute contrast in which 2 in. deep delaminations are evident.

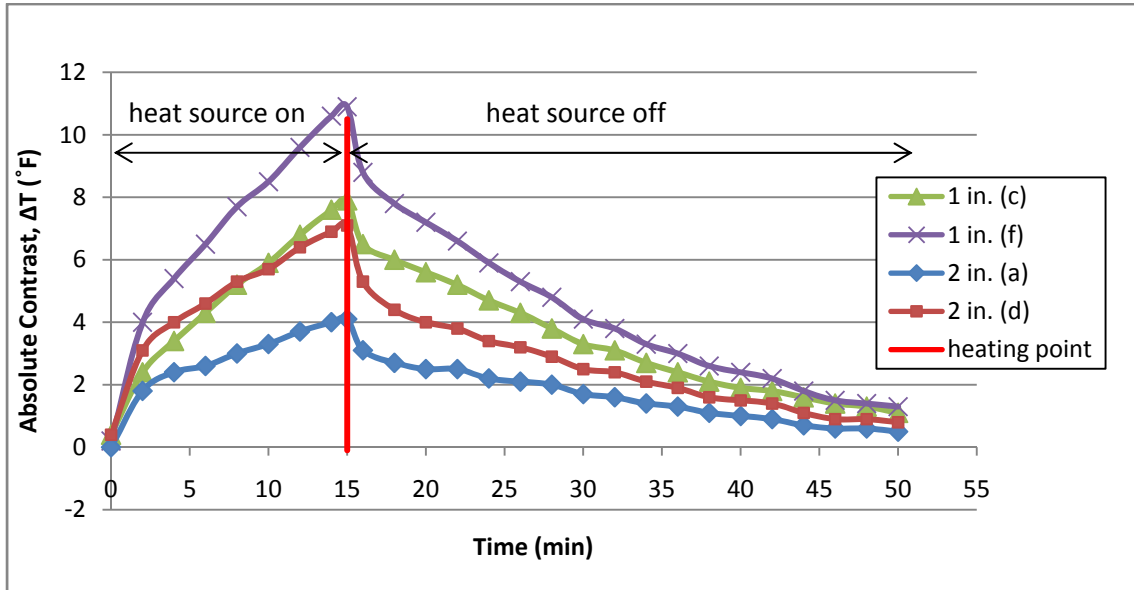


**Figure 5.18 Absolute contrast above delaminations at 1 in. and 2 in. depth using a single background area for analysis.**

### 5.3 Phase II – Developing a Method to Estimate the Depth of Each Delamination

According to the literature review of pulsed thermography discussed in Section 3.3.3.1, the time of observation (t) has a quadratic relationship with the defect depth (z) (Equation 5). The objective of Phase II is to predict the approximate depth of the delamination under the surface of the concrete element based on the relationship between the depth of the delamination (z), the observation time (t) and the absolute contrast  $\Delta T$ . Phase II was conducted on three concrete slabs; slab A, Slab I and Slab IV.

### ***5.3.1 Methodology of Data Collection and Processing***

The first stage of Phase II involved conducting active infrared thermography tests on the concrete slab A, and obtaining a relationship between the depth of the delamination ( $z$ ), the observation time ( $t$ ) and the absolute contrast ( $\Delta T$ ) based on the data collected on the concrete slab A and the data collected on Slab I in Phase I. The second stage of this study was conducted on Slab IV and the relationship between the aforementioned parameters ( $z$ ,  $t$  and  $\Delta T$ ) was obtained. Styrofoam blocks were placed in Slab IV at the depths of  $\frac{1}{2}$  in.,  $\frac{3}{4}$  in., 1 in., 1.44 in. (approximately square root of 2), 1.72 in. (approximately square root of 3) and 2 in. The Styrofoam block placement allowed for more data points to achieve a more precise relationship between the delamination depth ( $z$ ), the observation time ( $t$ ), and the absolute contrast ( $\Delta T$ ).

The same testing procedure as discussed in Phase I was used to conduct active infrared thermography on the concrete slabs (Slabs A and IV). A 1500W infrared heater was located at 3.5 ft above the concrete slabs and thermal infrared images were collected using the thermal IR camera at the height of 5.5 ft. Thermal infrared images were collected every 30 seconds to avoid any missing data points during the test.

The absolute contrast computation method used in Phase I was used once more here. The absolute contrast between the delamination and background area was computed by subtracting the average surface temperature within the area above the delamination and average surface temperature within the selected background area close to the area of delamination.

### ***5.3.2 Results and Analysis***

#### **5.3.2.1 Concrete slab I and Concrete slab A**

The collected data and results of the active infrared thermography testing on Slab I was presented and discussed in Phase I in Section 5.2.2. Results obtained in Phase I were



combined with the results obtained from the data collected on Slab A to estimate the relationship between the depth of the delaminations ( $z$ ) and time of observation ( $t$ ).

A plan layout of Slab A was shown previously in Figure 4.1. The camera distance and heat source distance from the concrete slab was 5.5 ft and 3.5 ft, respectively. Humidity in the laboratory at the time of data collection was 19.2% and temperature was 67.8°F. Delaminations F1 and F2 were the main focus of this data analysis due to the use of Styrofoam blocks at these locations similar to Slab I. These two delaminations were supposed to be located at 2 in. deep from the top surface of the concrete specimen. But passive thermography testing on this slab suggested the actual depth was somewhere closer to the surface ( $< 2$  in.).

Figure 5.19 shows the temperature variation for the simulated delaminated areas F1 and F2 during the 15 minute heating period and 45 minutes after the heat source was turned off.

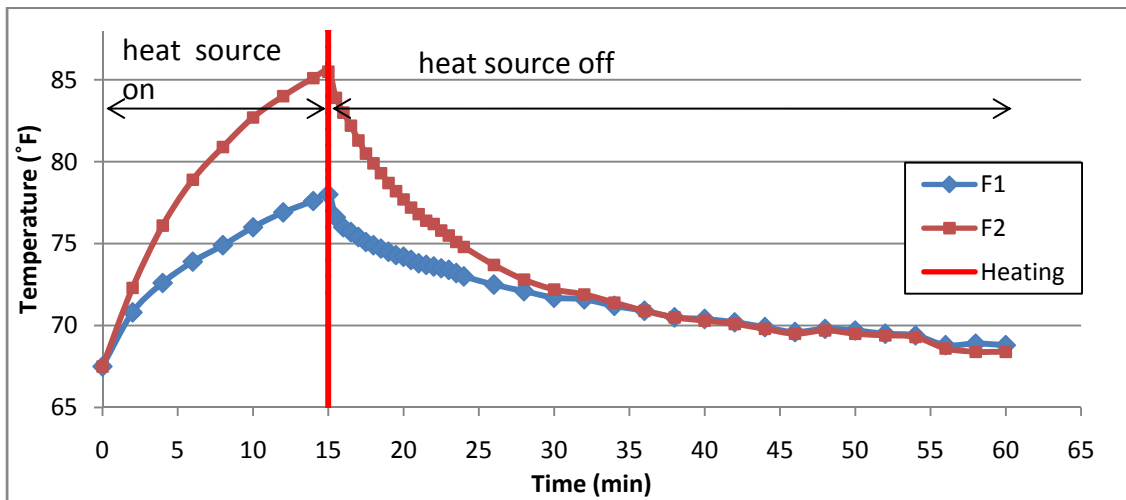


**Figure 5.19 Temperature variation within the delaminated areas F1 and F2 in concrete slab A during an active infrared thermography test.**

Figure 5.20 shows a plot of the variation of the absolute contrast ( $\Delta T$ ) versus time for delaminated areas F1 and F2 during the 15 minute heating period and 45 minutes after the heat source was turned off. Computation of the absolute contrast was similar to Phase

I and was based on subtracting the average surface temperature of the area above the delamination and the average surface temperature in the background area close to the delaminated area. Based on this figure, the maximum absolute contrast was observed at 15 minutes for defect F2 and at 20 minutes for defect F1. That makes the observation time for defect F2 to be close to 0 and observation time for defect F2 is 5 minutes. Observation time was determined based on the time at which the maximum absolute contrast occurred for each delamination.

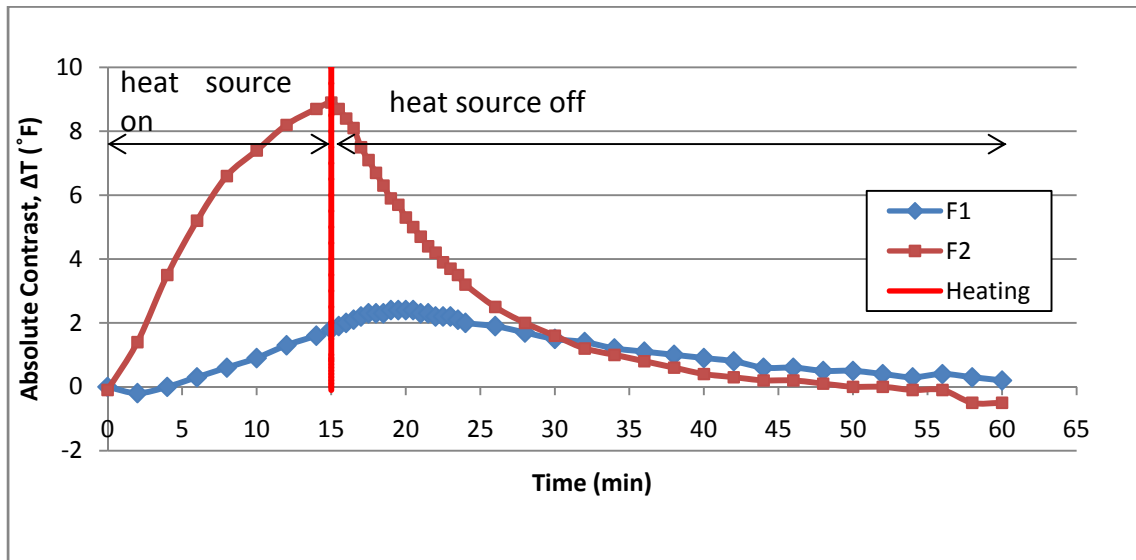


**Figure 5.20 Absolute contrast above delaminations F1 and F2 during the 15 minutes heating period and 45 minutes after the heat source was turned off.**

Figure 5.21 shows thermal IR images 15 minutes after the start of the data collection (when the heat source was turned off) and 20 minutes after the start of the data collection (when the defect F2 appeared on the thermal infrared image with the highest contrast).

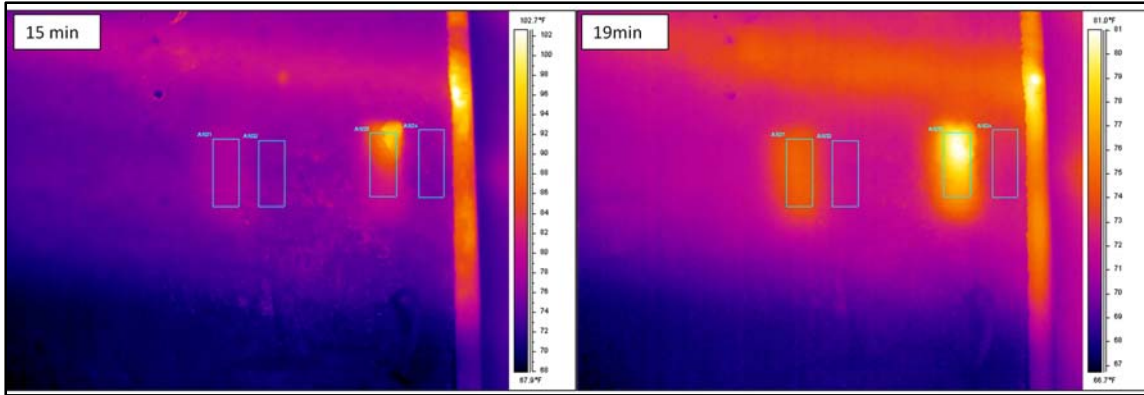


**Figure 5.21 Thermal infrared images for the active thermography test on slab A, shown at 15 minutes after data collection began and 19 minutes after data collection began (4 minutes after heat source was turned off).**

After the active infrared thermography test was completed on Slabs I and A, a coring test was done to find the exact depth of the delaminations located in these slabs. A summary of these cores and figures are presented in Appendix D. Table 5.6 summarized the observation time, depth ( $z$ ) (both planned and actual depth) and maximum absolute contrast ( $\Delta T$ ) for the delaminations located at different depth in slab I and slab A.

**Table 5.6 Summary of the results of active infrared thermography on slab I and slab A**

	Observation Time (min)	$z$ (in)	$z$ (in) cores*	$z^2$ (in <sup>2</sup> )	$\Delta T(\text{max})$ (°F)
Slab I	2.5	1 (c)	0.72	0.52	3.6
	1	1 (f)	0.75	0.56	4.6
	8	2 (d)	1.14	1.3	1.5
	6.5	2 (a)	1.04	1.08	1.1
Slab A	0	-	0.33	0.11	8.9
	4	-	0.89	0.79	2.4

\*obtained from the coring test

In Slab I, the observation time for 1 in. deep delaminations (c) and (f) were 2.5 and 1 minutes respectively, and for 2 in. deep delaminations (a) and (d) were 6.5 and 8 minutes, respectively. In slab A, the observation time for the 0.5 in. deep delamination (obtained from a core) (F2) was 0 minutes and for the 1 in. deep delamination (obtained from a

core) (F1) was 4 minutes. After the heating was stopped on the concrete slabs, the average surface temperature above delaminations located at 1 in. from the surface decreased rapidly with an almost linear slope, then the temperature remains constant or increased slightly before it decreased again. The point at which the absolute contrast remained constant or increased to the maximum contrast considered as the observation time and this will be the time that delamination appeared on the thermal infrared images. An observation time of 0 minutes means that maximum contrast within the delamination appeared to be at the time when heating was stopped.

The relationship between the depth of each delamination and the observation time was discussed in section 3.3.3.1. From this discussion and the literature review, the time of observation has a linear relationship to the depth square ( $z^2$ ) (Equation 5). Figure 5.22 shows the plot and relationship between the observation time and the square depth of the delaminations in Slabs I and A ( $n = 6$ ). Depths presented on this graph are the actual depth for each delamination obtained from cores. The linear regression line was drawn for these data points to confirm the linear relationship between  $t$  and  $z^2$ . The square of the correlation coefficient ( $R^2$ ) is determined to be 0.94 for the data set. An  $R^2$  value gives a measure for reliability of linear relationship for this data set. The  $R^2$  value of 1 implies that all data points are perfectly fit on the straight line. It can be seen from the graph and the equation in Figure 5.22 that the correlation coefficient for this data set is very close to 1 which confirms the linear relationship between  $t$  and  $z^2$ .

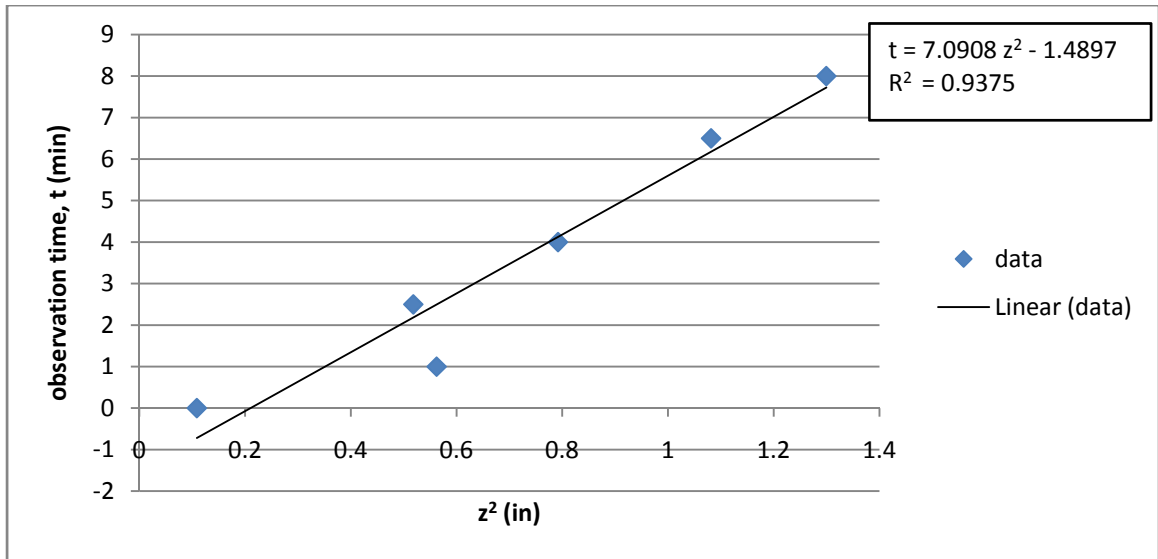


**Figure 5.22 Observation time versus the depth squared of each delamination.**

The relationship between the contrast and the depth of the flaws was discussed previously in Section 3.3.3.1. For the six data points obtained from Slabs A and I, the absolute contrast ( $\Delta T$ ) is plotted versus the inverse of the cubic depth of each delamination (Equation 5). This plot and the associated linear regression equation are shown in Figure 5.23. The relationship between the running contrast values and the inverse of the cubic depth of each delamination was also plotted in Figure 5.24. Definitions of absolute contrast and running contrast values were discussed previously in Section 3.3.3.1.2 of this document (Equations 8 and 9). The square of the correlation coefficient ( $R^2$ ) is determined to be 0.84 and 0.83 for the linear regression lines in Figure 5.23 and Figure 5.24, which confirms the almost perfect linear relationship. However, more data points between the  $1/z^3$  value of 2.4 and 8 will give a better estimation of these linear regression equations. Based on these two graphs and relationship between the contrast and the inverse of the cubic depth ( $1/z^3$ ), the depth of each delaminated area can be estimated.

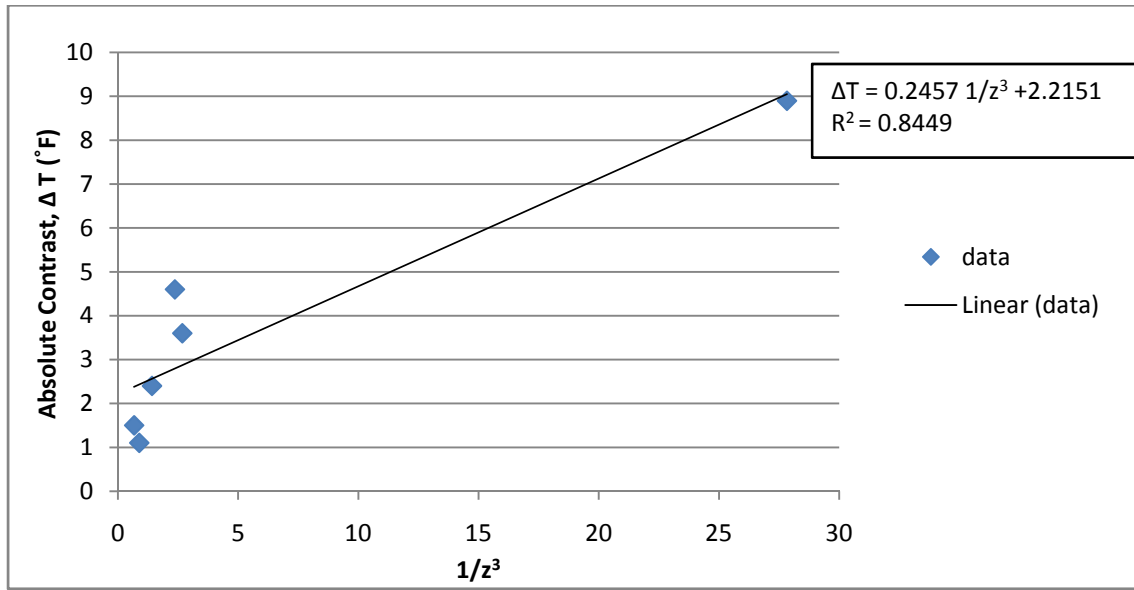


**Figure 5.23 Absolute contrast versus the inverse of the cubic depth for Slabs I and A.**

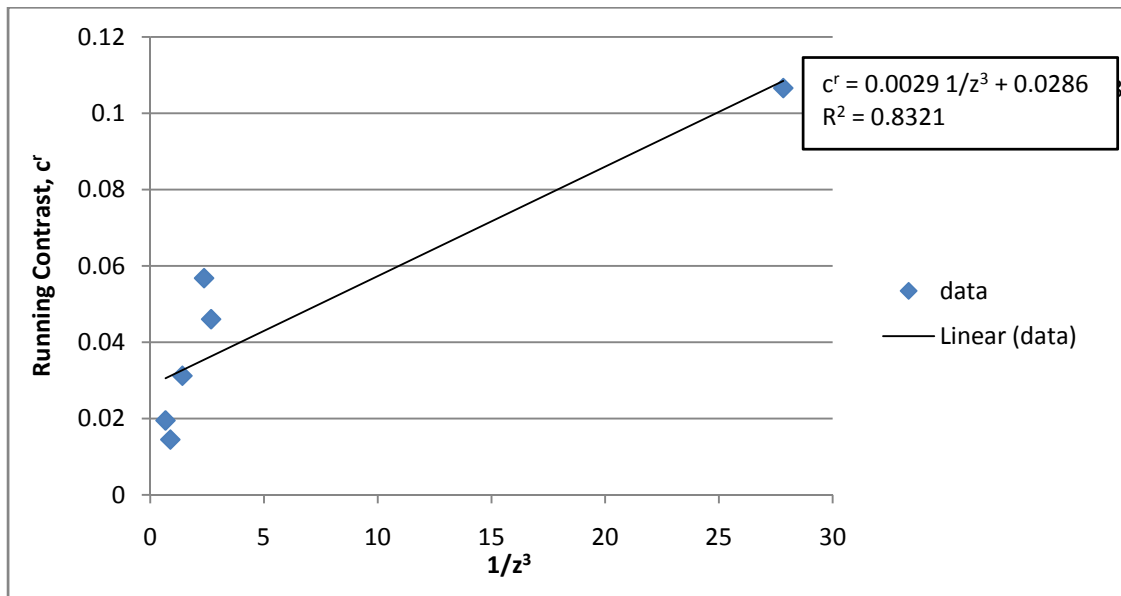


**Figure 5.24 Running contrast versus the inverse of the cubic depth for Slabs I and A.**

### 5.3.2.2 Concrete Slab IV

To achieve a more precise relationship between the depth of the delamination and the observation time, an active infrared thermography test was conducted on concrete slab IV. Styrofoam blocks were placed in this slab in such a way as to produce more data points on the graph farther out on the abscissa. Similar to the previous testing on Slab I and Slab A, Slab IV was heated for 15 minutes using an infrared heater and data were collected during the 15 minutes heating period and 60 minutes after the heat source was turned off. The ambient temperature in the laboratory was 75°F and the ambient humidity was 54% during the data collection. These two values, as well as the distance between the camera and the concrete slab were input in the infrared imaging software before starting the data collection.

The temperature variation above each simulated delamination (Styrofoam blocks of 3 in. x 3 in. x 3/8 in.) is presented in Figure 5.25. Similar to the results obtained in Phase I, the surface temperature above each delamination increased during the heating period and it decreased after heat source was turned off (15 minutes after the beginning of the data collection). In general, it was expected to observe higher temperatures above shallower delaminations compared to the deeper delaminations. However, the results presented in the temperature variation plot of concrete Slab IV showed that the surface temperature above the delamination located at the depth of 1.72 in. had the highest temperature after heating up the slab for 15 minutes, while delamination located at 1 in. had the lowest temperature after the 15 minutes heating period. The reason for this unexpected temperature values was a combination of non-uniform heating of the concrete slab surface and the reflection of heat off the concrete slab surface.

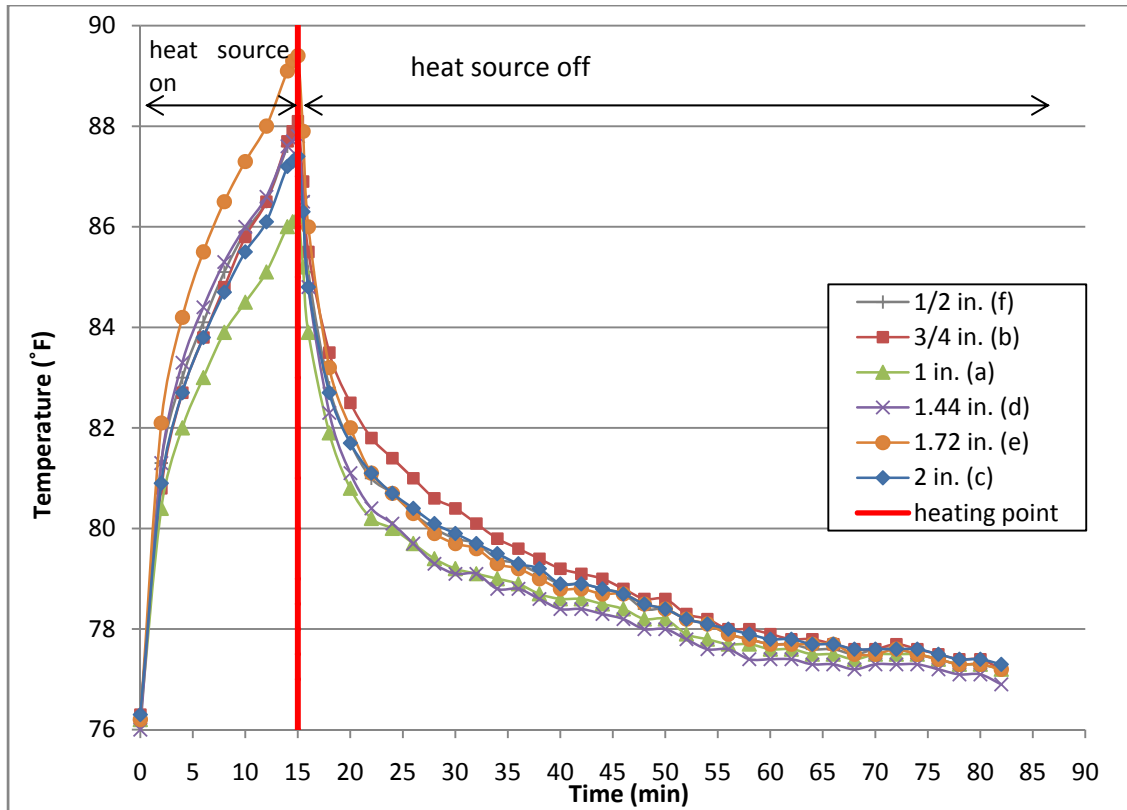


**Figure 5.25 Temperature variation above each delamination in an active thermography test on the concrete slab IV.**

After turning off the heat source, the surface temperature above the delamination, placed at 1.72 in. depth, decreased at a faster rate compared to the surface temperature above the delamination located at  $\frac{3}{4}$  in. depth. Comparing the surface temperature change above the delamination located at 1 in. and 1.44 in. depth showed a similar trend. The surface temperature above both 1 in. and 1.44 in. deep delaminations decreased after the heat source was turned off, however it can be seen from the graph that the surface temperature above the delamination located at 1.44 in. under the surface decreased a little bit more after about 34 minutes from the start of data collection (19 minutes after the heat source was turned off).

The absolute contrast variation plot for the six delaminations placed in concrete slab IV is shown in Figure 5.26. It can be seen from this graph that the absolute contrast decreases with a near vertical slope for a few minutes, then it stays constant and decreases at a



much lower rate. The linear slope observed on these graphs can be considered as a false signal due to the non-uniform heating and the observation time determined to be the time at which the absolute contrast remained constant after the rapid decrease. This value is more evident in the graph of the absolute contrast change for the delamination located at  $\frac{3}{4}$  in. (Figure 5.26). The absolute contrast above the delamination placed at  $\frac{3}{4}$  in. depth decreased from  $1.7^{\circ}\text{F}$  to  $1.5^{\circ}\text{F}$ , during the minute after the heat source was turned off (16 minutes after data collection began) and increased to back to  $1.7^{\circ}\text{F}$ , three minutes after the heat source was turned off (18 minutes after data collection began). It can be seen that the time of observation for delamination placed at  $\frac{3}{4}$  in. depth is about 3 minutes after the heating was stopped.

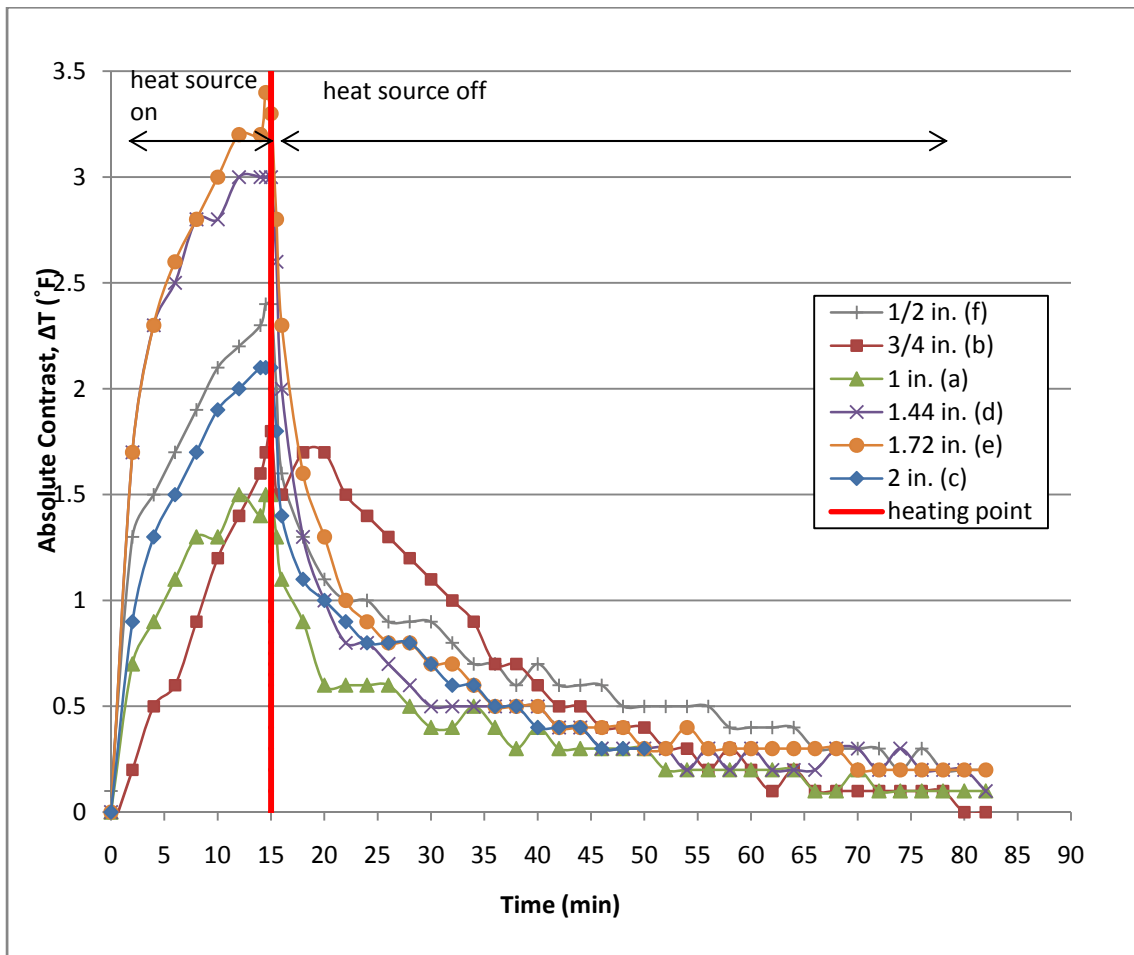


**Figure 5.26 Absolute contrast variations above simulated delaminations in concrete slab IV during an active infrared thermography test.**

The absolute contrast variation for other delaminations located deeper inside Slab IV is slightly different. The absolute contrast value for delaminations placed at  $\frac{1}{2}$ , 1, 1.44, 1.72 and 2 in. under the concrete surface decreased after the heat source was turned off, then the absolute contrast remained constant before decreasing again and did not increase to a higher value. Therefore, the observation time for delaminations placed at  $\frac{1}{2}$ , 1, 1.44, 1.72 and 2 in. were not evident from results obtained from Slab IV.

Thermal infrared images taken at the beginning of the data collection (0 minutes), at the time when the heat source was turned off (15 minutes) and at the times when defects appeared on the thermal infrared images (18, 20, 22 and 26 minutes), are shown in Figure 5.27. Although obtaining the observation time was not possible based on the results of the active infrared thermography testing on Slab IV, it is evident that all delaminations are apparent on thermal infrared images taken between 5 to 15 minutes after the heat source was turned off (20 to 30 minutes after data collection began). Absolute contrast for all delaminations is greater than  $0.5^{\circ}\text{F}$  between 5 to 15 minutes after the heat source was turned off.

Six cores were extracted from Slab IV at the six delaminations locations to investigate the condition of concrete above each delamination and the actual depth of the delamination at which the delamination was placed. Results from these cores are summarized in Appendix D. It was determined from these results that delaminations with the planned depth of  $\frac{1}{2}$ , 1, 1.44, and 1.72 were placed at deeper depths than planned. The actual depths of these delaminations were determined to be 1.5, 1.875, 2.25 and 2.125, respectively. The actual depth of the planned 2 in. deep delamination was determined to be 1.5 in., and delamination located at  $\frac{3}{4}$  in. was the only delamination that was at the same depth as it was planned.

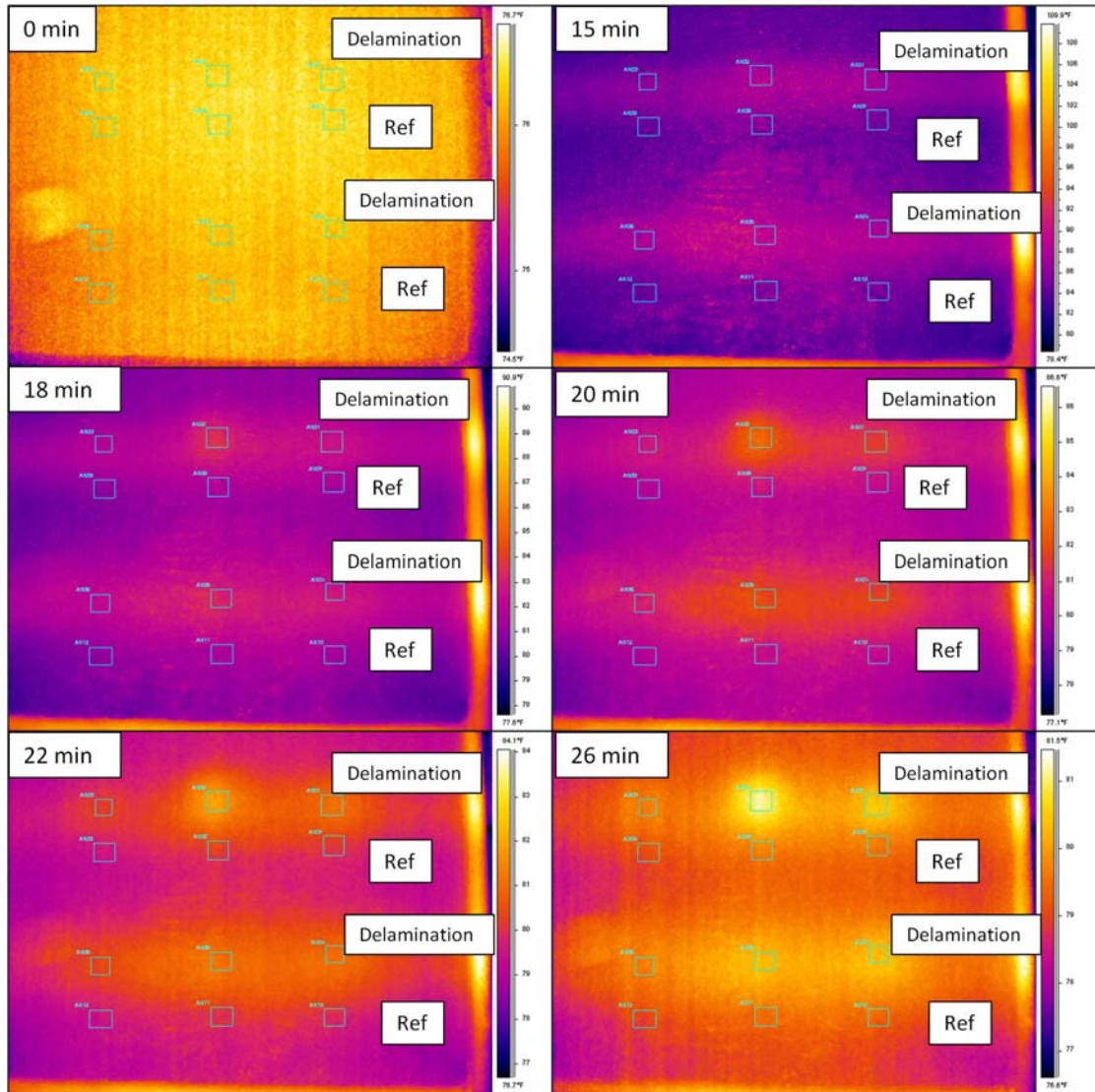


**Figure 5.27 Thermal infrared images of concrete slab IV, shown at 0, 15, 18, 20, 22 and 26 minutes after data collection began.**

### ***5.3.3 Discussion***

The relationship between the depth of the delamination ( $z$ ), the observation time ( $t$ ) and the contrast (absolute contrast or running contrast) was investigated in this phase of the study to achieve a relationship to estimate the depth of the delamination based on the results of an active infrared thermography testing. Although this relationship has been discussed theoretically, no literature was found to discuss this relationship applied to delaminations in concrete.

According to the results obtained in Phase II, it is evident that the time of observation has the linear relationship with the square of the depth of the delamination. Although, results obtained in this phase were limited to the three concrete slabs discussed in this phase, the findings were in agreement with the theoretical construct of the active infrared thermography testing.

Lack of a uniform heating on the concrete slab can be one of the reasons that produced a false alarm in data collection for the delamination located at 1 in. under the surface. However, there was no literature found to discuss the effects of the non-uniform heating method (surface heating method) on concrete slabs. Considering that the surface heating method may be a more practical method than linear heating method in the field, further research is required to prove the possibility of producing an unintentional false alarm due to the non uniform heating of the surface. This false alarm, that was discussed in the results presented for concrete slab IV, was also shown in FRP overlay evaluation conducted by Brown and Hamilton (Brown and Hamilton 2007).

There are several other variables that could have an influence on obtaining a true relationship between the delamination depth and observation time or the change of contrast. The width to depth ratio of defects is one of these variables that is discussed and investigated in detail in Phase III of this study. Other variables that also have an influence on this computation are the thermal conductivity and thermal diffusivity of concrete specimen. Moreover, further signal processing may produce a method to facilitate the estimation of observation time for defects in concrete bridge elements.

After cores were extracted from Slab IV, it was determined that four of the delaminations were placed deeper inside concrete than planned, thereby making the width to depth ratio of these delaminations to be 2 or less. This indicates another reason to prevent identifying the observation time of these delaminations from the absolute contrast variations plots.

## 5.4 Phase III – Discussion on Width to Depth Ratio of Delaminations

Phase III of the laboratory studies on concrete slabs was conducted with the objective of investigating the effects of the width to depth ratio of the delamination on conducting an infrared thermography test on a concrete bridge element. This concept was discussed in section 3.2.4. Based on the literature review, the ratio of the square root of the delaminated area to the depth of the delamination (Equation 11) should be greater than 2 for that delamination to be detectable with infrared thermography testing (Vavilov and Taylor 1982). In this phase, a pulsed (active) infrared thermography test was conducted on a concrete slab with simulated delaminations using square shaped Styrofoam blocks. The ratio of the square root of the defect area to the depth for the delaminations placed in Slab III was 6, 3, 2 and 1 for the 6 in. x 6 in. and 3 in. x 3 in. delaminations (Table 5.7).

**Table 5.7 Width to depth ratios for delaminations in slab III**

Delamination size	Delamination Depth	Width to depth ratio
3 in. x 3 in.	1 in.	3
3 in. x 3 in.	3 in.	1
6 in. x 6 in.	1 in.	6
6 in. x 6 in.	3 in.	2

### *5.4.1 Methodology of Data Collection and Processing*

Data was collected on Slab III 34 days after construction. The test set-up was similar to the test set-up in Phase I, using the 1500W infrared heater. The infrared heater was placed at a normal angle and a distance of 3.5 ft from the test specimen. The camera was placed at a distance of 5.5 ft from the specimen. The infrared heater and the camera were installed such that the heater was not in the field of view of the camera and did not affect the thermal image collection. The thermal IR camera was set up to collect images at 30 seconds intervals throughout the test. Intervals of 30 seconds were selected to assure constant monitoring and to avoid interruptions due to the auto focus set-up of the camera. The infrared heater heated the slab for 15 minutes. Data collection continued for about 35

minutes after the heater was turned off. The ambient temperature was 75°F and ambient humidity was 25% in the laboratory at the time of data collection.

The active infrared thermography test set-up for Slab III was shown in Figure 5.28. Similar to the previous phases, temperature variation on the surface of this slab is monitored during the test using the ThermoCAM Researcher Professional Software.

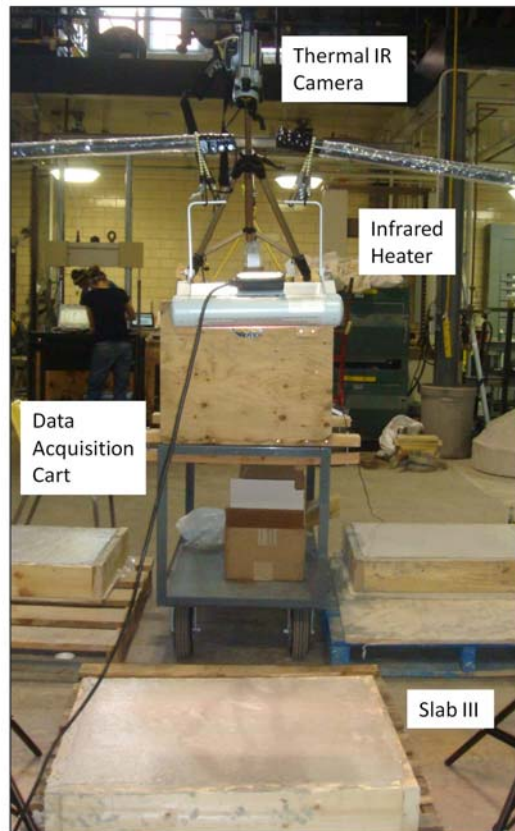


**Figure 5.28** Active infrared thermography test set-up for slab III using an infrared heater.

#### ***5.4.2 Results and Analysis***

Similar to the processing method in Phase I, approximate locations of the four simulated delaminations in this concrete slab were identified and average temperature above each delamination was obtained using the ThermoCAM Researcher Professional software. A plot of variation in surface temperature above each delaminated area during the test

period was obtained based on the average temperature above each delaminated area. The plot of the surface temperature variation for the four delaminated areas in concrete Slab III is shown in Figure 5.29. Comparing the average surface temperature change for the two delaminations located at 1 in. depth shows that the average surface temperature above the larger delamination (6 in. x 6 in. x 3/8 in.) is higher than the average temperature above the smaller delamination (3 in. x 3 in. x 3/8 in.) after 40 minutes from the beginning of the data collection (35 minutes after the heater was turned off).

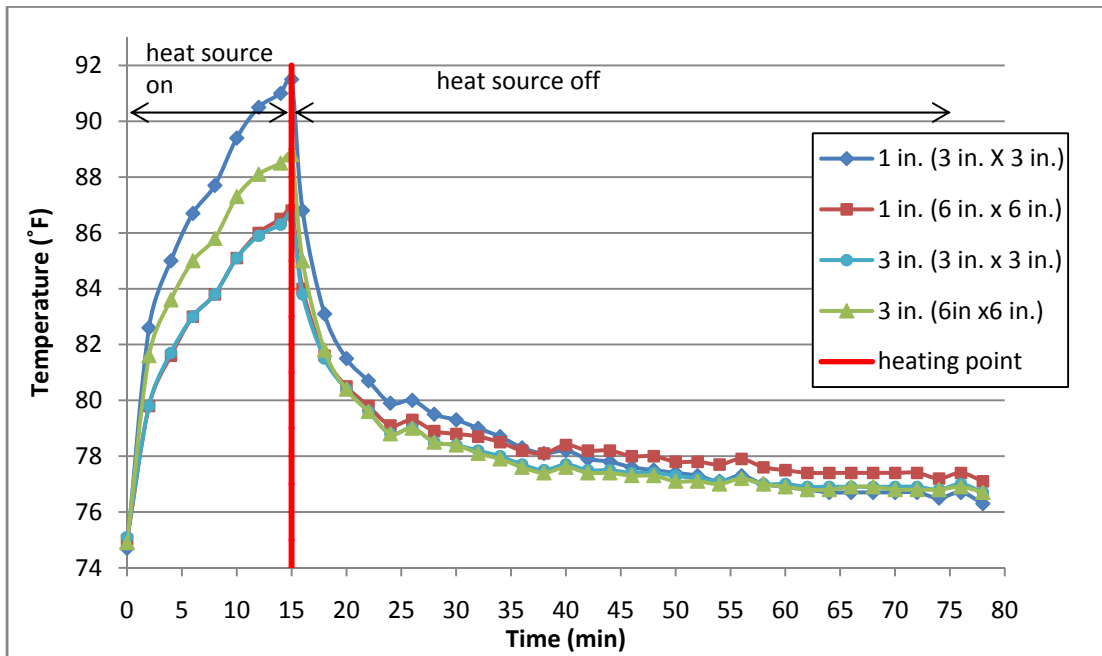


**Figure 5.29 Temperature variation in an active infrared thermography test on Slab III.**

The absolute contrast variation plot for the four delaminations in Slab III is shown in Figure 5.30. It can be seen from this graph that delaminations located 3 in. deep did not have enough contrast after the heater was turned off to appear on the thermal infrared images. The high contrast values of the 6 in. x 6 in. delamination placed at 3 in. deep during the 15 minutes heating period are likely due to the reflection from the concrete slab and do not reveal information regarding the location and size of the delamination inside the concrete slab. Moreover, it has been noted from comparing the graphs of absolute contrast change for the two delaminations located at 1 in. from the concrete

surface that the delamination with the smaller area lost contrast much faster than the larger delamination. In fact, 27 minutes from the time at which heating was stopped (42 minutes after the data collection began), the larger delamination at 1 in. depth appeared on the thermal infrared image with higher contrast compared to the smaller delamination.

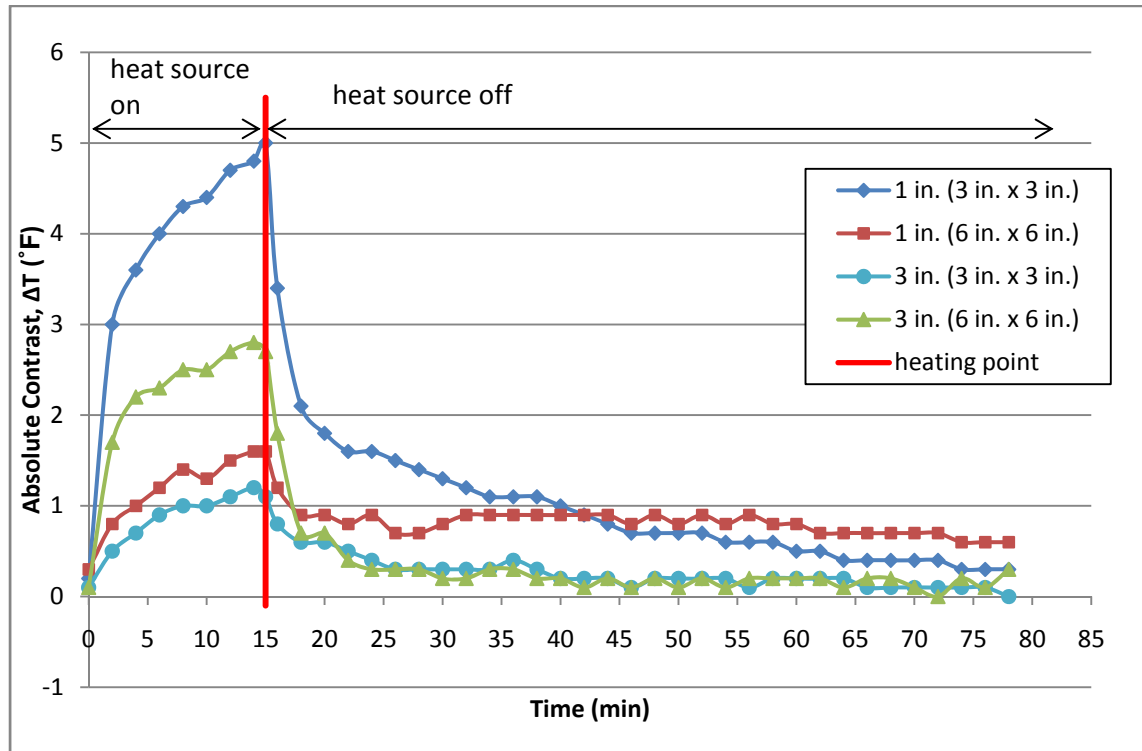


**Figure 5.30 Absolute contrast variations above simulated delaminations in slab III during an active infrared thermography testing.**

The average temperature values and absolute contrast values, in Figure 5.29 and Figure 5.30, are presented at 2 minutes intervals, while data was collected from the concrete slab at 30 seconds intervals. Collecting thermal infrared images with 30 seconds intervals prevents having missing data points in the data set due to the auto focus setting of the thermal IR camera.

Figure 5.31 shows the thermal infrared images taken from Slab III at 15, 32, 42, and 60 minutes after the beginning of the data collection. The heat source was turned off 15 minutes after the start of data collection. Thus, these discrete times also indicate 0, 17, 27, and 45 minutes after the heater was turned off.



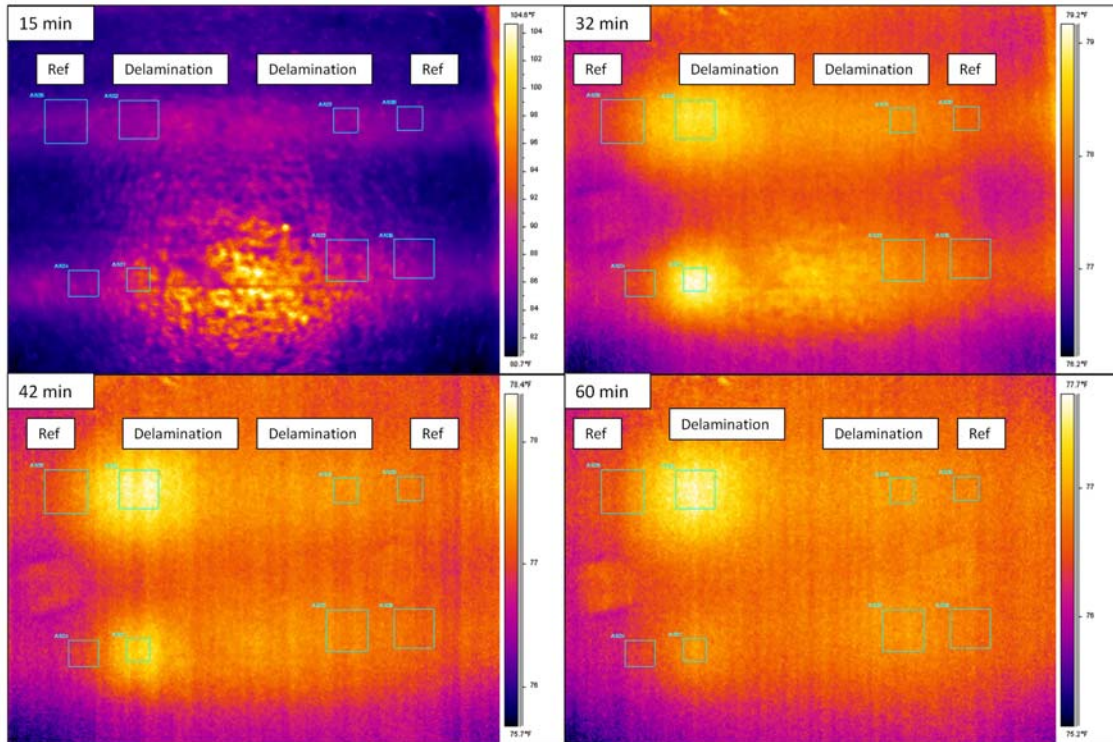


**Figure 5.31 Thermal infrared images obtained from an infrared thermography testing on the concrete slab III, shown 15, 32, 42, and 60 minutes after the beginning of the data collection.**

It is noticeable from the thermal infrared images and the plot of the absolute contrast change that captured a thermal infrared image of the concrete slab 17 minutes after heating was stopped reveals a more apparent image of the location and size of the delaminations.

### ***5.4.3 Discussion***

Phase III investigated the influence of the width to depth ratio of delaminations on the results obtained from an active infrared thermography test. The width to depth ratio for simulated delaminations placed in Slab III were 1 (for 3 in. x 3 in. delamination at 3 in. depth), 2 (for 6 in. x 6 in. delamination at 3 in. depth), 3 (for 3 in. x 3 in. delamination at 1 in. depth), and 6 (for 6 in. x 6 in. delamination at 1 in. depth). Figure 5.31 shows that delaminations with the width to depth ratio of 3 and 6 were detected using active infrared

thermography while delaminations with the width to depth ratio of 1 and 2 are not clearly evident in the thermal infrared images taken from Slab III.

The primary reason to select the sizes of 3 in. x 3 in. and 6 in. x 6 in. delaminations was to be able to classify delaminations based on AASHTO limit for identifying areas of condition state 2 or condition state 3. Based on the AASHTO Guide Manual for Bridge Element Inspection (AASHTO 2011) the depth of 1 in. and diameter of 6 in. are the thresholds for identifying the proper condition state. A previous passive infrared thermography study on concrete slabs showed that there is a potential for passive infrared thermography to detect larger delaminations (24 in. x 24 in.) at 2.5 in. depth (Kee et al. 2012). Note that this size delamination is expected to appear with active infrared thermography because the width to depth ratio was 9.6, which is significantly larger than 3 as was detected in Phase III, and greater than 2 as predicted with theory.

Comparing the results of Phase III to Phase I shows that although the width to depth ratio plays an important role in the ability to detect delaminations in concrete slabs, the depth of the delamination itself is an important factor that has to be considered. In Phase I, delaminations (3 in. x 3 in. x 3/8 in.) placed at 2 in. depth, with a width to depth ratio of 1.5 were detected using an active infrared thermography test. However, in Phase III of this experimental study, the large delaminated area (6 in. x 6 in.) placed at a 3 in. depth had a width to depth ratio of 2, yet the contrast associated with this delamination was so low (lower than 0.5°F) that it could not be identified on thermal infrared images taken of the slab.

The current study provides evidence to show that the width to depth ratios of delaminations that can be detected by active infrared thermography are generally equal to or greater than 2. While this limit can be used as a recommended threshold for the application of active infrared thermography, further study is required to investigate the possibility of detecting delaminations with the same width to depth ratio, which are placed at different depths inside the concrete slab and to establish a guideline for detecting delaminations at different depth using infrared thermography.

Another interesting remark that can be observed from Figure 5.29 and Figure 5.30 is that larger delaminations hold the heat for a longer period of time than smaller size delaminations. The maximum absolute contrast for the 6 in. x 6 in. delamination placed at a 1 in. depth occurred 32 minutes after the beginning of data collection and remained approximately the same for about 24 minutes before it dropped to a lower value 56 minutes after the beginning of data collection. This indicates that the size of the delamination is an important factor to be considered in establishing a time window for the concrete bridge element inspection after turning off the heat source.

Four cores were extracted from Slab III to determine the actual depth of the delamination at each location and to investigate the concrete condition with in the layer of concrete above each delamination. Results of this coring test are summarized in Appendix D. It was found out that the actual depth of the shallower 6 in. x 6 in. delamination was at 1.75 in. instead of 1 in. and the actual depth of the shallower 6 in. x 6 in. delamination was at 1.25 in. instead of 1 in. This fact clarifies the delay in the observation of the 6 in. x 6 in. delamination compared to the 3 in. x 3 in. delaminations. The observation times and the actual depth of the two observed delaminations on Slab III were added to the linear regression graph for  $t$  and  $z^2$  from Figure 5.22 (Figure 5.32). The observation time for 6 in. x 6 in delamination was at 17 minutes and the observation time for 3 in. x 3 in. delamination was at 7 minutes after the heat source was turned off.

The linear regression line obtained from the combined results of observed delaminations in Slabs A, I and III is shown in Figure 5.32. It can be seen that the square of the coefficient of correlation is 0.94, which still confirms the given linear relationship is a good fit between the observation time and the depth of the delaminations.

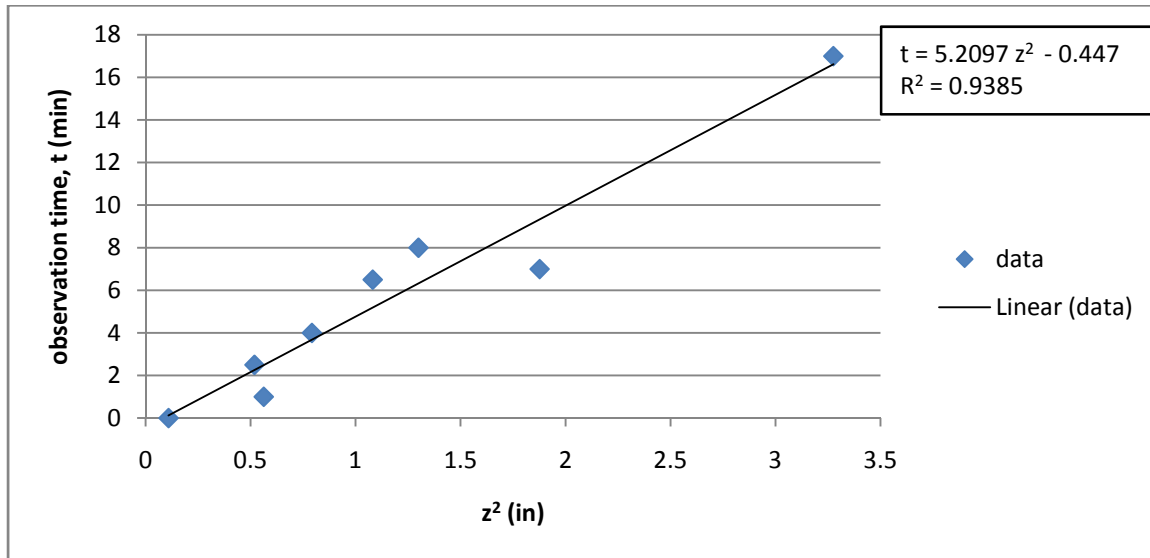


**Figure 5.32 Observation time versus the depth squared of each observed delamination in Slab A, I and III.**

The absolute contrast and the running contrast for the two observed delaminations in Slab III was also added to the linear regression relationship between the contrast and the inverse of the cubic depth discussed in 5.3.2.1. It can be seen from the two graphs presented in Figure 5.33 and Figure 5.34 that the  $R^2$  values were remained close to 0.84 and 0.83 which confirms the linear relationship. However, there exists the lack of data points for the values of  $1/z^3$  between 2.4 and 8, representing depths between  $\frac{3}{4}$  in. and  $\frac{1}{2}$  in.

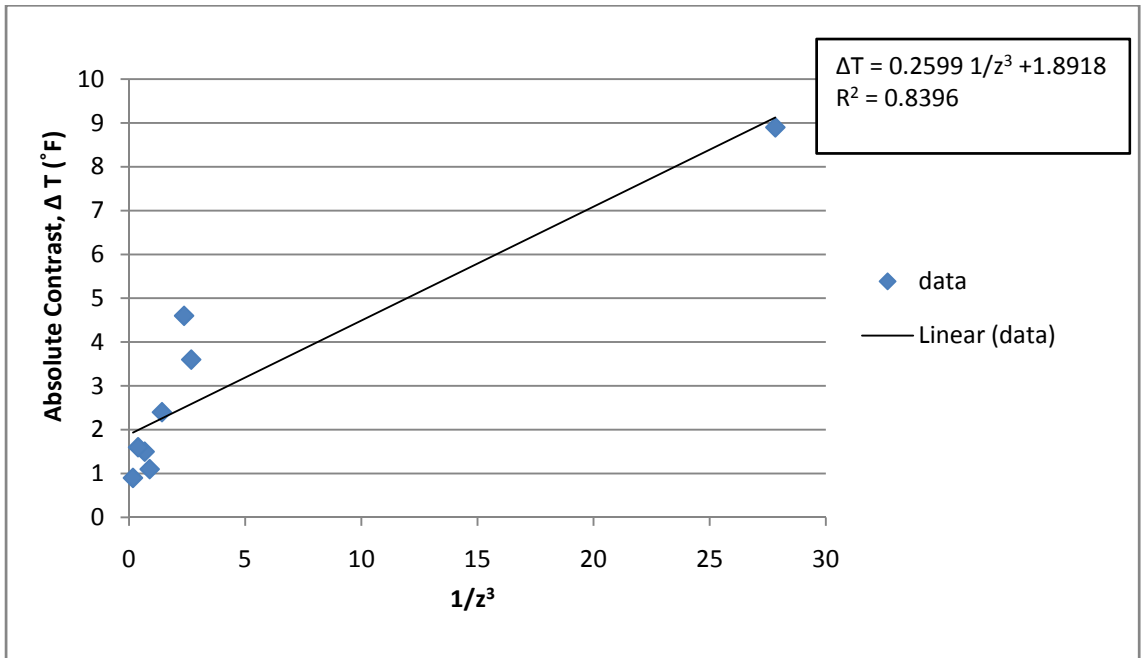


**Figure 5.33 Absolute contrast versus the inverse of the depth cubed for Slabs A, I and III.**

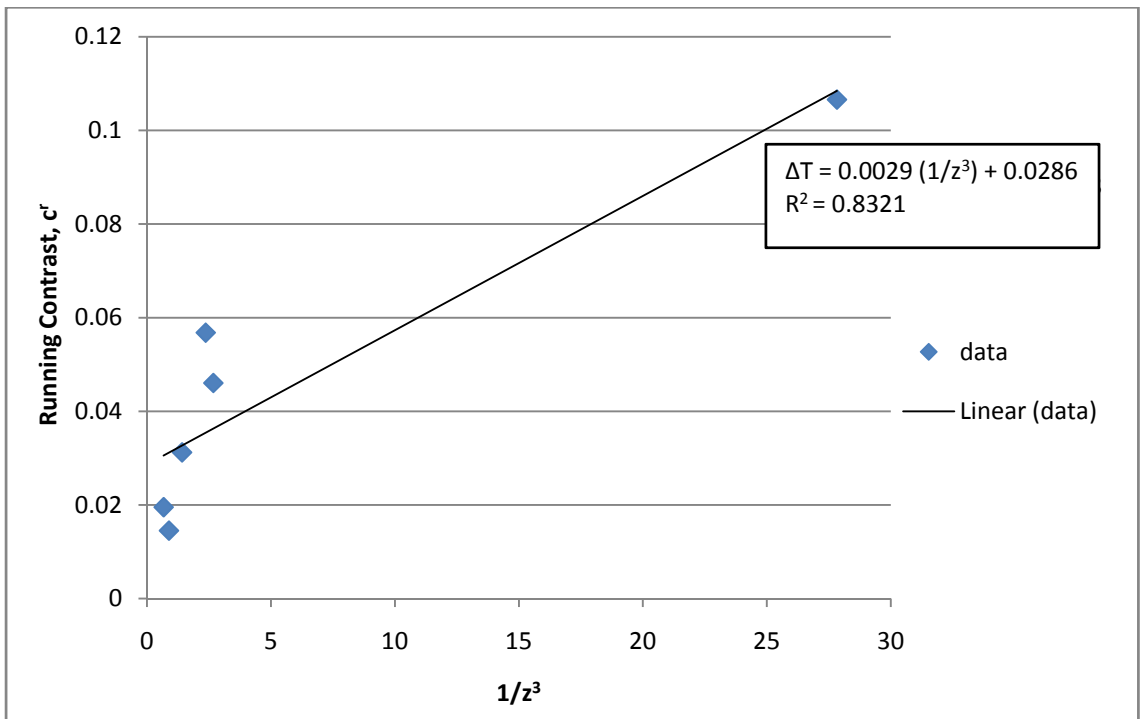


**Figure 5.34 Running contrast versus the inverse of the depth cubed for Slabs A, I and III.**

## 5.5 Infrared Thermography on Concrete Slab II

The results obtained from an active infrared thermography test on Slab II illustrate one of the reasons for hesitation yet in declaring active infrared thermography as a practice-ready NDT tool for bridge inspection. Active infrared thermography was deployed on this concrete slab using the same method to what was presented previously in phase II for slabs I and IV. Slab II was heated for 15 minutes using an infrared heater and thermal infrared images of the concrete slab were collected at 30 seconds intervals. The only delamination that was detected was the ½ in. deep delamination. Although it was expected that the other delaminations located at 1, 1.5, 2 and 2.5 in. depths in this concrete slab would be detectable, there were no indication of any other delaminations in this concrete slab. Figure 5.35 shows the thermal infrared images in an active infrared thermography test on concrete slab II which was conducted 45 days after the slab was constructed.

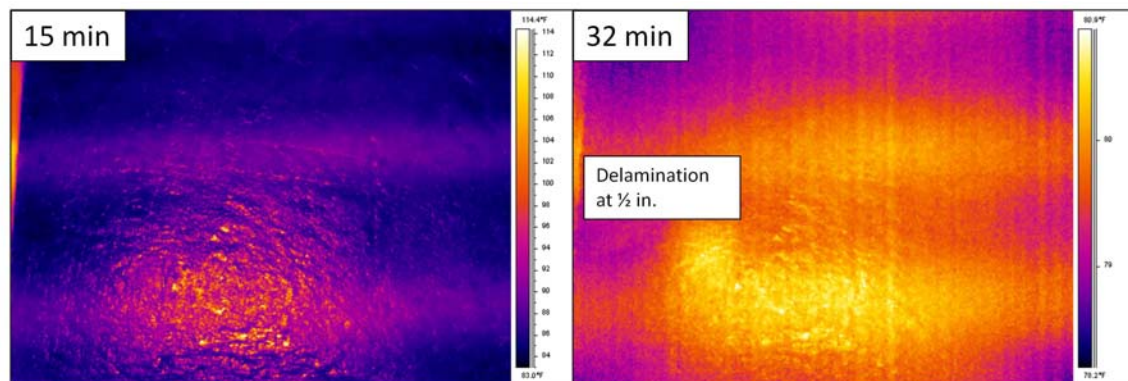


**Figure 5.35 Thermal infrared images obtained from an active infrared thermography test, shown 15 minutes after data collection began (when the heat source was turned off) and 32 minutes after data collection began.**

To further investigate the infrared thermography test on Slab II, passive infrared thermography was conducted on this specimen. Slab II was placed outside overnight and remained outside to be exposed to sunlight and the ambient temperature change. Thermal infrared image was taken from slab at 1:24 pm (see Figure 5.36), when it was expected to see the delaminations that were placed in the slab. Ambient temperature at the time of

data collection was 91.2°F and humidity was 51%. The lowest temperature at night was recorded as 61°F. The result from passive infrared thermography was similar to the active infrared thermography testing. The only delamination that showed some indications on the thermal infrared image was the delamination located at ½ in. depth from the concrete surface.

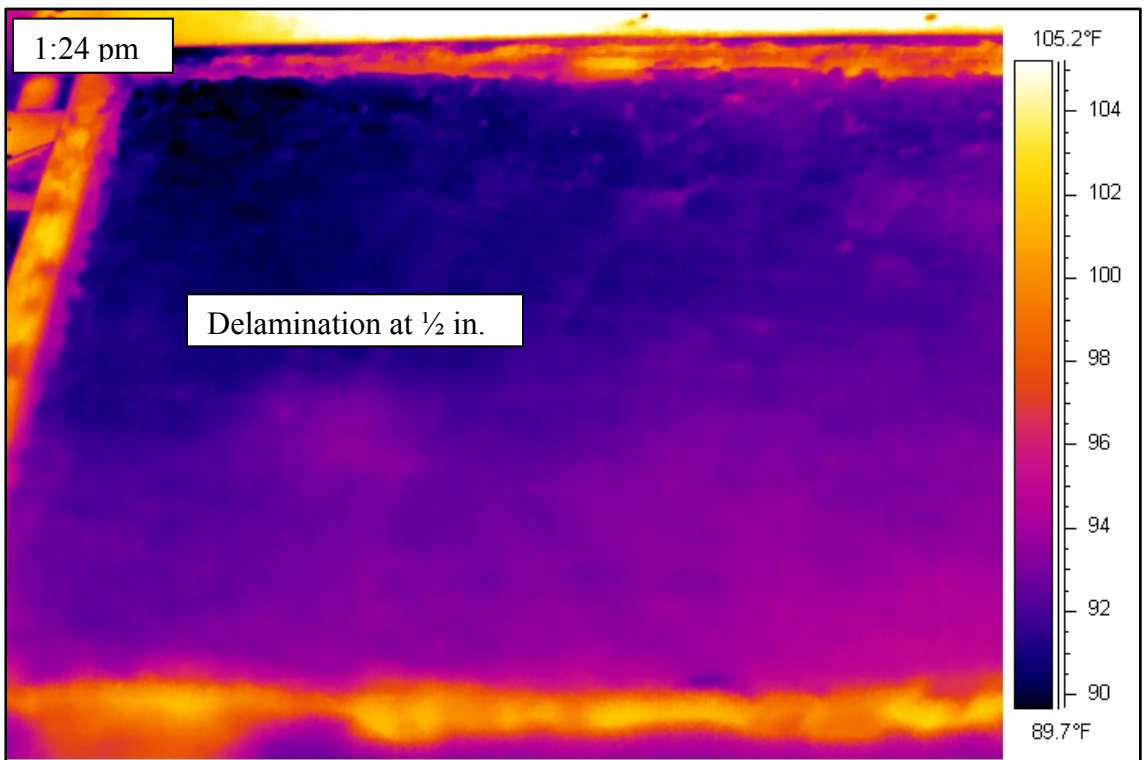


**Figure 5.36 Thermal infrared image obtained from a passive infrared thermography test on Slab II.**

After infrared thermography was conducted on Slab II, the timber forms were removed from the sides of the slab. As it can be seen in Figure 5.37, poor consolidation was observed at the edges of this slab.



**Figure 5.37 Slab II after the timber form was removed.**

Six cores were then extracted from six locations of delaminations to investigate the concrete condition above delaminations and relative location of delaminations inside the concrete. Results from this coring test are summarized in Appendix D. It has been determined from cores that the actual location for delamination that can be seen on the thermal infrared image is at  $1\frac{1}{2}$  in. from the top surface of the concrete slab and other five delaminations were all located deeper than  $2\frac{1}{4}$  in., which made them undetectable on the thermal infrared image.

## **5.6 Summary**

This chapter presents results obtained from active infrared thermography testing and confirms that the active infrared thermography technique has the potential to be used for condition assessment of concrete bridge elements. In this chapter, active infrared thermography tests were conducted on five concrete slabs using the surface heating method and a 1500W infrared heater. Based on the results obtained herein, for a 15 minute heating period, the best time to collect data is within the 15 minute period after the heat source was turned off. Achieving the highest contrast at a given time for each delamination depends on the depth of the delamination; in other words, shallower delaminations appear sooner on the thermal infrared images compared to the deeper ones. However, contrast for all delaminations appeared within 15 minutes after heating was stopped.



A summary of slab data is presented in Table 5.8 and includes data from cores extracted from all 24 locations of simulated delaminations. The depth of the delamination obtained from the coring test is presented in two columns. The average depth implies the average of the three measurements of depth on the concrete core at the three different locations using a micrometer with 0.01 in. accuracy. The smallest depth is the smallest of the three measured depths on the concrete core and represents the shortest distance to the delamination from the surface at which thermal infrared data was collected. Detectable delaminations in this table are based on the ability to detect the delamination on the thermal infrared images taken from the slab. Observation time from the absolute contrast plots could only be obtained for eight detected delaminations as discussed previously in Figure 5.32.

Results presented in Table 5.8 confirmed that delaminations with a depth greater than 2 in. were not detected by the active infrared thermography test conducted herein. All delaminations with the depth less than or equal 2 in. and the width to depth ratio of greater than 2 were detectable, except when the poor consolidation was present. For slab I, III and A all delaminations with the width to depth ratio of greater than 2 were detected and observation time could be obtained. The width to depth ratio for Slab A was determined using the smallest side dimension of the simulated delamination. Poor consolidation issues with concrete were observed at some of the core locations on Slab II and IV and indicate the discrepancy on the results obtained on these slabs.

**Table 5.8 Coring results obtained from concrete slabs**

Core No.	Size (in. x in.)	Planned Depth	Actual Depth Determined by Coring (in.)		Planned Width to Depth Ratio	Actual Width to Depth Ratio (in.)		Detected by Thermal IR Image	Observation Time ( $\Delta T - t$ Plot)	Notes
			Smallest	Avg.		smallest	Avg.			
I-a	3 x 3	2.0	0.94	1.04	1.50	3.19	2.89	√	6.5	
I-b	3 x 3	3.0	2.02	2.20	1.00	1.49	1.36	×	N/A	
I-c	3 x 3	1.0	0.71	0.72	3.00	4.25	4.16	√	2.5	
I-d	3 x 3	2.0	1.03	1.14	1.50	2.90	2.64	√	8	
I-e	3 x 3	3.0	2.02	2.13	1.00	1.49	1.41	×	N/A	
I-f	3 x 3	1.0	0.59	0.75	3.00	5.11	3.98	√	1	
II-a	3 x 3	2.0	2.55	2.72	1.50	1.18	1.10	×	N/A	Poor consolidation at the bottom of the delamination.
II-b	3 x 3	3.0	3.26	3.34	1.00	0.92	0.90	×	N/A	Poor consolidation at the bottom of the delamination.
II-c	3 x 3	2.5	2.90	2.95	1.20	1.04	1.02	×	N/A	
II-d	3 x 3	0.5	1.10	1.27	6.00	2.73	2.36	√	N/A	Poor consolidation on the top of the delamination.
II-e	3 x 3	1.5	2.34	2.37	2.00	1.28	1.27	×	N/A	
II-f	3 x 3	1.0	2.38	2.43	3.00	1.26	1.24	×	N/A	
III-a	6 x 6	1.0	1.88	1.92	6.00	3.19	3.12	√	17	
III-b	3 x 3	3.0	2.43	2.96	1.00	1.24	1.01	×	N/A	
III-c	3 x 3	1.0	1.28	1.37	3.00	2.34	2.19	√	7	
III-d	6 x 6	3.0	3.02	3.18	2.00	1.99	1.89	×	N/A	
IV-a	3 x 3	1.0	1.78	1.81	3.00	1.68	1.66	×	N/A	Poor consolidation at top and bottom.
IV-b	3 x 3	0.75	0.86	1.03	4.00	3.50	2.91	√	N/A	Questionable consolidation.
IV-c	3 x 3	2.0	1.40	1.46	1.50	2.15	2.06	√	N/A	Questionable consolidation.
IV-d	3 x 3	1.44	2.31	2.36	2.08	1.30	1.27	×	N/A	Poor consolidation at top and bottom.
IV-e	3 x 3	1.72	2.04	2.15	1.74	1.47	1.39	√	N/A	Poor consolidation at top and bottom.
IV-f	3 x 3	0.5	1.67	1.92	6.00	1.80	1.57	√	N/A	Poor consolidation at top and bottom.
A- F2	2.5 x 6	2.0	0.23	0.33	1.25*	10.8	7.66	√	0	
A- F1	2.75 x 6	2.0	0.82	0.89	1.38*	3.37	3.10	√	4	

N/A = Observation time was not seen for absolute contrast data

√ = yes, × = no

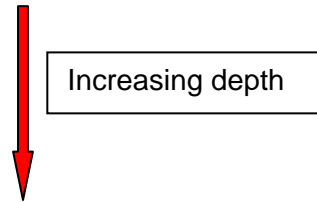
\* Width used to calculate the width to depth ratio is based on the smallest dimension of simulated delaminations.

Table 5.9 shows the relative order of the depth information that could be obtained for each slab based on the temperature variation plots (T-t) and the absolute contrast plots ( $\Delta T-t$ ) at the time when heater was turned off. It can be seen that the relative order of the depth for delaminations could be accurately estimated for Slabs I, III, A and delaminations b and c on Slab IV. Delaminations e and f were affected by poor consolidation on Slab IV. Also, delaminations c and f in Slab I have a difference of 0.03 in., and can be considered equal for practical purposes.

**Table 5.9 Relative order of the depth in Slabs I, III, IV and A**

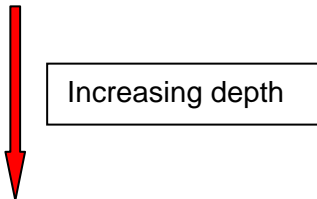
Depth order in slab I

Planned	T-t	$\Delta T-t$	actual
c (1 in.)	f	f	c (0.72 in.)
f (1 in.)	c	c	f (0.75 in.)
a (2 in.)	a	d	a (1.04 in.)
d (2 in.)	d	a	d (1.14 in.)



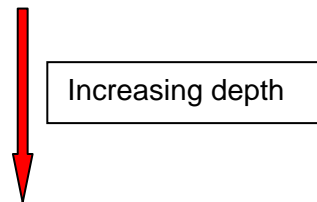
Depth order in slab III

Planned	T-t	$\Delta T-t$	actual
c (1 in.)	c	c	c (1.37 in.)
a (1 in.)	a	a	a (1.92 in.)



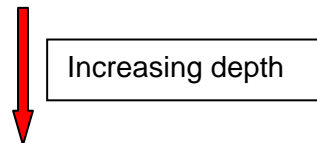
Depth order in slab IV

Planned	T-t	$\Delta T-t$	actual
f (0.5 in.)	e	e	b (1.03 in.)
b (0.75 in.)	b	f	c (1.46 in.)
e (1.72 in.)	f	b	f (1.92 in.)
c (2 in.)	c	c	e (2.15 in.)



Depth order slab A

Planned	T-t	$\Delta T-t$	actual
F2	F2	F2	F2 (0.33 in.)
F1	F1	F1	F1 (0.89 in.)



Moreover, the present data implies that the depth of each delamination can be estimated based on the relationships between the observation time, the temperature difference and the depth. However, further study of more samples is recommended to achieve a more accurate estimation of this relationship. One of the important factors that has to be considered in any infrared thermography testing and depth estimation is the size of the delamination that is being detected by infrared thermography, and as such, these relationships do not hold true for delaminations with a width to depth ratio of less than 2.

Coring test on these slabs produced interesting results regarding the depth to width ratios and depths at which delaminations can be detected using this active infrared thermography method. Cores extracted from Slabs I, III, and A confirmed the actual depth of the delaminations in these slabs and graph obtained from the active thermography (see Figure 5.32) proved the linear relationship between the square of the depth and the observation time for eight delaminations. Based on this linear relationship and a given value for observation time, the unknown depth for a delamination can be determined, provided that the delamination is less than 2 in. deep and the width to depth ratio is greater than 2.

## **Chapter 6 Silverbell Bridge Beam Study using Active Infrared Thermography**

The active infrared thermography technique was used to assess the condition of a segment of an out-of-service prestressed box beam bridge. This prestressed box beam segment was salvaged after the Silverbell Bridge demolition in Oakland County, Michigan in 2011. The beam segment was stored at the Road Commission for Oakland County (RCOC) facility until October 2012, when it was transferred to the Michigan Tech Cement and Concrete Research Facility. The active infrared thermography testing procedure and results obtained from deployment on this salvaged beam are presented in this chapter.

### **6.1 Specimen and Equipment Set-Up**

#### ***6.1.1 Thermal Infrared Camera and Heat Source***

The thermal infrared camera used during an active infrared testing on the Silverbell Bridge segment was the FLIR ThermaCAM SC 640 that was used previously during the experimental studies discussed in Chapter 5. The field of view of this camera allows for capturing approximately a 2 ft x 2.5 ft area of the beam in each image. Considering that this beam had a depth of 39 in., only a portion of it could be captured in each image.

A 1500W Infrared heater was used as the external heat source for conducting active infrared thermography on the Silverbell Bridge beam. The heat source was previously used for conducting the active infrared thermography tests on concrete slabs, discussed in Chapter 5 of this dissertation.

#### ***6.1.2 Silverbell Bridge Prestressed Box Beam***

Silverbell Bridge was built in 1981, crossing over the GTW railroad in Oakland County, MI. This bridge had a length of 221.8 ft and a width of 64.3 ft. Average daily traffic

(ADT) on this bridge in 2006 was 13,320. The bridge consisted of three spans with beams lengths of 73 ft-2¾ in. Each span was comprised of 20 adjacent prestressed box beams 36 in. wide and 39 in. deep (AASHTO BIII-36). These beams were post-tensioned in the transverse direction with three post-tensioning tendons in the middle of each span and two tendons at each end. The riding surface consisted of a 3 in. latex modified concrete overlay with no water proofing membrane between the concrete overlay and box beams. Only the reinforcement, used in the sidewalks and parapets, were epoxy coated. The bridge had a skew of 42°. Silverbell Bridge was demolished and replaced in February of 2011 due to the severe deterioration of the prestressed box beams. Figure 6.1 shows the location and orientation of this bridge before it was demolished. Figure 6.2 and Figure 6.3 show the prestressed concrete box beam cross section and Figure 6.4 shows the relative location of the bridge beams and post-tensioning tendons. Clear concrete cover over the stirrups to the sides of the box-beam was 2¼ in. and clear cover of the stirrup to the bottom surface of the box beam was around 1¾ in.

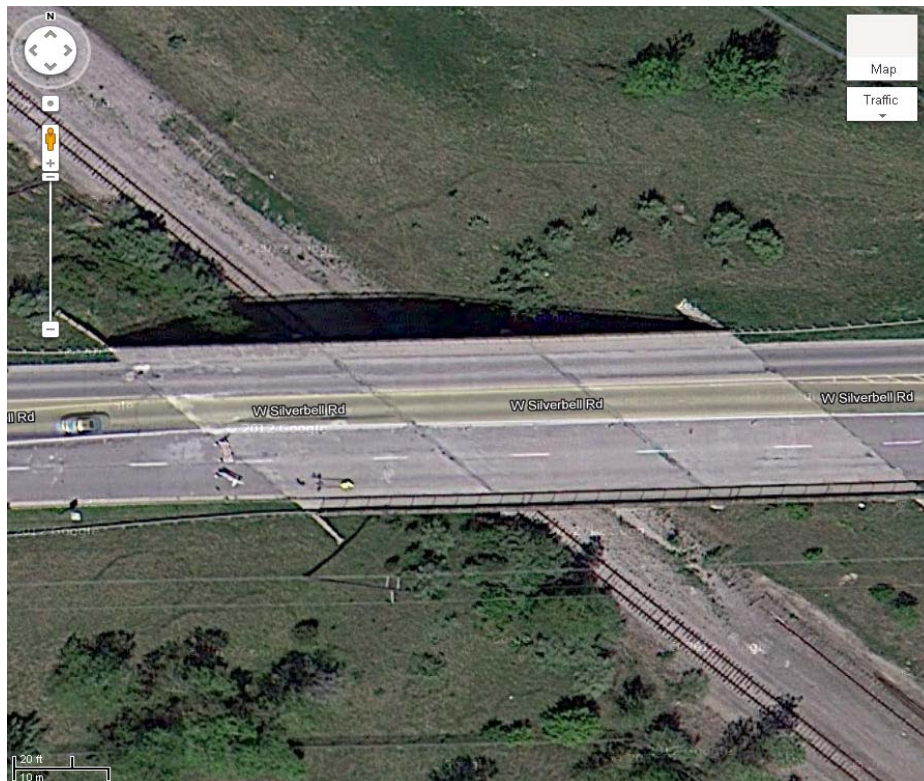


**Figure 6.1 Orientation of the Silverbell Bridge.**

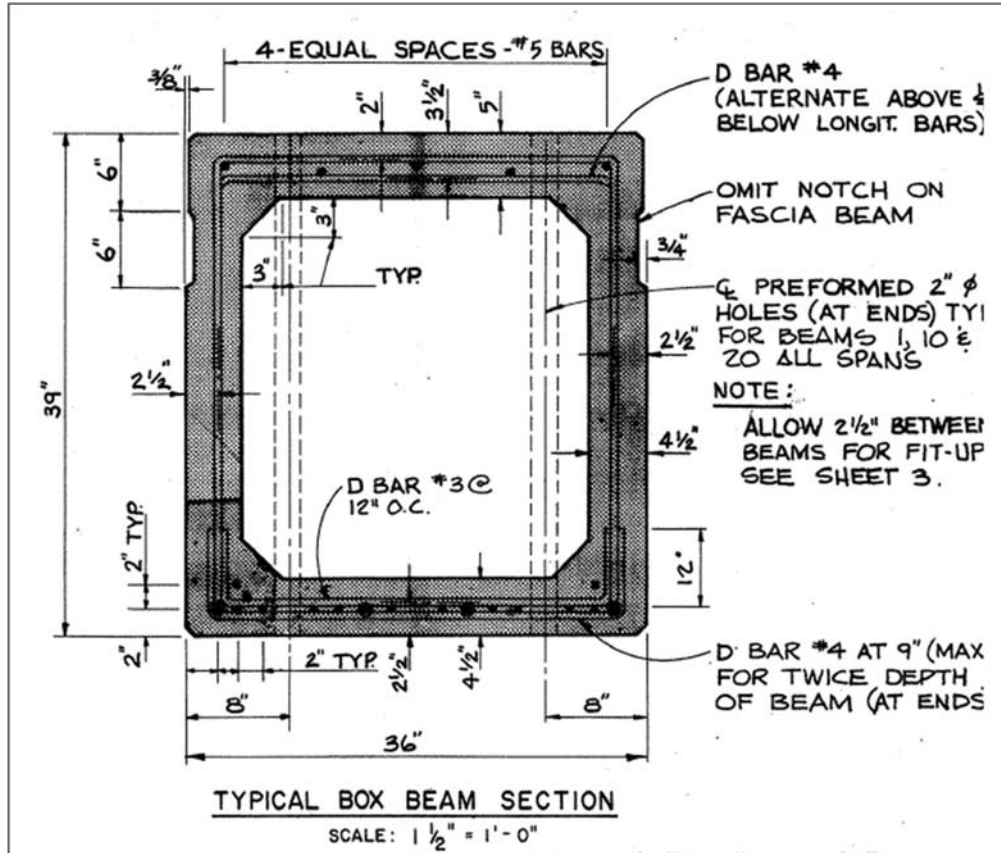


Figure 6.2 Silverbell Bridge box beam cross section.

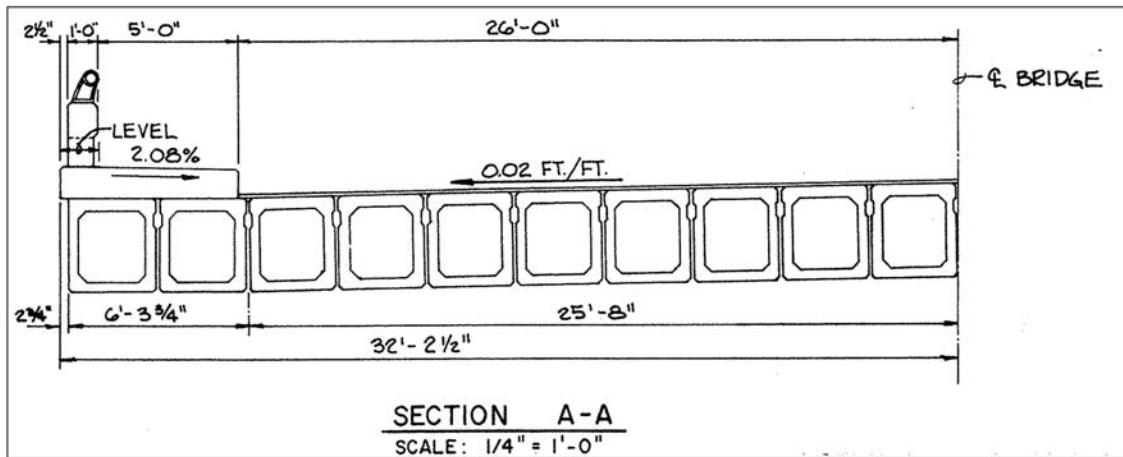


Figure 6.3 Cross section of Silverbell Bridge box beams.

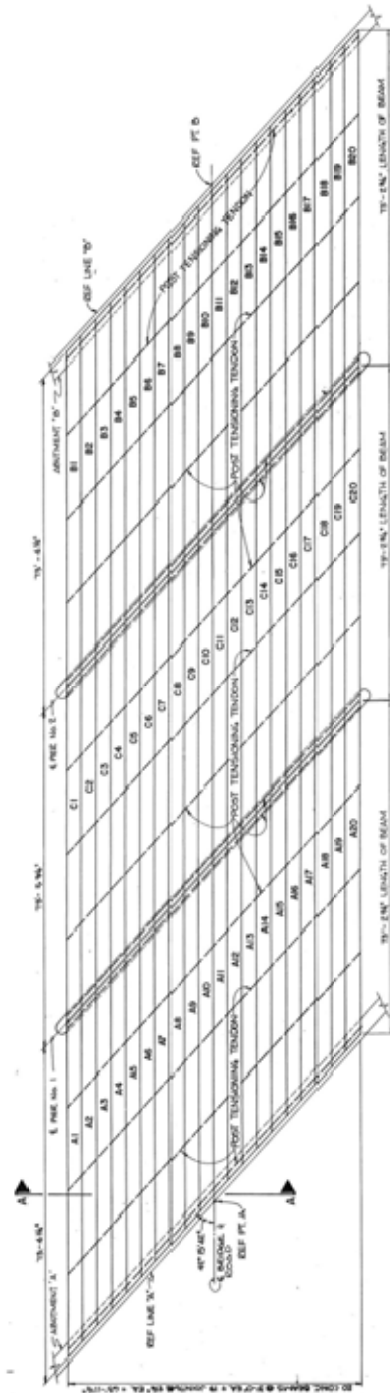


Figure 6.4 Silverbell Bridge box beam plan.



A bridge inspection conducted in March 2010 rated the bridge deck surface as 4 on the NBI scale (Bridge inspection reports are included in Appendix B). Severe longitudinal reflective cracks were observed on the bridge deck (up to 5 in. wide) and in some locations cracks had turned to deep spalls with surrounding delaminations. Adjacent box beams prevented inspection of the underside of the bridge deck. Leaching from the joints was also observed at some locations. The overall superstructure of this bridge was rated as a 2 on the NBI scale, which indicates a very poor condition bridge. Broken strands, exposed rebar, and severe spalls and delaminations on several box beams were observed during the inspection. Two lanes on this bridge were closed due to the severe deterioration of superstructure and pier caps. Figure 6.5 shows the condition of the Silverbell Bridge in April 2010.



**Figure 6.5 Silverbell Bridge deck and superstructure in April 2010.**

A 23 ft segment of this bridge was saved after demolition for future nondestructive testing study. This segment is shown in Figure 6.6 as it was stored in RCOC facility and before being transferred to Michigan Tech in October 2012. Figure 6.7 showed the placement of this bridge segment in the laboratory.



**Figure 6.6 Silverbell Bridge beam in Road Commission Oakland County facility (west face shown).**

This segment of the beam contains two post-tensioned tendons and has moderate delamination and spalling along the edges and on the sides. Hammer sound testing was conducted on the beam to determine the delaminated areas prior to active infrared thermography testing. Delaminated areas were detected on the sides but not at the bottom surface. No delamination was detected on the top side of the beam using the hammer sounding method. However, there was narrow transverse cracking noted on the concrete overlay on the top of the box beam toward the south side (direction is based on the placement of the beam in the laboratory.), and a wide longitudinal crack on the top side of the beam.



**Figure 6.7 Placement of Silverbell Bridge in the Michigan Tech laboratory.**

## **6.2 Methodology of Data Collection and Processing**

Active infrared thermography testing was carried out on seven locations of the box beam. These locations were selected based on the results of both the hammer sounding and visual inspection of the beam, and are shown in Figure 6.8 and Figure 6.9. In some locations, more than one delaminated area was detected. Directions on these figures are based on the orientation and placement of the beam in the laboratory, with the skewed end pointing north.

The same method of data collection used in Chapter 5 for the concrete slabs was used on the prestressed box beam. The heat source was placed at 3.5 ft distance from the beam and the camera collected images at a distance of 5.5 ft. The test set-up at each location on the beam is included in Appendix C.

The heater warmed up the concrete beam for 15 minutes and thermal infrared images were collected for about an hour, including the heating period. The selected thermal infrared images taken from each location are included in each associated section. The first image taken at the very beginning of the test (0:00) is right before the heater was turned on and the next image was taken 30 seconds after data collection began (0:30), when the infrared heater was running. The infrared heater was turned off 15 minutes after data collection began and the rest of the images were taken when the heater was off.

Graphs showing the variation of average temperature and the time of data collection were obtained for each location with possible delaminated areas. The depth of each delamination was estimated based on the results obtained from the active infrared thermography testing.

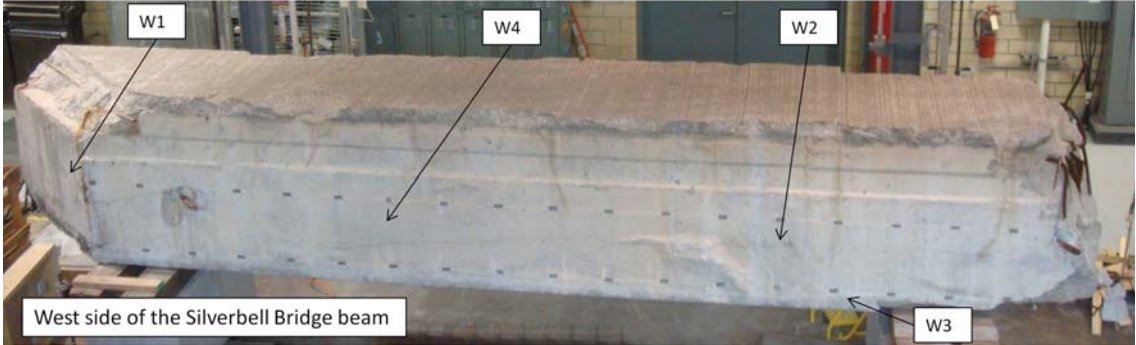


**Figure 6.8 West side of the Silverbell bridge beam.**



**Figure 6.9 East side of the Silverbell Bridge beam.**

The same data processing as discussed in Chapter 5 for the concrete slabs was used to analyze the data, collected from the beam, and obtain the graphs for temperature and absolute contrast variations. Absolute contrast was computed for each delamination by subtracting the average temperature above a delaminated area and a reference background area close to the delaminated area. Delaminated areas were identified on the thermal infrared images based on identifying the areas with a higher temperature than surrounding areas.

Data points in both temperature variation and absolute contrast variation plots were input at 2 minutes intervals. However, to monitor the temperature changes more precisely after

the heating was terminated, data points were plotted at 30 seconds intervals between the time when heater was turned off (15 minutes after data collection began) and 9 minutes after the heat was turned off (24 minutes after data collection began).

## **6.3 Results and Discussion**

### ***6.3.1 Delaminations Located on the West Side of the Beam***

Three locations on the west side of the Silverbell Bridge beam were identified as areas with possible delaminations using the hammer sounding technique. These three locations (W1, W2 and W3) were shown in Figure 6.8.

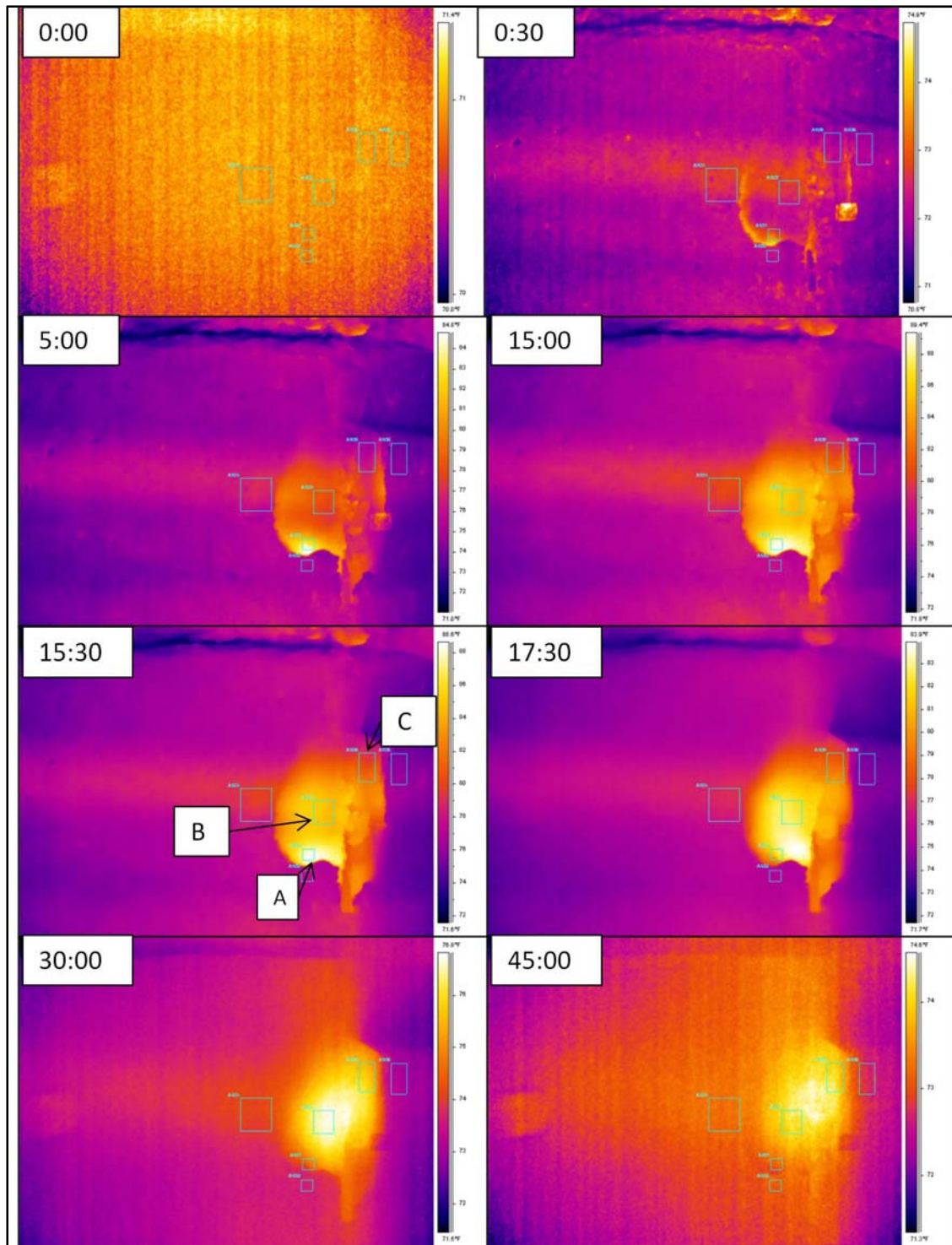
#### **6.3.1.1 Location W1**

The first delamination identified on the west side is area W1 at the skewed end of the beam. A corroded and exposed stirrup could be observed on the concrete surface. Figure 6.10 shows the visible condition of the concrete surface at the location W1. The dashed line indicates the approximate size of the thermal image. The ambient temperature was 74.1 °F and the ambient humidity was 32.7% during the data collection.



**Figure 6.10 Visible condition of the concrete surface at the location W1.**

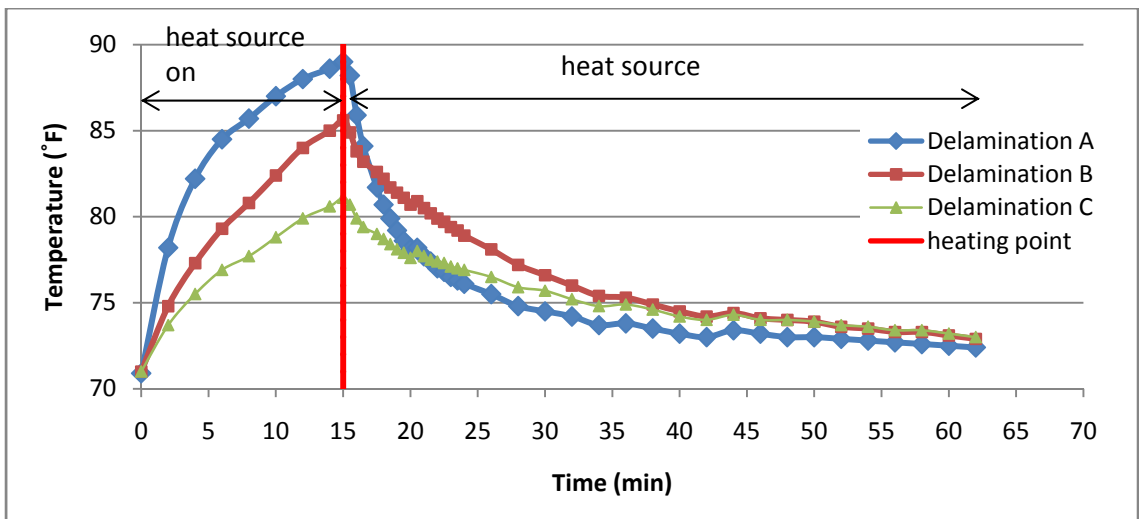
Figure 6.11 shows the thermal infrared images taken from the location W1 at different times during the data collection. Because the depth of this delamination is not constant within the total delaminated area, this area was divided into three sections; A, B, and C. Subarea A is a very small area at the edge of this delamination, which appeared with the highest temperature compared to the other two subareas (B and C) and indicates that the delamination is closer to the concrete surface in the subarea A. Subarea B is located within the delamination on the skewed end of the beam. Subarea C is located close to the skewed end and on the west side of the beam.



**Figure 6.11** Thermal infrared images taken from location W1 during an active infrared thermography test (timestamps on each image represents the relative times to the beginning of the data collection).

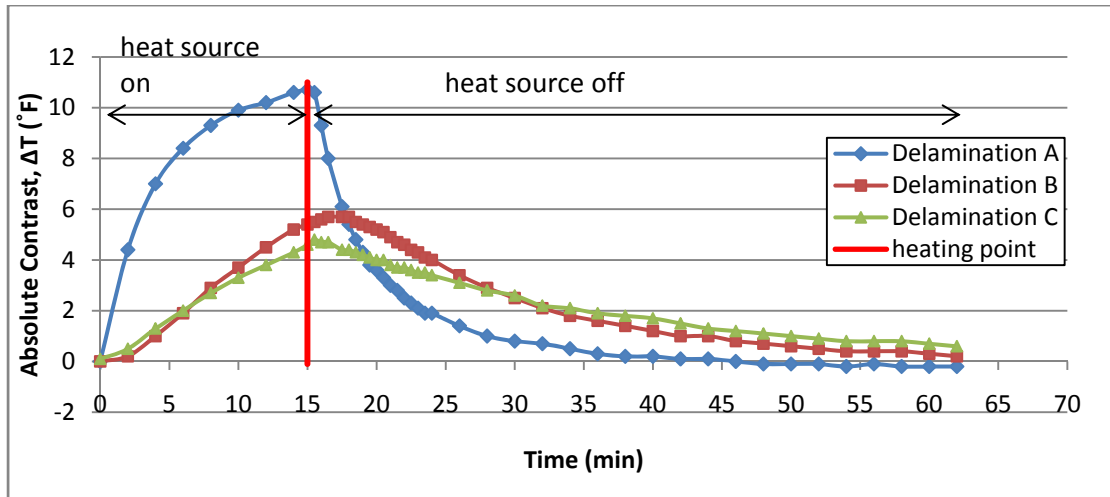


Figure 6.12 shows the plot of the surface temperature variation of concrete above each subarea of delamination located at A, B and C. Temperature values on this graph indicate the average temperature within the area of interest (subarea A, B or C). It can be seen from the plot that the temperature reached a higher value within the subarea A compared to the other two subareas. Also, the maximum average temperature for the subarea B is higher than the maximum average temperature for the subarea C. Comparing the maximum average temperature can be an indicator of deeper or shallower delaminations, however the exact decision on the depth of the delamination cannot be made by just looking at the temperature variation graph due to some non-uniform heating over the skewed end of the beam. Comparing absolute contrast variation plots can give more information regarding the depth of the delaminations.



**Figure 6.12 Temperature variation above the delamination at location W1.**

Figure 6.13 shows the absolute contrast variation for the aforementioned subareas (A, B, C) on the delaminated area located at W1. It can be seen from these graphs that the maximum absolute contrast for the subarea A is at the time when the heating was stopped (15 minutes after data collection began). The maximum absolute contrast for subareas B and C appeared at 2 minutes and 30 seconds (17:30) and 30 seconds (15:30) after the heat source was turned off. Based on these results it can be estimated that the maximum depth of this delamination (all subareas) is approximately 1 in. or less.



**Figure 6.13 Absolute contrast variations above the delamination at location W1.**

Another important observation obtained from the active infrared thermography test at location W1 is that the delamination is visible on the thermal infrared image until approximately 30 minutes after the heating was terminated (45 minutes after the data collection began). This observation helps in estimating the time window for taking the thermal infrared images on the concrete bridge element after the heat is terminated. Visibility and contrast of the delamination on thermal infrared images depend on the threshold value that can be considered for detecting delaminations. In general, the absolute contrast of 0.5°F is considered as the threshold value in identifying the area of delaminations compared to the intact surrounding area. In this case, the absolute contrast value for all three subareas were greater than 0.5°F, up to 15 minutes after the heater was turned off (30 minutes after the beginning of data collection).

### 6.3.1.2 Location W2

Location W2 was selected on the beam due to the different sound that was heard in this area during the hammer sounding test. There were no apparent signs of map cracking or delaminations on the concrete surface at this location. Figure 6.14 shows the visible condition of the concrete surface at the location W2. Duct tape was placed on the west side of the beam to be able to identify the location of the thermal infrared images collected there.

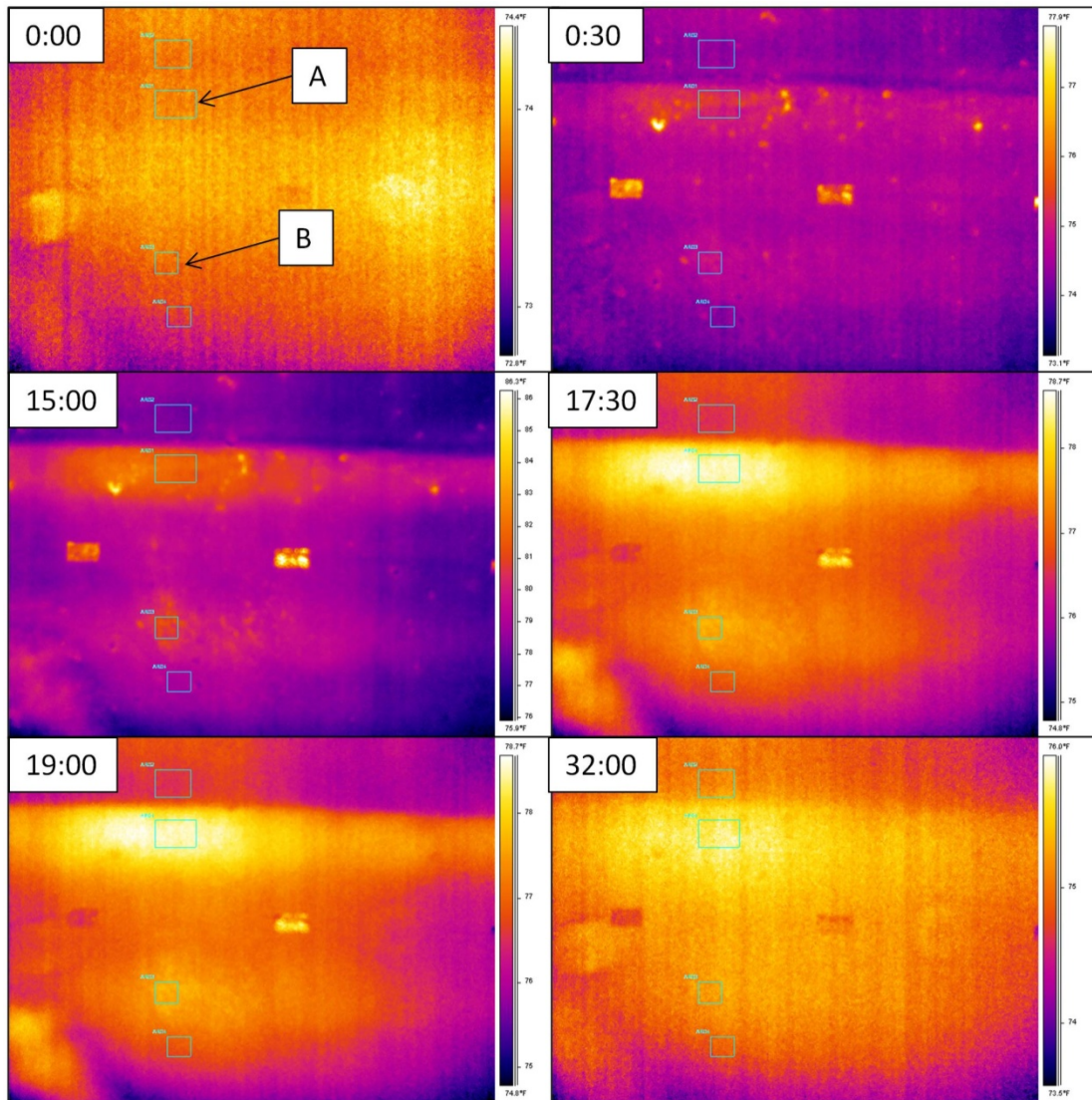


**Figure 6.14 Visible condition of the concrete surface at the location W2.**

The ambient temperature was 73.4°F and the ambient humidity was 34% during the data collection. Thermal infrared images were taken from the location W2 during the 15 minutes heating period and for about 38 minutes after the heater was turned off. Infrared heater was placed in a way to cover the whole area of interest. Figure 6.15 shows the thermal infrared images taken from location W2 at different timestamps during the active infrared thermography testing. The time at which each image was taken is indicated on the top left side of the image.

Two areas with indicators of delamination were identified on thermal infrared images. Area A is located at the bottom notch of the shear key on the beam and area B is located approximately 12 in. below the shear key. Note that due to the presence of the shear key and an unlevel surface, detection of delaminations at this location can be affected by the

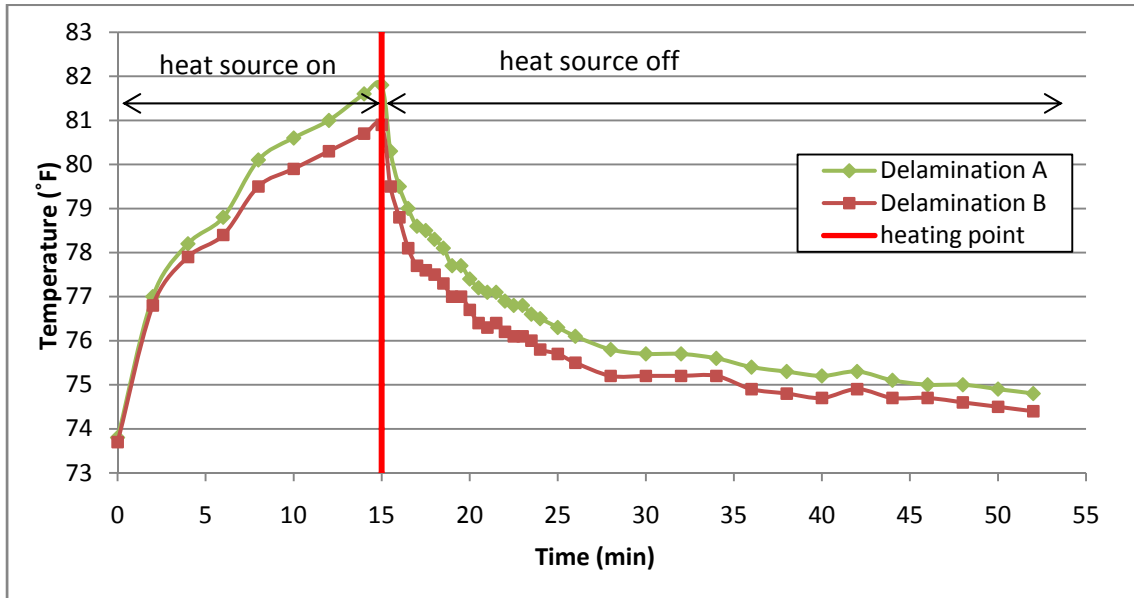
reflection off of the surface of the shear key and the apparent contrast may not necessarily represent the discontinuity below the concrete surface.



**Figure 6.15 Thermal infrared images taken from location W2 during an active infrared thermography test (timestamps on each image represents the relative times to the beginning of the data collection).**

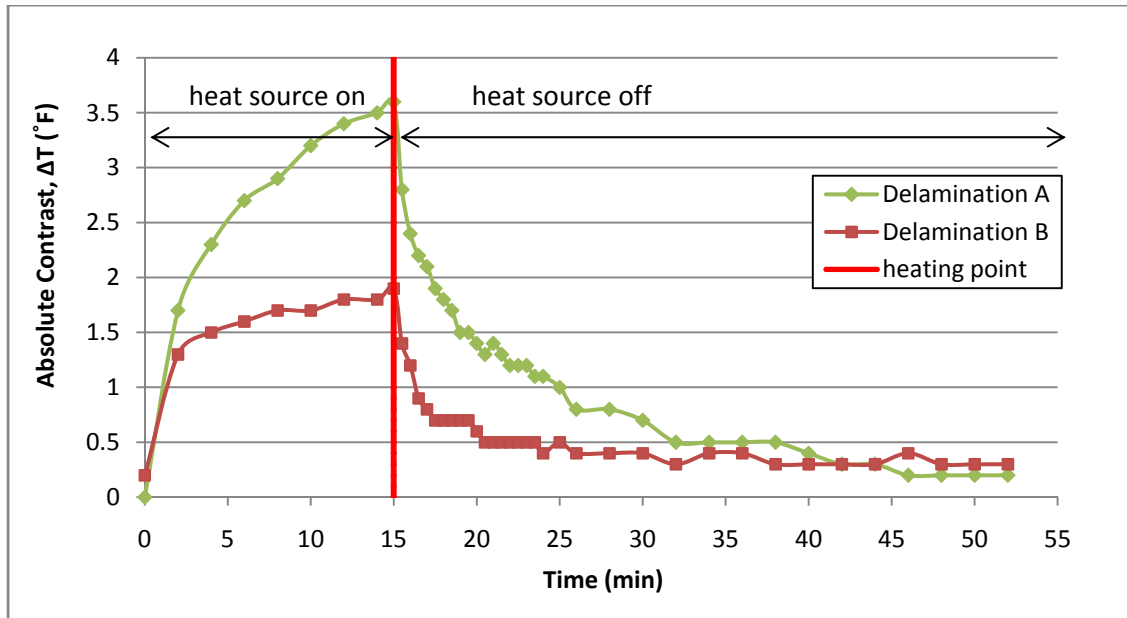
Figure 6.16 plots the surface temperature variation of concrete above each area of suspected delaminations, at A and B. These temperature values are the average surface temperature values within each area. It can be seen from this graph that the surface temperature of delamination A is slightly higher compared to the surface temperature of

delamination B. This higher value of temperature above the area A can be either because delamination A is closer to the surface than delamination B, or because of the different surface roughness or surface color on this area.



**Figure 6.16 Temperature variation above delaminations at location W2.**

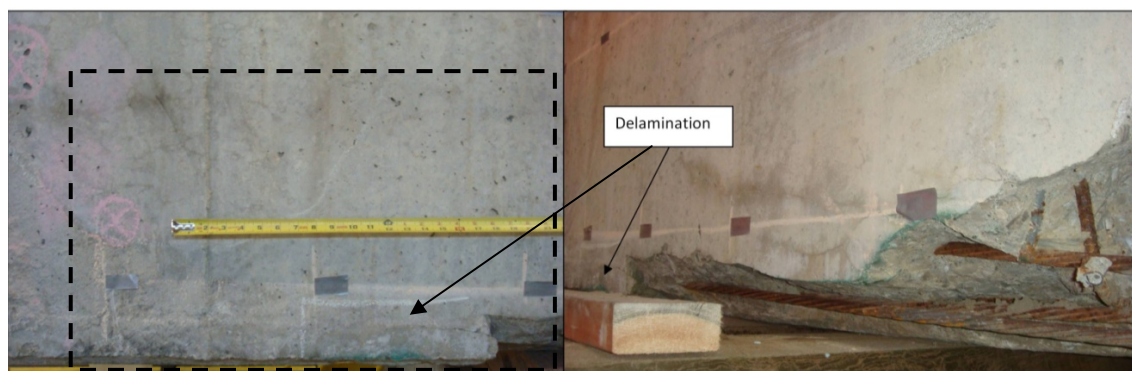
Figure 6.17 shows the absolute contrast variation of delaminations A and B on this location of the beam (location W2). It can be seen that delamination A had a higher absolute contrast than delamination B when the heater was turned off (15 minutes after data collection began). Because the trend of the absolute contrast variation does not show any maximum absolute contrast, it is not possible to estimate the exact depth of the delamination at this location. However, one can still estimate that delamination B is deeper from the concrete surface due to the lower absolute contrast value at this area. Absolute contrast for delamination B, remained constant at 0.7°F between 17.5 and 19.5 minutes after data collection began.



**Figure 6.17 Absolute contrast variations above delaminations at location W2.**

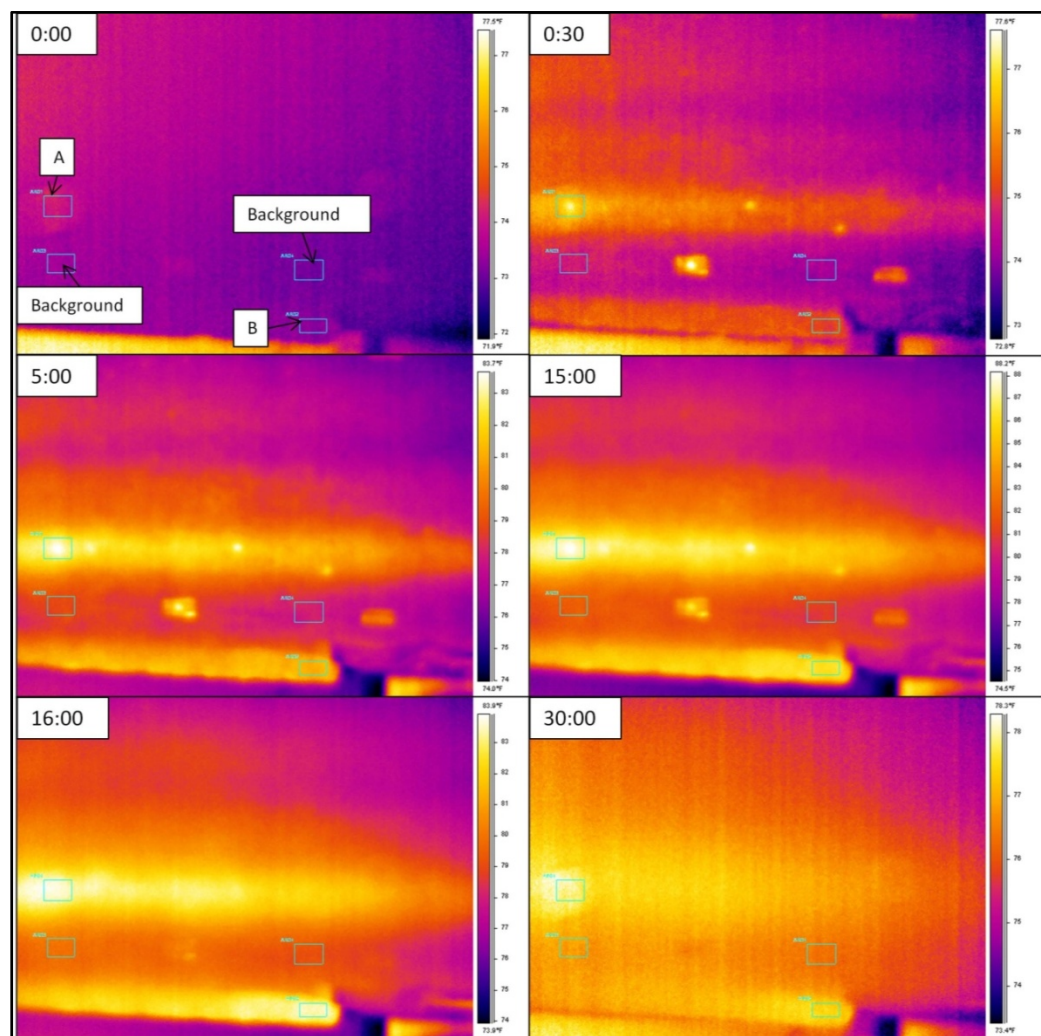
### 6.3.1.3 Location W3

Location W3 is close to the bottom of the beam on the south side where the corroded strands and stirrups are visible. Figure 6.18 shows the visible condition of the box beam specimen at the location W3. Active infrared thermography was conducted at this location and the temperature was monitored over the 15 minute heating period and for about 40 minutes after the heat source was turned off. The ambient temperature was 75.7 °F and the ambient humidity was 55.2% during the data collection.



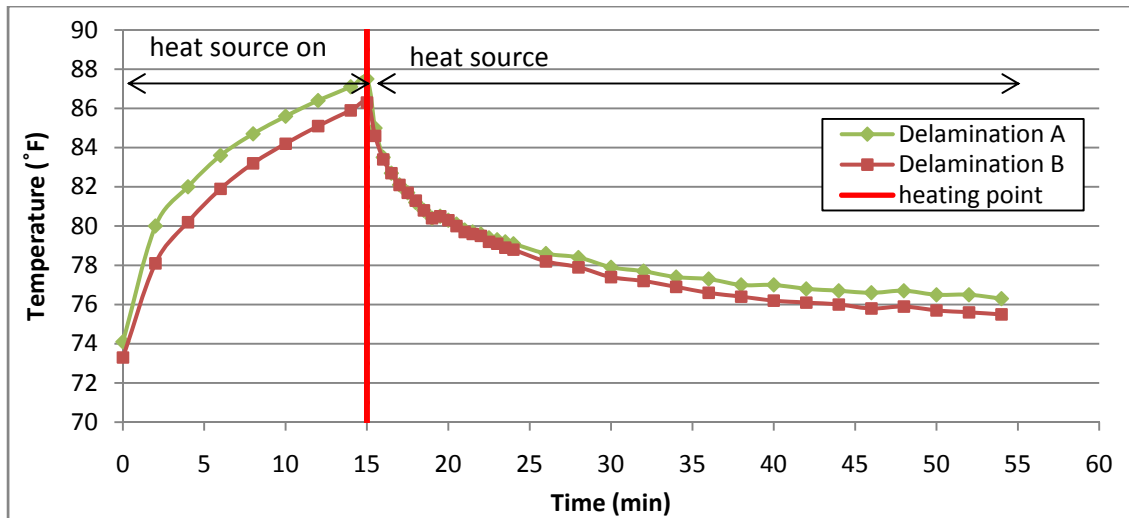
**Figure 6.18 Visible condition of the concrete surface at the W3 location.**

Figure 6.19 shows the thermal infrared images taken from the location W3 at different times. Timestamps on thermal infrared images indicate the time at which the image was taken relative to the beginning of the data collection. Two suspected areas of delamination can be observed at this location; delamination A, which does not have any visible indicator of delamination on the surface, and delamination B, which is close to the area of section loss and exposed stirrups and strands on the south end of the west side of the beam. These two areas were selected based on the subjective interpretation of the thermal infrared images taken from this location.



**Figure 6.19 Thermal infrared images taken from the location W3 during an active infrared thermography test (timestamps on each image represents the relative times to the beginning of the data collection).**

Figure 6.20 shows the plot of the surface temperature variation for delaminations A and B at the location W3. It can be seen that the average surface temperature above the delamination A increased to a slightly higher temperature compared to the average surface temperature above the delamination B, which means that delamination A is located at a shallower depth compared to the delamination B.



**Figure 6.20 Temperature variation above the delaminations at location W3.**

Figure 6.21 shows the absolute contrast variation of delaminations A and B at location W3. It can be seen that a few minutes after heating was stopped on the beam the absolute contrast for delamination B is higher than absolute contrast for delamination A. This higher absolute contrast right after the heating was stopped indicates a deeper delamination at area A compared to area B. Also, the change in absolute contrast is faster in delamination B compared to delamination A and 40 minutes after the data collection began, the absolute contrast of delamination A is higher than delamination B. This indicates that delamination A is deeper than delamination B.

There was no obvious maximum absolute contrast observed at this location to help in estimating the depth of the delaminations. Because delamination B is close to the exposed stirrups and strands, the depth of delamination could be measured. The depth of delamination for delamination B was approximately 1 in.



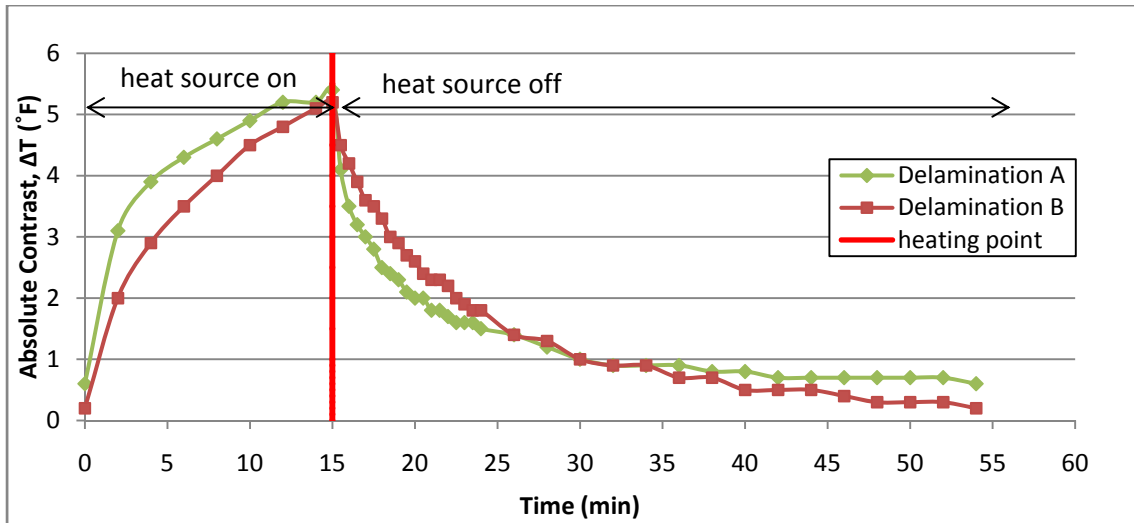


**Figure 6.21 Absolute contrast variations above the delamination at location W3.**

### ***6.3.2 Delaminations Located on the East Side of the Beam***

In the Silverbell Bridge, the shear keys between the adjacent box beams were grouted full depth. The thickness of the grout between the box beams was about 2 in. A segment of this grout was still attached to the box beam segment under study in this dissertation. Also, a section of the precast beam was cut during the demolition. Figure 6.22 shows the location of the grout segment and the precast section that was cut. Four locations on the east side of this beam were identified as possible delaminations. These four locations (E1, E2, E3 and E4) were shown in Figure 6.9.



**Figure 6.22 (a) Side of the Silverbell Bridge beam showing the grouted segment and the section that was cut during the demolition (b) grout that is delaminated from the precast section.**

### **6.3.2.1 Location E1**

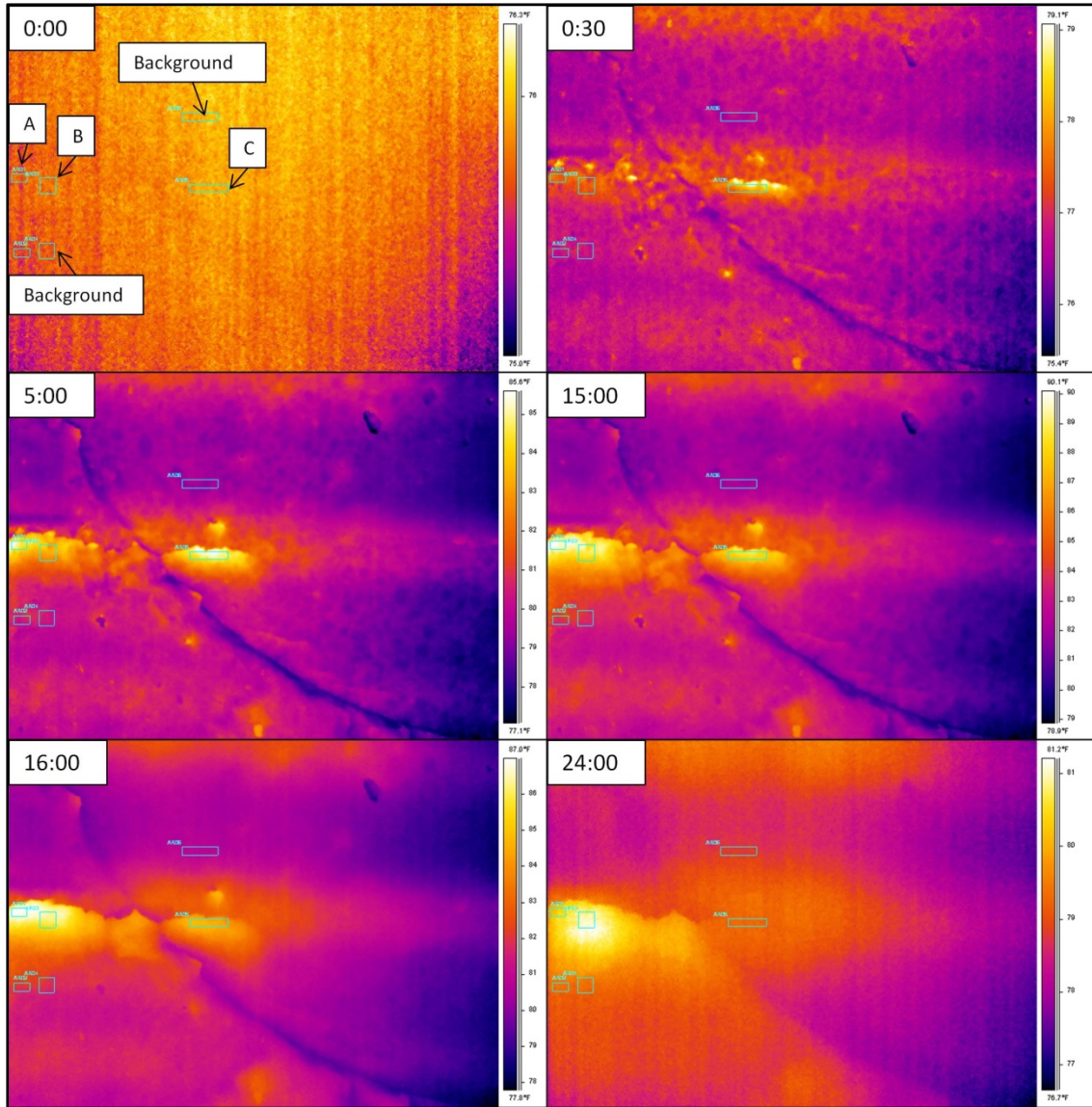
The delaminated area at location E1 was very close to the section that was cut during the demolition and it is situated on the precast section and not the grout. Figure 6.23 shows the visible condition of the beam at this location. There were no visible indicators of delamination on the concrete surface at location E1. The ambient temperature was 78.4°F and the ambient humidity was 37% during the data collection at this location.



**Figure 6.23 Visible condition of the concrete surface at location E1.**

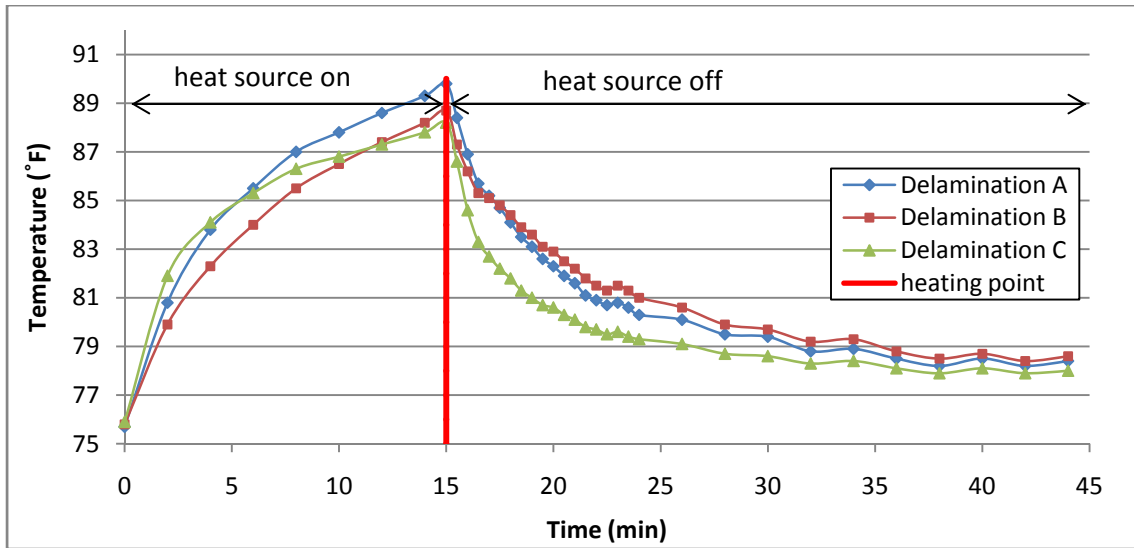
Figure 6.24 shows the thermal infrared images taken from the location W3 at different times. The delaminated area was divided into three subareas of delaminations similar to the analysis procedure for location W1, to assist in better estimation of the depth of the delaminations. These subareas of delamination (A, B and C) are shown on the thermal infrared image taken at 0 minutes in Figure 6.24. Subareas A and B are located on the surface of the beam and Subarea C is located on the section that was cut during the demolition.

It can be seen from these figures that after 24 minutes from the beginning of the data collection, subarea B appeared as a brighter area compared to the other two subareas, while the subareas A and C were brighter at 15 minutes and right after the heat source was turned off. This appearance of subarea B at a later time is an indicator of a deeper delamination on this area compared to the other two subareas of delaminations.



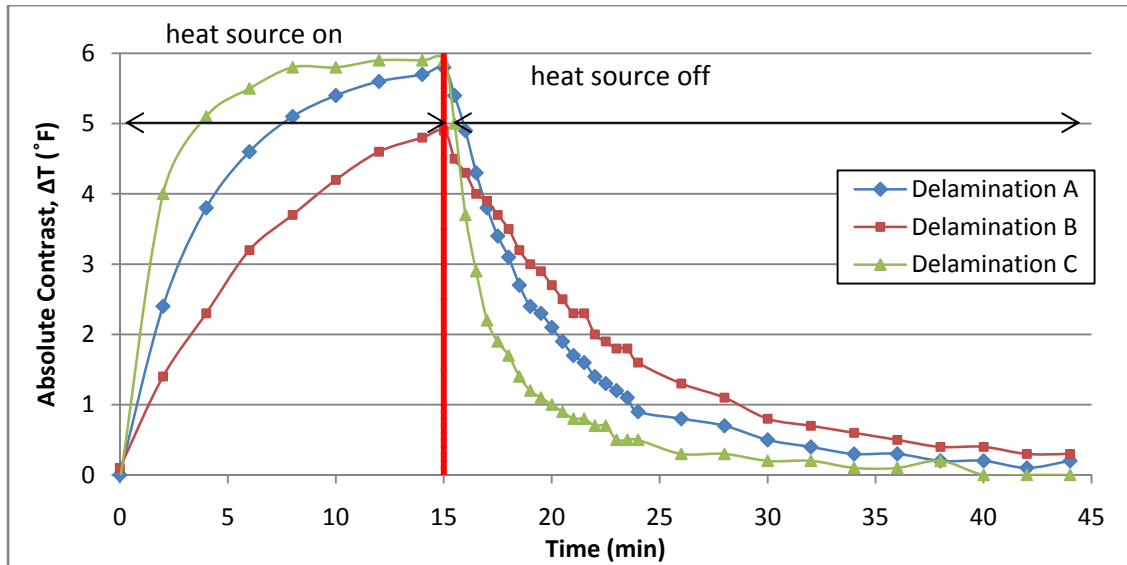
**Figure 6.24 Thermal infrared images taken from the location E1 during an active infrared thermography test (timestamps on each image represents the relative times to the beginning of the data collection).**

Figure 6.25 shows the plot of the surface temperature variation of concrete above each subarea of delamination A, B and C. Temperature digits showing on this graph indicate the average temperature within each subarea. It can be seen from the plot that the temperature reached a higher value within the subarea A after 15 minutes. This can be an indicator that delamination in subarea A is closer to the surface compared to the other two subareas.



**Figure 6.25 Temperature variation above the delamination at location E1.**

Figure 6.26 shows the absolute contrast variations for the three subareas of delamination located at E1. It can be seen that at the time when heating was stopped (15 minutes after data collection began), the absolute contrast for subareas A and C are higher than the subarea B. However, 5 minutes after the heater was turned off (20 minutes after data collection began), subarea B appeared with higher absolute contrast than subareas A and C. This change in absolute contrast can be an indicator of deeper delamination within the subarea B compared to the subarea A and C. This confirms the results obtained from the temperature variation plot. However, the depth of delamination cannot be estimated at this location because there was not any obvious maximum contrast value that can be observed.



**Figure 6.26 Absolute contrast variations above the delamination at location E1.**

### 6.3.2.2 Location E2

Location E2 is situated close to the bottom surface of the beam near the north support (beam is placed on two supports in the laboratory; north and south). Figure 6.27 shows the visible condition of the concrete surface at the location E2. At this location, a delamination is located around the spalled area close to the bottom of the beam. This delamination was detected by the hammer sounding technique. Also, there is another suspected delaminated area 6 in. away from the spall on the east side of the box beam. The ambient temperature was 77.7°F and the ambient humidity was 45% during the data collection at this location.



**Figure 6.27 Visible condition of the concrete surface at the location E2.**

Figure 6.28 shows the thermal infrared images taken from the location E2 at different times. It can be seen from these images that the highest contrast was observed at the time when the heat source was turned off (at 15:00). Suspected delaminations at this location (A, B, and C) are shown in Figure 6.28. Areas A and C are located close to the spalled area.

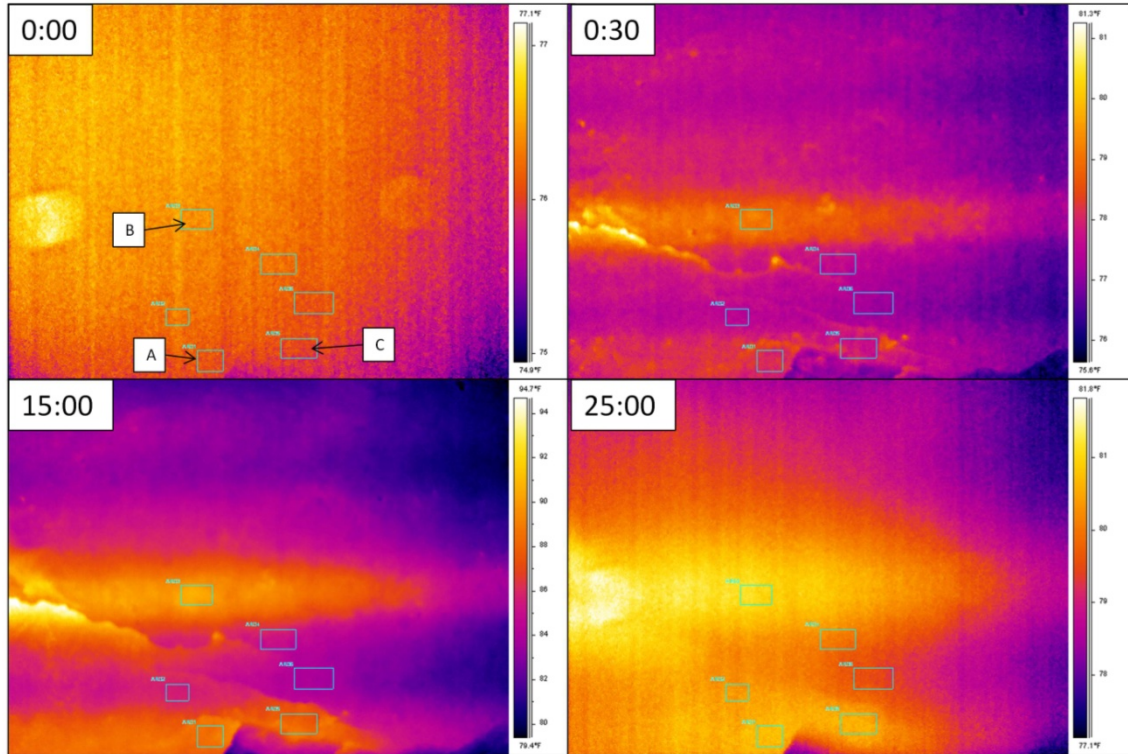


**Figure 6.28 Thermal infrared images taken from the location E2 during an active infrared thermography test (timestamps on each image represents the relative times to the beginning of the data collection).**

Figure 6.29 shows the plot of surface temperature variation of concrete above each area (A, B and C). It can be seen that at 15 minutes after data collection began (when the heater was turned off), delamination B had a higher temperature compared to the other two delaminations. However, all three delaminations appeared with the same temperature shortly after the heating was stopped. This higher temperature of delamination B before the heat source was turned off can be due to the closer distance of delamination B to the heat radiations and non uniform heating of the surface.



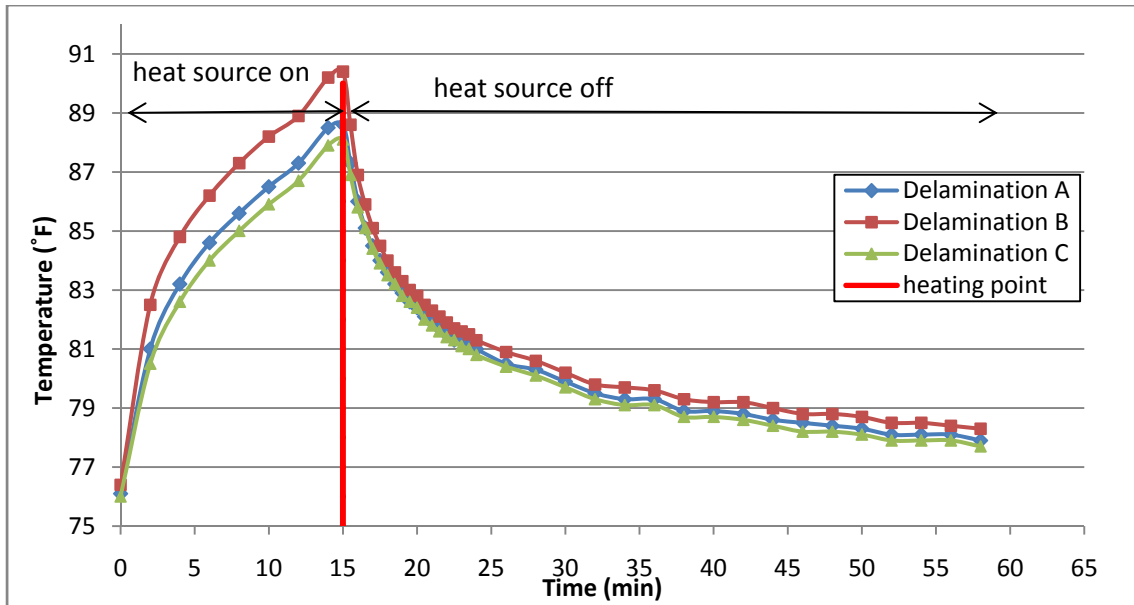


**Figure 6.29 Temperature variation above the delamination at location E2.**

Figure 6.30 shows the absolute contrast variation for the delaminations A, B and C situated at location E2. It can be seen from these graphs that 15 minutes after data collection began, delamination B had a higher absolute contrast compared to the other two delaminations. However, about 5 minute after heat source was turned off; the absolute contrast for delaminations B and C are the same and absolute contrast for delamination A was lower than the other two delaminations. About 10 minutes after the heat source was turned off the absolute contrast for delamination C is lower than delamination B and this indicates that delamination B must be deeper than delamination C. Decision on the depth of the delamination A is not possible because the absolute contrast values for this delamination is much lower than the other two areas.

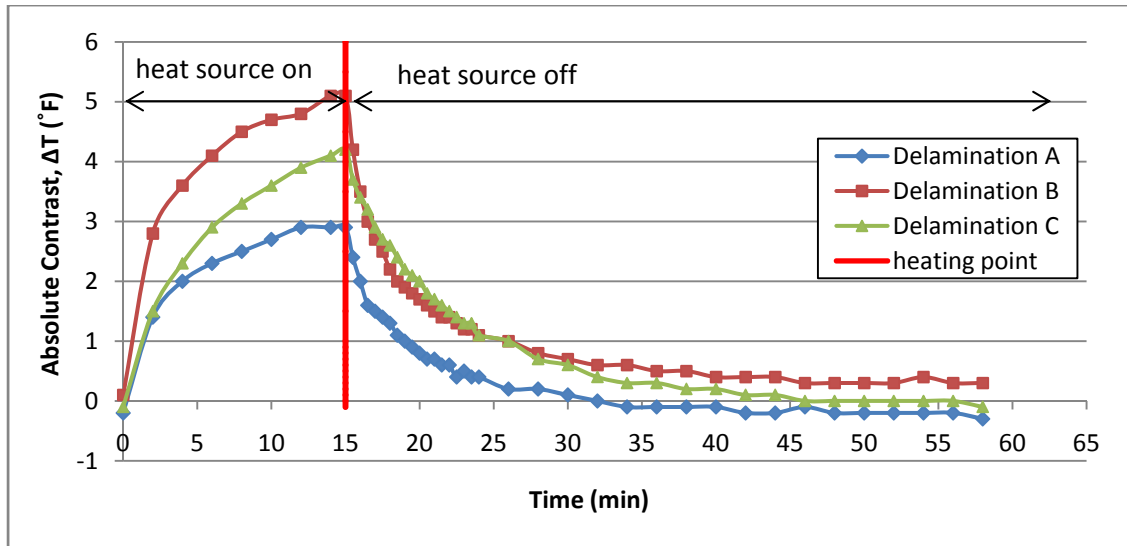


**Figure 6.30 Absolute contrast variations above delaminated areas at location E2.**

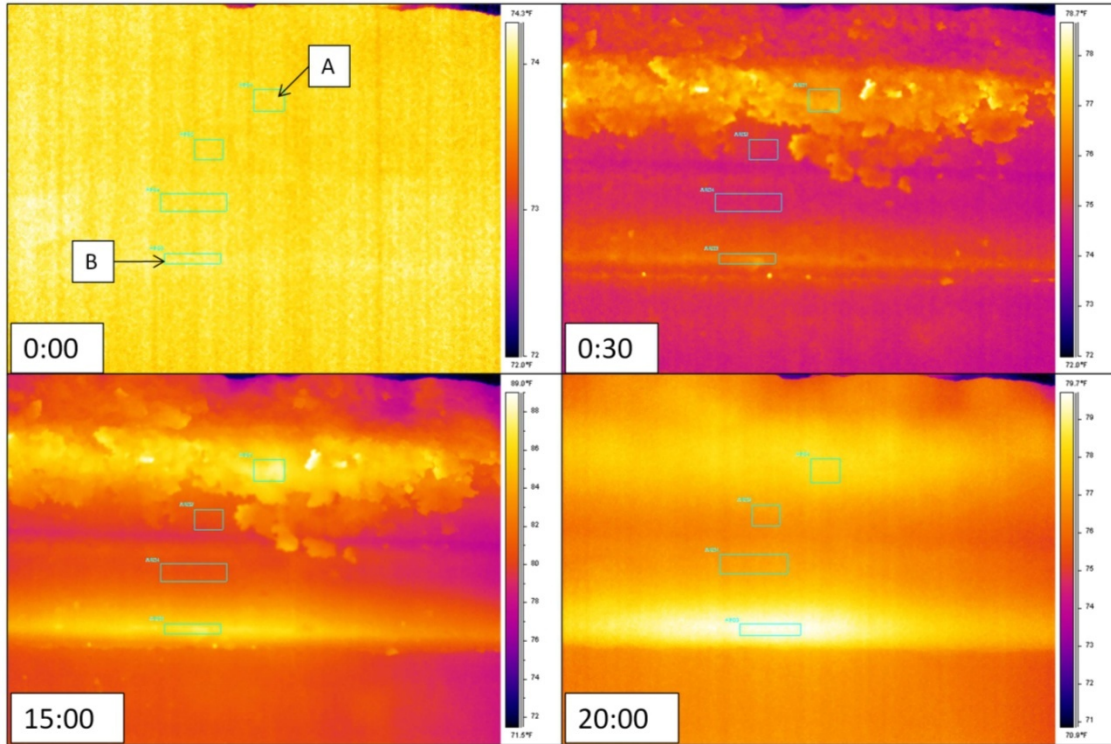
### 6.3.2.3 Location E3

Location E3 is situated within the precast beam section above the shear key and below the 3 in. concrete overlay on the top of the beam which was the riding surface of the bridge. Grout scaling is visible at this location which indicates the deteriorating condition of the grout segment that remains attached to the box beam. Figure 6.31 shows the visible surface condition of the concrete beam at location E3. The ambient temperature was 74.4°F and the ambient humidity was 27% during the data collection at this location.



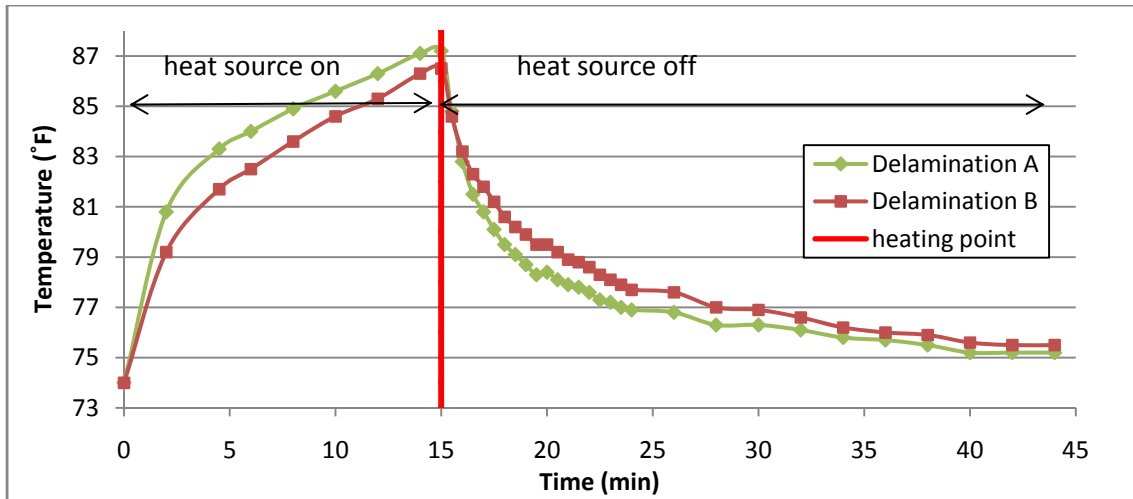
**Figure 6.31 Visible surface crusting on the concrete surface at location E3.**

Figure 6.32 shows the thermal infrared images taken from the location E3 at different times. It is very interesting to see the difference between the thermal infrared images when the heat source was on (0:30 and 15:00) and when the heat source was off (0:00 and 20:00) at this location.



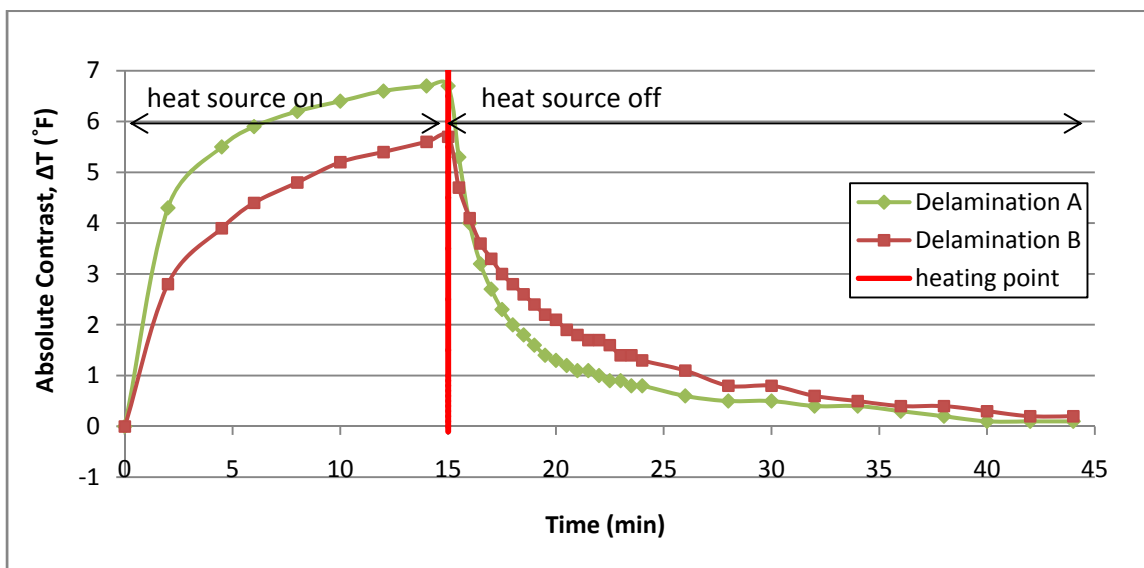
**Figure 6.32 Thermal infrared images taken from the location E3 during an active infrared thermography test (timestamps on each image represents the relative times to the beginning of the data collection).**

Figure 6.33 shows the plot of the surface temperature variation of concrete above delaminations at this location. Delamination A is considered to be an area above the section with scaling and delamination B is on the shear key segment of the grout. Note that the temperature change and contrast on the shear key segment can be due to the unlevel surface of the concrete and is not necessarily an indicator of a delamination underneath the surface.



**Figure 6.33 Plot of the temperature variation above the delamination at location E3.**

Figure 6.34 shows the absolute contrast variation on the concrete surface above delaminated areas A and B. As it can be seen from the graph when heating was stopped (15 minutes after data collection began), delaminated area A had a higher contrast compared to delaminated area B. However, 5 minutes after heating was stopped (20 minutes after data collection began), delamination B appeared to have a higher contrast compared to delamination A. This higher absolute contrast indicates that delamination B is deeper than delamination A.



**Figure 6.34 Absolute contrast variations above delaminated areas at location E3.**

It is not possible to estimate the depth of delaminations at location E3 because there was not any maximum absolute contrast that could be observed after the heat was stopped on the beam or grouted section.

#### **6.3.2.4 Location E4**

Location E4 is situated close to the south side of the beam. The delaminated area at this location is close to the exposed reinforcement and spalled area on the precast section. Figure 6.35 shows the visible condition of the concrete surface at the location E4. Delaminations, located closer to the exposed reinforcement, were detected by the hammer sounding technique. The ambient temperature was 70.1°F and the ambient humidity was 38.4% during the data collection at this location.



**Figure 6.35 Visible condition of the concrete surface and mild steel at the location E4.**

Figure 6.36 shows the thermal infrared images taken from the location E4 at different times. It can be seen from these images that the highest contrast was observed at the time when the heat source was turned off (at 15:00). Contrast was disappeared on the delamination areas after about 18 minutes from the beginning of the data collection. This loss can be due to the bright area on the image as a result of the precast section that was at the cut.

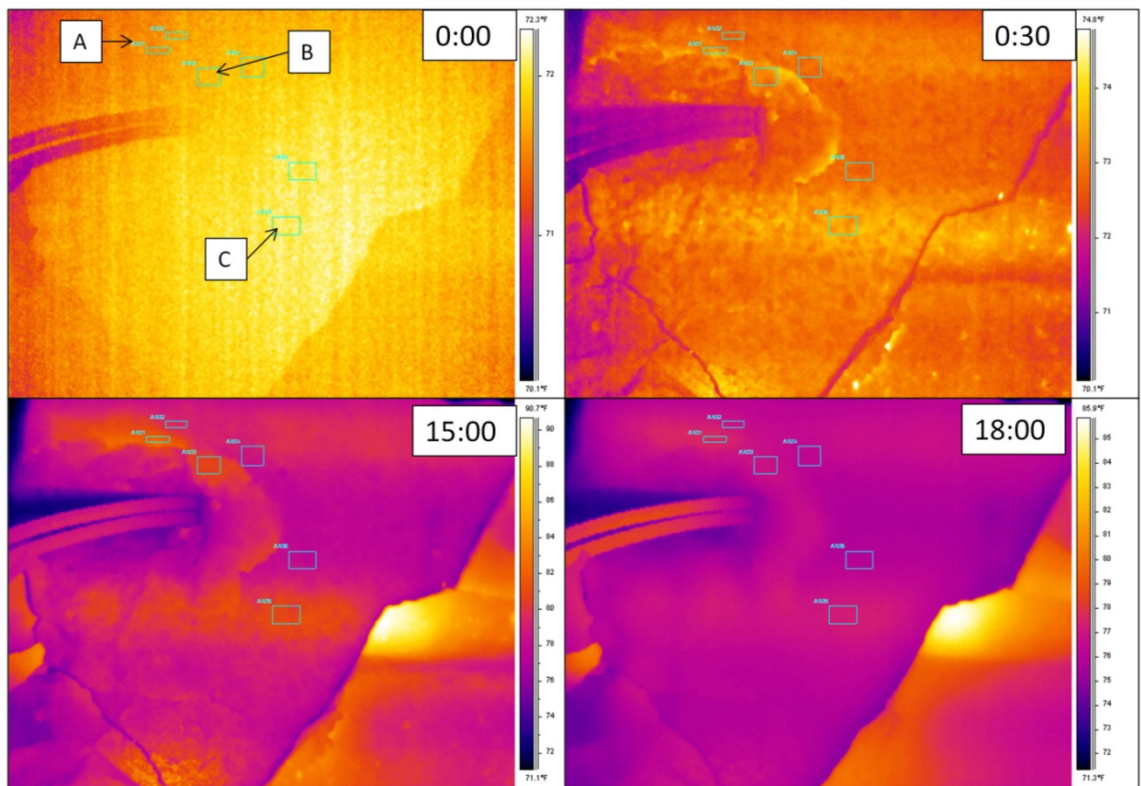


**Figure 6.36 Thermal infrared images taken from the location E4 during an active infrared thermography test (timestamps on each image represents the relative times to the beginning of the data collection).**

Figure 6.37 plots the surface temperature variation of concrete above delaminations. This delamination is divided into three subareas A, B and C to investigate the different depths at each subarea. It can be seen from the graphs presented in Figure 6.37 that the maximum temperature for delamination A is higher than delamination B and C. This higher maximum temperature can indicate that delamination A is closer to the concrete

surface than the other two delaminations. Monitoring the absolute contrast variation can give a better estimate of the depth of the delaminations.

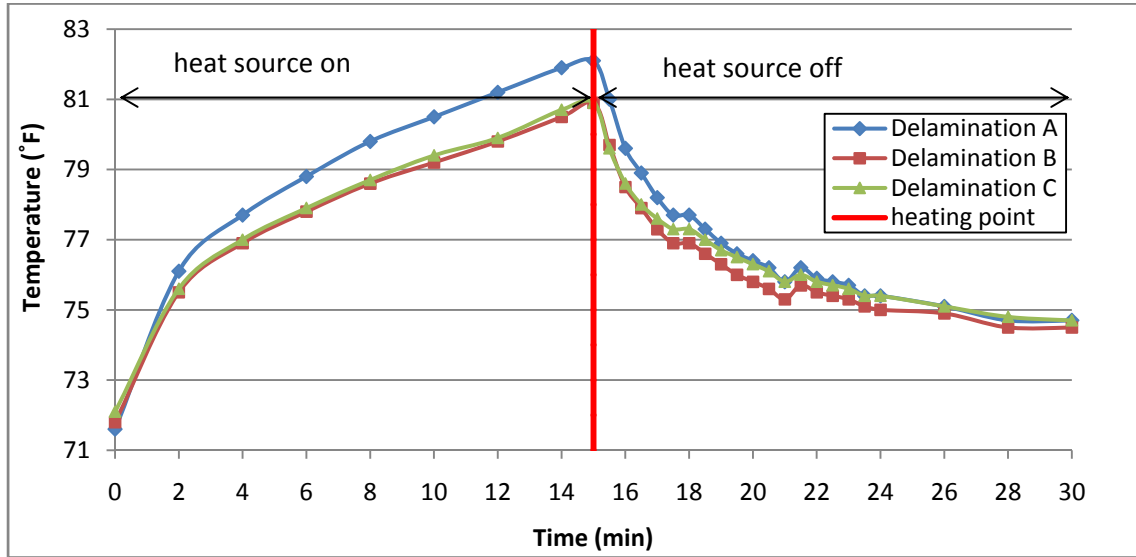


**Figure 6.37 Plot of the temperature variation above the delamination at location E4.**

Figure 6.38 shows the absolute contrast variation above subareas of delaminations (delamination A, B, and C). It can be seen from this graph that the constant absolute contrast for delamination C appeared at 19 minutes after data collection began. This indicated that the delamination C is located at a deeper depth compared the other two delaminations.



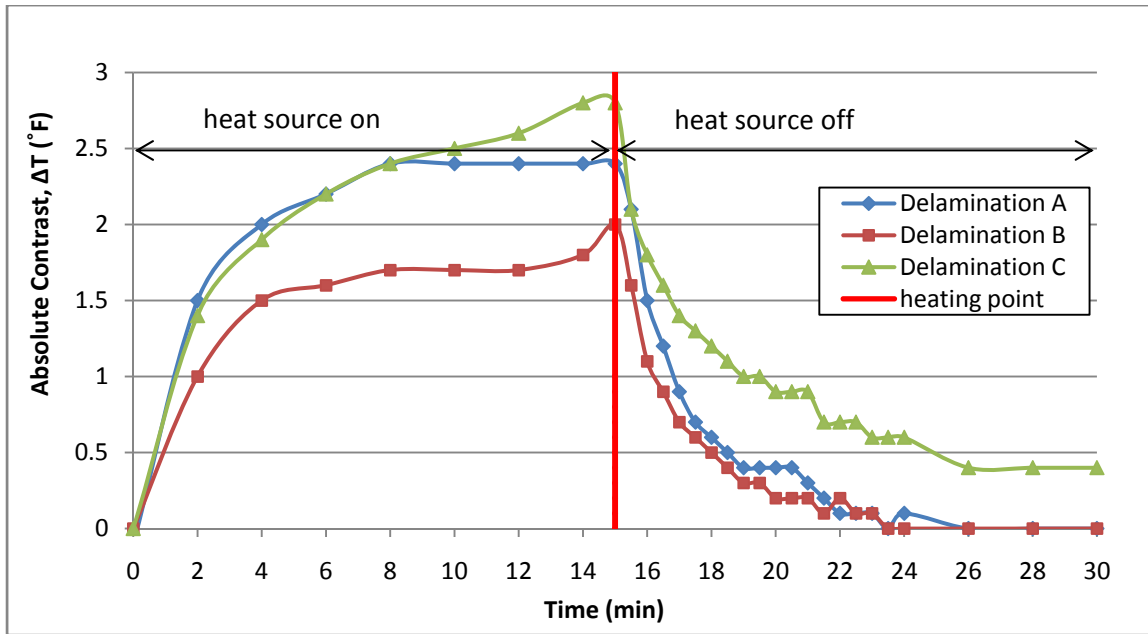


**Figure 6.38 Absolute contrast variations above delaminations at location E4.**

### ***6.3.3 Calculation of the Total Delaminated Area***

Total delaminated area at each location was determined by creating a rectangular shape area around each delamination and summing up the total number of pixels within each area. This calculation was performed by using the ThermoCAM Researcher Professional software and obtaining the coordinate information of each rectangle. Figure 6.40 shows the rectangular shape areas that considered in the total area calculation at each location on the beam. Positions of the pixels located at the top left corner and at the bottom right corner of the rectangle were obtained from this software and based on these coordinates the total number of pixels in each area was computed (see Figure 6.39).

Percentage of delamination at each location was calculated by dividing the number of pixels within each area of delamination by the total number of pixels at each area (307,200 pixels). Calculating the percentage of delamination was similar to the passive infrared thermography test and discussion for Equation 12 in section 4.1.1.1 of this dissertation. Knowing the field of view of the camera (2.5 ft x 2 ft), the area of delamination at each location and the total delaminated area were computed.

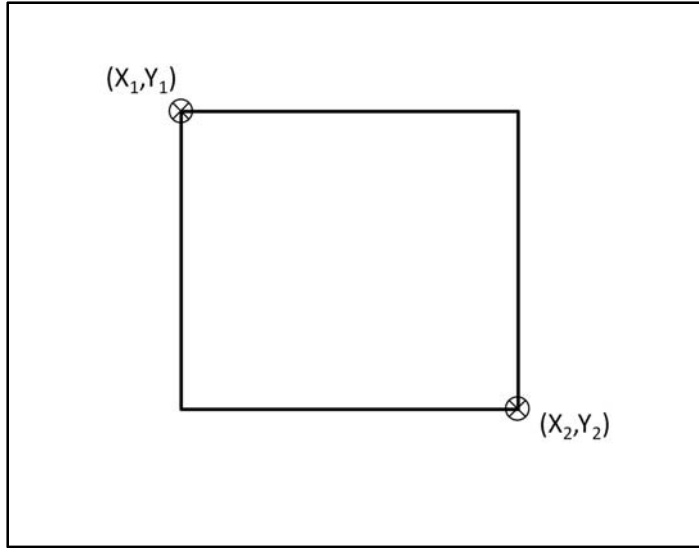


**Figure 6.39** Coordinates of the two corners of the rectangle around each delaminated areas that can be obtained from the software.

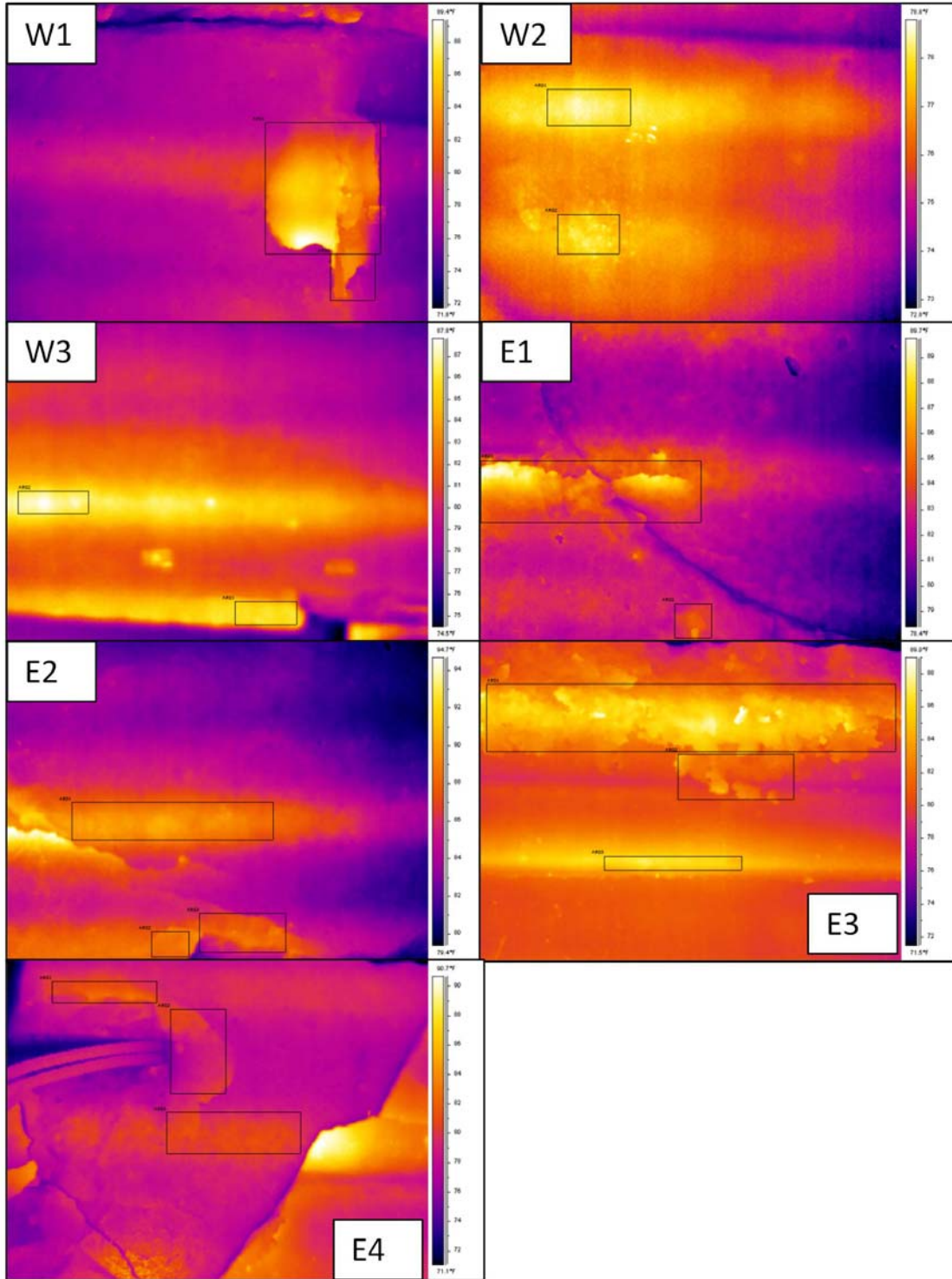


**Figure 6.40 Delaminated areas on the Silverbell Bridge beam considered in the total area calculation.**

A summary of the total number of pixels and delaminated areas at each location is presented in Table 6.1. The total delaminated area on the two sides (east and west) of this beam was determined to be 3.63 ft<sup>2</sup> using active infrared thermography which is about 2.25% of the total area of the sides of this beam. The total delaminated areas using hammer sounding technique was determined to be 5.94 ft<sup>2</sup>, which is about 3.69 % of the total area of the two side of this beam. It was noticed that in locations W1, W2, W3, E1, and E2 total delaminated areas determined by hammer sounding was larger than delaminated areas detected by infrared thermography and in locations E3 and E4, the total delaminated area detected by infrared thermography is larger than the total delaminated area detected by hammer sounding. This is due to the difficulty in estimating the exact location and boundaries of the delamination using the hammer sounding technique.

**Table 6.1 Total number of pixels and delaminated area at each location on the Silverbell bridge beam**

Delamination location	Total number of pixels in delaminated areas	% Delamination (in each image)	Area of delamination (ft <sup>2</sup> ) by active infrared thermography	Area of delamination (ft <sup>2</sup> ) by hammer sounding
W1	39,342	12.81	0.64	1.02
W2	12,625	4.11	0.21	0.75
W3	6,928	2.26	0.11	0.39
E1	34,067	11.09	0.55	2
E2	21,354	6.95	0.35	0.5
E3	80,186	26.10	1.31	1
E4	28,245	9.19	0.46	0.28
Total			3.63	5.94
% area of both sides of the beam			2.25%	3.69%

#### ***6.3.4 Active Infrared Thermography at an Intact Location***

Active infrared thermography with the same procedure as discussed before was conducted at a location on the beam with no delaminations. The objective of this test was

to compare the results with locations with delaminations. The location was selected on the east side of the beam. Figure 6.41 shows the location on the Silverbell Bridge beam with no delaminations for active infrared thermography testing. The shear key section of the beam is in the field of view of the thermal infrared images taken from this location.



**Figure 6.41 Location W4 with no delaminations.**

Images were collected from this location at 30 second intervals. Figure 6.42 shows the thermal infrared images taken from this intact location on the beam at 0, 0.5, 5, 15, 20 and 30 minutes after data collection began. It can be seen that duct tape on these images are shown as bright areas due to the reflective surface and lower emissivity than concrete. Heating was stopped on the beam after 15 minutes and images, taken at 20 and 30 minutes, were taken when no heat was present.

A bright area was observed on the shear key after the heating was terminated, however this bright area vanished from the thermal infrared image within a few minutes. No bright

areas were evident on the thermal infrared images about 10 minutes after the heat source was turned off, which means that no delaminations exist at this location.

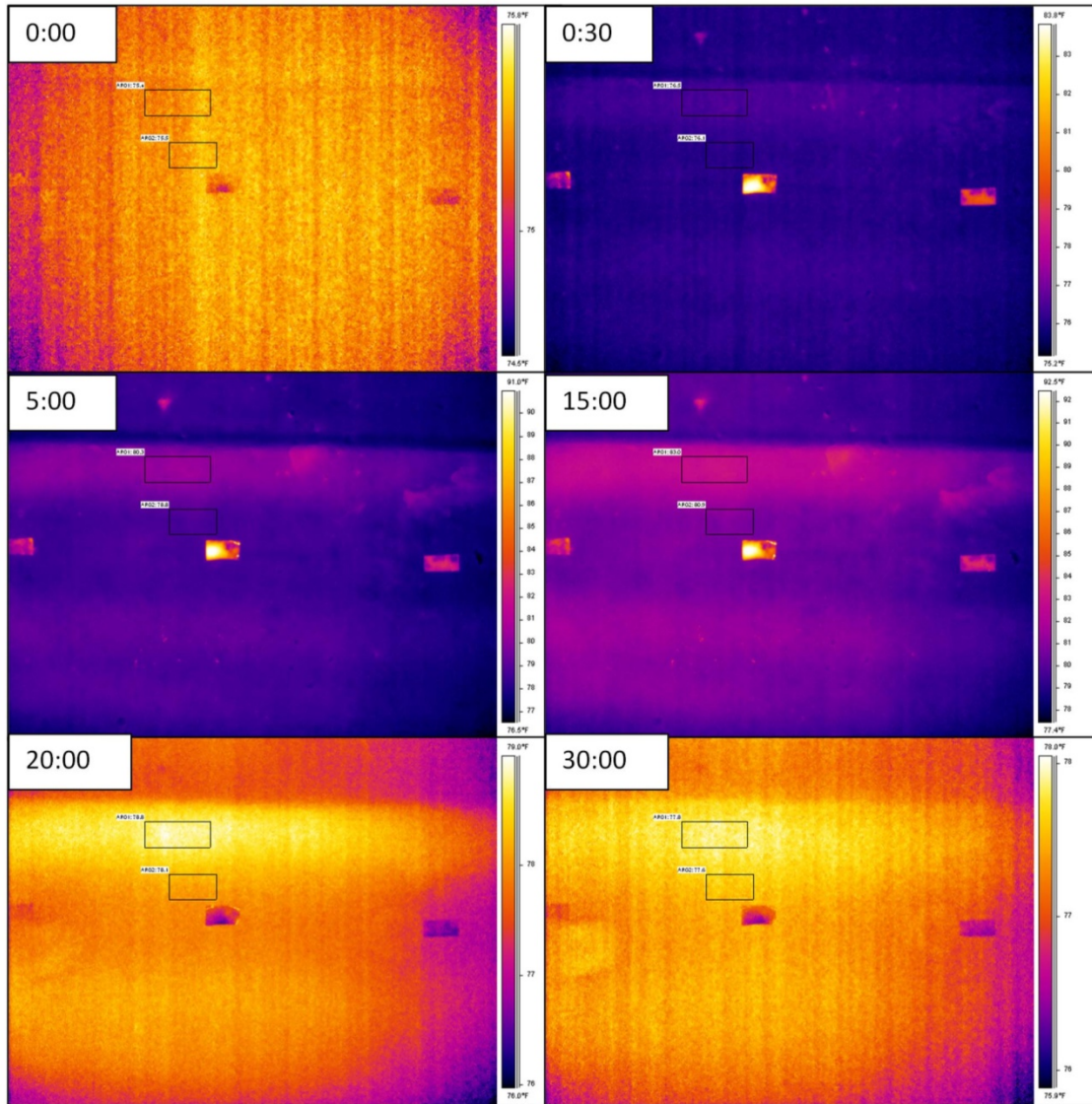


**Figure 6.42 Thermal infrared images taken from the intact location of the Silverbell Bridge beam, taken at 0, 0.5, 5, 15, 20, 30 min after data collection began.**

### ***6.3.5 Coring Test Results***



Nine cores were extracted from the seven locations of delaminations that was discussed previously. A summary of cores extracted from the Silverbell Bridge beam is presented in Table 6.2. The thickness of the webs of the precast concrete confirmed to be close to

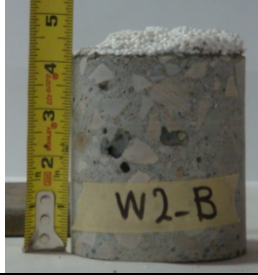



4¼ in. for all cores extracted from W2-A, W2-B, W3-A, and W4 (Note that Figure 6.2 shows the web wall thickness was designed to be 4½ in. Location W1-B was drilled up to 13.5 in. inside concrete but proved to be a solid section and did not reach the Styrofoam filling inside the box beam. Figure 6.43 shows the coring procedure and the way the drilling was carried out on the beam.



**Figure 6.43 Coring procedure on the Silverbell Bridge beam.**

**Table 6.2 Summary of the cores extracted from the Silverbell Bridge beam**

Core No.	Photo	Actual Depth	Comments
W1-B		½ in.	
W2-A		No delamination	Poor consolidation

W2-B		No delamination	Presence of voids Poor consolidation
W3-A		No delamination	Poor consolidation
W4		No delamination	Solid location
E1-C	*	-	
E1-B	*	-	
E2-C		$\frac{3}{4}$ in.	
E4-B	*	-	
E4-C	*	-	

\*Crane became inoperative in the last stages of coring

It can be seen from these results that delamination W1 and E2-C could be precisely predict as being located at less than 1 in. deep. Cores that were extracted from location W2 and W3 showed no delaminations although both these location were also shown some indicators of delaminations when tapped with a hammer. Note that some of the locations for extracting cores were selected on spots that did not have an obvious indicator of delaminations, such as W2-A that was placed below the shear key. Also, it has been noted that cores W2-A and W2-B contained some large voids (see Figure 6.44).



Concrete cover to the stirrup was confirmed to be 1¼ in. from the core obtained at location W3-A (see Figure 6.45).

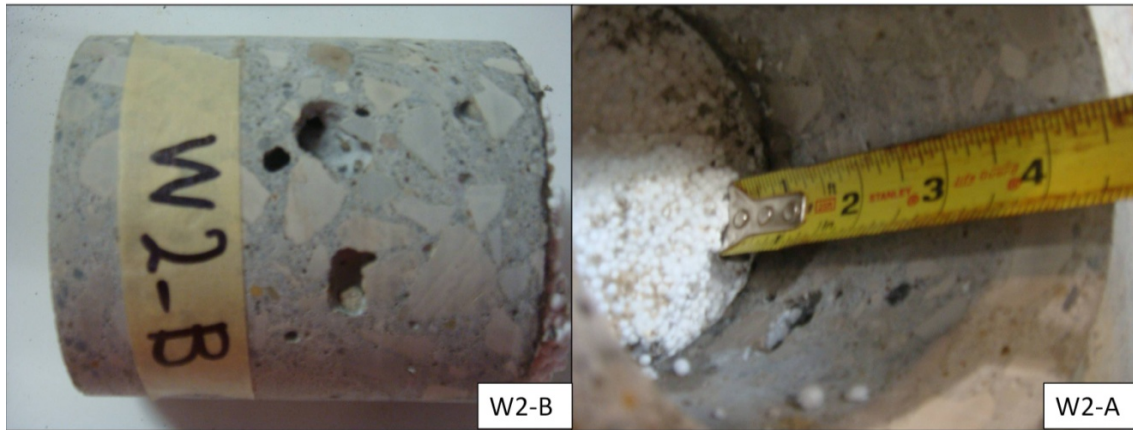


**Figure 6.44** Voids observed in the cores obtained from the Silverbell bridge box beam.

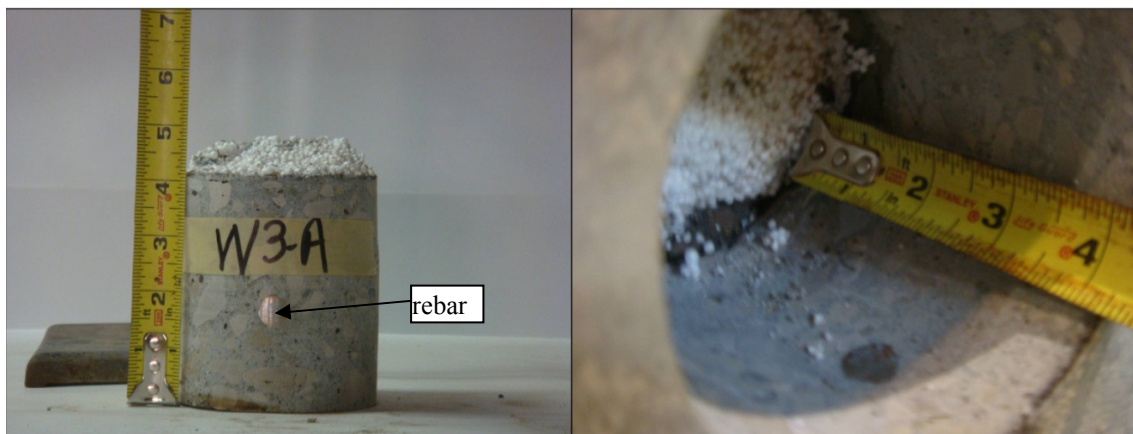


**Figure 6.45** Concrete core obtained from location W3-A, showing the 1¼ in. cover over the rebar.

## 6.4 Summary

This chapter discussed the active infrared thermography testing procedure for an out-of-service prestressed box beam and the results obtained from this test. Cores were extracted from the specific locations on this beam to further validate the results obtained from the active infrared thermography test. The core locations were selected based on infrared thermography and hammer sounding results. Table 6.3 presents a summary of the results

obtained in Chapter 6. The predicted depth column is the depth that could be predicted based on the absolute contrast variation plot and observation time. A summary of the predicted depth order from the temperature variation plot (T-t) and the absolute contrast variation plot ( $\Delta T-t$ ) are included in the comments.

Based on the results presented in Chapter 5, the depth of the delamination is predictable using active infrared thermography. Results in Chapter 6 showed that this conclusion is valid and the depth of the delamination was correctly predicted for location W1 to be less than 1 in. Using the equation shown in Figure 5.32 and the observation time of 2.5 minutes for location W1-B, the depth was determined to be 0.75 in. The actual depth of 0.5 in. was determined by coring at this location. In other locations on the beam, because no observation time could be observed in the absolute contrast variation plot, no prediction of depth can be made using the linear relationship equation obtained from Figure 5.32.

Based on the results from active infrared thermography and hammer sounding method it was anticipated to detect delaminations under the concrete surface at locations W2 and W3. However, the main issue that was observed from the cores obtained from this location was poor consolidation and not a delaminated area.

Only one core (E2-C) could be extracted from the east side of the beam because the crane that was used to hold the coring equipment on the beam became inoperative at the last stage of coring. This core showed a delamination of  $\frac{3}{4}$  in., however an observation time was not obtainable from the absolute contrast variation plots of this delamination. Scaling at the location E3 was one of the interesting part of this research and showed that the area of scaling has the potential to be estimated using active infrared thermography.

**Table 6.3 Summary of the results obtained from the beam study**

Delamination Label	Predicted depth	Planned for coring	Actual Depth	Comments
W1-A	Very close to surface		No core	depth order based on T-t: $A < B < C$ depth order based on $\Delta T$ -t: $A < B < C$
W1-B	< 1 in. (0.75 in.)	c	0.5 in.	
W1-C	< 1 in.		No core	
W2-A	No observation time	c	No delamination	depth order based on T-t: $A < B$ depth order based on $\Delta T$ -t: $A < B$ (Poor consolidation)
W2-B	No observation time	c	No delamination	
W3-A	No observation time	c	No delamination	Delamination W3-B is close to the spall at the south end of the east side of the beam. depth order based on T-t: $A < B$ depth order based on $\Delta T$ -t: $A < B$ (Poor consolidation)
W3-B	No observation time		1 in.	
W4	No observation time	c	Solid	Intact concrete
E1-A	No observation time		No core	depth order based on T-t: $A < B < C$ depth order based on $\Delta T$ -t: $C < A < B$
E1-B	No observation time	cx	No core	
E1-C	No observation time	cx	No core	
E2-A	No observation time		No core	Delamination E2-C is located close to the spalled area. depth order based on T-t: $A < B < C$ depth order based on $\Delta T$ -t: $B < C < A$
E2-B	No observation time		No core	
E2-C	No observation time	c	3/4 in.	
E3-A	No observation time		No core	Scaling depth order based on T-t: $A < B$ depth order based on $\Delta T$ -t: $A < B$
E3-B	No observation time		No core	
E4-A	No observation time		No core	Around the spalled and exposed mild steel on the south end of the east side of the beam. depth order based on T-t: $A < B < C$ depth order based on $\Delta T$ -t: $C < A < B$
E4-B	No observation time	cx	No core	
E4-C	No observation time	cx	No core	

c – core obtained from this location.

cx - core could not be extracted due to an inoperative crane

Further investigation is recommended to prove the applicability of active infrared thermography for locations very close to the edge of the concrete section or having a very poor consolidation as was the case for locations W2, W3 and E2. Also, other suspected

delaminated areas on the thermal infrared images without an apparent observation time on the absolute contrast variation plots might have a depth of greater than 2 in. or a width to depth ratio less than 2 in. Moreover, a better understanding of detectable delaminations and the effects of poor consolidation, surrounding intact concrete and surface condition can further refine the active infrared thermography testing procedure and results.

## **Chapter 7 Concluding Remarks and Future Works**

### **7.1 Summary of Conclusions**

Infrared thermography is a well-established non-destructive tool that is being widely used by different industries for repair and maintenance practices. This dissertation has investigated the potential of applying the infrared thermography technology on concrete bridge elements in both active and passive methods to assist bridge inspectors in inspecting both top and bottom sides of concrete bridge decks and girders. The objectives of this research were to enhance the infrared thermography technique beyond the current capabilities of the passive infrared thermography technique, and to quantify the area and the depth of the delaminations. The passive infrared thermography test was conducted on three concrete bridge decks at the early stages of this research to get a better understanding of the capabilities and limitations of this technology. The active infrared thermography test was then conducted on five concrete slabs and an out-of-service prestressed box beam to develop the active infrared thermography technique for bridge application and overcome some limitations of the passive infrared thermography technique.

Passive infrared thermography testing (Chapter 4) confirms previous findings and contributes additional evidence showing the method to be a valid non-destructive tool for concrete bridge deck inspection under reasonable conditions. The infrared thermography data collection method is highly dependent on the camera system and field of view of the camera being used. Having a grid pattern on the bridge deck was necessary to merge and assign the specific coordinate system. However, the grid pattern could affect the results and it will be more practical to use less duct tape on the bridge deck. Having a camera with a larger field of view can solve this issue to some extent, and having less images on the overall bridge deck can make the data processing procedure faster and more practical.

Presenting the results of bridge inspection using passive infrared thermography in the ArcGIS environment allows for an easy and fast method to locate and quantify the deficient areas within the bridge deck. Also, presentation of data can help bridge management teams to compare and combine the results of several non-destructive bridge inspection technologies to make more efficient decisions on prioritizing the maintenance and repair funding. The main limitation of applying the passive infrared thermography during a bridge inspection is the limited time window for inspection during the day to capture delaminations on the thermal infrared images. Also, identifying the exact time at which passive infrared thermography should be conducted is not explicit. Results of the cores extracted from the Mannsiding Rd. bridge deck confirm that delaminations deeper than 3 in. were not detected by infrared thermography. Also, there exists some uncertainties in interpretation of thermal infrared images and detecting delamination when the delaminations overlap with the traffic lines of reflective paint, as was the case for the Freer Rd. bridge deck.

Passive infrared thermography has been shown to be useful for inspecting bridge piers and detecting delaminations. In this study, passive infrared thermography was also conducted under the bridge deck and bridge girders. However, the presence of the sun on the top side of the concrete deck makes the infrared thermography set-up to be in a transmission mode rather than a reflection mode and delaminations should appear as dark areas instead of bright areas. On the other hand, the ambient temperature change between night and day time will induce a temperature change on the concrete and shallow delaminations will appear as bright areas on the thermal infrared image. As it can be seen from this discussion, there are some conflicting results obtained from the passive infrared thermography testing on the underside of the bridge deck which creates some uncertainties on using the passive infrared thermography in this location.

Active infrared thermography can be used for underside inspection of bridge decks. Having an external heater under the bridge deck can diminish the existing uncertainties with passive infrared thermography. In the present study, the surface heating method was applied to concrete slabs (Chapter 5) and a segment of the Silverbell Bridge box beam

(Chapter 6) to assess the potential of this technology to successfully be applied on the concrete bridge girders and underside of the bridge decks where the bridge elements are not exposed to the direct sunlight. Using the surface heating method, as opposed to the line heating method, can reduce the time of inspection significantly by using a heating period as short as 15 minutes. Moreover, the surface heating method was a more practical option in the field as the surface of the concrete bridge elements can be heated up from the shoulders using a more powerful heat source.

One of the disadvantages of the surface heating method is having non-uniform heating on the concrete surface, making it difficult to select one background point and compare delaminations to each other. Comparing the maximum average temperature can be an indicator of deeper or shallower delaminations. However, due to the non-uniform heating, the decision on the depth of the delamination cannot be made by just looking at the temperature variation graph. Using the analysis method described in this dissertation regarding the absolute contrast variations, the results are analyzed and depth predictions were made.

Furthermore, results obtained from the active infrared thermography testing on concrete slabs in Chapter 5 suggest the time window between 5 to 15 minutes after the heating was terminated as the suitable time for collecting thermal infrared images to capture all delaminations on the thermal infrared images. However, the size of delaminations, as well as the depth influence the time of observation for each delamination and must be considered in predicting the effective time window for collecting thermal infrared images. The size of simulated delaminations in Chapter 5 were selected based on the AASHTO limits of 6 in. diameter delaminations, however the smallest size of delamination that creates concerns for bridge owners was not explicit from the available codes and standards, and further investigation is required to prove that infrared thermography meets the needs of bridge inspectors.

Another limitation of the active infrared thermography testing is the maximum depth at which the delamination can be detected using this technique. Results obtained from

Chapter 5 and the coring tests summarized in Appendix D showed that active infrared thermography works best for delaminations with the width to depth ratio of more than 2. Results from the coring test on the Silverbell Bridge beam confirmed that the depth of the delamination can be successfully predicted using active infrared thermography, however improper consolidation of concrete under the surface can create some discrepancies in the results obtained from infrared thermography.

This research confirms the capabilities of active infrared thermography in predicting the delaminations in concrete bridge elements and estimating the depth of the delamination as well as size and location. Using the surface heating method can reduce the time of inspection compared to the line heating method and allow for bridge inspection at any time during the day, not only for a limited time window as is the case for passive infrared thermography testing. Also, evaluating bridge elements that are not exposed to direct sunlight is more appropriate using an external heater. Limitations of the application of the active infrared thermography testing (using surface heating method) include, the non-uniform heating on the concrete surface and the need for deploying an external heater. Moreover, delaminations located at a depth shallower than 2 in. and with a width to depth ratio greater than 2 can be detectable using active infrared thermography. Further refinement of the data processing method prior to full implementation is recommended.

This research contributes to the current knowledge of the application of infrared thermography for concrete bridge inspection by introducing active infrared thermography and the surface heating method for concrete bridge evaluation. While a few previous studies had mostly focused on the line heating method which heats up the concrete surface for about 1 to 3 hours, this study concentrates on the application of the surface heating method in pulsed thermography which has only been previously used for FRP overlays and not an existing concrete structure. Also, this research confirmed the theory of the linear relationship between the square of the depth and observation time for concrete elements with proper consolidation. This research also provides additional evidence that active infrared thermography can be used for delaminations shallower than 2 in. deep, and with the width to depth ratio greater than 2. The procedure of estimating



the depth based on the results of an active infrared test on concrete structures and the discussion about the effects of the width to depth ratio in detecting delamination in concrete structures introduced a unique method of infrared thermography data interpretation and can serve as a base for future studies.

## **7.2 Future Works**

Several topics can be further investigated to enhance the certainty of using infrared thermography for concrete bridge inspections. These potential topics for further research are summarized below.

- Determining the effective time window for passive infrared thermography is one of the critical topics in infrared thermography surveys. Bridge inspectors should understand the most suitable time for using passive infrared thermography for bridge inspection and what kind of information may be missing if data are collected outside the optimal time window. A study should be conducted on concrete slabs with simulated delaminations of different sizes and depths at different times during the day or collect images with half an hour intervals between 10 am to 6 pm on the bridge decks to confirm the best time window for data collection. Environmental conditions at the time of data collection will affect the results and has to be properly recorded, especially overcast conditions and temperature variations on the day of data collection.
- The size and depth of the delamination are both factors that can influence the prediction of the optimal time window for passive infrared thermography inspections. Both factors need additional study for the most precise prediction of the best time window for data collection.
- Applying the active infrared thermography (pulse thermography) with the same method of depth and size prediction discussed in this dissertation should be applied during a field study, and capabilities and limitations should be discussed

to confirm the potential of this technology to be a useful tool for bridge inspections.

- One of the major concerns for applying the active infrared thermography in the field is the possible conflicts between the effects of sun and ambient temperature change in creating the temperature gradient, and the effects of an external heating source that is present for active infrared thermography test. Prediction of the depth and size of the delamination, and exploring the influence of the environmental condition in this prediction, needs to be further explored during field deployment studies.
- Heating sources with higher heating output and various distances between the heat source and the concrete bridge elements should be further investigated to identify the most suitable heat source for the field inspection and the practical distance between the heat source and the bridge element for accurate delamination detection.
- Other active infrared thermography techniques, such as inductive thermography and Vibrothermography, also have the potential to be applied for more detailed inspections, and further study on field deployment of these technologies would enhance the application of infrared thermography during bridge inspections.
- Generating a FE model of the heat transfer through the concrete slabs, bridge deck and girders can assist in generating a more precise model to predict the depth of the delamination. This model should be validated based on the results obtained from experimental laboratory and field studies.
- Determining the reliability of both passive and active infrared thermography as a nondestructive testing technique for concrete bridge evaluations can reduce the uncertainties in applying this technology during bridge inspections and create more confidence in adding this technology to the bridge inspector's tool box.

## References

- AASHTO, 2007. AASHTO LRFD Bridge Design Specification. *First Edition*. Washington D.C., American Association of State Highway and Transportation Officials.
- AASHTO, 2011. AASHTO Guide Manual for Bridge Element Inspection. *First Edition*, American Association of State Highway and Transportation Officials.
- Abdel-Qader, I., S. Yohali, O. Abudayyeh and S. Yehia, 2008. "Segmentation of thermal images for non-destructive evaluation of bridge decks." *NDT & E International*, 41, pp. 395-405.
- ACI, 2001. Protection of Metals in Concrete against Corrosion (ACI 222R). Farmington Hills, MI, American Concrete Institute.
- ACI, 2013. Report on Nondestructive Test Methods for Evaluation of Concrete in Structures (ACI 228.2R-13). Farmington Hills, MI, American Concrete Institute.
- Ahlborn, T. M., C. G. Gilbertson, H. Aktan and U. Attanayake, 2005. Condition Assessment and Methods of Abatement of Prestressed Concrete Box-Beam Deterioration, Michigan Department of Transportation.
- Ahlborn, T. M., R. Shuchman, L. L. Sutter, D. K. Harris, C. N. Brooks and J. W. Burns, 2012. Bridge Condition Assessment using Remote Sensors. *Final project report*. [www.mtti.mtu.edu/bridgecondition/](http://www.mtti.mtu.edu/bridgecondition/), USDOT/RITA. Cooperative agreement # DTOS59-10-H-00001.
- Allport, J. J. and S. L. McHugh, 1988. "Quantitative evaluation of transient video thermography." *Review of progress in quantitative nondestructive evaluation*, Plenum Press, New York, 7a, pp. 253-262.
- Arndt, R. W., 2010. "Square pulse thermography in frequency domain as adaptation of pulsed phase thermography for qualitative and quantitative applications in cultural heritage and civil engineering." *Infrared Physics and Technology*, 53, pp. 246-253.
- ASTM, 1997a. ASTM D4580-86: Standard Practice for Measuring Delaminations in Concrete Bridge Decks by Sounding, American Society of Testing Materials.
- ASTM, 1997b. ASTM C128: Standard Test Method for Specific Gravity and Absorption of Fine Aggregate, American Society of Testing Materials.
- ASTM, 1997c. ASTM C231: Standard Test Method for Air Content of Freshly Mixed Concrete by the Pressure Method, American Society of Testing Materials.

- ASTM, 1998. ASTM C1383-98: Standard Test Method for Measuring the P-Wave Speed and the Thickness of Concrete Plates Using the Impact-echo Method, American Society of Testing Materials.
- ASTM, 2000. ASTM C143: Standard Test Method for Slump of Hydraulic-Cement Concrete, American Society of Testing Materials.
- ASTM, 2001. ASTM C127-88: Standard Test Method for Specific Gravity and Absorption of Coarse Aggregate, American Society of Testing Materials.
- ASTM, 2007. ASTM D4788-03: Standard test method for detecting delaminations in bridge decks using infrared thermography, American Society of Testing Materials.
- ASTM, 2008. ASTM D6087-08: Standard Test Method for Evaluating Asphalt-Covered Concrete Bridge Decks Using Ground Penetrating Radar, American Society of Testing Materials.
- Baek, S., W. Xue and M. Q. Feng, 2012. "Nondestructive corrosion detection in RC through integrated heat induction and IR thermography." *Journal of Nondestructive Evaluation*, 31(2), pp. 181-190.
- Brachelet, F., T. Du, D. Defer and E. Antczak, 2009. Detection of poor filling in prestressed beams specimen by inductive thermography and transfer function analysis. *Nondestructive Testing in Civil Engineering*. Nantes, France.
- Brown, J. R. and H. R. Hamilton, 2007. "Heating Methods and Detection Limits for Infrared Thermography Inspection of Fiber-Reinforced Polymer Composites." *ACI Material Journal*, 104(5), pp. 481-490.
- Clark, M. R., D. M. McCann and M. C. Forde, 2003. "Application of Infrared thermography to the non-destructive testing of concrete and masonry bridges." *NDT & E International*, 36, pp. 265-275.
- Crowe, G. V., 2009. *An introduction to nondestructive testing*, Columbus, OH, The American Society of Nondestructive Testing, Inc.
- Engineering ToolBox. "Thermal Conductivity of Some Common Material and Gases." Retrieved October 30th, 2012, from [http://www.engineeringtoolbox.com/thermal-conductivity-d\\_429.html](http://www.engineeringtoolbox.com/thermal-conductivity-d_429.html).
- FHWA, 1995. Recording and Coding Guide for Structure Inventory and Appraisal of the Nation's Bridges.
- FHWA. 2012. "National Bridge Inventory (NBI)." Retrieved March, 2013, from <http://www.fhwa.dot.gov/bridge/nbi/deck.cfm>.

- Fu, G., Ed., 2005. *Inspection and monitoring techniques for bridges and civil structures*. Cambridge, England, Woodhead Publishing in Materials.
- Ghosh, K. K. and V. M. Karbhari, 2006. "A critical review of infrared thermography as a method for non-destructive evaluation of FRP rehabilitated structures." *International Journal of Materials and Product Technology*, 25(4), pp. 241-266.
- Gucunski, N., A. Imani, F. Romero, S. Nazarian, D. Yuan, H. Wiggenhauser, P. Shokouhi, A. Taffe and D. Kutrubes, 2013. Nondestructive testing to identify concrete bridge deck deterioration. *SHRP2*. Washington, D.C.
- Halabe, U. B., H.-L. R. Chen, V. Bhandarkar and Z. Sami, 1997. "Detection of Sub-Surface Anomalies in Concrete Bridge Decks using Ground Penetrating Radar." *ACI Materials Journal*, 94(5), pp. 396-408.
- Halabe, U. B., H. V. S. GangaRao and N. Perisetty, 2012. Infrared Thermography and GPR Techniques for Condition Assessment of RC Bridges. *NDT/NDE for Highways and Bridges: Structural Materials Technology (SMT)*. New York City, NY.
- Hover, K. C., S. E. Burlingame and C. H. Lutz, 2004. "Opportunities and Challenges in Concrete with Thermal Imaging." *Concrete International*, December 2004, pp. 23-27.
- Jana, D., 2007. "Delamination - A State of The Art Review", *Proceedings of the Twenty-Ninth Conference on Cement Microscopy* Quebec City, PQ, Canada.
- Jenson, J., 2007. *Remote sensing of the environment: an earth resource perspective*, Pearson Education, Inc.
- Kee, S.-H., T. Oh, J. S. Popovics, R. W. Arndt and J. Zhu, 2012. "Nondestructive Bridge Deck Testing with Air-Coupled Impact-Echo and Infrared Thermography." *ASCE Journal of Bridge Engineering*, 17(6), pp. 928-939.
- Kurita, K., M. Oyado, H. Tanaka and S. Tottori, 2009. "Active infrared thermographic inspection technique for elevated concrete structures using remote heating system." *Infrared Physics and Technology*, 52, pp. 208-213.
- Lamond, J. F. and J. H. Pielert, Eds., 2006. *Significance of Test and Properties of Concrete and Concrete-Making materials*. Bridgeport, NJ, ASTM International.
- Levar, J. M. and H. R. Hamilton, 2003. "Nondestructive evaluation of carbon fiber-reinforced polymer-concrete bond using infrared thermography." *ACI Material Journal*, 100(1), pp. 63-72.

- Maierhofer, C., R. Arndt and M. Rolling, 2007. "Influence of concrete properties on the detection of voids with impulse-thermography." *Infrared Physics and Technology*, 49, pp. 213-217.
- Maierhofer, C., R. Arndt, M. Rolling, C. Rieck, A. Walther, H. Scheel and B. Hillemeier, 2006. "Application of impulse-thermography for non-destructive assessment of concrete structures." *Cement and Concrete Composites*, 28, pp. 393-401.
- Maierhofer, C., A. Brink, M. Rolling and H. Wiggerhauser, 2002. "Transient thermography for structural investigation of concrete and composites in the near surface region." *Infrared Physics and Technology*, 43, pp. 271-278.
- Maldague, X. P. V., 1993. *Nondestructive evaluation of materials by infrared thermography*, London, Springer-Verlag.
- Maldague, X. P. V., 2001. *Theory and practice of infrared thermography for nondestructive testing*, John Wiley and Sons, INC.
- Maldague, X. P. V. and P. O. Moore, 2001. *Nondestructive Testing Handbook: Infrared and Thermal Testing*, American Society for Nondestructive Testing.
- Markow, M. J. and W. A. Hyman, 2009. Bridge Management Systems for Transportation Agency Decision Making, National Cooperative Highway Research Program. 397.
- Maser, K., N. Martino, J. Doughty and R. Birken, 2012. "Understanding and Detecting Bridge Deck Deterioration with Ground-Penetrating Radar." *Transportation Research Record*, 2313, pp. 116-123.
- MDOT, 2003. Standard Specifications for Construction. Lansing, Michigan, Michigan Department of Transportation.
- MDOT. 2008. "Typical Work Activities for Bridge Preservation Components." Lansing, MI. Retrieved October 2012, from [http://www.michigan.gov/documents/mdot/MDOT\\_BridgePreservationActivities\\_343736\\_7.pdf](http://www.michigan.gov/documents/mdot/MDOT_BridgePreservationActivities_343736_7.pdf).
- MDOT. 2009. "Project Scoping Manual." Lansing, MI. Retrieved October 2012, from [http://www.michigan.gov/documents/mdot/mdot\\_design\\_svc\\_scoping\\_manual\\_chpt\\_07\\_331753\\_7.pdf](http://www.michigan.gov/documents/mdot/mdot_design_svc_scoping_manual_chpt_07_331753_7.pdf).
- MDOT. 2011a. "Bridge Safety Inspection NBI Rating Guidelines." Lansing, MI. Retrieved October 2012, from [http://www.michigan.gov/documents/mdot/MDOT\\_BIR\\_Ratings\\_Guide\\_367482\\_7.pdf](http://www.michigan.gov/documents/mdot/MDOT_BIR_Ratings_Guide_367482_7.pdf).

- MDOT. 2011b. "Bridge Deck Preservation Matrix." Lansing, MI. Retrieved July 2012, from [http://www.michigan.gov/documents/mdot/MDOT\\_BridgeDeckMatrix\\_withUncoatedBlackRebar\\_355077\\_7.pdf](http://www.michigan.gov/documents/mdot/MDOT_BridgeDeckMatrix_withUncoatedBlackRebar_355077_7.pdf).
- MDOT, 2011c. Prestressed Concrete Box-Beam Superstructure Evaluation Handbook. Center for Structural Durability, Michigan Technological University, Houghton, MI, for the Michigan Department of Transportation.
- Moore, M., B. Phares, B. Graybeal, D. Rolander and G. Washer, 2000. Reliability of visual inspection for highway bridges, NDE Validation Center/FHWA.
- Morey, R. M., 1998. Ground Penetrating Radar for Evaluating Subsurface Conditions for Transportation Facilities. Washington D.C., National Academy Press, Transportation Research Board. Synthesis of Highway Practices 255.
- Naito, C., R. Sause, I. Hodgson, S. Pessiki and T. Macioce, 2010. "Forensic Examination of a Noncomposite Adjacent Precast Prestressed Concrete Box Beam Bridge." *ASCE Journal of Bridge Engineering*, 15(4), pp. 408-418.
- PCI, 1997. Prestressed Precast Concrete Institute Bridge Design Manual *AASHTO/PCI Standard Products-Appendix B*. Chicago, IL, Prestressed/Precast Concrete Institute.
- PCI, 2011. The State of the Practice of Precast/Prestressed Adjacaent Box Beam Bridges. Chicago, IL, Prestressed/Precast Concrete Institute.
- Pollock, D. G., K. J. Dupuis, B. Lacour and K. R. Olsen, 2008. Detection of Voids in Prestressed Concrete Bridges using Thermal Imaging and Ground Penetrating Radar, Washington State University.
- Russell, H. G., 2009. Adjacent Precast Concrete Box Beam Bridges: Connection Details, National Cooperative Highway Research Program. 393.
- Ryan, T. W., R. A. Hartle, J. Eric Mann and L. J. Danovich, 2006. Bridge Inspector's Reference Manual. Washington D.C., FHWA.
- Sakagami, T. and S. Kubo, 2002. "Development of a new non-destructive testing technique for quantitative evaluations of delamination defects in concrete strudtures based on phase delay measurement using lock-in thermography." *Infrared Physics and Technology*, 43, pp. 311-316.
- Scott, M., A. Rezaizadeh, A. Delahaza, C. G. Santos, M. Moore, B. Graybeal and G. Washer, 2003. "A comparison of nondestructive evaluation methods for bridge deck assessment." *NDT & E International*, 36, pp. 245-255.

- Shokouhi, P., J. Wostmann, G. Schneider, B. Milmann, A. Taffe and H. Wiggerhauser, 2011. "Nondestructive detection of delamination in concrete slabs: a multi-method investigation." *Transportation Research Record*, 2251, pp. 103-113.
- Spring, R., R. Huff and M. Schwoegler, 2011. "Infrared Thermography: A Versatile Nondestructive Testing Technique." *Materials Evaluation*, 69(8), pp. 935-942.
- Starnes, M. A., 2002. Development of technical bases for using infrared thermography for nondestructive evaluation of fiber reinforced polymer composites bonded to concrete. *Civil and Environmental Engineering*, Massachusetts Institute of Technology. PhD.
- Starnes, M. A. and N. J. Carino, 2005. "Active Infrared Thermography for NDT of Concrete Structures Strengthened with Fiber Reinforced Polymer." *Materials Evaluation*, pp. 56-63.
- Starnes, M. A., N. J. Carino and E. A. Kausel, 2003. "Preliminary Thermography Studies for Quality Control of Concrete Structures Strengthened with Fiber-Reinforced Polymer Composites." *ASCE Journal of Materials in Civil Engineering*, 15(3), pp. 266-273.
- TransSystems Corporation, 2011. Asset Management Guide for Local Agency Bridges in Michigan Michigan Transportation Asset Management Council.
- Vaghefi, K., T. M. Ahlborn, D. K. Harris and C. N. Brooks, 2013. "Combined Imaging Technologies for Concrete Bridge Deck Condition Assessment." *ASCE Journal of Performance of Constructed Facilities*, Accepted April 2013, <http://ascelibrary.org/doi/abs/10.1061/%28ASCE%29CF.1943-5509.0000465>.
- Vaghefi, K., R. C. Oats, D. K. Harris, T. M. Ahlborn, C. N. Brooks, K. Endsley, C. Roussi, R. Shuchman, J. W. Burns and R. Dobson, 2012. "Evaluation of Commercially Available Remote Sensors for Highway Bridge Condition Assessment." *ASCE Journal of Bridge Engineering*, 17(6), pp. 886-895.
- Van Leeuwen, J., M. Nahant and S. Paez, 2011. "Study of pulsed phase thermography for the detection of honeycombing defects in concrete structures", *NDT&E of Composite Materials*.
- Vavilov, V. P. and R. Taylor, 1982. "Theoretical and Practical Aspects of the Thermal Nondestructive Testing of Bonded Structures." *Research Techniques in NDT: Academy Press*, 5, pp. 238-279.
- Vedula, S., 2010. Infrared Thermography and Ultrasonic Inspection of Adhesive Bonded Structures, Overview and validity. *Mechanical Engineering*, Clemson University. Master of Science.



Washer, G., 2010. Thermal Imaging of Damage in Bridge Soffits. *NDE/NDT for Highways and Bridges Structural Materials Technology* NYC.

Washer, G., R. Fenwick and N. Bolleni, 2009a. Development of hand-held thermographic inspection technologies. *Final Report*, Missouri Department of Transportation. RI06-038/OR10.007.

Washer, G., R. Fenwick, N. Bolleni and J. Harper, 2009b. "Effects of environmental variable on infrared imaging subsurface features of concrete bridges." *Journal of the Transportation Research Board*, 2108, pp. 107-114.



# Appendices

## Appendix A – Passive Thermography Field Demonstration Results

### *Freer Rd. Bridge*

Cell No.	Delaminated area (ft <sup>2</sup> )				Correspondence (%)		
	Thermal IR	Sounding	Overlapped	Total	Thermal IR	Sounding	Total
I22							
I21							
I20							
I19	0.0004						
I18							
I17							
I16		0.0002		0.0002			
I15							
I14							
I13							
H22							
H21							
H20							
H19	0.7397			0.7398			
H18							
H17							
H16							
H15							
H14							
H13							
H12	0.8109	2.0397	0.5703	2.2802	70.33	27.96	25.01
H11		1.6224		1.6224			
H10	1.2190	0.7457	0.1755	1.7886	14.40	23.53	9.81
H9	0.2615	1.3253		1.5869	0.00	0.00	0.00
H8							
H7							
H6							
H5							
H4							
H3							
G22							
G21							
G20							
G19							
G18							
G17							
G16							
G15							
G14							
G13							
G12							
G11							

Cell No.	Delaminated area (ft <sup>2</sup> )				Correspondence (%)		
	Thermal IR	Sounding	Overlapped	Total	Thermal IR	Sounding	Total
G10	1.0382	1.0656	0.3218	1.7828	31.00	30.20	18.05
G9		0.9935		0.9935			
G8							
G7							
G6							
G5							
G4	0.6377	0.7071	0.4301	0.9145			
G3	0.8910	2.3334	0.5263	2.6982	59.07	22.56	19.51
G2							
G1							
F22							
F21							
F20	1.7844	8.6876	1.6707	8.8001	93.63	19.23	18.99
F19	1.3173	6.8428	1.3173	6.8425	100.00	19.25	19.25
F18	1.3389	3.5024	0.8777	3.9635	65.55	25.06	22.14
F17	1.4808	4.9854	1.2754	5.1908	86.13	25.58	24.57
F16	0.3270	2.3277		2.6547	0.00	0.00	0.00
F15	0.3145	4.1930	0.2678	4.2395	85.15	6.39	6.32
F14							
F13	0.0027			0.0000			
F12							
F11							
F10	0.3524			0.3524			
F9	0.0598						
F8							
F7							
F6							
F5							
F4							
F3	0.4718			0.4718			
F2							
F1							
E22							
E21							
E20							
E19							
E18	0.0220			0.0220			
E17	0.0941	0.3513	0.0877	0.3575	93.20	24.96	24.53
E16	0.5920	0.2638		0.8558			
E15	0.2580	1.5101	0.2015	1.5665	78.10	13.34	12.86
E14							
E13	4.8715	7.4574	3.5404	8.7877	72.68	47.47	40.29
E12							
E11	0.5623	1.4853	0.1419	1.9057	25.24	9.55	7.45
E10	5.0552	6.6901	1.6515	10.0929	32.67	24.69	16.36
E9	0.1500	2.4421	0.0417	2.5503	27.80	1.71	1.64
E8	0.6240	1.9586		2.5825			
E7	0.6945			0.6947			

Cell No.	Delaminated area (ft <sup>2</sup> )				Correspondence (%)		
	Thermal IR	Sounding	Overlapped	Total	Thermal IR	Sounding	Total
E6	0.1014			0.1014			
E5	1.4720	4.1312	1.0352	4.5681	70.33	25.06	22.66
E4		3.7551		3.7551			
E3	0.0804	10.9211		11.0015			
E2		1.7106		1.7106			
E1							
D22							
D21		0.1188		0.1188			
D20							
D19							
D18							
D17							
D16							
D15							
D14							
D13							
D12							
D11	0.0536			0.0536			
D10	0.0492	0.0058		0.0550			
D9							
D8	1.1033			1.1033			
D7	0.4162			0.4161			
D6							
D5							
D4		3.8114		3.8114			
D3		1.0385		1.0385			
D2		4.7718		4.7718			
D1		3.9982		3.9982			
C22							
C21		0.6857		0.6857			
C20							
C19							
C18							
C17							
C16							
C15							
C14							
C13							
C12							
C11							
C10							
C9							
C8							
C7							

Cell No.	Delaminated area (ft <sup>2</sup> )				Correspondence (%)		
	Thermal IR	Sounding	Overlapped	Total	Thermal IR	Sounding	Total
C6							
C5							
C4							
C3							
C2							
C1							
B13							
B12							
B11							
B10							
B9							
B8							
B7							
B6							
B5							
B4							
B3							
B2							
B1							
A4							
A3							
A2							
A1							
Total	29.2477	98.4787	14.1328	116.7844	48.32	13.89	12.09

Delaminated area outside the grid line 3.2573

***Willow Rd. Bridge***

Cell No.	Delaminated area (ft <sup>2</sup> )				Correspondence (%)		
	Thermal IR	Sounding	Overlapped	Total	Thermal IR	Sounding	Total
V6				0			
V5	0.1362			0.1362			
V4		0.93		0.93			
V3		0.3538		0.3538			
V2	1.1607			1.1607			
V1		0.0192		0.0192			
U6				0			
U5	0.0337			0.0337			
U4		0.0257		0.0257			
U3		0.057		0.057			
U2	1.2566	3.2968		4.5534			
U1	0.7588	3.2576	0.1519	3.8633	20.02	4.66	3.93
T6				0			
T5				0			
T4		0.0585		0.0585			
T3				0			
T2	0.0006			0.0006			
T1	0.51	0.0097		0.5197			
S6		0.0084		0.0084			
S5				0			
S4	3.039	0.0295		3.0685			
S3	2.1049			2.1049			
S2	0.0045	0.0127		0.0172			
S1		0.0156		0.0156			
R6		3.265		3.265			
R5	1.5136	1.2344	0.8328	1.9146	55.02	67.47	43.50
R4	1.3233	1.9699		3.2932	0.00	0.00	0.00
R3	11.0645	2.848	0.0433	13.8692	0.39	1.52	0.31
R2	1.0017	0.4856	0.0003	1.487	0.03	0.06	0.02
R1		0.2684		0.2684			
Q7				0			
Q6		2.189		2.189			
Q5	1.5264	2.8825	0.6681	3.74	43.77	23.18	17.86
Q4	0.3939	2.678	0.1028	2.9672	26.10	3.84	3.46
Q3	2.1736			2.1736			
Q2	1.9915	3.3349	1.1046	4.2208	55.47	33.12	26.17
Q1		1.5883		1.5883			
P7		0.0113		0.0113			
P6				0			
P5				0			
P4	0.4526	0.0428		0.4954			
P3	4.1714	3.6666		7.838			
P2	3.2912	1.4898		4.781			
P1				0			
O7		1.6723		1.6723			

Cell No.	Delaminated area (ft <sup>2</sup> )				Correspondence (%)		
	Thermal IR	Sounding	Overlapped	Total	Thermal IR	Sounding	Total
O6	1.1165	0		1.1165			
O5	1.606	0		1.606			
O4	5.1327	4.3911	1.4976	8.0262	29.18	34.11	18.66
O3	5.3707	7.4144	1.5015	11.2828	27.96	20.25	13.31
O2	0.0792	0		0.0792			
O1		0.006		0.006			
N7		0.7425		0.7425			
N6	5.9642	0.9899		6.9541			
N5	1.6984	0		1.6984			
N4	1.3262	2.5504	0.4583	3.4184	34.56	17.97	13.41
N3	0.5275	0.5809	0.0207	1.0878	3.92	3.56	1.90
N2	4.7165	2.2696	0.4893	6.4964	10.37	21.56	7.53
M7		0		0			
M6	0.0204	0		0.0204			
M5	16.3657	0		16.365			
M4	2.7955	1.353	0.0717	4.0768	2.56	5.30	1.76
M3	0.0227	0.7091	0.0168	0.7152	74.01	2.37	2.35
M2	1.0874	4.3327	0.4283	4.991	39.39	9.89	8.58
L7		1.5152		1.5152			
L6		0		0			
L5	0.0531	1.301		1.3541			
L4	0.0144	1.5485	0.0021	1.561	14.58	0.14	0.13
L3	1.4549	3.0811	0.0782	4.4579	5.37	2.54	1.75
L2	0.8876	5.5094	0.4062	5.9906	45.76	7.37	6.78
K7	2.0531	1.5936		3.6467			
K6	0.3941	0		0.3941			
K5	0.1825	0.0454		0.2279			
K4	4.2986	0		4.2986			
K3	0.0756	0.3498	0.0756	0.3497	100.00	21.61	21.62
K2	0.1121	0.8934	0.1119	0.8934	99.82	12.53	12.53
J8		0		0			
J7	0.6742	2.8721		3.5463	0.00	0.00	0.00
J6		0		0			
J5	0.121	0.0566		0.1776			
J4	6.1105	1.6518		7.7623	0.00	0.00	0.00
J3		0		0			
J2		0		0			
I8		0		0			
I7	1.6193	0.3388		1.9581	0.00	0.00	0.00
I6	0.6013	0.6522	0.1256	1.1276	20.89	19.26	11.14
I5	0.1617	1.6504	0.0052	1.8071	3.22	0.32	0.29
I4	0.9799	2.6085	0.3766	3.2116	38.43	14.44	11.73
I3	1.4058	0		1.4058			
I2		0		0			
H8		0		0			



Cell No.	Delaminated area (ft <sup>2</sup> )				Correspondence (%)		
	Thermal IR	Sounding	Overlapped	Total	Thermal IR	Sounding	Total
H7	1.3669	3.5331	0.1233	4.7767	9.02	3.49	2.58
H6	3.9983	2.7079	0.0477	6.6585	1.19	1.76	0.72
H5	0.1675	1.183		1.3505	0.00	0.00	0.00
H4	2.4216	5.5525	0.0974	7.8764	4.02	1.75	1.24
H3	1.0425	1.2038	0.0158	2.2306	1.52	1.31	0.71
H2		0		0			
G8		0.0303		0.0303			
G7	4.9148	5.4019	2.3336	7.983	47.48	43.20	29.23
G6	1.9741	0.2586	0.0023	2.2303	0.12	0.89	0.10
G5	1.1839	0.6026	0.4256	1.3608	35.95	70.63	31.28
G4	4.434	5.7178	3.242	6.9084	73.12	56.70	46.93
G3	1.004	4.3975	0.7552	4.6457	75.22	17.17	16.26
G2		0		0			
F8		0		0			
F7	0.0328	0		0.0328			
F6	3.8064	1.7298	0.4597	5.0755	12.08	26.58	9.06
F5	1.7719	0.8682	0.123	2.5172	6.94	14.17	4.89
F4	0.9883	1.1259	0.6743	1.4383	68.23	59.89	46.88
F3	1.8429	0.8459	0.4725	2.216	25.64	55.86	21.32
E8		0.0062		0.0062			
E7	0.0534	0		0.0534			
E6	2.0779	0.8209		2.8988			
E5	0.0411	0.1636		0.2047			
E4	0.7891	0		0.7891			
E3	0.189	0		0.189			
D8		0		0			
D7	0.3198	0		0.3198			
D6	1.3247	0.8318	0.1459	2.0106	11.01	17.54	7.26
D5		0.0195		0.0195			
D4	3.6249	0		3.6249			
D3	0.5299	0.0163		0.5462			
C8	1.1019	0		1.1019			
C7	0.0454	0		0.0454			
C6		0.0828		0.0828			
C5	0.13	0		0.13			
C4	2.1617	0		2.1617			
C3		0		0			
B9		0.1174		0.1174			
B8	0.3322	0.9364		1.2686			
B7	0.0686	0		0.0686			
B6		0.0123		0.0123			
B5	0.0005	0.9542		0.9547			
B4	7.1077	0		7.1077			
B3		0		0			
A9		0		0			

Cell No.	Delaminated area (ft <sup>2</sup> )				Correspondence (%)		
	Thermal IR	Sounding	Overlapped	Total	Thermal IR	Sounding	Total
A8		0		0			
A7		0		0			
A6		0		0			
A5		0		0			
A4	0.044	0		0.044			
A3		0		0			
Total	157.8297	127.8289	17.4877	299.8847	11.08	10.96	5.83

Delaminated area  
outside the grid line 31.71384

**Mannsiding Rd. Bridge**

Cell No.	Delaminated area (ft <sup>2</sup> )				Correspondence (%)		
	Thermal IR	Sounding	Overlapped	Total	Thermal IR	Sounding	Total
A1							
A2							
A3							
A4							
A5							
A6							
A7							
A8							
B1							
B2							
B3							
B4	1.0296			1.03			
B5							
B6							
B7							
B8							
C2							
C3							
C4	1.0044			1.00			
C5	2.6585			2.66			
C6							
C7							
C8							
C9							
D2							
D3		2.7832		2.78			
D4		1.3343		1.33			
D5	3.6493			3.65			
D6	0.0014			0.00			
D7							
D8							
D9							
D10							
E3	0.1651	0.2507	0.0055	0.41	3.33	2.19	1.34
E4	2.6975	6.238	0.5725	8.36	21.22	9.18	6.85
E5	1.707	0.1536	0.0042	1.86	0.25	2.73	0.23
E6	2.4473			2.45	0.00		0.00
E7							
E8							
E9							
E10							
F4							
F5	0.3414	8.0088	0.3215	8.03	94.17	4.01	4.00
F6	0.9598	10.9628	0.7557	11.17	78.74	6.89	6.77

Cell No.	Delaminated area (ft <sup>2</sup> )				Correspondence (%)		
	Thermal IR	Sounding	Overlapped	Total	Thermal IR	Sounding	Total
F7	1.5862	8.6017	0.5696	9.62	35.91	6.62	5.92
F8							
F9							
F10							
F11							
G4							
G5		5.8969		5.90		0.00	0.00
G6	0.9524	16.0474	0.9524	16.05	100.00	5.93	5.93
G7	2.2819	6.3223	1.5338	7.07	67.22	24.26	21.69
G8	2.1753	3.2285	1.0718	4.33	49.27	33.20	24.74
G9							
G10							
G11							
G12							
H5							
H6	14.8967	3.2383	0.3374	17.80	2.26	10.42	1.90
H7	4.6945	1.5688	0.0188	6.24	0.40	1.20	0.30
H8	6.2095	8.7542	3.69	11.27	59.43	42.15	32.73
H9							
H10							
H11							
H12							
H13							
I6	1.5878	1.0618	0.0296	2.62	1.86	2.79	1.13
I7	10.4492	8.4951	1.1524	17.79	11.03	13.57	6.48
I8	0.1018	3.4414		3.54	0.00	0.00	0.00
I9	3.4151	9.0902	1.7134	10.79	50.17	18.85	15.88
I10	3.2082			3.21	0.00		0.00
I11							
I12							
I13							
J6							
J7	5.2891			5.29			
J8	16.4208			16.42			
J9	0.6836			0.68			
J10	6.3865	6.6552	2.0359	11.01	31.88	30.59	18.50
J11	1.1077	0.5635	0.0376	1.63	3.39	6.67	2.30
J12							
J13							
J14							
K7							
K8	9.4515	2.857	2.3462	9.96	24.82	82.12	23.55
K9	5.2866	2.4108	0.4238	7.27	8.02	17.58	5.83
K10	6.045	9.3342	3.8545	11.52	63.76	41.29	33.45

Cell No.	Delaminated area (ft <sup>2</sup> )				Correspondence (%)		
	Thermal IR	Sounding	Overlapped	Total	Thermal IR	Sounding	Total
K11	3.3068			3.31			
K12	1.2084			1.21			
K13							
K14							
K15							
L8							
L9							
L10							
L11	0.455			0.46			
L12	5.0713			5.07			
L13	0.7771			0.78			
L14							
L15							
M9							
M10				0.00			
M11	0.0032			0.00			
M12	0.7299			0.73			
M13	2.2349			2.23			
M14							
M15							
M16							
N9							
N10							
N11							
N12	0.2392			0.24			
N13	2.5549			2.55			
N14	0.6551			0.66			
N15							
N16							
N17							
O10							
O11							
O12							
O13							
O14							
O15							
O16							
O17							
P11							
P12							
P13							
P14							
P15							
P16							

Cell No.	Delaminated area (ft <sup>2</sup> )				Correspondence (%)		
	Thermal IR	Sounding	Overlapped	Total	Thermal IR	Sounding	Total
P17							
Total	136.1265	127.2987	21.43	242.00	21.68	16.83	8.85

# Appendix B – Silverbell Bridge Inspection Reports

Form 1717A- 01/2002

**Michigan Department of Transportation**  
**Structure Inventory and Appraisal**

Control Section

MDOT Bridge ID   
 83 2 8010301R01

NBI Bridge ID  Struct Num  Region  TSC County  City Resp  City Location  7- Facility Carried  User Name   
 83280103000R010 8191 07 7B 83 0 SILVER BELL TRAHEYAMY

6- Feature Intersected  9- Location  Latitude  Longitude  Owner  Maint Resp   
 GTW RR EAST OF GIDDINGS 42° 43' 21.65" 83° 15' 24.12" 2 2

Bridge History, Type, Materials	Route Carried By Structure (ON Record)	Route Under Structure (UNDER Record)
27- Year Built <span style="float: right;">1981</span>	5A- Record Type <span style="float: right;">1</span>	5A- Record Type <span style="float: right;"></span>
106- Year Reconstructed	5B- Route Signing <span style="float: right;">4</span>	5B- Route Signing <span style="float: right;"></span>
202- Year Painted	5C- Level of Service <span style="float: right;">0</span>	5C- Level of Service <span style="float: right;"></span>
203- Year Overlay	5D- Route Number <span style="float: right;">02059</span>	5D- Route Number <span style="float: right;"></span>
43- Main Span Bridge Type <span style="float: right;">1 05</span>	5E- Direction Suffix <span style="float: right;">0</span>	5E- Direction Suffix <span style="float: right;"></span>
44- Appr Span Bridge Type <span style="float: right;">1 05</span>	10L- Best 10ft Uncl- Lt <span style="float: right;">0 0</span>	10L- Best 10ft Uncl- Lt <span style="float: right;"></span>
77- Steel Type <span style="float: right;">0</span>	10R- Best 10ft Uncl- Rt <span style="float: right;">99 99</span>	10R- Best 10ft Uncl- Rt <span style="float: right;"></span>
78- Paint Type <span style="float: right;">0</span>	PR Number <span style="float: right;"></span>	PR Number <span style="float: right;"></span>
79- Rail Type <span style="float: right;">4</span>	Control Section <span style="float: right;"></span>	Control Section <span style="float: right;"></span>
80- Post Type <span style="float: right;"></span>	11- Mile Point <span style="float: right;"></span>	11- Mile Point <span style="float: right;"></span>
107- Deck Type <span style="float: right;">1</span>	12- Base Highway Network <span style="float: right;">0</span>	12- Base Highway Network <span style="float: right;"></span>
108A- Wearing Surface <span style="float: right;">3</span>	13- LRS Route-Subroute <span style="float: right;">0000006261 00</span>	13- LRS Route-Subroute <span style="float: right;"></span>
108B- Membrane <span style="float: right;">0</span>	19- Detour Length <span style="float: right;">0</span>	19- Detour Length <span style="float: right;"></span>
108C- Deck Protection <span style="float: right;">1</span>	20- Toll Facility <span style="float: right;">3</span>	20- Toll Facility <span style="float: right;"></span>
	26- Functional Class <span style="float: right;">17</span>	26- Functional Class <span style="float: right;"></span>
	28A- Lanes On <span style="float: right;">4</span>	28B- Lanes Under <span style="float: right;"></span>
	29- ADT <span style="float: right;">13220</span>	29- ADT <span style="float: right;"></span>
	30- Year of ADT <span style="float: right;">2006</span>	30- Year of ADT <span style="float: right;"></span>
	32- Appr Roadway Width <span style="float: right;">52</span>	42B- Service Type Under <span style="float: right;">2</span>
	32A/B- Ap Pvt Type/Width <span style="float: right;">6   52.0</span>	47L- Left Horizontal Clear <span style="float: right;"></span>
	42A- Service Type On <span style="float: right;">1</span>	47R- Right Horizontal Clear <span style="float: right;"></span>
	47L- Left Horizontal Clear <span style="float: right;">0.0</span>	54A- Left Feature <span style="float: right;">R</span>
	47R- Right Horizontal Clear <span style="float: right;">62.0</span>	54B- Left Underclearance <span style="float: right;"> </span>
	53- Min Vert Clr Ov Deck <span style="float: right;">99   99</span>	54C- Right Feature <span style="float: right;">R</span>
	100- STRAHNET <span style="float: right;">0</span>	54D- Right Underclearance <span style="float: right;">0   0</span>
	102- Traffic Direct <span style="float: right;">2</span>	Under Clearance Year <span style="float: right;"></span>
	109- Truck % <span style="float: right;">8</span>	55A- Reference Feature <span style="float: right;">R</span>
	110- Truck Network <span style="float: right;">0</span>	55B- Right Horiz Clearance <span style="float: right;">4-6</span>
	114- Future ADT <span style="float: right;">17805</span>	56- Left Horiz Clearance <span style="float: right;">0.0</span>
	115- Year Future ADT <span style="float: right;">2026</span>	100- STRAHNET <span style="float: right;"></span>
	Freeway <span style="float: right;">0</span>	101- Traffic Direction <span style="float: right;"></span>
		109- Truck % <span style="float: right;"></span>
		110- Truck Network <span style="float: right;"></span>
		114- Future ADT <span style="float: right;"></span>
		115- Year Future ADT <span style="float: right;"></span>
		Freeway <span style="float: right;"></span>

Structure Dimensions	
34- Skew <span style="float: right;">42</span>	
35- Struct Flared <span style="float: right;">0</span>	
45- Num Main Spans <span style="float: right;">1</span>	
46- Num Appr Spans <span style="float: right;">2</span>	
48- Max Spar Length <span style="float: right;">72.8</span>	
49- Structure Length <span style="float: right;">221.8</span>	
50A- Width Left Curb/SW <span style="float: right;">4.9</span>	
50B- Width Right Curb/SW <span style="float: right;">4.9</span>	
33- Median <span style="float: right;">0</span>	
51- Width Curb to Curb <span style="float: right;">52.2</span>	
52- Width Out to Out <span style="float: right;">64.3</span>	
112- NBIS Length <span style="float: right;">Y</span>	

Inspection Data	
90- Inspection Date <span style="float: right;">03/10/2010</span>	
91- Inspection Freq <span style="float: right;">6</span>	
92A- Frac Crit Req/Freq <span style="float: right;">N</span>	
93A- Frac Crit Insp Date <span style="float: right;"></span>	
92B- Und Water Req/Freq <span style="float: right;">N</span>	
93B- Und Water Insp Date <span style="float: right;"></span>	
92C- Oth Spec Insp Req/Freq <span style="float: right;">N</span>	
93C- Oth Spcp Insp Date <span style="float: right;"></span>	
176A- Und Water Insp Method <span style="float: right;">0</span>	
58- Deck Rating <span style="float: right;">4</span>	
58A- Deck Surface Rtg <span style="float: right;">4</span>	
59- Superstructure Rating <span style="float: right;">2</span>	
59A- Paint Rating <span style="float: right;">N</span>	
60- Substructure Rating <span style="float: right;">3</span>	
61- Channel Rating <span style="float: right;">N</span>	
62- Culvert Rating <span style="float: right;">N</span>	

Structure Appraisal	
36A- Bridge Railing <span style="float: right;">1</span>	
36B- Rail Transition <span style="float: right;">1</span>	
36C- Approach Rail <span style="float: right;">0</span>	
36D- Rail Termination <span style="float: right;">1</span>	
67- Structure Evaluation <span style="float: right;">2</span>	
68- Deck Geometry <span style="float: right;">4</span>	
69- Underclearance <span style="float: right;">N</span>	
71- Waterway Adequacy <span style="float: right;">N</span>	
72- Approach Alignment <span style="float: right;">8</span>	
103- Temporary Structure <span style="float: right;"></span>	
113- Scour Criticality <span style="float: right;">N</span>	

Proposed Improvements	
75- Type of Work <span style="float: right;"></span>	
76- Length of Improvement <span style="float: right;"></span>	
94- Bridge Cost <span style="float: right;"></span>	
95- Roadway Cost <span style="float: right;"></span>	
96- Total Cost <span style="float: right;"></span>	
97- Year of Cost Estimate <span style="float: right;"></span>	

Load Rating and Posting	
31- Design Load <span style="float: right;">6</span>	
41- Open, Posted, Closed <span style="float: right;">P</span>	
63- Oper Rtg Method <span style="float: right;">2</span>	
64F- Fed Operating Rtg <span style="float: right;">28.7</span>	
64M- Mich Oper Rtg <span style="float: right;">9   45</span>	
65- Inv Rtg Method <span style="float: right;">2</span>	
66- Inventory Load <span style="float: right;">10.6</span>	
70- Posting <span style="float: right;">0</span>	
141- Posted Loading <span style="float: right;">334345</span>	
195- Analysis ID <span style="float: right;"></span>	
193- Overload Class <span style="float: right;"></span>	

Navigation Data	
38- Navigation Control <span style="float: right;">N</span>	
39- Vertical Clearance <span style="float: right;">0.0</span>	
40- Horizontal Clearance <span style="float: right;">0.0</span>	
111- Pier Protection <span style="float: right;"></span>	
116- L/R Bldg Vert Clear <span style="float: right;"></span>	

Miscellaneous	
37- Historical Significance <span style="float: right;">5</span>	
98A- Border Bridge State <span style="float: right;"></span>	
98B- Border Bridge % <span style="float: right;"></span>	
101- Parallel Structure <span style="float: right;">N</span>	
EPA ID <span style="float: right;"></span>	
Stay in Place Forms <span style="float: right;"></span>	

Print Date 6/9/2010 16:27:26

**Bridge Safety Inspection Report**

Facility	Federal Structure ID	Inspector Name	Agency / Consultant	Inspection Date	<b>LEGEND</b> 9 New 7-8 Good 5-6 Fair 3-4 Poor 2 or Less Critical			
SILVER BELL	83260103000R010	TRAHEYAMY	great lakes engineer	03/10/2010				
Feature	Latitude	Longitude	Struc Num	Insp Freq		Insp Key		
GTW RR	424321.65	831524.12	8191	5		GHPG		
Location	Length	Width	Year Built	Year Recon		Br Type	Scour Eval	No.Pins
EAST OF GIDDINGS	221.7847	64.304	1981			1	05	N

09 09 10

**NBI INSPECTION**

**Deck**

1. Surface SIA-58A	4 4 4	Travel width reduced to two lanes due to deterioration in beams and pier caps. One EB and one WB lane now run where the original WB lanes were located. Several open longitudinal reflective cracks along beam lines (up to 5" wide), some opening into deep spalls with surrounding delamination. The cracks in span 1w were being patched with flashcrete at the time of inspection. The full depth hole (5" x 5") in eastbound right lane at joint 1w, span 1w has been patched with bituminous. Some bituminous patched spalls. Ponding along south curb, all spans.(2010). Several open longitudinal reflective cracks along beam lines (up to 5" wide), some opening into deep spalls in spans 1 & 3w, with surrounding delamination. Full depth hole (5" x 5") in eastbound right lane at joint 1w, span 1w. Wet, open transverse cracks in span 2w with surrounding delamination. Some bituminous patched spalls. Ponding along south curb, all spans (wet day).(2009). Several open longitudinal reflective cracks, some opening into deep spalls, in spans 1 & 3, with surrounding delamination. Some bit patched spalls. Wet, open transverse cracks in span 2 with surrounding delamination (2009).
2. Expansion Jts	3 3 3	Block out expansion joint 2w is loose, missing filler and leaking heavily onto superstructure and substructure elements below. Bituminous patches along 70% of length of joint 2w. (2010). Block out expansion joint 2w is loose, missing filler and leaking heavily onto superstructure and substructure elements below. Bituminous patches along 70% of length of joint 2w.(2009). Block out exp. jt. is loose, missing filler and leaking heavily onto superstructure and substructure elements below. Bit patching at both expansion joints (2009).
3. Other Joints	3 3 3	West end joint: Bituminous patched spalls along full length of joint causing impact to vehicles. Leaking. Compression seal joint 1w: Full depth hole (5" x 5") in eastbound right lane, span 1w has been patched with bituminous. Adhesion failures and heavy leakage observed below. Bituminous filled spalls along 70% of joint. East end joint: Bituminous patches along 50% of joint. Leaking. (2010). West end joint: Bituminous patched spalls along full length of joint causing impact to vehicles. Leaking. Compression seal joint 1w: Full depth hole (5" x 5") in eastbound right lane, span 1w. Adhesion failures and heavy leakage observed below. Bituminous filled spalls along 70% of joint. East end joint: Bituminous patches along 50% of joint. Leaking.(2009). Compression seal has open spalls in EB direction lanes, only a few are bit filled. Full depth spall at south end of compression seal joint. Adhesion failures and heavy leakage observed below. Impact at the west end joint from spalls.(2009).
4. Railings	7 7 7	Open concrete parapet railing with handrail. Vertical cracks, typical. Pedestrian fencing on both sides. Moderate corrosion along pedestrian fences. (2010). Open concrete parapet railing with handrail. Vertical cracks, typical. Pedestrian fencing on both sides. Moderate corrosion along pedestrian fences.(2009). Open concrete parapet railing with handrail, typical vertical cracking. Pedestrian fencing on both sides. (2009).
5. Sidewalks or curbs	6 6 6	Concrete curb and gutter in approaches has transverse cracks with some small spalls. Tight random cracks in sidewalks. Large accumulation of debris on sidewalks. (2010). Concrete curb and gutter in approaches has transverse cracks with some small spalls. Tight random cracks in sidewalks. Large accumulation of debris on sidewalks. (2009). Curb & gutter in approaches cracked, some spalls. Large accumulation of debris on sidewalks (2009).
6. Deck SIA-58	4 4 4	Fascias: Leaching cracks, typical. Surface: Travel width reduced to two lanes due to deterioration in beams and pier caps. One EB and one WB lane now run where the original WB lanes were located. Several open longitudinal reflective cracks along beam lines (up to 5" wide), some opening into deep spalls with surrounding delamination. The cracks in span 1w were being patched with flashcrete at the time of inspection. The full depth hole (5" x 5") in eastbound right lane at joint 1w, span 1w has been patched with bituminous. Some bituminous patched spalls. Ponding along south curb, all spans. Soffit: Side by side concrete box beams prevent inspection of the deck bottom surface. Wetness and leaching at joints between beams. Damage to box beams indicates wetness is permeating through wearing surface.(2010). Fascias: Leaching cracks, typical. Surface: Several open longitudinal reflective cracks along beam lines (up to 5" wide), some opening into deep spalls in spans 1 & 3w, with surrounding delamination. Full depth hole (5" x 5") in eastbound right lane at joint 1w, span 1w. Wet, open transverse cracks in span 2w with surrounding delamination. Some bituminous patched spalls. Ponding along south curb, all spans (wet day). Soffit: Side by side concrete box beams prevent inspection of the deck bottom surface. Wetness and leaching at joints between beams. Damage to box beams indicates wetness is permeating through wearing surface. (2009). Leaching cracks typical in both deck fascias. Extensive wetness observed below and damage to box beams indicates wetness is permeating through wearing surface. (2009).
7. Drainage		Catch basins in approach shoulders at all quads 30-50' from reference lines. (2010). Catch basins in approach shoulders at all quads 30-50' from reference lines.(2009).
9. Paint SIA-59A	N N N	
10. Section Loss	N N N	
11. Bearings	5 5 5	Elastomeric bearing pads at abutments and piers. Difficult to inspect, but appear to be bulging. (2010). Elastomeric bearing pads at abutments and piers. Difficult to inspect, but appear to be bulging. (2009). Elastomeric bearing pads. Hard to inspect, but appear to be bulging (2009).

**Substructure**



**Bridge Safety Inspection Report**

63 2 8010301R01

Facility SILVER BELL	Federal Structure ID 83280103000R010	Inspector Name TRAHEYAMY	Agency / Consultant great lakes engineer	Inspection Date 03/10/2010
Feature GTW RR	Latitude 424321.65	Longitude 831524.12	Struc Num 8191	Insp Freq 6
Location EAST OF GIDDINGS	Length 221.7847	Width 64.304	Year Built 1981	Year Recon 1
			Br Type 05	Scour Eval N
				No.Pins

LEGEND	
9	New
7-8	Good
5-6	Fair
3-4	Poor
2 or Less	Critical

**NBI INSPECTION**

12. Abutments SIA-60 3 3 3 | Vertical leaching cracks in both abutments. Delaminated areas at both abutments, approximately 10 sft total. Heavy map cracks at base of southeast wingwall. Heavy wetness observed along both abutments due to leaking end joints. (2010). Vertical leaching cracks in both abutments. Delaminated areas at both abutments, approximately 10 sft total. Heavy wetness observed due to leaking end joints. (2009). Few vertical leaching cracks in both abutments. Delaminated areas at both abutments, approximately 10sft total. Wetness observed due to leaking enc joints. (2009).
13. Piers SIA-60 3 3 3 | Pier 1w: Spalls to steel in west face of cap below beams 1-3s (40 sft), 5-8s (60 sft), and 17-20s (100 sft). Spall to steel in east face of cap below beams 17-20s (100 sft). Spall to steel in underside of cap between columns 7s and 8s. Open horizontal crack along top of cap. 10 sft spall to steel at north end of crash wall. Pier 2w: Spalls to steel in west face of cap below beams 1-3s (60 sft) and 6-7s (10 sft). Spalls to steel in east face of cap below beams 1-3s (60 sft) and 17-19s (30 sft). Spalls to steel in underside of cap between columns 1-2s and 7-8s. Horizontal crack in west face of cap between columns 2-3s (15'). Open vertical crack in column 2s (1/8" wide). (2010). Pier 1w: Spall to steel and heavy map cracking with efflorescence in west face of cap below beams 5-8s. Open horizontal crack along top of cap. Approximately 40 sft spall to steel at south end of cap below beams 1-3s, 100 sft at north end below beams 17-20s. 10 sft spall to steel at north end of crash wall. Pier 2w: Spall to steel in cap under beams 1-3s (60 sft), 6-7s (10 sft), and 17-19s (30 sft). Horizontal crack in west face of cap between columns 2-3s (15'). Open vertical crack in column 2s (1/8") (2009). Pier 1w: Spall to steel and heavy map cracking with efflorescence in face of cap below beams 5-8s. Open horizontal crack along top of cap. Approx 40 sft spall to steel at south end of cap. 90 sft at north end. 10 sft spall to steel at north end of crash wall. Pier 2w: Spall to steel in cap under beams 1-3s (60 sft), 6-7s (10 sft), and 17-19s (30 sft) (2009). Slope paving has minor cracks and some heaving on west slope. Debris accumulation on slopes due to spalled box beams. (2010). Slope paving has minor cracks and some heaving on west slope. Debris accumulation on slopes due to spalled box beams. (2009). Slope paving has minor cracks and some heaving on west slope. (2009).
14. Slope Protection 3 6 6 | Approach
15. Approach Pavt 3 5 5 | Bituminous paved approaches. Minor rutting, open transverse cracks, and tight longitudinal cracks. West approach has patched potholes near end joint causing impact, heaviest at westbound lanes. (2010). Bituminous paved approaches. Minor rutting, open transverse cracks, and tight longitudinal cracks. West end approach has patched potholes near end joint causing impact, heaviest at westbound lanes. (2009). Bituminous paved approaches. Minor rutting, open transverse cracking. West end approach has patched potholes near end joint causing impact. (2009).
16. Approach Shldr Swalks 3 5 5 | Concrete curb and gutter at approaches has transverse cracks with some small spalls. Catch basins in all quads 30-50' from reference lines. (2010). Concrete curb and gutter at approaches has transverse cracks with some small spalls. Catch basins in all quads 30-50' from reference lines. (2009). Curb & gutter in approaches cracked, some spalls. (2009).
17. Approach Slopes | Vegetated. (2010). Vegetated. (2009). Vegetated. (2009).
18. Utilities | Overhead lines to the south. (2010). Overhead lines to the south. (2009). Overhead lines to the south. (2009).
19. Channel SIA-61 N N N |
20. Drainage Culverts

**MISCELLANEOUS**

Guard Rail	09 10 10	Crit Feat Insp(SIA-92)	71 Watr Adeq	General Notes
36A	1 0 1 1	92A Frac Crit	72 Appr Align	6 month frequency due to deteriorated box beams, broken strands, and spalled pier caps. Travel reduced to two lanes. Recommend load analysis for additional broken strands in beam 8s, span 1w. Posted 33/43/45T.
36B	1 1 1 1	92B Und. Watr	Temp Supp	
36C	0 0 0 0	92C Spl. Insp	Hi Ld Hit (M)	
36D	1 1 1 1		Special Insp Equip.	

<b>Facility Carried</b> SILVER BELL	<b>Federal Structure ID</b> 83280103000R010	<b>Inspector Name</b> TRAHEYAMY	<b>Agency Consultant</b> great lakes infrastructure group	<b>Inspection Date</b> 03/10/2010			
<b>Feature Intersected</b> GTW RR	<b>Latitude</b> 424321.65	<b>Longitude</b> 831524.12	<b>Struc Num</b> 8191	<b>Region</b> 7- Metro	<b>Insp Freq</b> 8	<b>Insp Key</b> FGOF	
<b>Location</b> EAST OF GIDDINGS	<b>Length</b> 87.6	<b>Width</b> 19.6	<b>Year Built</b> 1961	<b>Year Recon</b>	<b>Br Type</b> 1 05	<b>Scour Eval</b> N	<b>No Pins</b>

## CORE ELEMENTS INSPECTION

English Units

Element Number	Element Name	Total Quantity	State 1		State 2		State 3		State 4		State 5	
			Old	New	Old	New	Old	New	Old	New	Old	New
22 / 4	Conc Deck W Rigid Ov	14316	0	0	0	0	14316	0	0	0	0	0
402 / 4	Compression Jt Seal	95	0	0	0	0	95	0	0	0	0	0
411 / 4	Block Out Exp Joint	95	0	0	0	0	95	0	0	0	0	0
72 / 4	Sidewalk	2659	2619	40	0	0	0	0	0	0	0	0
321 / 4	Reinf Conc Appr Slab	2	0	0	0	2	0	0	0	0	0	0
104 / 4	Prestr Conc Box Beam	4439	3239	1000	100	100	100	0	0	0	0	0
331 / 4	Concrete Bridge Rail	443	403	40	0	0	0	0	0	0	0	0
310 / 4	Elastomeric Bearing	80	0	80	0	0	0	0	0	0	0	0
205 / 4	Reinf Conc Column	16	12	4	0	0	0	0	0	0	0	0
215 / 4	Reinf Conc Abut	259	219	30	10	0	0	0	0	0	0	0
234 / 4	Reinf Conc Pier Cap	190	50	50	60	30	0	0	0	0	0	0

## CREW RECOMMENDATIONS

Deck Patching	H	Patch open spalls and cracks in surface.
Approach Pavement		
Joint Repair	H	Replace joints.
Railing Repair		
Detailed Inspection		
Zone Paint		
Substructure Repair	H	Patch spalls in both pier caps.
Slope Repair		
Brush Cut		
Other Crew Work	H	Monitor beams for further deterioration. Perf

## CONTRACT RECOMMENDATIONS

Bridge Replacement	H	Replace structure.
Superstructure Replacement	H	Replace superstructure, repair substructu
Deck Replacement		
Overlay		
Widen		
Paint		
Zone Paint		
Pin and Hanger		
Substructure Repair	H	Substructure repair to piers.
Other Contract Work		

## Appendix C – Test Set-up for Active Infrared Thermography on the Silverbell Bridge Beam



Figure C.1 Active infrared thermography test set-up at the location W1.



Figure C.2 Active infrared thermography test set-up at the location W2.



Figure C.3 Active infrared thermography test set-up at location W3.



**Figure C.4 Active infrared thermography test set-up at the location E1.**



**Figure C.5 Active infrared thermography test set-up at the location E2.**



**Figure C.6 Active infrared thermography test set-up at the location E3.**



**Figure C.7 Active infrared thermography test set-up at the location E4.**



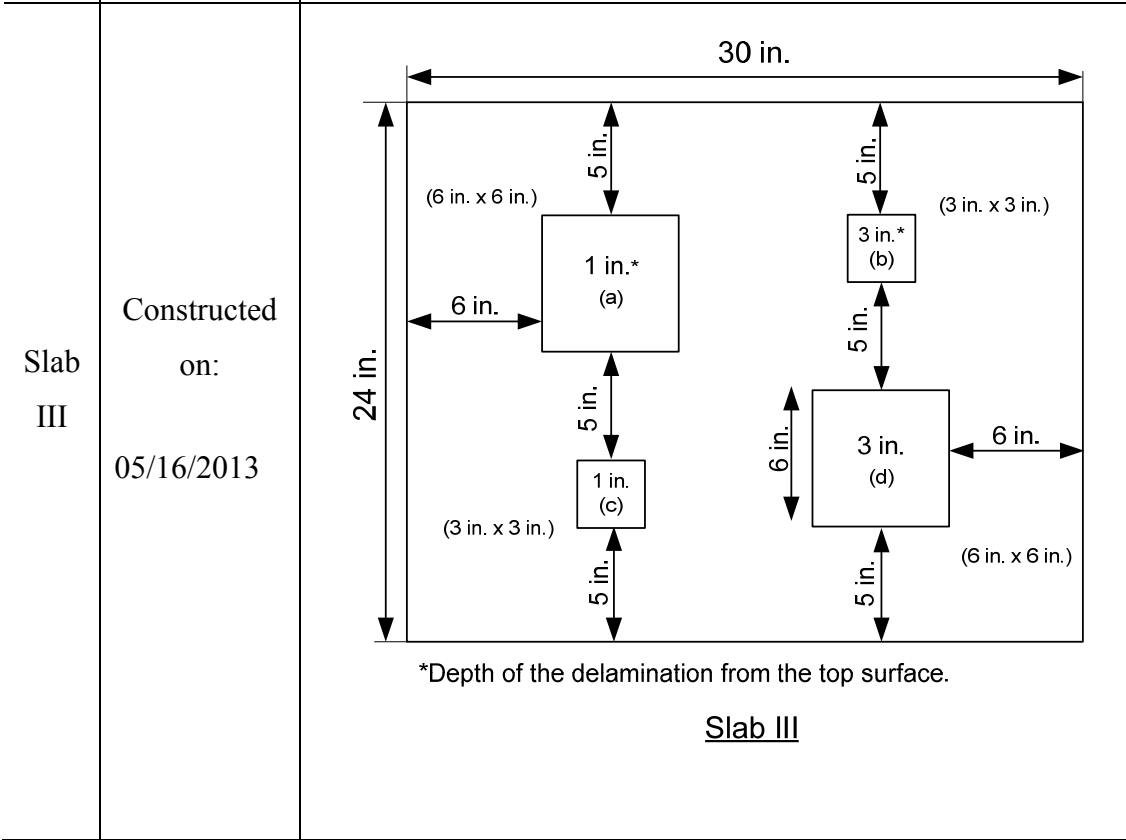
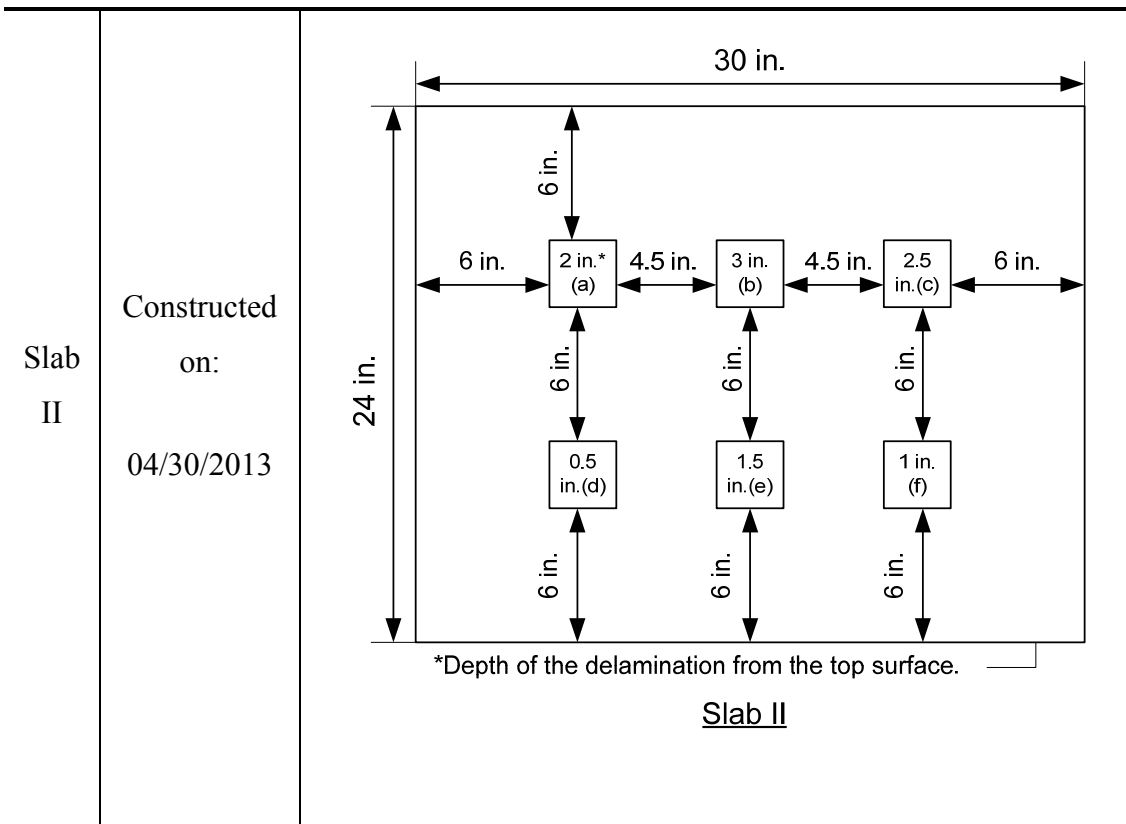
**Figure C.8 Set-up for Active infrared thermography at location W4, where no delamination is evident.**



## Appendix D – Coring Results for Concrete Slabs in Chapter 5

### Slabs Plan

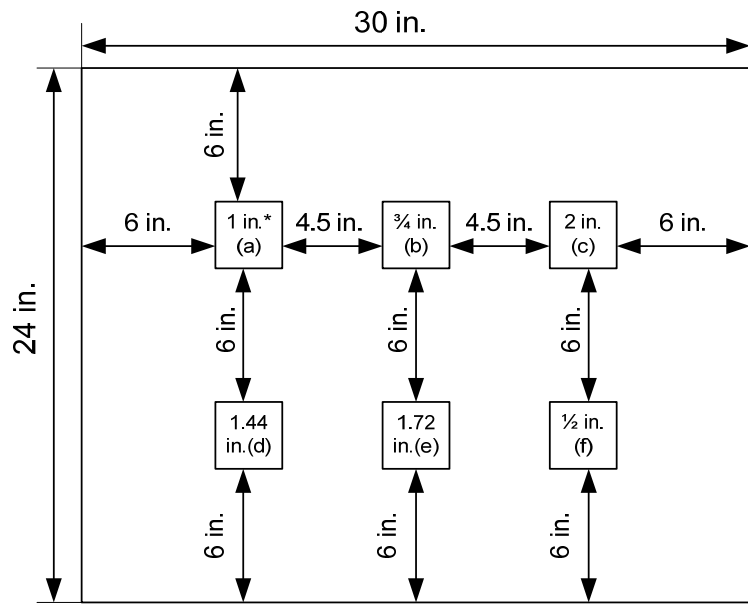
<p>Slab A</p>	<p>Constructed on:  January 2010</p>	<p>48"</p> <p>48"</p> <p>A: 3.5" x 2.75"x1.5" wood located at 2" from the top surface          B: 2 x # 3 rebar located at 4.5" from the top surface          C: 6" x 6"x 1/4" Corroded plate located at 2.5" from the top surface          D1: 2.75" x 6" x 5/8" Styrofoam located at 4" from the top surface          D2: 2.5" x 6" x 1.5" Styrofoam located at 4" from the top surface          E: 2" x 12" x 1/8" metal bar located at 4" from the top surface          F1: 2.75" x 6" x 5/8" Styrofoam located at 2" from the top surface          F2: 2.5" x 6" x 1.5" Styrofoam located at 2" from the top surface          G: 4" x 3.5" x 1.5" and 1" x 3" x 1/2" Galvanized scrap metal located at 4" from the top surface          H: 6" x 9" x 0.003" Plastic bag located at 2" from the top surface</p>
<p>Slab I</p>	<p>Constructed on:  11/15/2012</p>	<p>30 in.</p> <p>24 in.</p> <p>6 in.</p> <p>6 in.</p> <p>6 in.</p> <p>6 in.</p> <p>6 in.</p> <p>6 in.</p> <p>6 in.</p> <p>6 in.</p> <p>4.5 in.</p> <p>4.5 in.</p> <p>6 in.</p> <p>2 in.* (a)</p> <p>3 in. (b)</p> <p>1 in. (c)</p> <p>2 in. (d)</p> <p>3 in. (e)</p> <p>1 in. (f)</p> <p>* Depth of the delamination from the top surface.</p> <p><u>Slab I</u></p>





Slab  
IV




06/06/2013









\*Depth of the delamination from the top surface.





Slab IV





## Cores

Core No.	Location	Photo	Planned Depth	Depth determined by coring	Width to Depth Ratio (actual)	Detected?
I-a	Slab I		2	1.25	2.4	√
I-b	Slab I		3	2.25	1.33	×
I-c	Slab I		1	0.75	4	√




Core No.	Location	Photo	Planned Depth	Depth determined by coring	Width to Depth Ratio (actual)	Detected?
I-d	Slab I		2	1.5	2	√
I-e	Slab I		3	2.25	1.33	×
I-f	Slab I		1	0.75	4	√

Core No.	Location	Photo	Planned Depth	Depth determined by coring	Width to Depth Ratio (actual)	Detected?
II-a	Slab II		2	2.875	1.04	×
II-b	Slab II		3	3.5	0.86	×
II-c	Slab II		2.5	3	1	×


Core No.	Location	Photo	Planned Depth	Depth determined by coring	Width to Depth Ratio (actual)	Detected?
II-d	Slab II		0.5	1.5	2	√
II-e	Slab II		1.5	2.25	1.33	×
II-f	Slab II		1	2.625	1.14	×
III-a	Slab III		1	1.75	3.42	√

Core No.	Location	Photo	Planned Depth	Depth determined by coring	Width to Depth Ratio (actual)	Detected?
III-b	Slab III		3	2.875	1.04	×
III-c	Slab III		1	1.25	2.4	√
III-d	Slab III		3	3	2	×
IV-a	Slab IV		1	1.875	1.6	√

Core No.	Location	Photo	Planned Depth	Depth determined by coring	Width to Depth Ratio (actual)	Detected?
IV-b	Slab IV		0.75	0.75	4	√
IV-c	Slab IV		2	1.5	2	√
IV-d	Slab IV		1.44	2.25	1.33	√

Core No.	Location	Photo	Planned Depth	Depth determined by coring	Width to Depth Ratio (actual)	Detected?
IV-e	Slab IV		1.72	2.125	1.41	√
IV-f	Slab IV		0.5	1.5	2	√
A- F2	Slab A		2	0.5	5	√



Core No.	Location	Photo	Planned Depth	Depth determined by coring	Width to Depth Ratio (actual)	Detected?
A- F1	Slab A		2	1	2.75	√



## Appendix E – Permissions to Reprint Copyrighted Materials

### *Permission to Reprint Figure 3.2*



Legal/Permissions  
One Lake Street  
Upper Saddle River, NJ 07458  
Fax: 201-236-3290  
Phone: 201-236-3564  
Cheryl.Freeman@Pearson.com

Jul 10, 2013

PE Ref # 178309

KHATEREH VAGHEFI  
Michigan Technological University  
Civil Eng. Dept.  
1400 Townsend Dr.  
Houghton, MI 49931

Fax #: 906-487-2943

Dear Ms. Vaghafi:

You have our permission to include content from our text, ***REMOTE SENSING OF THE ENVIRONMENT: AN EARTH RESOURCE PERSPECTIVE, 2nd Ed.*** by **JENSEN, JOHN R.**, in your Ph.D. dissertation for your studies at Michigan Technological University.

Content to be published in PDF format on website at Michigan Technological University and several copies for personal use:

- Page 275 Figure 8-22

Please credit our material as follows:

***JENSEN, JOHN R, REMOTE SENSING OF THE ENVIRONMENT: AN EARTH RESOURCE PERSPECTIVE, 2nd Edition, © 2007. Reprinted by permission of Pearson Education, Inc., Upper Saddle River, NJ***

Sincerely,

A black rectangular box redacting the signature of Cheryl Freeman.

Cheryl Freeman, Permissions Administrator

## Permission to Reprint Figure 3.3

6/26/13

Michigan Technological University Mail - copyright permission

**Michigan Tech**

Khatereh Vaghefi <[kvaghefi@mtu.edu](mailto:kvaghefi@mtu.edu)>

---

### copyright permission

---

Cindi Leeman <[CLEeman@asnt.org](mailto:CLEeman@asnt.org)>  
To: Khatereh Vaghefi <[kvaghefi@mtu.edu](mailto:kvaghefi@mtu.edu)>

Thu, Jun 20, 2013 at 8:09 AM

I'm really sorry for the delay!

Yes, you have permission to use the figure. Please use this disclaimer:

Used with permission from "Thermal Imaging of Damage in Bridge Soffits," by Glen Washer published in ASNT NDE/NDT for Highways and Bridges: Structural Materials Technology (SMT) 2010. The American Society for Nondestructive Testing, Columbus, OH.

Cindi

Cynthia M. Leeman

Educational Materials Supervisor  
ASNT  
P.O. Box 28518  
Columbus, OH 43228-0518  
[cleeman@asnt.org](mailto:cleeman@asnt.org)  
800/222-2768; 614/274-6003 X225  
Hours: M-F 7:30 a.m. to 4 p.m.  
[www.asnt.org](http://www.asnt.org)

From: Khatereh Vaghefi <[kvaghefi@mtu.edu](mailto:kvaghefi@mtu.edu)<<mailto:kvaghefi@mtu.edu>>>  
Date: Wednesday, June 19, 2013 12:29 PM  
To: Cindi Leeman <[cleeman@asnt.org](mailto:cleeman@asnt.org)<<mailto:cleeman@asnt.org>>>  
Subject: Re: FW: copyright permission

Cindi

I was wondering if you have been able to get the proper citation and copyright permission for reprinting this figure (email below). Please let me know if you need additional information from me.

Thanks,  
- Khatereh

---

Khatereh Vaghefi  
PhD Candidate  
Department of Civil and Environmental Engineering  
Michigan Technological University  
829 Dow Building, 1400 Townsend Drive, Houghton, MI 49931  
[kvaghefi@mtu.edu](mailto:kvaghefi@mtu.edu)<<mailto:kvaghefi@mtu.edu>>

On Thu, Jun 6, 2013 at 12:22 PM, Khatereh Vaghefi <[kvaghefi@mtu.edu](mailto:kvaghefi@mtu.edu)<<mailto:kvaghefi@mtu.edu>>> wrote:  
Cindi

<https://mail.google.com/mail/u/0/?ui=2&ik=42ae17a3f4&view=pt&cat=Dissertation&search=cat&msg=13f617c897955d37>

1/3